Deep Penetration Magnetoquasistatic Sensors

by

Yanko Sheiretov

B.S., Massachusetts Institute of Technology (1992)
M.S., Massachusetts Institute of Technology (1994)
E.E., Massachusetts Institute of Technology (1998)

Submitted to the Department of Electrical Engineering and Computer Science
in partial fulfillment of the requirements for the degree of

Doctor of Philosophy

at the

MASSACHUSETTS INSTITUTE OF TECHNOLOGY

June 2001

Author .....
Department of Electrical Engineering and Computer Science
May 24, 2001

Certified by .....
Markus Zahn
Professor of Electrical Engineering
Thesis Supervisor

Accepted by .....
Arthur C. Smith
Chairman, Department Committee on Graduate Students

Deep Penetration Magnetoquasistatic Sensors

by

Yanko Sheiretov

Submitted to the Department of Electrical Engineering and Computer Science
on May 24, 2001, in partial fulfillment of the
requirements for the degree of
Doctor of Philosophy

Abstract

This research effort extends the capabilities of existing model-based spatially periodic quasistatic-field sensors. The research developed three significant improvements in the field of nondestructive evaluation. The impact of each is detailed below:

1. ***The design of a distributed current drive magnetoresistive magnetometer that matches the model response sufficiently to perform air calibration and absolute property measurement.*** Replacing the secondary winding with a magnetoresistive sensor allows the magnetometer to be operated at frequencies much lower than ordinarily possible, including static (DC) operation, which enables deep penetration defect imaging. Low frequencies are needed for deep probing of metals, where the depth of penetration is otherwise limited by the skin depth due to the shielding effect of induced eddy currents. The capability to perform such imaging without dependence on calibration standards has both substantial cost, ease of use, and technological benefits. The absolute property measurement capability is important because it provides a robust comparison for manufacturing quality control and monitoring of aging processes. Air calibration also alleviates the dependence on calibration standards that can be difficult to maintain.

2. ***The development and validation of cylindrical geometry models for inductive and capacitive sensors.*** The development of cylindrical geometry models enable the design of families of circularly symmetric magnetometers and dielectrometers with the "model-based" methodology, which requires close agreement between actual sensor response and simulated response. These kinds of sensors are needed in applications where the components being tested have circular symmetry, e.g. cracks near fasteners, or if it is important to measure the spatial average of an anisotropic property.

3. ***The development of accurate and efficient two-dimensional inverse interpolation and grid look-up techniques to determine electromagnetic and geometric properties.*** The ability to perform accurate and efficient grid interpolation is important for all sensors that follow the model-based principle, but it is particularly important for the complex shaped grids used with the magnetometers and dielectrometers in this thesis.

A prototype sensor that incorporates all new features, i.e. a circularly symmetric magnetometer with a distributed current drive that uses a magnetoresistive secondary element, was designed, built, and tested. The primary winding is designed to have no net dipole moment, which improves repeatability by reducing the influence of distant objects. It can also support operation at two distinct effective spatial wavelengths. A circuit is designed that places the magnetoresistive sensor in a feedback configuration with a secondary winding to provide the necessary biasing and to ensure a linear transfer characteristic. Efficient FFT-based methods are developed to model magnetometers with a distributed current drive for both Cartesian

and cylindrical geometry sensors. Results from measurements with a prototype circular dielectrometer that agree with the model-based analysis are also presented.

In addition to the main contributions described so far, this work also includes other related enhancements to the time and space periodic-field sensor models, such as incorporating motion in the models to account for moving media effects. This development is important in low frequency scanning applications. Some improvements of the existing semi-analytical collocation point models for the standard Cartesian magnetometers and dielectrometers are also presented.

Thesis Supervisor: Markus Zahn
Title: Professor of Electrical Engineering

Acknowledgments

This research project was sponsored by JENTEK Sensors, Inc. I would like to thank Dr. Neil Goldfine, president of JENTEK and member of the thesis committee, for providing financial sponsorship, encouragement, many helpful suggestions, and enthusiastic support. Dr. Goldfine fosters a supportive and accommodating work environment at JENTEK, which allowed me to take advantage of the company's resources, and gave me freedom to direct my efforts towards areas of greatest interest to me.

Many thanks go to my thesis supervisor, Professor Markus Zahn, not only for his guidance and critical support of my work in this thesis, but also for being a mentor for many years. I consider myself very lucky to have been able to learn from Professor Zahn for almost thirteen years, starting from my first year at MIT. Since then I have gone to him for advice on numerous occasions, not only for academic matters, but for personal and career choices as well. I would also like to thank the other thesis committee members, Professors Jeffrey Lang, Terry Orlando, and Bernard Lesieutre, for their insightful comments at the defense and at our committee and individual meetings.

Darrell Schlicker provided the highest level of support throughout the entire project. This was especially important in the last several months. He designed the impedance analyzer instruments used in most experiments. I have drawn on his expertise in electronics in the design of the interface and support circuitry of the magnetoresistive sensor. Whenever baffled by a particular measurement result or a theoretical derivation, I went to Darrell for a brainstorm session. His willingness to help and generosity with which he lends his time are qualities I have rarely found in others. Many aspects of this thesis would have been much more difficult without his help. Thanks!

I would like to thank my other co-workers at JENTEK for their help in my work on this project and for making it possible to devote so much of my time to my thesis. In particular, I would like to thank Joni Goday for handling the financial aspects of my research, Dr. Andrew Washabaugh for our numerous discussions of the mathematical and physical models, Paula Gentile for help with graphics and literature, Dr. Vladimir Zilberstein for help with the choice and design of the test samples, Vladimir Tsukernik for the drawing and machining of the sensors and samples, Chris Root for finding potentially useful material samples, Wayne Ryan for help with the ferrofluid experiments, and Dr. Karen Walrath for help with the sensor prototype and for general advice. I would also like to thank my close friends Michelle McDevitt and Jacqueline Aylas for manuscript review and emotional support.

Finally, I am truly grateful to my partner, Leo T. Mayer, for his love, support, and patience over the last five years. He has helped me through many difficult times, and his unwavering faith in me has always been a steady source of confidence and motivation.

Contents

List of Figures

List of Tables

Chapter 1

Introduction

The goal of this research effort is to extend the capabilities of existing sensor technology based on quasistatic magnetic and electric fields with imposed spatial periodicity. The main application area for such sensors is in nondestructive evaluation of materials, especially detection of flaws such as cracks, voids, and inclusions in metal components. They can also be used for more general measurement of a material's magnetic and dielectric properties, i.e. electric conductivity, magnetic permeability, and dielectric permittivity, which can be related to other physical properties of interest, such as density, thermal conductivity, chemical composition, residual mechanical stress, etc. Geometric parameters of a test structure, such as layer thickness and proximity, can also be measured with such sensors. An overview of existing sensor technology is presented in Section 1.1.

The most important new idea explored in this work is the use of a giant magnetoresistive sensor in place of the secondary magnetometer winding. This makes it possible to operate the magnetometer at frequencies much lower than ordinarily possible, including DC operation, since the magnetoresistive sensors respond to the magnitude of the magnetic flux density, as opposed to the induced voltage in a secondary winding, which is proportional to the rate of change of the linked magnetic flux. Low frequency operation is necessary for deep probing of metals, where at higher frequencies the depth of penetration of the magnetic fields is limited by the skin depth effect, caused by induced eddy currents.

Until now almost all sensors have been designed with rectangular geometry, suitable for analysis in Cartesian coordinates. While modeling and numerical simulation of eddy current sensors in cylindrical geometry have been done in the past, the existing semi-analytical collocation point models cannot be used to describe sensors in alternative coordinate systems. In this work the existing semi-analytical collocation point methods, used to model the meandering winding magnetometer and the interdigital dielectrometer, are extended to cylindrical coordinates, making them suitable to model sensors with circular geometry. These kinds of sensors are needed in applications where parts being tested have cylindrical geometry, e.g. testing for cracks near fasteners, or when it is important to measure the average of an anisotropic property, as discussed in more detail in Chapter 3.

One of the main difficulties in developing semi-analytical models for the magnetometers is that magnetic diffusion effects cause the winding current to be nonuniform across the winding traces. Thus the drive current density is not known at the outset, requiring the use of collocation point methods. The sensor models can be made significantly simpler and more efficient if the nonuniformity of the current distribution inside the conductors can be ignored, because the known excitation current density can then be broken down into its constitutive spatial

Fourier modes, and the magnetic fields can be obtained as a superposition of the solutions for all wavenumber modes.

There is a class of sensors where this assumption can be justified. There the magnetic fields are shaped by a number of windings, each with a varying number of turns, that follow a sinusoidal envelope function in Cartesian geometry or a first order Bessel function in cylindrical geometry. The physical dimensions of each winding, width and thickness, are much smaller than the imposed spatial wavelength, the distance between the windings in the primary, and the distance between the secondary winding and the nearest primary winding segment. This makes it possible to treat the windings as infinitely thin, allowing the driven current density to be modeled as a series of spatial impulse functions.

Methods are developed for efficient modeling of this class of sensors. Such sensors are needed in applications that require high depth of sensitivity, where the standard periodic sensor geometry would result in sensor footprints too large to be practical. Using a distributed current drive makes it possible to have an imposed spatial period on the order of the sensor length and width. These methods are also extended to cylindrical coordinates.

A prototype sensor incorporating all of these features, i.e. a circularly symmetric magnetometer with a distributed current drive using a magnetoresistive secondary element, is built and tested in a variety of representative applications, confirming the validity of the semi-analytical models, and demonstrating the new capability of low frequency operation for deep penetration in metals.

The order in which material is presented in this thesis is chosen to avoid using a result before its derivation. The existing collocation point models, with some changes and improvements, are described in Chapter 2. Chapter 3 develops the corresponding models in cylindrical geometry. The methods used to model distributed current drive sensors are presented in Chapter 4, and the design and experimental results of the circularly symmetric, distributed current drive, magnetoresistive sensor are presented in Chapter 5.

1.1 Imposed ω-k quasistatic sensors

Almost all of the work in this research project is aimed at extending the capabilities of sensor technology based on spatially periodic quasistatic fields. Such dielectrometer and magnetometer sensors have been the focus of several research projects at the Laboratory of Electromagnetic and Electronic Systems (LEES) at MIT for many years [1–11]. This section describes some of the commercially developed sensors based on this work.

The basic idea behind the imposed ω-k quasistatic sensors is that the magnetometer windings or dielectrometer electrodes are laid out in a spatially periodic pattern on a substrate, making one-sided contact with the material under test. The imposed spatial period (wavelength) λ determines the rate of decay of the fields away from the sensor and is chosen to achieve the desired depth of sensitivity. The frequency of excitation does not affect this depth of sensitivity of the dielectrometer,* and also of the magnetometer at low frequency or with nonconducting materials. Skin depth effects on the magnetic field at high frequency in conductors result in a calculable decrease in magnetic field penetration depth with increasing frequency. The periodic nature of the potentials and fields allows for the use of Fourier series methods in the semi-analytical models.

*See the foot note on page 70.

The spatially periodic quasistatic sensors have several advantages over alternative sensing technologies:

1. Control over the depth of sensitivity allows for measuring profiles of material properties by combining the results of measurements at varying depths, controlled by varying sensor wavelength, or by varying frequency in good conductors with magnetometers.

2. The layout allows for a good match between simulated and measured sensor response with the simulations carried out with efficient collocation point methods, described in Chapter 2. This reduces the need for elaborate calibration standards and procedures.

3. The flexible substrate makes it possible to measure on curved surfaces, with the curvature having no appreciable effect on sensor response.

4. The sensor geometry allows for the creation of sensor arrays, with good uniformity between individual array elements. The simulation methods remain valid for arrays.

1.1.1 Meandering Wavelength Magnetometer (MWM™)

The MWM,* originally called the Inter-Meander Magnetometer, was conceived at the MIT Laboratory for Electromagnetic and Electronic Systems by Professor James R. Melcher as the magnetic analogue of the interdigital electrode dielectrometer. It is suitable for measurements of conductivity, complex permeability, and thickness for single- and multiple-layered magnetic and/or conducting media. The sensor was further developed at JENTEK and has been successfully applied to a variety of practical applications [12–17]:

- Early stage fatigue measurement of metallic components and fatigue test coupons [18–23].
- Anisotropic property measurement [24], e.g. permeability, related to residual stress, or conductivity, resulting from cold working.
- Crack detection in metal components [19, 22, 25, 26].
- Coating characterization [25–28], e.g. thermal barrier coatings.
- Ceramic coating thickness measurement [28].
- Quality control for shotpeened and cold worked areas, independent of surface roughness [18, 26, 27, 29].
- Weld quality [29].
- Measurement of applied and residual stress in ferromagnetic materials, such as carbon steel [30].
- Surface characterization and measurement of subsurface corrosion [27, 31].

The sensor geometry, with flat rectangular meandering windings, provides a number of advantages over conventional eddy current sensors, including the following:

- Accurate modeling of sensor response.
- Ability to determine absolute properties such as electrical conductivity and magnetic permeability.
- Ability to perform one-sided magnetic anisotropy measurements.
- Accurate determination of lift-off, i.e. proximity to a conductive or magnetic surface.
- Ability to conform to curved surfaces, including areas of double curvature.

*MWM is a trademark of JENTEK Sensors, Inc.

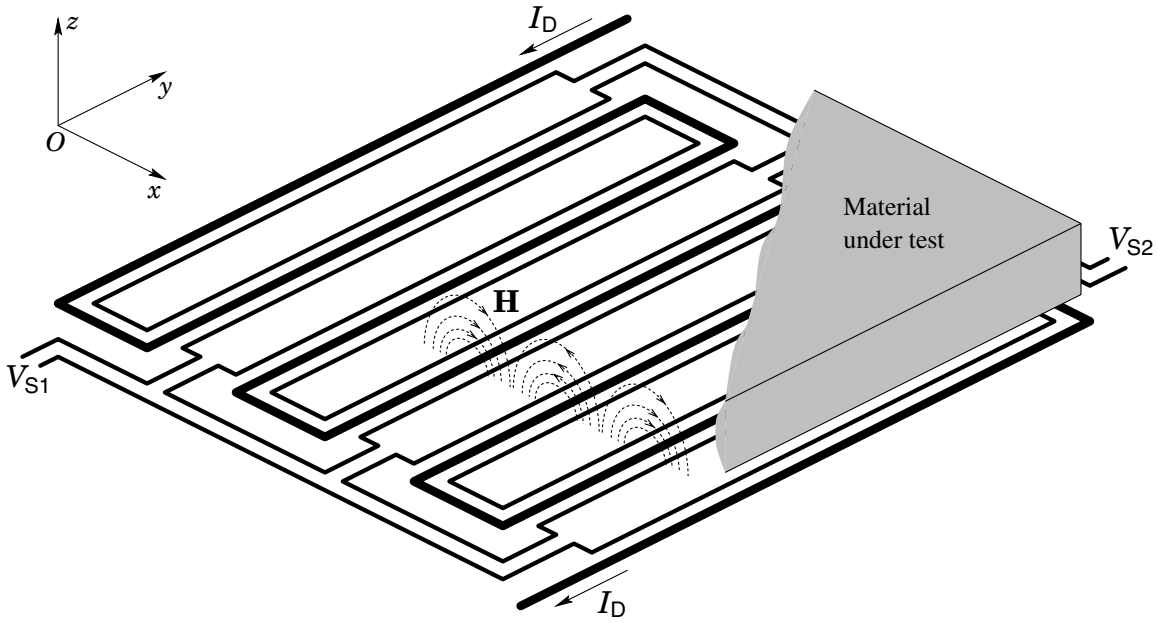

Figure 1-1: Layout of a typical MWM. The primary winding (wider trace) is driven with a current I_D. It generates a spatially periodic magnetic field **H**, shown for three meanders for $z > 0$. The secondary windings (narrower trace) link some of this flux, and the voltages induced at their terminals are V_{S1} and V_{S2}. The two secondary windings are usually connected in series ($V_S = V_{S1} + V_{S2}$) or in parallel ($V_S = V_{S1} = V_{S2}$). The sensor's complex transimpedance, defined as $Z_{21} = V_S/I_D$, is directly linked to the properties of the material under test.

- Additional control over the depth of sensitivity through the spatial winding wavelength.
- Ability to be permanently mounted in poorly accessible locations for on-line monitoring of damage [21].
- Ability to scan with and without direct contact with a component.

Figure 1-1 shows a schematic of the MWM. It consists of a primary winding and one or more secondary windings laid out in a periodic pattern on an insulating flexible substrate. The imposed spatial periodicity of the current excitation results in a periodic magnetic vector potential. In the absence of conducting materials the vector potential and the magnetic field intensity satisfy Laplace's equation and decay away from the sensor surface with a characteristic length proportional to the imposed spatial wavelength. In most cases, however, the material under study is metal, which means that the governing equation is the magnetic diffusion equation. The characteristic decay rate in this case is a function of both the imposed spatial wavelength and the skin depth of the material, with the shorter one dominating, according to equation (2.14).

The methods used to calculate the predicted sensor response are described in detail in Chapter 2.

1.1.2 Magnetometer arrays

The possibility of two-dimensional imaging provided by magnetometer arrays is important in military and civilian de-mining operations because the more detailed information that an image provides can be used to reduce the number of false positives caused by other buried

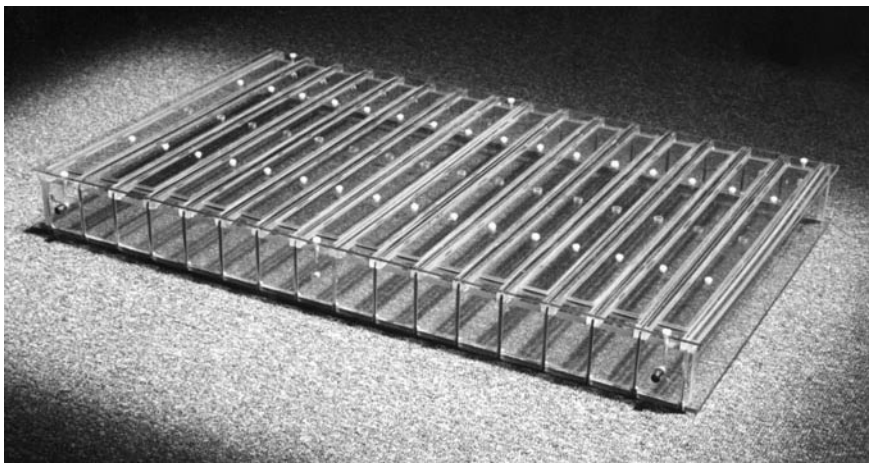

Figure 1-2: Photograph of large (0.85×0.50 m) MWM Array, developed at JENTEK for use in metal land mine detection [32]. There are eight sensing elements, not visible in this photograph, situated in a row between the two center windings.

metal debris [32, 33]. These arrays implement the idea of using several windings to shape the magnetic field so that the fundamental wavelength is approximately equal to the sensor width [34, 35]. This idea is further discussed in Chapter 4.

Figure 1-2 shows a photograph of large MWM Array developed at JENTEK for use in metal land mine detection [32]. An array of secondary windings provides a one-dimensional profile of the material properties along the direction of the primary windings. Moving the sensor array in the perpendicular direction extracts a two-dimensional image of the material properties such as the one shown in Figure 1-3.

1.1.3 Interdigitated electrode dielectrometer (IDED™)

The layout of a typical interdigitated dielectrometer is shown in Figure 1-4. A voltage V_{D} is applied to the driven electrode, while the sensing and guard electrodes are kept at ground potential. A spatially periodic electric field is generated, which penetrates the material under

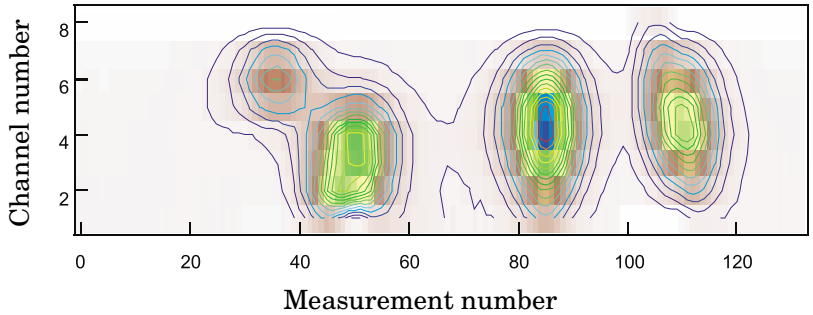

Figure 1-3: Two-dimensional scan image generated with the large MWM array at JENTEK [32]. This is a contour plot of the sensor signal. Four large metal objects have been identified in this scan. The measurement number corresponds to the x coordinate where the scan length is approximately equal to $80''$. The channel number, identifying each array element, corresponds to the y coordinate, with scan area width of $15''$.

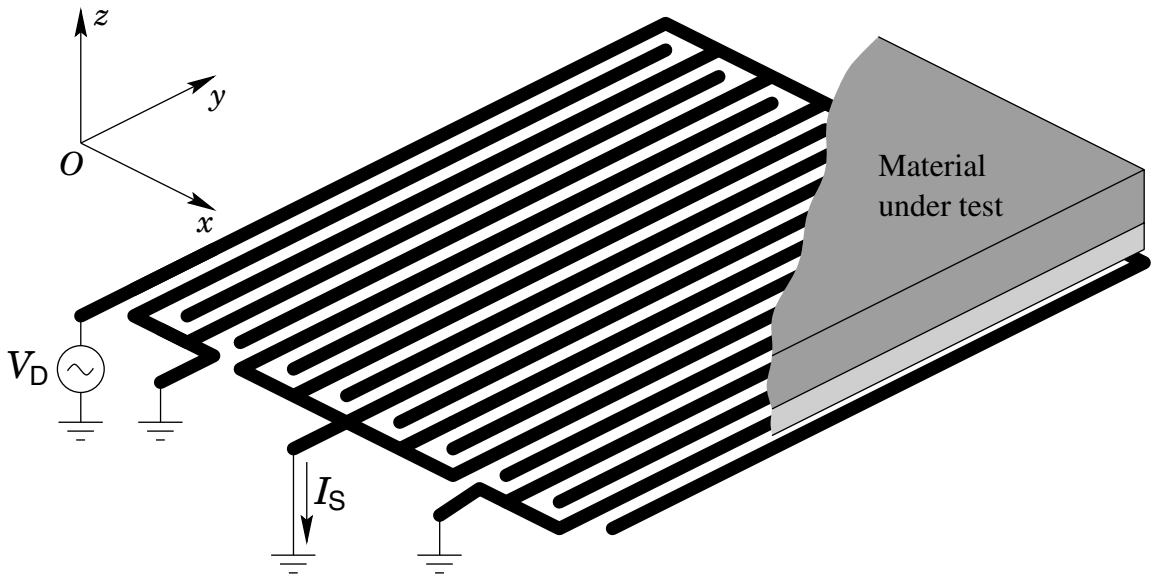

Figure 1-4: Schematic layout of an IDED. There are two interdigitated comb electrodes. A driving voltage V_D is applied to one of them, the driven electrode, while the second one, the sensing electrode, is kept at ground potential. The sensor transadmittance is defined as $Y_{21} = I_S/V_D$, where I_S is the current out of the sensing electrode. Two grounded fingers at either side do not contribute to the signal I_S in order to reduce the end effects due to the sensor's finite length.

test. The electric field lines originate on the driven electrode and terminate on the sensing or guard electrodes. The changing surface charge on the sensing electrode is balanced by the terminal current I_S. The sensor's complex transadmittance, defined as $Y_{21} = I_S/V_D$, is directly linked to the properties of the material under test. The model used to simulate the interdigital dielectrometer is presented in Section 2.2.

The IDED* is suitable for measurements on insulating or slightly conducting dielectric materials. For reasons discussed in Section 3.2, measurements with the dielectric sensors are generally more difficult than the magnetic sensors, because there are often more unknown parameters than degrees of freedom. Still, the interdigitated dielectrometer is in use in several practical applications:

- Cure monitoring of polymers, epoxy, etc. [36].
- Measurement of porosity and thermal conductivity in ceramic thermal barrier coatings [28].
- Moisture measurement in transformer oil and pressboard [3, 5–8, 11].
- Thin film characterization.

The cure monitoring application has received some attention recently [36]. During the chemical reactions of the curing process the materials exhibit significant conductivity, which is a strong function of the curing stage and continues to decrease for a long time after the compound has officially attained its full strength. The conductivity is due to the presence of free radicals during curing. Its value and rate of change are directly related to the curing process, making it possible to identify clearly the different stages of the chemical reaction.

*IDED is a trademark of JENTEK Sensors, Inc.

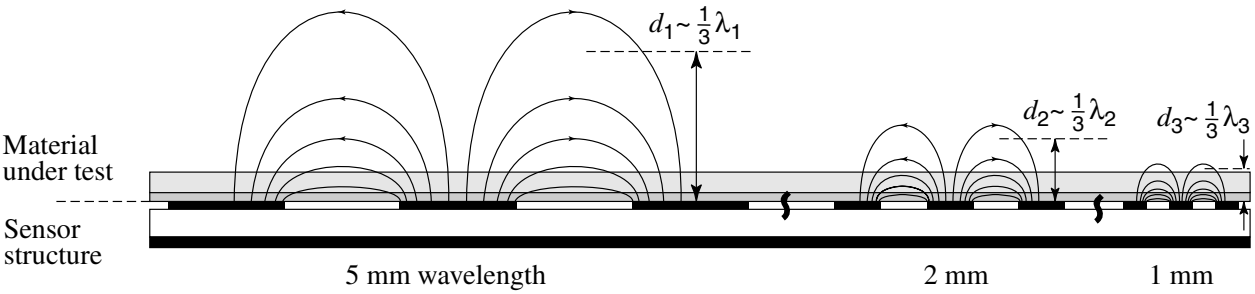

Figure 1-5: Electric field lines for a three-wavelength dielectric sensor. The electric field lines generated by the sensor with the largest wavelength penetrate furthest into the material. The depth of sensitivity d is considered to be roughly one third of the spatial wavelength λ.

Furthermore, from the point of view of the parameter estimation methods, the presence of conductivity adds another degree of freedom in the form of nonzero transcapacitance phase angle. The measurement of moisture in dielectrics also takes advantage of the presence of finite conductivity in the insulation.

1.1.4 Multiple-Wavelength Dielectrometer

The depth of sensitivity of the sensor depends on the imposed spatial wavelength, as seen in Figure 1-5. Combining the results of sensors with different wavelengths can be used to measure properties as a function of depth or to estimate more than one unknown parameter. This is especially useful for measurements where direct contact with the material is not possible, such as noncontact cure monitoring [36]. The lift-off, i.e. the air gap thickness, is usually not known, especially with the material deposited on a moving web, where some vertical motion, or flutter, is inevitable. This requires the simultaneous estimation of three unknown parameters: the permittivity and conductivity, which change with cure state, and the lift-off. What complicates matters even more is that the thickness of the film may be nonuniform, adding another unknown to the set of properties that need to be estimated simultaneously.

In cases like this it is beneficial to combine the response of several sensors with different spatial periods. Figure 1-6 shows the layout of a three-wavelength sensor. Although it is possible, the use of multiple wavelengths in magnetometers is usually not necessary, since inside conducting materials magnetic diffusion makes it possible to change the depth of sensitivity by changing the frequency, which changes the skin depth.

Multiple-wavelength dielectrometers have also been used to monitor the diffusion of moisture into pressboard. The moisture content is related to the conductivity and permittivity. The use of multiple wavelength sensors makes it possible to measure the variation of the conductivity and permittivity with depth [7, 8, 11].

1.2 Goals

The goal of this research effort is to extend the capabilities of the existing spatially periodic quasistatic-field sensors, with a focus on the magnetometers. Stated concisely, the main goals are:

1. Incorporate magnetoresistive technology into sensor design to allow low frequency magnetometry measurements.

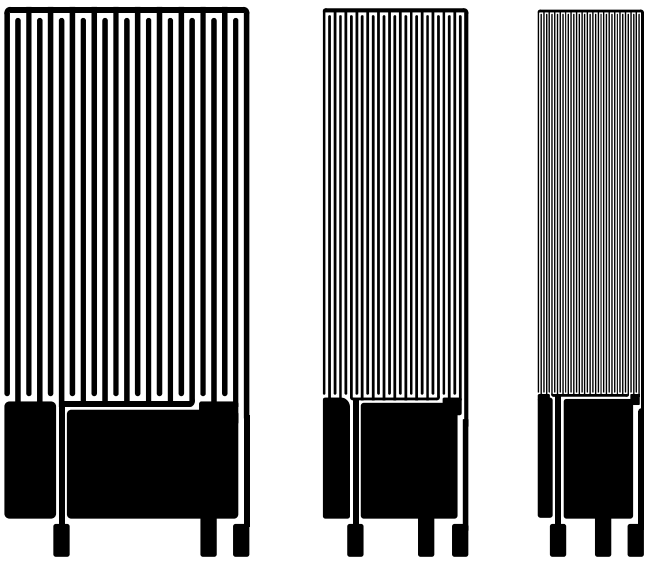

Figure 1-6: Layout of a $5/2/1$ mm three-wavelength dielectric sensor.

   (a) Build prototype magnetometers that use magnetoresistive sensors.
   (b) Build interface circuitry to connect to existing instrumentation.
   (c) Make measurements to illustrate a variety of practical applications.

2. Extend models to describe sensors with cylindrical geometry. Using circularly symmetric sensors offers advantages in a variety of applications.

   (a) Develop mathematical models for dielectric and magnetic sensors.
   (b) Implement models numerically to generate measurement grids.
   (c) Build and test magnetometer and dielectrometer prototypes.

3. Build and model sensors with distributed current drive to allow for sensors whose spatial wavelength is on the order of the sensor footprint.

   (a) Develop efficient semi-analytical models for this type of sensor.
   (b) Implement models numerically to generate measurement grids.
   (c) Demonstrate validity of the models in practice.

4. Combine all these ideas in the design of a circularly symmetric magnetoresistive magnetometer with a distributed primary winding. Use it to make measurements on a set of representative test structures.

1.3 Motivation

Sensing and measurement of magnetic fields in general is an important field that has many applications in science and industry. In the area of nondestructive evaluation (NDE) of materials, magnetic fields are used to find structural defects, such as cracks, corrosion, etc., in metals, using eddy current or other techniques based on magnetic fields. There are many applications in medicine, where magnetic fields are used to create images of tissues and internal organs.

1.3.1 Magnetoresistive sensors

The main reason to explore the use of magnetoresistive and giant magnetoresistive sensors as an alternative to the secondary winding of the standard magnetometers is their ability to operate at low excitation frequencies, down to DC. Operation at low frequencies is required when testing materials for deeply buried flaws, which are otherwise hidden by the skin depth, $\delta \propto 1/\sqrt{\omega}$.

Magnetizable materials can even be measured with constant magnetic fields. In the absence of magnetic diffusion, the problem of calculating the magnetic field becomes analogous to the electroquasistatic sensor.

Another reason for lowering the frequency of excitation is that at high frequencies a material's conductivity and magnetic permeability cannot be measured independently [1]. This considerably complicates conductivity measurements of ferromagnetic materials, such as steel, because local permeability variations pollute the conductivity measurement. Such permeability variations may be due, for example, to residual stresses.

There are several complications associated with the use of magnetoresistive sensors in the magnetometer design. They have a highly nonlinear transfer characteristic. The nonlinearity is in fact very extreme, since the sensors are insensitive to the polarity of the magnetic field (see Figure 5-5). For this reason they are typically biased at an appropriate operating point by an independent constant magnetic field source, such as a permanent magnet or a solenoid. Since the magnetic field effects a resistivity change, the sensors also need electrical biasing and an appropriate bridge configuration. Many of these issues are addressed by placing the sensor in a feedback loop, as discussed in Chapter 5.

A few examples where low frequency operation, made possible by the use of magnetoresistive sensors, is beneficial are:

- Subsurface corrosion (airplane skins, etc.).
- Flaws in magnetic media (hard drives, etc.).
- Detection of deeply buried defects in metals, or features in metals positioned below a shielding material.
- Thickness measurement for metal components ($0.1 - 2''$).
- Stress profile measurement in steel.

1.3.2 Modeling sensors with rotational symmetry

So far all periodic field magnetometers and dielectrometers, like the MWM and the IDED, have been designed with Cartesian geometry, i.e. the magnetic or electric fields have an imposed periodicity in the x-direction and are considered invariant in the y-direction. Designing circularly symmetric sensors offers several advantages and may be preferred in some applications:

1. They have fewer unmodeled end effects:
    - The edges due to finite sensor width in the y-direction are completely eliminated, since there are no edges in the φ-direction in cylindrical coordinates.
    - In the dielectric case the edges due to the finite length in the x-direction can be removed far from length scales of interest in the r-direction in cylindrical coordinates, since the models assume the electric potential to be fixed at zero by a ground plane at distances from the origin greater than the end of the inter-electrode gap.

2. The circular geometry ensures insensitivity to anisotropic properties, by effectively taking an average of the property in all directions in the x-y plane. This is useful in certain applications, since it eliminates the need for precise sensor alignment when measuring ferromagnetic materials whose magnetic permeability is anisotropic.

3. Many material defects and human-made structures have rotational symmetry, making them ideal candidates for testing with rotationally symmetric sensors. An example application is testing for cracks near rivets and bolts.

1.3.3 Magnetometers with distributed current drive

There are applications where the imposed spatial wavelength of the magnetic field needs to be large for large penetration distances. An application that has such a requirement is land mine detection. In order to be sensitive to a metal object located 15 cm below the surface, the magnetometer must have a spatial wavelength of about 50 cm or more, which results in a footprint of several square meters with the standard MWM geometry shown in Figure 1-1. Since this is impractical, sensors have been developed where the magnetic field is generated by several windings, each having a different number of turns, that follows a sinusoidal envelope function. The fundamental wavelength of this envelope function is several times greater than the winding spacing. This makes it possible to reduce the sensor footprint to be on the order of the wavelength, or approximately 0.4 square meters. The distributed current drive concept was developed by Dr. Neil Goldfine at JENTEK [32, 34, 35].

Another class of applications where a larger effective spatial wavelength is required, relative to the sensor footprint, is testing for deeply buried flaws in metals. Use of low excitation frequencies and magnetoresistive secondary elements, as discussed in Section 1.3.1, overcomes the depth limitation due to skin depth. In order to overcome the depth limitation due to the imposed spatial wavelength, the sensor wavelength must be made several times larger than the desired depth of sensitivity. Whereas in this application the resulting footprint of a standard magnetometer layout may not be too large from a logistical perspective, a smaller footprint makes the flaw signature more localized and improves sensitivity, since the flaw signature is not averaged over a large area.

A further advantage of having a distributed current drive is that the effective spatial wavelength may be changed dynamically, e.g. by varying the relative phase of two or more superimposed windings, an idea discussed further in Section 4.10.

From a modeling perspective, an advantage of this kind of magnetic field excitation is that the drive current distribution is known from the beginning, since the width of the windings is small compared to the wavelength and may be approximated as being infinitely narrow. This significantly simplifies numerical computation, since it makes it possible to apply fast discrete Fourier transform methods directly, as shown in Chapter 4. These efficient methods may also be applied to the MWM if one of the following circumstances is met:

1. Low frequency operation; the current is uniform across each winding.

2. High frequency operation; the current is concentrated at the winding edges and may be represented by spatial impulse functions.

3. The current distribution effects are negligible or can be calibrated out, using the standard calibration methods discussed in Appendix D.

1.4 Inverse estimation methods

Chapter 2 describes the forward models used to calculate the response of the MWM and IDED from the sensor geometry parameters and the properties of the materials. During a measurement the reciprocal task needs to be accomplished, which is to obtain absolute material properties from the measured sensor response.

Several different methods have been used to approach this inverse problem. The method most commonly used in practice uses measurement grids. It is described in Section 1.4.1. An alternative approach is to use a root-finding method, which uses the forward model over many iterations [7, 8]. There are many difficulties with this approach. The function that relates sensor response to material properties is nonlinear, resulting in failure of the method if the solution is not unique or if noise in the data leads to the lack of an exact solution. Furthermore, because the method seeks an exact solution, the number of unknowns must equal the number of degrees of freedom exactly. For example, if three unknowns are being measured with an MWM at several frequencies [26], this method cannot be used, as every frequency produces two constraints. While it is possible to simply ignore the extra constraints, there is a much better alternative, which makes use of all data. This alternative to the root-finding methods uses a least squares minimization technique to estimate multiple unknowns, and has been successfully applied in a number of practical problems [26]. It is discussed in Section 1.4.2.

Another approach proposed recently [37], which also avoids the need for iteration, can be taken for estimating the conductivity and permittivity of a single unknown layer in a dielectrometer measurement. In this method the inverse problem is formulated as a generalized eigenvalue problem, where the complex unknown parameter is one of the generalized eigenvalues. The multiple layers problem can be posed as a multi-variable eigenvalue problem.

1.4.1 Measurement grids

The method of parameter estimation using measurement grids was invented by Dr. Neil Goldfine [1, 38]. The standard two-dimensional measurement grid is a database of sensor responses calculated for a range of values of two material properties. For every combination of values of the two parameters, the magnetometer transinductance or dielectrometer transcapacitance are computed and tabulated. The parameter estimation is then carried out by using a two-dimensional inverse interpolation technique, to obtain the material properties that correspond to the measured sensor response. It is also possible to have one-dimensional grids, which relate a single unknown parameter to one measured quantity. Interpolation in this case is usually trivial.

Measurement grids may be visualized by plotting every point in magnitude/phase space and connecting points that correspond to a constant parameter with lines. Figure 5-8 shows a typical conductivity/lift-off grid, where the two variable material properties are the conductivity of an infinitely thick metallic layer and the sensor lift-off, which is the distance between the material and the sensor windings. The two measured variables do not have to be magnitude and phase, although this is by far the most common situation. Figure 3-6 shows a magnitude/magnitude grid [54], combining the response of two separate dielectric sensors to measure dielectric permittivity and lift-off independently. Similarly, Figure 5-10 shows a magnetic magnitude/magnitude grid, where the two magnitudes correspond to magnetometer measurements at two different spatial wavelength modes, excited within the same sensor footprint. Other examples of two-dimensional measurement grids include the thickness/lift-

off magnetometer grid in Figure 5-13 and the conductivity/thickness magnetometer grid in Figure 5-15.

Visual inspection of a measurement grid can be used to assess in which region of the grid the measurements have the highest sensitivity. In regions where the grid cells have small areas, small changes in the instrument magnitude and phase lead to large changes in the estimated properties, so that measurements that fall in such regions have lower accuracy than measurements in the grid regions with large cell areas. Another aspect of the quality of a measurement is its selectivity, which is a measure of how independent the two estimated parameters are of each other [13]. The orthogonality of the cell edges is related to the measurement selectivity in that region of the grid. The sensitivity and selectivity of a measurement can be analyzed using singular value decomposition of the Jacobian matrix [1, 13].

Although grid methods have been in use for a long time now, a new implementation has been developed, presented in Section 6.2, which leads to significant improvements both in the efficiency of the grid look-up and the accuracy of the results from the interpolation.

The power of parameter estimation via measurement grids stems from two important advantages that this method has over alternative techniques:

1. ***Reliability.*** The parameter estimation is guaranteed to succeed if the data are on the grid, i.e. if the measurement data fall inside the range area of the grid in magnitude/phase space. All other methods are iterative, which means that there is always some danger of nonconvergence for a point that should have a solution, especially if the initial guess is too far from the solution. Even for points off the grid, but still close to it, the estimated properties are usually reasonable, while if iterative methods fail to converge, the errors are typically dramatic. Reliability is a very important requirement in commercial applications, where the individual user may not have the ability to assess the quality of the data in a way possible in a laboratory environment.

2. ***High speed.*** Although the efficiency of the forward models has been greatly improved by a judicious formulation that allows for much of the computations to be carried out only once for a given sensor geometry (see Chapter 2), in general all iterative methods are orders of magnitude slower than the grid look-up method. With present day technology, typical numbers may be 5 to 10 seconds for a minimization algorithm estimation versus 20 to 30 milliseconds for a grid look-up. This makes it possible to carry out parameter estimation in real time, which is another feature of commercial value, especially in scanning and imaging applications [23, 31, 32].

The main practical disadvantage of using measurement grids is that this approach on its own cannot be used to estimate more than two unknowns.* It can still be possibly used as a step in some different iterative estimation algorithm. Since the properties are estimated via interpolation, there is always some error for points lying between the grid points. The accuracy can be improved by generating denser grids, but the need to store large amounts of data in operative memory and on disk necessarily creates an unfavorable trade-off situation between efficiency and accuracy. Stated another way, the cost of the estimation rises very rapidly with improved accuracy, in contrast with iterative methods, where the opposite is typically true.

*In theory, the grid methods may be extended to three or more dimensions, but the complexity of the grid look-up and inverse interpolation increases exponentially with the number of dimensions. Grid look-ups in more than two dimensions have not yet been demonstrated in practice.

1.4.2 Minimization methods

The least-squares minimization parameter estimation algorithm appears to be the best choice for estimating more than two unknowns. It operates by defining an error function based on the differences between measured and simulated sensor response. Using iterative applications of the forward model, a set of parameters are found where the error function has a minimum, establishing the set of material properties most likely to yield results matching the measured data. If the problem is not over-determined, i.e. if the number of degrees of freedom equals the number of unknowns, then finding a minimum where the value of the error function is zero is equivalent to finding an exact solution.

The main advantage of this method is its universal applicability, most useful in cases where there are no alternative estimation methods. It is also valuable in attempting to find the most likely material property values over a range of experimental conditions. For example, standard grid methods can be used for measuring the conductivity of a metal at several frequencies independently, but the least-squares minimization method can combine the data from all frequencies in a single estimation, thus finding the optimal solution over the entire frequency range. Finally, since the forward model is run with the exact set of material properties, the final result is typically more accurate than the grid interpolation method.

As discussed before, the reason that this method is not used universally is that it is relatively slow and that it is not guaranteed to find a solution, or that the solution is the correct one when it does, since the error function can have many local minima.

1.5 Magnetic field sensing technologies

One possible way of enhancing magnetometer performance is by using an alternative to replace the secondary winding as the means of detecting the magnetic field by a different type of magnetic sensor. This section describes in very general terms some of the existing methods for detecting and measuring magnetic fields, how they compare to each other, and whether they are suitable for this application.

The simplest magnetic sensor is a “search coil,” which is a winding typically on a circular or square frame. The voltage induced at its terminals responds to changing magnetic flux linked by the winding. Since it only depends on the rate of change of the linked magnetic flux, a sensor of this type is limited to higher frequencies, and when stationary is incapable of measuring DC fields. The magnetoresistive sensors, on the other hand, are sensitive over a wide frequency range, including zero. Along with sensors based on the Hall effect and the giant magnetoresistive effect, these sensors are used when the application requires measurement of low-frequency magnetic fields. A review and comparison of existing magnetic field sensors is presented in [39].

Some of the methods used for measuring magnetic fields, along with their range of sensitivity, are listed in Figure 1-7. Table 1.1 shows a list of the advantages of the magnetoresistive sensor and some application areas, as shown in [40].

There are many other factors, such as cost, size, ease of calibration, temperature sensitivity and temperature range of operation, which affect the choice of magnetic sensor for a given application. Eddy current sensors used in nondestructive evaluation applications, for example, are based on the search-coil sensor. Since they are sensitive to the rate of change of magnetic flux, their use is often limited to relatively high frequencies, typically 1 kHz – 10 MHz. At these frequencies, however, structural materials such as aluminum and steel

Advantages	
High sensitivity	– allowing operation over relatively great distances
Low source resistance	– giving low sensitivity to electrical interference
High-temperature operation	– 150°C continuous, 175°C peak (chip alone can withstand 175°C continuous)
Operation over a wide frequency range	– from DC up to several MHz
Metal-film technology	– giving excellent long-term stability
Low sensitivity to mechanical stress	– facilitating mounting of the sensor and allowing its use in relatively rough environments
Small size	– can be fabricated with micron dimensions
Application areas	
Traffic control	– detection of vehicles
Low-cost navigation	– allowing the production of simple compass systems with an accuracy of around 1°, ideal for automotive applications
Long-distance metal detection	– for the detection of, for example, military vehicles by measuring disturbances in the earth's magnetic field
Motion detectors	– by measuring position changes relative to the earth's magnetic field
Current detection	– for example, earth leakage switches
General magnetic field measurement	– from 10 A/m to 10 kA/m
Direct-current measurement	– starting currents in motor vehicles
Angular or position measurement	– sensing of accelerator pedal or throttle position (engine-management systems) – position sensing in industrial automation systems (commercial sensor arrays that can measure positions with an accuracy of 30 m) – force/acceleration/pressure measurement using a moving magnet, for example: engine-intake-manifold pressure sensors, fluid-level sensors, low-cost weighing systems, geosonic (seismic) sensors, accelerometers
Mark detection and counting	– camshaft or flywheel position sensors for engine ignition systems – end-point sensors – wheel-speed sensors for anti-blocking systems – rpm counters (0 to 20 kHz) for engine tachometers and for electronic synchromesh systems – flow meters – zero speed detectors — rpm control in electric motors – general instrumentation
Magnetic recording	– thin-film replay heads for tape and disk systems. Swipe readers for credit cards, bus tickets, door locks, etc.

Table 1.1: Magnetoresistive sensors: advantages and application areas.

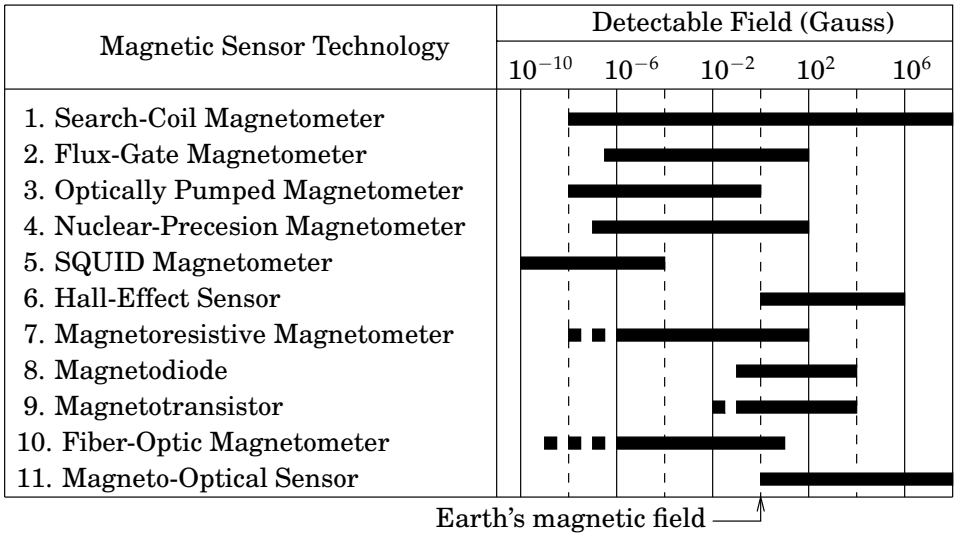

Figure 1-7: Sensitivity comparison of magnetic sensor technologies [39]. The magnetoresistive sensor includes the giant magnetoresistive sensor as well.

have skin depth on the order of tenths of a millimeter, which is a severe limitation to the ability to examine materials for buried flaws. This is an example of an application where low frequency sensitivity, as provided by the magnetoresistive sensor, is of critical importance.

On the other hand, a search-coil based sensor that does not use a magnetizable core has the advantage of having a perfectly linear transfer characteristic, which is a property of this type of sensor only. In order to approach linearity, magnetoresistive and other sensors need to be biased with a constant magnetic field, and operated within a small dynamic range. Linearity concerns for the magnetoresistive sensor are discussed in more detail in [41].

Eddy-current sensor arrays used for two-dimensional imaging have been developed and used successfully to map surface defects in a metal plate [42]. As discussed before, it is difficult to measure buried metal flaws, such as cracks and voids, that lie below a layer of metal with thickness on the order of, or greater than, the skin depth at the excitation frequency. In order to detect such flaws it is necessary to use lower excitation frequencies, which proportionally reduce the sensitivity of eddy current sensors.

To overcome this limitation, SQUID magnetometers have been used for defect mapping, with some limited success [43]. Although SQUID technology has progressed substantially over the last few years [44, 45], it has not yet reached the level of miniaturization and cost that are required for the development of high-density imaging arrays.

The SQUID magnetometer is another extreme example of the tradeoff between the performance characteristics of magnetic sensors [46]. It is sensitive to changes on the order of a fraction of the flux quantum $\Phi_0 = h/2e = 2.07 \times 10^{-7}\text{G}\cdot\text{cm}^2 = 2.07 \times 10^{-15}$ Wb, where h is Planck's constant and e is the electron charge, which makes it the most sensitive magnetic sensor known. However, its response to values of enclosed flux which differ by an integral number of flux quanta is identical. This means that SQUIDs are incapable of measuring absolute magnetic field intensity and that local variations of the Earth's magnetic field and other interference must be "calibrated out", shielded very carefully, or more than one sensor must be connected in a differential mode, before any meaningful data may be obtained from a SQUID. Furthermore, the need for operating the sensor at cryogenic temperatures makes it a costly and rather bulky device, although SQUIDs based on high-T_C superconducting mate-

rials developed recently [44], which can operate at liquid nitrogen temperatures, have made the SQUID magnetometer somewhat more practical.

An interesting application of the SQUID magnetometer to the detection of buried flaws is presented in [45]. In this application the magnetic sensor is used to detect weak magnetic fields generated by local current loops induced by the thermoelectric Seebeck effect when a host metal material contains an inclusion of a different metal and a thermal gradient is present. Magnetizable inclusions can also be detected by this method without the need for a thermal gradient. In this application the ambient fields are canceled out by a second-order gradiometer configuration that uses three SQUID heads.

Magnetoresistive and giant magnetoresistive sensors are discussed in more detail in Chapter 5.

1.6 Summary of Chapter 1

In this chapter the subject of nondestructive evaluation using time and space periodic-field quasistatic inductive and capacitive sensors has been introduced. The chapter has also introduced some of the fundamental concepts on which much of the rest of the thesis depends:

1. General principles of operation of the model-based quasistatic periodic-field inductive and capacitive sensors (Section 1.1).

2. Measurement grid methods for absolute dielectric, magnetic, conduction, and geometric property estimation (Section 1.4).

3. Review of the state of the art technologies for sensing and measuring magnetic fields (Section 1.5).

A range of new applications that require capabilities of these sensors not available until now have motivated the research for improvements in the following areas:

1. Design of magnetometers with high depth of sensitivity by increasing low frequency signal strength with the use of magnetoresistive sensors, and by exciting magnetic fields with high effective spatial wavelength with the help of a distributed current drive.

2. Development and validation of cylindrical geometry models for inductive and capacitive sensors.

3. Development and validation of efficient numerical techniques for modeling magnetometers with distributed current drive in Cartesian and cylindrical coordinates.

4. Improvement in the accuracy and efficiency of two-dimensional inverse interpolation and grid look-up techniques.

The results of the efforts in all of these areas are presented in the remaining chapters of the thesis.

Chapter 2

Forward Models of the Spatially Periodic Sensors

The analytical models of the cylindrical geometry sensors, developed in Chapter 3, are structured similarly to the collocation point methods in Cartesian geometry. The latter are also often referenced by the methods used to model the magnetometers with distributed current drive, presented in Chapter 4. To supply the background for these topics, it is necessary to include a description of the Cartesian geometry collocation point methods for both magnetoquasistatic and electroquasistatic sensors, along with all important formulas. This is done in this chapter.

Although these methods have appeared many times in the literature [1–3, 7, 47], it has always been difficult to find needed details, and different sources use different conventions. In addition to providing a self-consistent source on which to base the material in the remaining chapters, this chapter describes some changes to the models not previously published. While most of these changes are not fundamental, but aimed mainly at improving computational efficiency and at simplifying the equations, some are quite significant. The most important of these is perhaps the way the zero-order Fourier mode is treated for the dielectric sensors. This is discussed further in Section 2.2.

The MWM is analyzed in the magnetoquasistatic (MQS) regime, which ignores the term in Ampère's law due to the displacement current density. Similarly, the IDED is treated in the electroquasistatic (EQS) regime, which ignores Faraday's law and sets the curl of the electric field intensity to zero. Both cases assume that the contribution of electrodynamic (wave) effects is negligible, which is justified if the spatial period of the electromagnetic waves at the operating frequency is much greater than the characteristic length of the structure. The IDED and the MWM are not operated at frequencies higher than 30 MHz, so that this requirement is typically satisfied by a margin of three orders of magnitude. The magnetoquasistatic approximation is further discussed in Section 2.1.1.

In this chapter and for the rest of the thesis the sensors are assumed to be operated in sinusoidal steady state with angular frequency ω. This means that all time dependent quantities can be written in the following form:

$$F(\mathbf{r},t) = \Re\left\{\widehat{F}(\mathbf{r})e^{i\omega t}\right\} \tag{2.1}$$

where $\widehat{F}$ is a complex amplitude function only of spatial coordinates. Derivatives with respect to time are transformed into multiplications by $i\omega$. The hat accents will be dropped in

subsequent analysis.

For other notation conventions and symbol definitions, refer to Appendix A.

2.1 Mathematical model and simulation method for the MWM

This section contains the formulas used to calculate the response of the MWM, based on the physical models. The equations are put in a form that closely parallels the steps and name conventions used in the numerical simulation code.

This model assumes a secondary winding on either side of the primary, connected in series. All material properties are considered independent of x, y, and time. The material structure is assumed to consist of a number of homogeneous layers stacked up in the z-direction, where the material interfaces are planes parallel to the x-y plane.

2.1.1 Magnetic diffusion

In the magnetoquasistatic regime in the presence of conducting materials the magnetic field must satisfy the magnetic diffusion equation:

$$\nabla^2\mathbf{H} - i\omega\sigma\mu\mathbf{H} = 0 \tag{2.2}$$

which is a direct consequence of Maxwell's equations and Ohm's law [48–50]. For the purpose of this analysis, it is more convenient to find solutions to the magnetic vector potential $\mathbf{A}$, which satisfies the following definition:

$$\nabla \times \mathbf{A} = \mathbf{B} \tag{2.3}$$

Equation (2.3) only defines the curl of the vector potential. Its divergence must also be specified, if $\mathbf{A}$ is to be determined uniquely (within a constant of integration). The divergence can be chosen in a particular problem to simplify the resulting equations, as will be shown later in this section.

Using Faraday's law $\nabla \times \mathbf{E} = -i\omega\mathbf{B}$, where the time derivative has been replaced with a multiplication by $i\omega$ according to equation (2.1), and combining it with equation (2.3) yields

$$\nabla \times \mathbf{E} = -i\omega\nabla \times \mathbf{A} \tag{2.4}$$

Vector fields with equal curl may differ by the gradient of a scalar field, which makes it possible to express $\mathbf{E}$ in terms of $\mathbf{A}$ as

$$\mathbf{E} = -i\omega\mathbf{A} - \nabla\Phi \tag{2.5}$$

where Φ is the electric scalar potential. Combining Ampère's law and Ohm's law with the results obtained so far yields

$$\nabla \times \mathbf{H} = \mathbf{J} = \sigma\mathbf{E} = -\sigma\big(i\omega\mathbf{A} + \nabla\Phi\big) \tag{2.6}$$

which can be manipulated as follows:

$$\nabla \times \big(\nabla \times \mathbf{A}\big) = -\sigma\mu\big(i\omega\mathbf{A} + \nabla\Phi\big) \tag{2.7}$$

$$\nabla^2\mathbf{A} - \nabla\big(\nabla\cdot\mathbf{A}\big) = i\omega\sigma\mu\mathbf{A} + \sigma\mu\nabla\Phi \tag{2.8}$$

$$\nabla^2\mathbf{A} - i\omega\sigma\mu\mathbf{A} = \nabla\big(\nabla\cdot\mathbf{A} + \sigma\mu\Phi\big) \tag{2.9}$$

As mentioned earlier, there is freedom in the choice of the divergence of the vector potential. Therefore the right hand side of equation (2.9) can be set to zero by letting

$$\nabla\cdot\mathbf{A} = -\sigma\mu\Phi \tag{2.10}$$

The differential equation that must be satisfied by $\mathbf{A}$ then becomes

$$\nabla^2\mathbf{A} - i\omega\sigma\mu\mathbf{A} = 0 \tag{2.11}$$

Ignoring end effects, the current in the MWM is always in the y-direction and is independent of y, which means that the same must be true of the vector potential:

$$\mathbf{A} = A_y(x,z)\hat{\mathbf{y}} \tag{2.12}$$

The sensor structure is periodic in the x-direction with period λ, extending to infinity, so that the appropriate set of solutions to equation (2.11) are given by:

$$\mathbf{A} = \big[a_1\sin(kx) + a_2\cos(kx)\big]\big[b_1e^{\gamma z} + b_2e^{-\gamma z}\big]\hat{\mathbf{y}} \tag{2.13}$$

with the complex wavenumber γ defined as

$$\gamma = \sqrt{k^2 + i\omega\sigma\mu} \tag{2.14}$$

or equivalently

$$\gamma = \sqrt{k^2 + \frac{2i}{\delta^2}} \qquad\qquad \delta = \sqrt{\frac{2}{\omega\sigma\mu}} \tag{2.15}$$

where δ is the skin depth in the material.

In the absence of convection, treated separately in Section 6.1, and with an appropriate choice for the point $x = 0$, symmetry considerations, shown later in equation (2.29), eliminate the sine term in equation (2.13).

An important point to consider is that the solutions for the magnetic vector potential in equation (2.13) have no divergence, i.e. $\nabla\cdot\mathbf{A} = 0$. Equation (2.10) then requires the electric scalar potential Φ also to be zero, which means that the electric field in equation (2.5) can be written as

$$\mathbf{E} = -i\omega\mathbf{A} \tag{2.16}$$

While the electric field $\mathbf{E}$ given by equation (2.16) satisfies the boundary conditions at the interfaces of conducting homogeneous metal layers, which require that the tangential component of the field be continuous, in insulating layers and near the winding surface in general it does not. Equation (2.13) shows that $\mathbf{E}$ has only a y-component, while a z-component is needed to account for the electric field component normal to the conductors in the insulating regions. This apparent inconsistency is resolved by realizing that in insulating regions, where $\sigma = 0$, equation (2.10) does not force Φ to zero, and in such regions appropriate solutions to Laplace's equation $\nabla^2\Phi = 0$ will make it possible to determine $\mathbf{E}$ consistently via equation (2.5).

A conclusion that can be drawn from this discussion is that the model applies only when the sensor windings are surrounded by an insulating material. This is anyhow required to constrain the winding current to remain within the windings. Although it is possible to solve for the electric field $\mathbf{E}$ everywhere via Φ, it is not necessary, since the only contribution to the magnetic field by the electric field component due to Φ comes from surface charge and displacement current density, which are effects ignored in the magnetoquasistatic regime.

Another assumption tacitly made in the discussion so far, and a direct consequence of the MQS approximation, is that the materials are either insulators, where $\sigma = 0$, $\Phi \neq 0$, and the electric field lines have a component normal to the conductor surfaces; or good conductors, such as metals, where $\sigma \neq 0$, $\Phi = 0$, and the electric field lines are tangential to the surfaces. In the MQS regime in a current carrying wire the electric field is always tangential to the surface. In the MWM model, the electric field is also tangential to the interface between two conducting layers, because the winding current and the magnetic vector potential everywhere have only a y-component.

If there are materials with conductivity ranges where one of the effects does not dominate the other, it will be necessary to consider the full set of Maxwell's equations, including the treatment of surface charge and displacement current density, with $\Phi \neq 0$ everywhere. This is a much more complicated problem that does not appear to be of great practical significance and will not be considered in this analysis.

It is important to show quantitatively under what conditions the MQS approximation is justified, in addition to the frequency restriction described earlier. This can be done by comparing the magnetic diffusion time $\tau_{\mathrm{m}} = \mu\sigma\ell^2$, where ℓ is a characteristic length scale, such as the sensor spatial wavelength, to the charge relaxation time $\tau_{\mathrm{e}} = \epsilon/\sigma$ [50, §2.3]. In the MQS regime $\tau_{\mathrm{m}} \gg \tau_{\mathrm{e}}$. The conductivity at which the two time constants become equal to each other is given by

$$\sigma = \frac{1}{\ell}\sqrt{\frac{\epsilon}{\mu}} \tag{2.17}$$

which is on the order of 0.1–1 S/m for typical magnetometers. Metal conductivities are typically five or more orders of magnitude greater, as shown in Table 5.2. This justifies the MQS approximation in treating the MWM, which is used almost exclusively for measurements on metals. The same is true for measurements on other relatively conductive nonmetallic materials like graphite, whose conductivity is typically on the order of a few hundred S/m. On the other hand, when considering materials like salt water, for example in soil moisture and contamination measurements, it would be necessary to include the full set of Maxwell's equations.

2.1.2 Normalization

Most of the quantities in the model are normalized appropriately so that they are all dimensionless. This has many advantages, such as simplicity, but also saves on computation, because many variables only appear in expressions of the same form. Moreover, some parameters, such as the frequency, sensor wavelength, meander length, and coil thickness, are altogether eliminated from further computations.

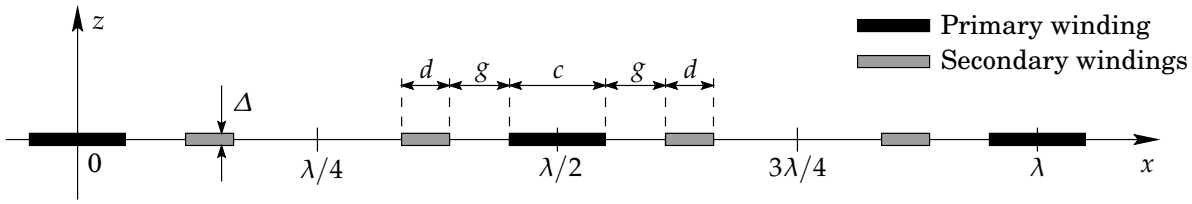

Figure 2-1: Definition of geometry parameters of the MWM. Due to symmetry, only one quarter of a wavelength needs to be considered.

Coordinates

All spatial coordinates are normalized by the wavelength λ:

$$\bar{x} = \frac{x}{\lambda} \qquad \bar{y} = \frac{y}{\lambda} \qquad \bar{z} = \frac{z}{\lambda} \tag{2.18}$$

Sensor parameters

The geometrical parameters of the MWM are shown in Figure 2-1. One period of the sensor is shown in the figure. A period contains the two legs of the primary winding, carrying current in opposite directions, and the two secondary windings. All length parameters, such as the primary winding width c, secondary winding width d, and gap between the windings g, are normalized by the sensor wavelength λ:

$$\bar{c} = \frac{c}{\lambda} \qquad \bar{d} = \frac{d}{\lambda} \qquad \bar{g} = \frac{g}{\lambda} \tag{2.19}$$

One sensor period contains two primary winding traces, four secondary winding traces, and four gaps, which leads to the following inequalities that must be satisfied by the normalized sensor parameters:

$$0 < \frac{\bar{c}}{2}; \bar{d}; \bar{g} < \frac{1}{4} \qquad 0 < \frac{\bar{c}}{2} + \bar{d} + \bar{g} < \frac{1}{4} \tag{2.20}$$

The conductivity always appears in expressions like $\omega\sigma\mu$ (e.g. equation (2.15)) that have units of $[\text{length}^{-2}]$. The proper normalization for the winding conductivity is

$$\bar{\sigma}_{\text{coil}} = \sigma_{\text{coil}} \cdot \mu_0 \omega \lambda \Delta \tag{2.21}$$

where one of the length parameters, Δ, is the thickness of the traces shown in Figure 2-1. The choice of normalizing parameters is motivated by the form of the boundary condition in equation (2.55), derived later. The coil thickness is assumed to be much smaller than the skin depth, $\Delta \ll \delta$.

In deriving the two-port impedance matrix of the MWM, if each port is driven in turn by current with unity magnitude, the terminal voltages will be equal to the two-port impedances. The currents are normalized by the driving current magnitude I_{D}, and the voltages are normalized as follows:

$$\bar{v} = \frac{v}{M_{\text{L}} \mu_0 \omega I_{\text{D}}} \tag{2.22}$$

where M_L is the meander length of the sensor, defined as the total length of the primary winding.

Material parameters

Similar arguments hold for the geometric and physical properties of the material under test. Each layer's properties are normalized as follows:

$$\bar{t} = \frac{t}{\lambda} \qquad \bar{\mu}^* = \frac{\mu^*}{\mu_0} \qquad \bar{\sigma} = \sigma \cdot \mu_0 \omega \lambda^2 \tag{2.23}$$

where t is the layer thickness, μ^* is the complex magnetic permeability, including magnetic loss, and σ is the conductivity.

Other parameters

Other parameters that are normalized include the Fourier harmonic wavenumbers

$$\bar{k}_n = k_n \cdot \lambda = \frac{2\pi n}{\lambda} \cdot \lambda = 2\pi n \tag{2.24}$$

and similarly the complex wavenumbers

$$\bar{\gamma}_n^2 = \bar{k}_n^2 + i\bar{\sigma}\bar{\mu}^* \tag{2.25}$$

The complex wavenumber γ appears in equation (2.13) and is defined by equation (2.14).

For the rest of this chapter the bars will be dropped from the normalized variables to simplify notation. All appropriate variables should be assumed to be normalized, unless explicitly stated otherwise.

2.1.3 Collocation points

The goal is to calculate the two-port matrices of impedances and admittances:

$$\begin{bmatrix} v_1 \\ v_2 \end{bmatrix} = \begin{bmatrix} Z_{11} & Z_{12} \\ Z_{21} & Z_{22} \end{bmatrix} \begin{bmatrix} i_1 \\ i_2 \end{bmatrix} \qquad \begin{bmatrix} i_1 \\ i_2 \end{bmatrix} = \begin{bmatrix} Y_{11} & Y_{12} \\ Y_{21} & Y_{22} \end{bmatrix} \begin{bmatrix} v_1 \\ v_2 \end{bmatrix} \qquad Z = Y^{-1} \tag{2.26}$$

This is accomplished by first finding the vector potential A_y at the surface as a function of the two terminal voltages, and then using it to find the surface current density K_S, integrated across the width of the windings to obtain the terminal currents. For this purpose A_y is represented as a piecewise-linear function, which connects its values at a set of collocation points x_m with linear segments.

If the origin of the x-axis is chosen at the center of the primary winding, symmetry considerations constrain the vector potential in the following way (see Figure 2-1):

$$\left.\frac{\partial A_y}{\partial x}\right|_x = \left.\frac{\partial A_y}{\partial x}\right|_{-x} \tag{2.27a}$$

$$A_y(x) = -A_y\left(x + \frac{1}{2}\right) \tag{2.27b}$$

The constraint on A_y that results from equation (2.27a) is

$$A_y(x) = A_y(-x) + A_C \tag{2.28}$$

where A_C is an arbitrary constant of integration. Since only derivatives of the vector potential are meaningful, this constant may be set to zero for convenience, letting the symmetry constraints be written as

$$A_y(x) = A_y(-x) \tag{2.29a}$$

$$A_y(x) = -A_y\left(x + \frac{1}{2}\right) \tag{2.29b}$$

Choosing $A_C = 0$ also ensures that the Fourier series expansion, developed in Section 2.1.4, has no zero order term.

The symmetry properties in equation (2.29) mean that specifying A_y over one quarter of the period is sufficient to determine it everywhere else. The piecewise-linear representation of A_y in this interval is given by:

$$A_y(x) = \frac{(x_{m+1} - x)a_m + (x - x_m)a_{m+1}}{x_{m+1} - x_m} \qquad x_m < x < x_{m+1} \quad m = 0, 1, \ldots, 4K-1 \tag{2.30}$$

where a_m are the values of A_y at the points x_m. Lower case a is used because A_n are reserved for the Fourier series amplitude coefficients. There are a total of $4K+1$ collocation points, K over each of the four intervals into which the quarter-period is subdivided: one-half of the primary winding, the gap between the windings, the secondary winding, and one-half of the secondary gap. A consequence of the constraints in equation (2.29) is that

$$A_y\left(\frac{1}{4}\right) = A_y\left(-\frac{1}{4}\right) = -A_y\left(\frac{1}{4}\right) = 0 \tag{2.31}$$

This means that

$$a_{4K} = A_y\left(\frac{1}{4}\right) = 0 \tag{2.32}$$

leaving $4K$ independent unknowns that need to be determined.

The unknowns will be found by generating $4K$ equations by applying boundary conditions over $4K$ intervals. The collocation points themselves cannot be used to delimit these intervals, because the problem is numerically unstable in this case. To understand why this is so, consider the following: suppose that the integral over a particular interval is constrained to be zero. This is achievable even if at the two end points the values are large, but opposite in sign. A possible solution for the entire function could be a large magnitude oscillatory function. On the other hand, if the collocation point lies in the middle of the interval, then this constraint would force it to zero, as necessary.

The boundary conditions differ over the windings and in the gaps. As a consequence, the edges of the windings must also be integration limit points. The points that delimit the integration intervals, x_m^*, should be concentrated near the edges of the windings, because the

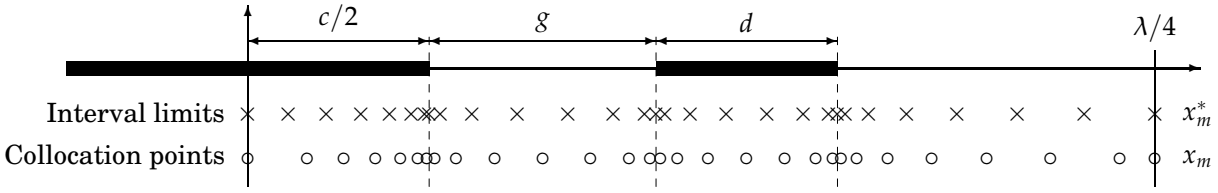

Figure 2-2: Collocation points and interval limits used in the analysis of the MWM, as defined in equations (2.33) and (2.34). The distribution shown assumes $K = 7$.

magnetic fields are strongest there. The following definitions are used:

$$\left.\begin{aligned} x_m^* &= \frac{c}{2}\sin\left(\frac{\pi}{2}\cdot\frac{m}{K}\right) \\ x_{K+m}^* &= \frac{c}{2} + g\cdot\frac{1-\cos(\pi m/K)}{2} \\ x_{2K+m}^* &= \frac{c}{2} + g + d\cdot\frac{1-\cos(\pi m/K)}{2} \\ x_{3K+m}^* &= \frac{c}{2} + g + d + \left(\frac{1}{4} - \frac{c}{2} - g - d\right)\left[1-\cos\left(\frac{\pi}{2}\cdot\frac{m}{K}\right)\right] \end{aligned}\right\} \quad 0 \le m \le K \tag{2.33}$$

The collocation points x_m are situated in the middle of the integration intervals, except at the two ends:

$$x_m = \begin{cases} x_m^* & m = 0, 4K \\ \dfrac{x_{m+1}^* + x_m^*}{2} & m = 1, 2, \ldots, 4K-1 \end{cases} \tag{2.34}$$

The resulting distribution for the two sets of points is shown in Figure 2-2 for $K = 7$ intervals in each of the four regions.

2.1.4 Fourier series representation

The magnetic field can be represented as a superposition of different spatial Fourier modes, because a closed form solution exists for each mode, given by equation (2.13). The magnetic vector potential at $z = 0$ is represented as a Fourier Cosine Series:

$$A_y(x) = \sum_{\substack{n=1 \\ n \text{ odd}}}^{\infty} A_n \cos(k_n x) \tag{2.35}$$

Only odd-numbered modes are necessary, because of the constraints given in equation (2.29). To obtain the Fourier coefficients A_n in terms of the values at the collocation points, the

following integral must be solved:

$$\begin{aligned} A_n &= 8\int_0^{1/4} A_y(x)\cos(k_n x)\,dx \\ &= 8\sum_{m=0}^{4K-1}\int_{x_m}^{x_{m+1}} \frac{(x_{m+1}-x)a_m + (x-x_m)a_{m+1}}{x_{m+1}-x_m}\cos(k_n x)\,dx \\ &= \frac{8}{k_n^2}\sum_{m=0}^{4K-1}\frac{\cos(k_n x_{m+1})-\cos(k_n x_m)}{x_{m+1}-x_m}\big(a_{m+1}-a_m\big) \\ &\qquad + \frac{8}{k_n}\sum_{m=0}^{4K-1}\Big[a_{m+1}\sin(k_n x_{m+1}) - a_m\sin(k_n x_m)\Big] \end{aligned} \tag{2.36}$$

The summation in the last term of equation (2.36) cancels out on a term by term basis, with the exception of the first and last terms:

$$\sum_{m=0}^{4K-1}\Big[a_{m+1}\sin(k_n x_{m+1}) - a_m\sin(k_n x_m)\Big] = a_{4K}\sin(k_n x_{4K}) - a_0\sin(k_n x_0) = 0 \tag{2.37}$$

The two end terms are also equal to zero because $x_0 = 0$ and $a_{4K} = 0$. The remaining summation in equation (2.36) may be rewritten in a more convenient form:

$$\begin{aligned} A_n = \frac{8}{k_n^2}\Bigg\{ & a_0\frac{1-\cos(k_n x_1)}{x_1} \\ & - \sum_{m=1}^{4K-1} a_m\left[\frac{\cos(k_n x_{m+1})-\cos(k_n x_m)}{x_{m+1}-x_m} - \frac{\cos(k_n x_m)-\cos(k_n x_{m-1})}{x_m - x_{m-1}}\right]\Bigg\} \end{aligned} \tag{2.38}$$

where the term multiplying a_{4K} has been dropped because $a_{4K} = 0$.

2.1.5 Normalized surface reluctance density

All information about the material that affects the sensor response can be distilled to the value of the surface inductance density, evaluated in the plane of the windings for each spatial mode n. It is most convenient to work with the ***normalized surface reluctance density***, defined as

$$R_n(z) = \frac{1}{k_n}\cdot\frac{H_{x,n}(z)}{A_{y,n}(z)} \tag{2.39}$$

The even symmetry required by equation (2.29a) eliminates the sine term in equation (2.13), so that for each spatial Fourier mode n the magnetic vector potential can be written as

$$A_{y,n}(x,z) = \widetilde{A}_n(z)\cos(k_n x) \tag{2.40}$$

The tangential magnetic field intensity can be expressed in terms of the vector potential using equation (2.3):

$$H_{x,n}(x,z) = -\frac{1}{\mu^*}\cdot\frac{\partial}{\partial z}A_{y,n}(x,z) \tag{2.41}$$

which can be written in abbreviated form as

$$\widetilde{H}_n(z) = -\frac{1}{\mu^*} \cdot \frac{d}{dz}\widetilde{A}_n(z) \tag{2.42}$$

where $H_{x,n}(x,z) = \widetilde{H}_n(z)\cos(k_n x)$. With this notation the normalized surface reluctance density can be written as

$$R_n(z) = \frac{1}{k_n} \cdot \frac{\widetilde{H}_n(z)}{\widetilde{A}_n(z)} \tag{2.43}$$

First consider a layer that extends to infinity in the positive z-direction, with bottom interface at $z = z_0$. Out of the solutions in equation (2.13), only the $e^{-\gamma z}$ term remains finite at $z = \infty$, leading to

$$\widetilde{A}_n(z) = \widetilde{A}_n(z_0)e^{-\gamma_n(z-z_0)} \tag{2.44}$$

and

$$\widetilde{H}_n(z) = \frac{\gamma_n}{\mu^*}\widetilde{A}_n(z_0)e^{-\gamma_n(z-z_0)} \tag{2.45}$$

Consequently, at the bottom interface of an infinitely thick layer,

$$R_n(z_0) = \frac{\gamma_n}{\mu^* k_n} \tag{2.46}$$

The next step is to relate R_n at the bottom interface of a layer of thickness t to its value at the upper interface ($z = z_0 + t$). In regions of finite thickness it is more convenient to work with the hyperbolic function equivalent of equation (2.13):

$$\mathbf{A} = \left[c_1 \sinh(\gamma z) + c_2 \cosh(\gamma z)\right] \cos(kx)\hat{\mathbf{y}} \tag{2.47}$$

making it possible to express the vector potential in the layer in terms of its values at the two interfaces as

$$\widetilde{A}_n(z) = \frac{\widetilde{A}_n(z_0+t)\sinh\gamma_n(z-z_0) - \widetilde{A}_n(z_0)\sinh\gamma_n(z-z_0-t)}{\sinh\gamma_n t} \tag{2.48}$$

Applying equations (2.42) and (2.43) to equation (2.48) yield the following equations for $R_n(z)$ at the two interfaces:

$$R_n(z_0) = -\frac{\gamma_n}{\mu^* k_n}\left[\frac{\widetilde{A}_n(z_0+t)}{\widetilde{A}_n(z_0)} \cdot \frac{1}{\sinh(\gamma_n t)} - \coth(\gamma_n t)\right] \tag{2.49a}$$

$$R_n(z_0+t) = -\frac{\gamma_n}{\mu^* k_n}\left[\coth(\gamma_n t) - \frac{\widetilde{A}_n(z_0)}{\widetilde{A}_n(z_0+t)} \cdot \frac{1}{\sinh(\gamma_n t)}\right] \tag{2.49b}$$

from which the ratio $\widetilde{A}_n(z_0+t)/\widetilde{A}_n(z_0)$ can be eliminated to arrive at the following transfer

relation:

$$R_n(z_0) = \frac{\gamma_n}{\mu^* k_n} \cdot \frac{\mu^* k_n R_n(z_0 + t) \coth(\gamma_n t) + \gamma_n}{\mu^* k_n R_n(z_0 + t) + \gamma_n \coth(\gamma_n t)} \tag{2.50}$$

A more general treatment of transfer relations, including different coordinate systems, can be found in [50, §2.16].

This makes it possible to calculate $R_n(z = 0)$ in the plane of the windings by starting with the infinite half-space layer that is furthest from the windings, using equation (2.46), and then sequentially applying equation (2.50) across each layer until the winding surface is reached

In the winding plane the symbol R_n is redefined to stand for the difference of the value of the surface reluctance density above and below the windings as:

$$R_n \equiv [\![R_n(z)]\!] = R_n(0^+) - R_n(0^-) = \frac{1}{k_n} \cdot \frac{H_{x,n}(z = 0^+) - H_{x,n}(z = 0^-)}{A_{y,n}(z = 0)} \tag{2.51}$$

because only this difference appears in the equations. The jump in the tangential component of the magnetic field in the numerator of equation (2.51) is equal to the surface current density K_S in the plane of the windings, so that:

$$K_{\mathrm{S}n} = R_n k_n A_n \tag{2.52}$$

The surface reluctance density R_n is the only quantity that changes when the same MWM is used with different material structures.

2.1.6 Boundary conditions

To obtain the equations needed to solve for the values a_m of the vector potential A_y at the collocation points x_m, the appropriate boundary conditions are integrated over $4K$ intervals. The boundary condition in the two gap regions is simple: the surface current must be zero.

$$K_\mathrm{S}(x) = H_x(x, z = 0^+) - H_x(x, z = 0^-) = 0 \tag{2.53}$$

Over the windings the boundary condition derives from equation (2.4), which can be transformed via Stokes' Theorem into the following contour integral:

$$\oint_C \mathbf{E} \cdot d\mathbf{s} = -i\omega \oint_C \mathbf{A} \cdot d\mathbf{s} \tag{2.54}$$

The chosen contour goes down the length of the windings in the y-direction, following all meanders, and then across the sensor terminals. The integral of the electric field across the terminals gives the terminal voltage v, while inside the windings the electric field can be expressed in terms of the surface current density K_S. The resulting boundary condition, ***in unnormalized form***, is

$$v = i\omega M_\mathrm{L} A(x) + M_\mathrm{L} \frac{K_\mathrm{S}(x)}{\Delta\sigma_\mathrm{coil}} \tag{2.55}$$

After normalization it becomes

$$K_{\mathrm{S}}(x) + iA(x)\sigma_{\mathrm{coil}} = v\sigma_{\mathrm{coil}} \tag{2.56}$$

To generate the equations, the boundary conditions given in equations (2.53) and (2.56) must be integrated over each integration interval. The following equation is used for the integral of K_{S}, which appears in both equation (2.53) and equation (2.56):

$$\begin{aligned}
\int_{x_m^*}^{x_{m+1}^*} K_{\mathrm{S}}(x)\,dx &= \sum_{\substack{n=1\\ n\ \text{odd}}}^{\infty} R_n k_n \int_{x_m^*}^{x_{m+1}^*} A_n \cos(k_n x)\,dx \\
&= \sum_{\substack{n=1\\ n\ \text{odd}}}^{\infty} R_n \Big[\sin\big(k_n x_{m+1}^*\big) - \sin\big(k_n x_m^*\big)\Big] \Bigg\{ a_0 \frac{1-\cos(k_n x_1)}{x_1} \\
&\qquad - \frac{8}{k_n^2} \sum_{j=1}^{4K-1} a_j \left[\frac{\cos(k_n x_{j+1}) - \cos(k_n x_j)}{x_{j+1} - x_j} - \frac{\cos(k_n x_j) - \cos(k_n x_{j-1})}{x_j - x_{j-1}} \right] \Bigg\} \\
&= \sum_{\substack{n=1\\ n\ \text{odd}}}^{\infty} R_n \sum_{j=0}^{4K-1} M_{m,j}^n a_j
\end{aligned} \tag{2.57}$$

where use has been made of equation (2.38). The coefficients $M_{m,j}^n$ constitute the contribution to the integral over the mth interval of the vector potential at the jth collocation point for the nth spatial Fourier mode. They can be derived from equation (2.57):

$$\begin{aligned}
M_{m,j}^n = \frac{4}{k_n^2} \Bigg\{ & - \frac{1}{x_{j+1} - x_j} \Big[\sin k_n\big(x_{m+1}^* + x_{j+1}\big) + \sin k_n\big(x_{m+1}^* - x_{j+1}\big) \\
& \qquad - \sin k_n\big(x_m^* + x_{j+1}\big) - \sin k_n\big(x_m^* - x_{j+1}\big) \Big] \\
& + \left[\frac{1}{x_{j+1} - x_j} + \frac{1}{x_j - x_{j-1}} \right] \cdot \Big[\sin k_n\big(x_{m+1}^* + x_j\big) + \sin k_n\big(x_{m+1}^* - x_j\big) \\
& \qquad - \sin k_n\big(x_m^* + x_j\big) - \sin k_n\big(x_m^* - x_j\big) \Big] \\
& - \frac{1}{x_j - x_{j-1}} \Big[\sin k_n\big(x_{m+1}^* + x_{j-1}\big) + \sin k_n\big(x_{m+1}^* - x_{j-1}\big) \\
& \qquad - \sin k_n\big(x_m^* + x_{j-1}\big) - \sin k_n\big(x_m^* - x_{j-1}\big) \Big] \Bigg\} \qquad \text{for } j > 0
\end{aligned} \tag{2.58a}$$

and

$$\begin{aligned}
M_{m,0}^n = \frac{4}{k_n^2} \cdot \frac{1}{x_1} \Big[& 2\sin k_n x_{m+1}^* - 2\sin k_n x_m^* - \sin k_n\big(x_{m+1}^* + x_1\big) \\
& - \sin k_n\big(x_{m+1}^* - x_1\big) + \sin k_n\big(x_m^* + x_1\big) + \sin k_n\big(x_m^* - x_1\big) \Big]
\end{aligned} \tag{2.58b}$$

In principle, all Fourier terms up to infinity must be summed up to build the matrix of equations. This high computational burden may be reduced by observing that for high values of n, R_n asymptotically converges to a constant, labeled R_∞. This can be deduced by looking

at equations (2.25), (2.39), and (2.46), and keeping in mind that the layers adjacent to the windings are insulating. In fact, unless the windings are embedded in magnetizable material, then $R_\infty = 2$, a unit from either side of the sensor. If N is such that $R_n - R_\infty \approx 0$ for $n \geq N$, then the integral can be written as a finite summation:

$$\begin{aligned}\int_{x_m^*}^{x_{m+1}^*} K_{\mathrm{S}}(x)\,dx &\approx \sum_{\substack{n=1\\ n\text{ odd}}}^{N} \big(R_n - R_\infty\big) \sum_{j=0}^{4K-1} M_{m,j}^n a_j + R_\infty \sum_{\substack{n=1\\ n\text{ odd}}}^{\infty} \sum_{j=0}^{4K-1} M_{m,j}^n a_j \\ &= \sum_{\substack{n=1\\ n\text{ odd}}}^{N} \big(R_n - R_\infty\big) \sum_{j=0}^{4K-1} M_{m,j}^n a_j + R_\infty \sum_{j=0}^{4K-1} M'_{m,j} a_j\end{aligned} \tag{2.59}$$

where the coefficients $M'_{m,j}$ are given by:

$$\begin{aligned}M'_{m,j} = \sum_{\substack{n=1\\ n\text{ odd}}}^{\infty} M_{m,j}^n = \frac{1}{\pi^2}\Bigg\{ &- \frac{1}{x_{j+1} - x_j}\Big[f\big(x_{m+1}^* + x_{j+1}\big) + f\big(x_{m+1}^* - x_{j+1}\big) \\ &\qquad - f\big(x_m^* + x_{j+1}\big) - f\big(x_m^* - x_{j+1}\big)\Big] \\ &+ \left[\frac{1}{x_{j+1} - x_j} + \frac{1}{x_j - x_{j-1}}\right] \cdot \Big[f\big(x_{m+1}^* + x_j\big) + f\big(x_{m+1}^* - x_j\big) \\ &\qquad - f\big(x_m^* + x_j\big) - f\big(x_m^* - x_j\big)\Big] \\ &- \frac{1}{x_j - x_{j-1}}\Big[f\big(x_{m+1}^* + x_{j-1}\big) + f\big(x_{m+1}^* - x_{j-1}\big) \\ &\qquad - f\big(x_m^* + x_{j-1}\big) - f\big(x_m^* - x_{j-1}\big)\Big]\Bigg\} \qquad \text{for } j > 0\end{aligned} \tag{2.60a}$$

and

$$\begin{aligned}M'_{m,0} = \sum_{\substack{n=1\\ n\text{ odd}}}^{\infty} M_{m,0}^n = \frac{1}{\pi^2} \cdot \frac{1}{x_1}\Big[&2f\big(x_{m+1}^*\big) - 2f\big(x_m^*\big) - f\big(x_{m+1}^* + x_1\big) \\ &- f\big(x_{m+1}^* - x_1\big) + f\big(x_m^* + x_1\big) + f\big(x_m^* - x_1\big)\Big]\end{aligned} \tag{2.60b}$$

The function $f(x)$ used in equation (2.60) is defined as

$$f\Big(\frac{x}{2\pi}\Big) = \sum_{n=0}^{\infty} \frac{\sin(2n+1)x}{(2n+1)^2} = -\frac{1}{2}\int_0^x \ln\left(\tan\frac{t}{2}\right) dt \tag{2.61}$$

where the use of odd-numbered modes only in equation (2.60) has been made explicit. The closed form of the sum shown in equation (2.61) is given in [51, eq. 1.29].* It can also be derived via term by term integration of [52, eq. 1.442.2].

The function $f(x)$ in equation (2.61) can be computed by performing the summation until convergence is reached, but it converges rather slowly. An alternative formulation, which uses the Bernoulli numbers B_n makes the computation of the function much faster, due to the

*There is a printing error in this reference. Equation (2.61) is the correct expression.

factorial term in the denominator:

$$f\left(\frac{x}{2\pi}\right) = \frac{x}{2}\left(1 + \ln\frac{2}{x}\right) - \sum_{n=1}^{\infty} \frac{(-1)^{n+1}\left(2^{2n-1}-1\right)B_{2n}x^{2n+1}}{2n(2n+1)!} \tag{2.62}$$

This expression is obtained by taking the derivative of [1, eq. A.4]. In practice, the summation never needs more than about 25 terms. The coefficients that multiply x^{2n+1} under the summation may all be pre-computed and stored in static memory, making the infinite summation very fast in practice.

In [1] the formulation is in terms of the integral of $f(x)$, which includes a numerically calculated constant of integration. Formulating in terms of the definitions in this section is one of the advantages of this method compared to the one given in [1], because the computations often require taking small differences, and the machine precision limitation of using this constant is a source of error. One consequence of this error is that the precision of the simulated results stops improving past a certain relatively low number of collocation points.

The boundary condition in equation (2.56) also incorporates the integral of the vector potential. It is written as follows:

$$\int_{x_m^*}^{x_{m+1}^*} A(x)\,dx = \sum_{j=0}^{4K-1} M''_{m,j}a_j \tag{2.63}$$

Since equation (2.30) gives an explicit form for $A(x)$ in terms of a_m, it is not necessary to take the route via the Fourier series representation, although it is possible. The coefficients $M''_{m,j}$ may be computed directly by substituting equation (2.30) into equation (2.63). Since the integration intervals x_m^* are interleaved with the collocation points x_m, only the collocation point enclosed in the interval and its two neighbors affect the integral. The result is a band matrix:

$$M'' = \begin{bmatrix} M''_{0,0} & M''_{0,1} & & & & \\ M''_{1,0} & M''_{1,1} & M''_{1,2} & & 0 & \\ & M''_{2,1} & M''_{2,2} & M''_{2,3} & & \ddots \\ & & M''_{3,2} & M''_{3,3} & M''_{3,4} & \\ & 0 & & M''_{4,3} & M''_{4,4} & \ddots \\ & & \ddots & & \ddots & \ddots \end{bmatrix} \tag{2.64}$$

whose nonzero elements are

$$\begin{aligned} M''_{m,m} &= \frac{1}{2}\left[\frac{x_{m+1}^* - x_m}{x_{m+1} - x_m}\left(2x_{m+1} - x_m - x_{m+1}^*\right) + \frac{x_m^* - x_m}{x_m - x_{m-1}}\left(x_m^* + x_m - 2x_{m-1}\right)\right] \\ M''_{m,m+1} &= \frac{1}{2}\cdot\frac{\left(x_{m+1}^* - x_m\right)^2}{x_{m+1} - x_m} \\ M''_{m+1,m} &= \frac{1}{2}\cdot\frac{\left(x_m^* - x_m\right)^2}{x_m - x_{m-1}} \end{aligned} \tag{2.65}$$

Note that all of these matrices, M^n, M', and M'', are independent of the material prop-

erties, and therefore need to be computed only once for a particular sensor geometry. This is at least in part intentional, by choosing appropriate normalization and definition for the surface reluctance density R_n in equation (2.39). Moreover, only N of the M^n matrices need to be pre-computed, with more of them being computed and stored on the fly as needed. This leads to tremendous savings in computation, especially if the forward model is a component of an iterative method, or when measurement grids for a particular MWM are generated.

2.1.7 Setting up the matrix equation

All of the equations that result from the boundary conditions are brought together in matrix form,

$$Ma = b \tag{2.66}$$

where a is a vector of the values a_m of the potential at the collocation points. The matrix M is built from the pre-computed matrices using the following equations:

$$M_{m,j} = \begin{cases} \sum\limits_{\substack{n=1 \\ n \text{ odd}}}^{N} \left(R_n - R_\infty\right) M^n_{m,j} + R_\infty M'_{m,j} & \begin{cases} K \le m < 2K \\ 3K \le m < 4K \end{cases} \\ \sum\limits_{\substack{n=1 \\ n \text{ odd}}}^{N} \left(R_n - R_\infty\right) M^n_{m,j} + R_\infty M'_{m,j} + i\sigma_{\text{coil}} M''_{m,j} & \begin{cases} 0 \le m < K \\ 2K \le m < 3K \end{cases} \end{cases} \tag{2.67}$$

which result directly from the boundary conditions and definitions in the previous section.

Since we are looking for the full two-port admittance matrix Y, the right hand side b of the matrix equation contains two columns, one for driving each of the two windings separately, i.e. for the first column $v_1 = 1$ and $v_2 = 0$, while for the second column $v_1 = 0$ and $v_2 = 1$. Integrating the right hand side of equation (2.56) amounts to a simple multiplication by $x^*_{m+1} - x^*_m$. Thus all components of b are zero, with the exception of:

$$\begin{aligned} b_{m,0} &= \sigma_{\text{coil}} \left(x^*_{m+1} - x^*_m\right) && 0 \le m < K \\ b_{m,1} &= \frac{1}{2} \sigma_{\text{coil}} \left(x^*_{m+1} - x^*_m\right) && 2K \le m < 3K \end{aligned} \tag{2.68}$$

The factor of $1/2$ comes from the fact that there are two secondary windings per primary.

Solving the matrix equation yields values for a_m for each of the two driving conditions, which fully determine the vector potential A_y in both cases.

2.1.8 Terminal currents

The last step is obtaining the terminal currents of the two windings for the two separate driving voltage conditions. This can be accomplished by integrating the surface current K_S over each of the two windings. Fortunately this is very easy, because the total current in a winding is simply the sum of the integrals of K_S over the intervals contained within the boundaries of the windings. If the following two-row matrix F is set up with the use of the

pre-computed matrices:

$$\begin{aligned} F_{0,j} &= 2\sum_{m=0}^{K-1}\left[\sum_{\substack{n=1\\ n\text{ odd}}}^{N}\left(R_n - R_\infty\right)M^n_{m,j} + R_\infty M'_{m,j}\right] \\ F_{1,j} &= \sum_{m=2K}^{3K-1}\left[\sum_{\substack{n=1\\ n\text{ odd}}}^{N}\left(R_n - R_\infty\right)M^n_{m,j} + R_\infty M'_{m,j}\right] \end{aligned} \tag{2.69}$$

where the factor of 2 in the first line is needed because only half of the primary winding is contained in the quarter period, then the two-port admittance matrix can be obtained directly by multiplying the matrix a of vector potential coefficients by the matrix F:

$$\begin{bmatrix} Y_{11} & Y_{12} \\ Y_{21} & Y_{22} \end{bmatrix} = \begin{bmatrix} \qquad F \qquad \end{bmatrix} \begin{bmatrix} \\ a \\ \\ \\ \\ \end{bmatrix} \tag{2.70}$$

The impedance matrix is the inverse of the admittance matrix: $Z = Y^{-1}$.

2.2 Mathematical model and simulation method for the IDED

Although the principle of duality provides many parallels between the magnetoquasistatic and electroquasistatic regimes, there is one fundamental difference: there is no equivalent to magnetic diffusion, i.e. the electrostatic potential Φ obeys Laplace's equation. From the point of view of the model, this means that for each spatial mode the decay constant in the z-direction is purely real and equal to the wavenumber, i.e. it is independent of the excitation frequency ω.

The model of the interdigital sensor is presented in [2] and [3]. In the course of a NASA and JENTEK sponsored research project at MIT in 1995–96, which used IDEDs to measure porosity in ceramic thermal barrier coatings [28], it became clear that the model presented in the aforementioned sources is incorrect, or at least incomplete, with significant consequences in a number of practical applications.* The issue is how the zero-order Fourier mode is treated, which is important in the presence of a grounded layer on the other side of the test structure. This was first discussed in a report [47] written in 1997. The model presented in this section does treat the zero-order mode correctly, which is its major contribution to previously published versions of the model. There are other changes too, primarily in the way the various quantities are defined, similar to the MWM model of the previous section. This results in simpler formulas and improvements in the performance of the numerical methods. Others have

*This analysis was done in collaboration with Dr. Philip A. von Guggenberg.

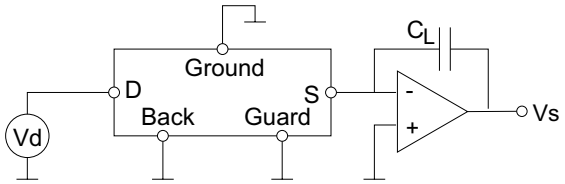

Figure 2-3: Electronic interface of the IDED, designed to keep the sensing electrode virtually grounded.

also made improvements to the original model, such as accounting for the nonzero electrode height [37].

Many of the steps in this algorithm closely follow the steps in the MWM model of the previous section. Consequently, only the features characteristic of the dielectrometer are discussed in detail, with only the formulas shown for steps that parallel the magnetometer method.

The structure of the IDED is shown in Figure 1-4. A cross section of half a period of the sensor is also shown in Figure 2-4. The sensing electrode is kept at ground potential via a feedback circuit, such as the one shown in Figure 2-3. The value of the electrostatic potential is thus known at both electrodes, being equal to the driving voltage V_{D} at the driven electrode, and zero at the sensing electrode. In the gap between the electrodes it is determined via a collocation point method, as discussed below.

2.2.1 Laplace's equation

For the purpose of this model it is assumed that the sensor is infinite and uniform in the y-direction. Due to the spatial periodicity in the x-direction, the useful set of solutions to Laplace's equation $\nabla^2\Phi = 0$ are

$$\Phi(x,z) = \left[a_1 \sin(kx) + a_2 \cos(kx)\right]\left[b_1 e^{kz} + b_2 e^{-kz}\right] + (c_1 + c_2 x)(d_1 + d_2 z) \tag{2.71}$$

Unlike the magnetic case, where the constant component of the vector potential is set to zero (see Section 2.1.3), the zero reference of the electric scalar potential is fixed by the presence of grounded electrodes and cannot be set to an arbitrary value. As a consequence, at the electrode surface the potential can have a nonzero spatially constant component, requiring the consideration of the last term in equation (2.71).

If the $x = 0$ point is chosen at the middle of one of the electrodes, the sensor symmetry dictates that $a_1 = 0$ and $c_2 = 0$ in equation (2.71). The remaining relevant solutions are

$$\Phi(x,z) = \left(b_1 e^{kz} + b_2 e^{-kz}\right)\cos(kx) + d_1 + d_2 z \tag{2.72}$$

2.2.2 Normalization

As in Section 2.1, it is convenient to keep most quantities normalized in order to simplify the analysis and speed up computation. The spatial coordinates are normalized according to equation (2.18).

The geometrical parameters of the IDED are shown in Figure 2-4. The electrode widths c and d, as well as all other length parameters, such as the substrate thickness h and the

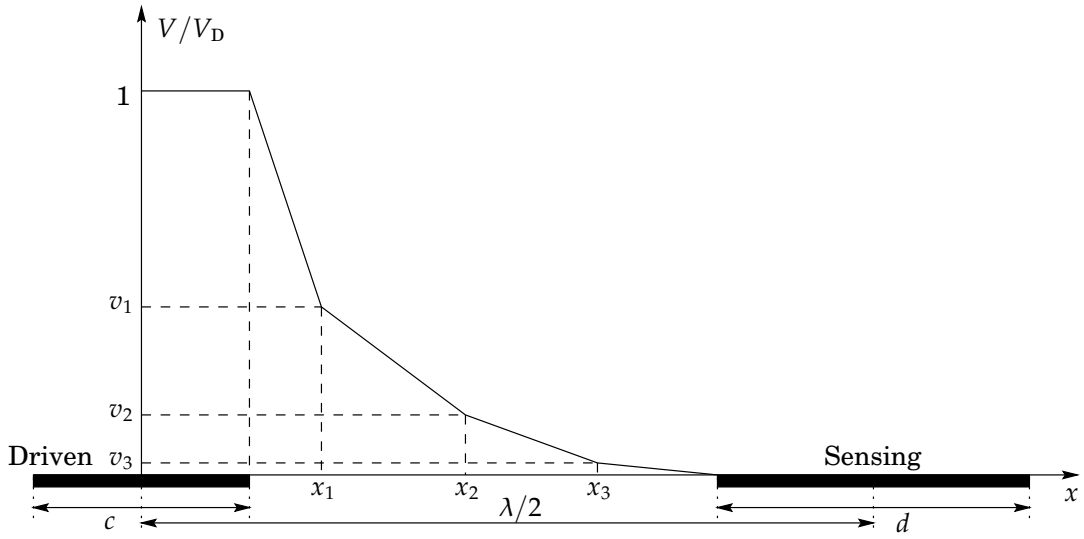

Figure 2-4: Piecewise-smooth collocation-point approximation to the electrostatic potential of the IDED. Three collocation points at x_1, x_2, and x_3 are shown. The sensing electrode is shown wider than the driven electrode to emphasize the fact that they do not need to have the same width.

various layer thicknesses t, are normalized by the wavelength λ:

$$\bar{c} = \frac{c}{\lambda} \qquad \bar{d} = \frac{d}{\lambda} \qquad \bar{h} = \frac{h}{\lambda} \qquad \bar{t} = \frac{t}{\lambda} \tag{2.73}$$

All permittivities are normalized by the permittivity of vacuum ϵ_0:

$$\bar{\epsilon}^* = \frac{\epsilon^*}{\epsilon_0} \qquad \bar{\epsilon}_S = \frac{\epsilon_S}{\epsilon_0} \tag{2.74}$$

where ϵ^* is the complex permittivity defined by equation (2.87), and ϵ_S is the permittivity of the substrate.

The terminal voltages and the electrostatic potential Φ are normalized by the driving voltage V_D, such that the potential at the driven electrode is equal to 1. The normalization of the sensing electrode current is

$$\bar{I} = \frac{I}{M_L \epsilon_0 \omega V_D} \tag{2.75}$$

where M_L is the meander-length of the sensor, i.e. the total length of the sensing electrode fingers, and ω is the excitation frequency. The wavenumber is normalized as

$$\bar{k}_n = k_n \cdot \lambda = 2\pi n \tag{2.76}$$

For the rest of this section, the bars will be dropped from the normalized variables to simplify notation. All appropriate variables should be assumed to be normalized, unless explicitly stated otherwise.

2.2.3 Collocation points

In the sensor gap the electrostatic potential is approximated as an interpolation of its value between a set of $K+2$ collocation points, x_m. With the $x = 0$ point chosen as shown in Figure 2-4, symmetry dictates that

$$\Phi(x) = \Phi(-x) \tag{2.77}$$

which means that only one half of the period needs to be considered in order to determine $\Phi(x)$ uniquely everywhere. The piecewise-linear representation of $\Phi(x)$ in the gap is given by

$$\Phi(x) = \frac{(x_{m+1} - x)v_m + (x - x_m)v_{m+1}}{x_{m+1} - x_m} \qquad x_m < x < x_{m+1} \quad m = 0, 1, \ldots, K \tag{2.78}$$

where v_m are the values of Φ at the points x_m. There are a total of $K+2$ collocation points. The first one, x_0, and last one, x_{K+1}, are located at the electrode edges, where the potential is known. Therefore there are K unknowns that must be determined to find Φ. The collocation points are concentrated near the edges, where the potential is changing the fastest, following a simple cosinusoidal distribution:

$$x_m = \frac{c}{2} + \frac{1 - c - d}{4}\left[1 - \cos\left(\frac{\pi m}{K+1}\right)\right] \qquad 0 \le m \le K+1 \tag{2.79}$$

The value of the potential at the collocation points is determined by integrating the appropriate boundary conditions over a set of K intervals, delimited by the points x_m^*. Each interval encloses one collocation point. The interval boundaries are positioned half way between the collocation points, except at the two ends:

$$x_m^* = \begin{cases} x_0 & m = 0 \\ x_{K+1} & m = K \\ \dfrac{x_{m+1} + x_m}{2} & m = 1, 2, \ldots, K-1 \end{cases} \tag{2.80}$$

2.2.4 Fourier series representation

As in the magnetic case, the electric field is represented as a superposition of different spatial Fourier modes:

$$\Phi(x) = \Phi_0 + \sum_{n=1}^{\infty} \Phi_n \cos(k_n x) \tag{2.81}$$

Unlike the magnetic case, both odd ***and*** even modes must be included in this case, because there is no analogy to the quarter-wave symmetry here. Furthermore, the expansion includes a zero-order term Φ_0, since the reference point of the potential cannot be chosen arbitrarily, having already been determined by the ground potential at the sensing electrode, the back plane, and the ground plane. The summation expressions in this section include all values of n.

Expressing the series coefficients Φ_n in terms of v_m leads to the following expressions:

$$\begin{aligned}
\Phi_n &= 4\int_0^{1/2} \Phi(x)\cos(k_n x)\,dx \\
&= 4\int_0^{x_0} \cos(k_n x)\,dx + 4\sum_{m=0}^{K}\int_{x_m}^{x_{m+1}} \frac{(x_{m+1}-x)v_m + (x-x_m)v_{m+1}}{x_{m+1}-x_m}\cos(k_n x)\,dx \\
&= \frac{4}{k_n}\sin(k_n x_0) + \frac{4}{k_n^2}\sum_{m=0}^{K}\frac{\cos(k_n x_{m+1})-\cos(k_n x_m)}{x_{m+1}-x_m}\left(v_{m+1}-v_m\right) \\
&\qquad + \frac{4}{k_n}\sum_{m=0}^{K}\Big[v_{m+1}\sin(k_n x_{m+1}) - v_m\sin(k_n x_m)\Big]
\end{aligned} \tag{2.82}$$

The first term in equation (2.82) results from integration over the driven electrode, where the potential is fixed at the driving voltage, whose normalized value is unity. The potential is zero at the sensing electrode and therefore this interval is not included.

The last summation in equation (2.82) cancels out on a term-by-term basis, except for the two end terms multiplying v_0 and v_{K+1}. The latter is at the sensing electrode edge, where the potential is zero, and can be ignored. The v_0 term makes a contribution that exactly cancels the leading term in equation (2.82), since $v_0 = 1$. Carrying out these simplifications results in:

$$\begin{aligned}
\Phi_n = -\frac{4}{k_n^2}\sum_{m=1}^{K} v_m\left[\frac{\cos(k_n x_{m+1})-\cos(k_n x_m)}{x_{m+1}-x_m} - \frac{\cos(k_n x_m)-\cos(k_n x_{m-1})}{x_m - x_{m-1}}\right] \\
- \frac{4}{k_n^2}\cdot\frac{\cos(k_n x_1)-\cos(k_n x_0)}{x_1 - x_0}
\end{aligned} \tag{2.83}$$

Note than in equation (2.83) the index of the summation starts at $m = 1$. The first term has been written out separately because $v_0 = 1$ is known, and thus its coefficient will contribute to the right hand side of the matrix equation.

The constant term may similarly be evaluated as:

$$\begin{aligned}
\Phi_0 = 2\int_0^{1/2}\Phi(x)\,dx &= 2\int_0^{x_0} dx + 2\sum_{m=0}^{K}\int_{x_m}^{x_{m+1}}\frac{(x_{m+1}-x)v_m + (x-x_m)v_{m+1}}{x_{m+1}-x_m}\,dx \\
&= 2x_0 + 2\sum_{m=0}^{K}(v_m x_{m+1} - v_{m+1}x_m) + 2\sum_{m=0}^{K}(v_{m+1}-v_m)(x_{m+1}-x_m) \\
&= x_0 + x_1 + \sum_{m=1}^{K} v_m(x_{m+1}-x_{m-1})
\end{aligned} \tag{2.84}$$

2.2.5 Surface capacitance density

There are two parameters of a medium that determine the quasistatic distribution of electric fields: the dielectric permittivity ϵ and the conductivity σ. The former determines the displacement current density from the electric field, while the latter relates the conduction current density to the electric field. The permittivity governs energy storage (reactive power) phenomena, while the conductivity determines the power dissipation (active power). It is

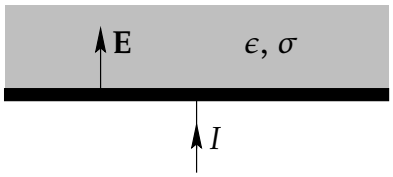

Figure 2-5: Terminal current of an electrode in contact with a conducting dielectric medium.

possible to combine these two effects by adding the effect of the ohmic conductivity to the imaginary (loss) component of the complex permittivity.

Consider an electrode in contact with a medium as shown in Figure 2-5. In the one-dimensional geometry in the figure, the current density and the electric field are perpendicular to the electrode. Let the normal component of the electric field at the electrode surface be E. The terminal current I can be obtained by integrating the total current per unit electrode area J that flows into the electrode. The total current density is given by

$$J = J_{\mathrm{C}} + J_{\mathrm{D}} = \sigma E + \frac{d}{dt}(\epsilon E) \tag{2.85}$$

where J_{C} is the conduction current density and J_{D} is the displacement current density.

Under sinusoidal steady state operation equation (2.85) becomes

$$J = J_{\mathrm{C}} + J_{\mathrm{D}} = \sigma E + i\omega\epsilon E = i\omega E\left(\epsilon + \frac{\sigma}{i\omega}\right) \tag{2.86}$$

It is convenient to define the ***complex permittivity*** ϵ^* of a medium as:

$$\epsilon^* = \epsilon' - i\epsilon'' = \epsilon - i\frac{\sigma}{\omega} \tag{2.87}$$

making it possible to rewrite equation (2.86) as

$$J = i\omega\epsilon^* E \tag{2.88}$$

In analogy to the surface reluctance density defined in Section 2.1.5, in the electroquasistatic regime it is possible to define the ***complex surface capacitance density*** as

$$C_n^*(z) = \frac{1}{k_n} \cdot \frac{\epsilon^*(z) E_{z,n}(z)}{\Phi_n(z)} \qquad n > 0 \tag{2.89a}$$

$$C_0^*(z) = \frac{\epsilon^*(z) E_{z,0}(z)}{\Phi_0(z)} \tag{2.89b}$$

As before, all information about the material under test is contained in the value of C_n^* at $z = 0$ for all spatial Fourier modes.

Taking advantage of duality, it is possible to use equations (2.40) through (2.51), after

making the following substitutions:

$$\begin{aligned} \Phi &\longleftrightarrow A_y \\ \epsilon^* E_z &\longleftrightarrow H_x \\ C_n^* &\longleftrightarrow R_n \\ \epsilon^* &\longleftrightarrow \frac{1}{\mu^*} \end{aligned} \tag{2.90}$$

and letting $\gamma_n \to k_n$, since there is no diffusion term in the electroquasistatic case.

At the bottom interface ($z = z_0$) of any layer, for high mode numbers

$$\lim_{n\to\infty} C_n^*(z_0) = \epsilon^* \tag{2.91}$$

and the transfer relation across a layer of thickness t and complex permittivity ϵ^* is

$$C_n^*(z_0) = \epsilon^* \frac{C_n^*(z_0+t)\coth(k_n t) + \epsilon^*}{C_n^*(z_0+t) + \epsilon^* \coth(k_n t)} \qquad n > 0 \tag{2.92}$$

To calculate the transfer relation for $n = 0$, the linear component of equation (2.72) must be used, leading to

$$\Phi_0(z) = \frac{(z-z_0)\Phi_0(z_0+t) - (z-z_0-t)\Phi_0(z_0)}{t} \tag{2.93}$$

and

$$E_{z,0}(z) = -\frac{d}{dz}\Phi_0(z) = -\frac{\Phi_0(z_0+t) - \Phi_0(z_0)}{t} \tag{2.94}$$

At the two interfaces, $C_0(z)$ is

$$C_0(z_0) = -\frac{\epsilon^*}{t}\left[\frac{\Phi_0(z_0+t)}{\Phi_0(z_0)} - 1\right] \tag{2.95a}$$

$$C_0(z_0+t) = -\frac{\epsilon^*}{t}\left[1 - \frac{\Phi_0(z_0)}{\Phi_0(z_0+t)}\right] \tag{2.95b}$$

which can be combined to yield the following transfer relation:

$$C_0^*(z_0) = \frac{\epsilon^* C_0^*(z_0+t)}{t C_0^*(z_0+t) + \epsilon^*} \tag{2.96}$$

A material structure with several homogeneous layers is shown in Figure 2-6. One notable difference is that while in the magnetic case there always is a top layer of infinite thickness, in the electrostatic case the top layer is limited by a ground plane. This is true even if no such electrode is present in an experimental setup, since there are many objects in the vicinity which are at ground potential, which act as a ground at a certain effective distance. In fact, it is better to explicitly place a grounded metal plate behind the material under test, so that it is at a controlled distance to be used in the model. Nonetheless, it is still possible to model a structure with no ground plane by letting the thickness of the top layer approach infinity.

The surface capacitance density at the bottom interface of this ground-limited top layer

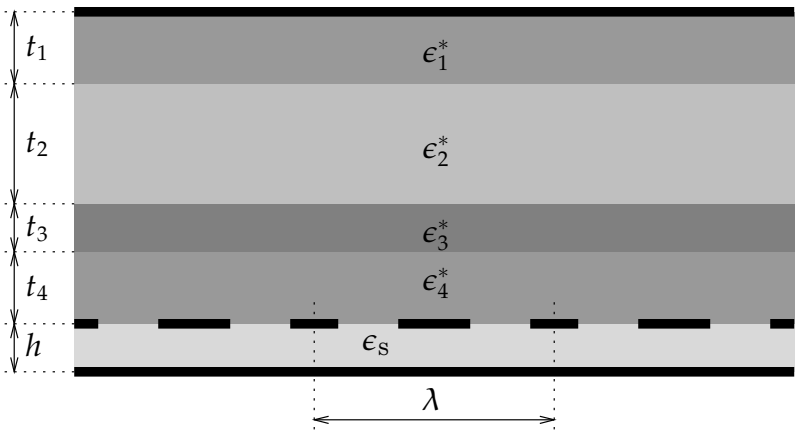

Figure 2-6: Material structure with several layers of homogeneous materials

can be computed from equations (2.92) and (2.96) by taking the limit where $C_n(z_0+t) \to \infty$, since $\Phi_n(z_0+t) = 0$ at the top interface in contact with the ground plane:

$$C_n^*(z_0) = \epsilon^* \coth(k_n t) \qquad n > 0 \tag{2.97a}$$

$$C_0^*(z_0) = \frac{\epsilon^*}{t} \tag{2.97b}$$

which approaches ϵ^* for all $n > 0$ at sufficiently large values of the thickness t.

The quantity σ_S^* is defined as the jump in the normal component of $\epsilon^* E$:

$$\sigma_S^*(x) = [\![\epsilon^* E_z(x)]\!] = \epsilon^*(z=0^+) E_z(x, z=0^+) - \epsilon^*(z=0^-) E_z(x, z=0^-) \tag{2.98}$$

It would be equal to the surface charge density in the absence of ohmic conduction in the medium. Incorporating the conductivity as part of the complex permittivity changes ϵ, C, and σ_S to ϵ^*, C^*, and σ_S^*. The jump in the normal component of the total current density, conduction and displacement, is expressed in terms of σ_S^* via equation (2.88):

$$[\![J_z]\!] = i\omega\sigma_S^* \tag{2.99}$$

Using equation (2.98), the values of the surface capacitance density above and below the electrodes can be combined in a single quantity:

$$C_n^* \equiv [\![C_n^*(z)]\!] = C_n^*(0^+) - C_n^*(0^-) = \frac{1}{k_n} \cdot \frac{\sigma_{S\,n}^*}{\Phi_n(z=0)} \tag{2.100}$$

resulting in the following expression for the coefficients of the Fourier series expansion of $\sigma_S^*(x)$:

$$\sigma_{S\,n}^* = C_n^* k_n \Phi_n \tag{2.101}$$

2.2.6 Boundary conditions

Compared to the magnetometer, formulating the boundary conditions that need to be applied over the integration intervals around each collocation point is much simpler in the dielectric case. This is due to the fact that in the electroquasistatic regime the metal electrodes can be

treated as infinitely conducting, so that the potential at the electrodes is known. It needs to be determined only in a single region in the gap, unlike the MWM where there are four separate regions, as seen in Figure 2-1.

The relevant boundary condition between electrodes is

$$\sigma_{\mathrm{S}}^{*}(x) = 0 \tag{2.102}$$

which results from equation (2.99), since there is no electrode to act as a current source or sink, and no surface conduction is considered. Surface conductivity and permittivity may be modeled by introducing an extra layer and letting its thickness approach zero. The integral of the condition in equation (2.102) is

$$\begin{aligned}
\int_{x_m^*}^{x_{m+1}^*} \sigma_{\mathrm{S}}^{*}(x)\,dx &= \sum_{n=1}^{\infty} \int_{x_m^*}^{x_{m+1}^*} C_n^* \Phi_n k_n \cos(k_n x)\,dx + \int_{x_m^*}^{x_{m+1}^*} C_0^* \Phi_0\,dx \\
&= -\sum_{n=1}^{\infty} \Bigg(C_n^* \Big[\sin\big(k_n x_{m+1}^*\big) - \sin\big(k_n x_m^*\big) \Big] \times \\
&\qquad \times \frac{4}{k_n^2} \Bigg\{ \sum_{j=1}^{K} v_j \left[\frac{\cos(k_n x_{j+1}) - \cos(k_n x_j)}{x_{j+1} - x_j} - \frac{\cos(k_n x_j) - \cos(k_n x_{j-1})}{x_j - x_{j-1}} \right] \\
&\qquad\qquad + \frac{\cos(k_n x_1) - \cos(k_n x_0)}{x_1 - x_0} \Bigg\} \Bigg) \\
&\qquad + C_0^* \big(x_{m+1}^* - x_m^* \big) \left[x_0 + x_1 + \sum_{j=1}^{K} v_j (x_{j+1} - x_{j-1}) \right] \\
&= \sum_{n=0}^{\infty} C_n^* \sum_{j=1}^{K} M_{m,j}^{n} v_j = 0
\end{aligned} \tag{2.103}$$

In matrix form this set of equations is $Mv = b$, where v is a vector of the unknown potential values v_m. The matrix M is calculated for a particular material structure as:

$$M = \sum_{n=1}^{\infty} C_n^* M^n + C_0^* M^0 \tag{2.104}$$

where the sub-matrices M^n are defined in equation (2.103). The advantage of formulating M as a summation of sub-matrices is that they depend only on the sensor parameters, and need to be computed once when calculating the sensor response for a variety of material properties and geometries. After substituting equations (2.83) and (2.84) into equation (2.103), the

elements of M^n are determined to be:

$$\begin{aligned} M^n_{m,j} = \frac{2}{k_n^2}\Bigg\{ & -\frac{1}{x_{j+1}-x_j}\Big[\sin k_n\big(x^*_{m+1}+x_{j+1}\big)+\sin k_n\big(x^*_{m+1}-x_{j+1}\big) \\ & \qquad -\sin k_n\big(x^*_m+x_{j+1}\big)-\sin k_n\big(x^*_m-x_{j+1}\big)\Big] \\ & +\left[\frac{1}{x_{j+1}-x_j}+\frac{1}{x_j-x_{j-1}}\right]\cdot\Big[\sin k_n\big(x^*_{m+1}+x_j\big)+\sin k_n\big(x^*_{m+1}-x_j\big) \\ & \qquad -\sin k_n\big(x^*_m+x_j\big)-\sin k_n\big(x^*_m-x_j\big)\Big] \\ & -\frac{1}{x_j-x_{j-1}}\Big[\sin k_n\big(x^*_{m+1}+x_{j-1}\big)+\sin k_n\big(x^*_{m+1}-x_{j-1}\big) \\ & \qquad -\sin k_n\big(x^*_m+x_{j-1}\big)-\sin k_n\big(x^*_m-x_{j-1}\big)\Big]\Bigg\} \qquad \text{for } n>0 \end{aligned} \tag{2.105a}$$

and

$$M^0_{m,j} = \big(x^*_{m+1}-x^*_m\big)\big(x_{j+1}-x_{j-1}\big) \tag{2.105b}$$

As in the magnetic case, the surface capacitance density approaches a limit C^*_∞ for large values of n. Using a similar definition, it is possible to separate the C^*_∞ component:

$$\begin{aligned} \int_{x^*_m}^{x^*_{m+1}} \sigma^*_{\mathrm{S}}(x)\,dx &\approx \sum_{n=1}^{N}\big(C^*_n-C^*_\infty\big)\sum_{j=1}^{K}M^n_{m,j}a_j + C^*_\infty\sum_{n=1}^{\infty}\sum_{j=1}^{K}M^n_{m,j}a_j \\ &= \sum_{n=1}^{N}\big(C^*_n-C^*_\infty\big)\sum_{j=1}^{K}M^n_{m,j}a_j + C^*_\infty\sum_{j=1}^{K}M'_{m,j}a_j \end{aligned} \tag{2.106}$$

where the elements of the matrix M' are given by

$$\begin{aligned} M'_{m,j} = \sum_{n=1}^{\infty}M^n_{m,j} = \frac{1}{\pi^2}\Bigg\{ & -\frac{1}{x_{j+1}-x_j}\Big[g\big(x^*_{m+1}+x_{j+1}\big)+g\big(x^*_{m+1}-x_{j+1}\big) \\ & \qquad -g\big(x^*_m+x_{j+1}\big)-g\big(x^*_m-x_{j+1}\big)\Big] \\ & +\left[\frac{1}{x_{j+1}-x_j}+\frac{1}{x_j-x_{j-1}}\right]\cdot\Big[g\big(x^*_{m+1}+x_j\big)+g\big(x^*_{m+1}-x_j\big) \\ & \qquad -g\big(x^*_m+x_j\big)-g\big(x^*_m-x_j\big)\Big] \\ & -\frac{1}{x_j-x_{j-1}}\Big[g\big(x^*_{m+1}+x_{j-1}\big)+g\big(x^*_{m+1}-x_{j-1}\big) \\ & \qquad -g\big(x^*_m+x_{j-1}\big)-g\big(x^*_m-x_{j-1}\big)\Big]\Bigg\} \end{aligned} \tag{2.107}$$

In the dielectric case the summation does include the even-numbered Fourier terms, so

that the function $g(x)$ differs from $f(x)$ of equation (2.61). The definition of $g(x)$ is

$$g\Big(\frac{x}{2\pi}\Big) = \sum_{n=1}^{\infty} \frac{\sin(nx)}{n^2} = -\int_0^x \ln\left(2\sin\frac{t}{2}\right)\,dt \tag{2.108}$$

The closed form of the sum is taken from [51, eq. 1.25], or via term-by-term integration of [52, eq. 1.441.2]. As for $f(x)$, a fast converging series expression is also possible for $g(x)$ [3, eq. A.6]:

$$g\Big(\frac{x}{2\pi}\Big) = x\big[1+\ln(x)\big] - \sum_{n=1}^{\infty} \frac{(-1)^{n+1}B_{2n}x^{2n+1}}{2n(2n+1)!} \tag{2.109}$$

The function $g(x)$ is further discussed in Appendix B.

2.2.7 Setting up the matrix equation

The set of equations generated by equation (2.103) are written in matrix form as $Mv = b$. The matrix M is already defined in equation (2.104). Forming the right hand side vector b in the dielectric case is quite different. In the magnetic case the constant term comes from the boundary conditions over the windings, which include the terminal voltages. Here, however, the constant terms arise from the expressions multiplying $v_0 = 1$, written out explicitly outside the sums in equation (2.103). It also has a contribution due to the $n = 0$ term, so that

$$b = \sum_{n=1}^{\infty} C_n^* b^n + C_0^* b^0 \tag{2.110}$$

Extracting the appropriate terms from equation (2.103) gives

$$\begin{aligned} b_m^n = \frac{2}{k_n^2}\cdot\frac{1}{x_1-x_0}\Big[&\sin k_n\big(x_{m+1}^*-x_1\big)+\sin k_n\big(x_{m+1}^*+x_1\big)\\ &-\sin k_n\big(x_m^*-x_1\big)-\sin k_n\big(x_m^*+x_1\big)\\ &-\sin k_n\big(x_{m+1}^*-x_0\big)-\sin k_n\big(x_{m+1}^*+x_0\big)\\ &+\sin k_n\big(x_m^*-x_0\big)+\sin k_n\big(x_m^*+x_0\big)\Big] \qquad \text{for } n>0 \end{aligned} \tag{2.111a}$$

and

$$b_m^0 = -\big(x_{m+1}^*-x_m^*\big)\big(x_0+x_1\big) \tag{2.111b}$$

Solving the matrix equation results in full knowledge of the electrostatic potential $\Phi(x)$ at the electrode surface.

2.2.8 Calculating transcapacitance

In the magnetometer case, the entire two-port impedance matrix is computed. Although full measurement information is contained in the transinductance term, having all components is useful, because it makes it possible to include parasitic source and load impedances in the model and account for them. In the case of the dielectrometer, the only useful component of the two-port matrix is the transcapacitance, because the sensing electrode voltage is always at zero potential and the current into the driven electrode is generally too small for any source impedance to have an appreciable effect on the measurement results.

Obtaining the transcapacitance term is done by integrating σ_S^* over the area of the virtually grounded sensing electrode. In the magnetic case this integral was already computed for the windings, but in the dielectric case the electrode surface needs to be considered separately. Using equation (2.99), the transcapacitance is determined as follows:

$$\begin{aligned} C_T &= -\sum_{n=1}^{\infty} \int_{x_{K+1}}^{1/2} C_n^* \Phi_n k_n \cos(k_n x)\, dx - \int_{x_{K+1}}^{1/2} C_0^* \Phi_0\, dx \\ &= -\sum_{n=1}^{\infty} C_n^* \sin(k_n x_{K+1}) \frac{4}{k_n^2} \left\{ \sum_{j=1}^{K} v_j \left[\frac{\cos(k_n x_{j+1}) - \cos(k_n x_j)}{x_{j+1} - x_j} - \frac{\cos(k_n x_j) - \cos(k_n x_{j-1})}{x_j - x_{j-1}} \right] \right. \\ &\qquad \left. + \frac{\cos(k_n x_1) - \cos(k_n x_0)}{x_1 - x_0} \right\} \\ &\quad - C_0^* \left(\frac{1}{2} - x_{K+1} \right) \left[x_0 + x_1 + \sum_{j=1}^{K} v_j (x_{j+1} - x_{j-1}) \right] \end{aligned} \tag{2.112}$$

where the sensing electrode extends from $x_{K+1} = 1/2 - d/2$ to $1/2$.

2.3 Summary of Chapter 2

In this chapter the semi-analytical collocation point models for the MWM and the IDED, which are the inductive and capacitive implementations of the Cartesian geometry quasistatic spatially periodic sensors, have been presented in detail. The new concepts in this formulation include:

1. The equations are written in a form that lends itself to efficient numerical implementation.
2. The infinite series are formulated in a way that minimizes sensitivity to machine imprecision.
3. The distributions of collocation points and integration interval limits are chosen to maximize the numerical stability of the collocation point method.
4. The zero-order term in the dielectric case is treated appropriately, correcting errors in earlier work.

Although most of the material in this chapter has appeared in previous publications, the formulation and conventions used here have the advantages of completeness, consistency, and efficiency of the numerical implementation. These qualities make the material in this chapter a solid base for the development of the cylindrical geometry models in Chapter 3, the distributed current drive magnetometer models in Chapter 4, and the moving media analysis in Section 6.1. Furthermore, this chapter has already become a useful reference source for users of the MWM and IDED Cartesian geometry sensors and arrays.

Chapter 3

Modeling sensors with rotational symmetry

As already briefly discussed in the introductory Section 1.3.2, there are several reasons why it may be advantageous to design rotationally symmetric sensors. In the case of the Cartesian geometry sensors, such as the existing MWM and IDED, it is necessary to assume that: (1) the extent of the sensor is infinite in the y-direction, and all physical quantities are independent of y; and (2) all physical quantities are spatially periodic in the x-direction with a period equal to the spatial wavelength λ, and extend to infinity in the x-direction. Whereas the second assumption is generally justified when guard electrodes or windings are used near the two sides, as illustrated in the IDED schematic in Figure 1-4, there is really no easy way to justify the first one, unless impractically long sensors are designed.

The circular geometry completely eliminates the y edge effect, because the counterpart of y in cylindrical coordinates for this geometry is φ. The x edge effect, which corresponds to r in cylindrical coordinates, can also be minimized by making the radius R, used in the mathematical model, large compared to the relevant length scales.

A further possible advantage of the rotationally symmetric sensors is their insensitivity to anisotropy of the material. Anisotropy plays a particularly important role in magnetometer measurements, where a metal's conductivity may be anisotropic, due to processing, such as rolling or directional solidification. Furthermore, in ferromagnetic metals the magnetic permeability can manifest strong anisotropy due to residual or applied stress. Whereas there are many cases when it is useful to measure this anisotropy [18, 24], at other times it may be preferable to measure the directional average of a property. For example, when comparing two parts, the lack of sensitivity to direction eliminates the need for precise alignment of the sensor to the anisotropy axis.

Finally, certain structures, such as holes and fasteners, are by nature rotationally symmetric. Cracks that originate from a hole propagate radially out, and thus a sensor with concentric windings is ideal for this application, since it is uniformly sensitive to cracks around the entire circumference of the hole. Such sensors have already been developed at JENTEK, called Rosettes [23], whose basic structure is shown in Figure 3-1. At present the measurement grids for these sensors are still being generated with the Cartesian coordinate methods outlined in Section 2.1, which can be justified only if the width of the annulus that contains the active windings is small compared to the radius, which is not true for practical sensors. Using the method developed in this chapter will result in more accurate models for these sensors.

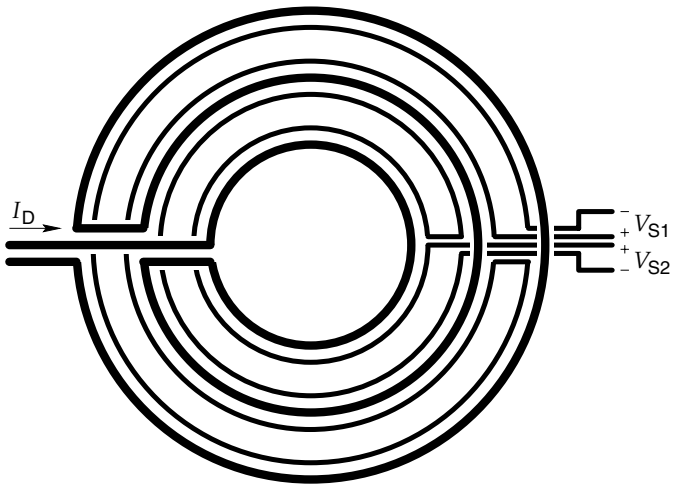

Figure 3-1: Basic structure of the circularly symmetric magnetometer (Rosette).

This chapter presents mathematical models and numerical techniques used to calculate the response of sensors with rotational symmetry. Both the magnetic and dielectric cases are presented in Sections 3.1 and 3.2 respectively. Section 3.3 shows experimental results with the dielectric sensor, which confirm the validity of the model developed in Section 3.2. Only the collocation point methods are discussed in this chapter; methods for modeling of the circular magnetometer with distributed current drive are presented in Sections 4.8 and 4.9.

The problem is approached similarly to the Cartesian collocation point methods in Chapter 2. Frequent references to that chapter are made, in order to illustrate the parallels and the differences between the two coordinate systems. ***Unlike Chapter 2, in this chapter no normalization is included in the equations.***

Perhaps the most important difference is that the periodicity built into the Cartesian geometry sensors, which makes it possible to use Fourier series methods efficiently, does not exist in cylindrical geometry. This is not to say that the idea of imposing a certain spatial periodicity as a way of controlling the effective depth of sensitivity no longer holds; on the contrary, this still is the main factor that determines the radii and spacing of the electrodes or windings. In cylindrical coordinates Fourier-Bessel Series is used instead, but the radius R over which the Bessel Series is applied is chosen large compared to the characteristic lengths of the sensor. As a consequence of choosing a large radius, terms of much higher order must be considered for the same numerical precision. This, coupled with the lack of convenient closed form product and summation formulas for Bessel functions, makes the computational burden much higher than the Cartesian coordinate methods.

3.1 Magnetometer

In this section the equations needed for developing the numerical method used to model the circularly symmetric magnetometer are developed.

The magnetometer windings are formed on a planar substrate in the form of concentric annuli, as shown in Figure 3-1. It is most convenient to formulate the problem in cylindrical coordinates, with the origin at the center of the sensor, and the z-axis perpendicular to the plane of the sensor. Because of the winding layout, the current always flows only in the φ-

direction, and all physical quantities are independent of the angle coordinate φ. The magnetic vector potential must therefore be of the following form:

$$\mathbf{A} = A_\varphi(r,z)\hat{\boldsymbol{\varphi}} \tag{3.1}$$

The magnetic diffusion equation (2.11) requires that the function $A_\varphi(r,z)$ be a solution to the following partial differential equation:

$$\frac{\partial}{\partial r}\left[\frac{1}{r}\cdot\frac{\partial}{\partial r}(rA_\varphi)\right] + \frac{\partial^2}{\partial z^2}A_\varphi - i\omega\sigma\mu A_\varphi = 0 \tag{3.2}$$

A useful solution to equation (3.2) is

$$\mathbf{A} = J_1(\beta r)\left(c_1 e^{+\gamma z} + c_2 e^{-\gamma z}\right)\hat{\boldsymbol{\varphi}} \qquad\qquad \gamma = \sqrt{\beta^2 + i\omega\sigma\mu} \tag{3.3}$$

where J_1 is the Bessel function of the first kind of order one. The Bessel function of the second kind Y_1, which also satisfies the radial part of equation (3.2), is not suitable, because it has a singularity at $r = 0$, where $\mathbf{A}$ must remain finite. The role of the wavenumber k in equation (2.14) is played by β in cylindrical coordinates. In terms of equation (3.3), the electromagnetic flux density $\mathbf{B}$ is:

$$\begin{aligned}\mathbf{B} = \nabla\times\mathbf{A} &= \frac{1}{r}\cdot\frac{\partial}{\partial r}(rA_\varphi)\hat{\mathbf{z}} + \frac{\partial}{\partial z}A_\varphi\hat{\mathbf{r}} \\ &= \beta J_0(\beta r)\left(c_1 e^{+\gamma z} + c_2 e^{-\gamma z}\right)\hat{\mathbf{z}} + \gamma J_1(\beta r)\left(c_1 e^{+\gamma z} - c_2 e^{-\gamma z}\right)\hat{\mathbf{r}}\end{aligned} \tag{3.4}$$

3.1.1 Use of Fourier-Bessel series

The form of equation (3.3) suggests that A_φ, at a given value of z, may conveniently be represented by a Fourier-Bessel series based on J_1. A function $f(r)$ may be represented as an infinite summation of Bessel functions over an interval $(0, R)$ as follows [53]:

$$f(r) = \sum_{n=1}^{\infty} A_n J_1\left(\frac{\alpha_n}{R}r\right) \qquad\qquad 0 < r < R \tag{3.5}$$

where α_n are the positive real zeros of J_1. The trivial zero $\alpha_0 = 0$ does not participate in this series. To find the series coefficients A_n, the following integral must be evaluated:

$$A_n = \frac{1}{Q_n}\int_0^R r f(r) J_1\left(\frac{\alpha_n}{R}r\right)\,dr \tag{3.6}$$

where the coefficients Q_n are given by:

$$Q_n = \int_0^R r J_1^2\left(\frac{\alpha_n}{R}r\right)\,dr = \frac{R^2}{2}J_2^2(\alpha_n) = \frac{R^2}{2}J_0^2(\alpha_n) \tag{3.7}$$

The transformation of J_2 to J_0 in the last equation is possible because of the following equality:

$$J_2(x) = \frac{2}{x}J_1(x) - J_0(x) \tag{3.8}$$

which means that $J_2(\alpha_n) = -J_0(\alpha_n)$, since $J_1(\alpha_n) = 0$. Attempting to express everything in terms of J_0 and J_1 only is motivated by the desire to maintain the analogy of the relationship between these two functions to the sine/cosine pair in Cartesian coordinates. The roles of J_0 and J_1 are reversed in the dielectric case, as seen in Section 3.2. Furthermore, restricting the use of Bessel functions to J_0 and J_1 is beneficial from the point of view of computational efficiency.

The radius R is the outer limit of the interval over which the Bessel series expansion is applied. It is chosen to be several times greater than the outer radius of the sensor, in order to make the effect of any phantom magnetic fields that result from the summation of the series outside of this radius negligible.

3.1.2 Collocation points

Since no specific winding layout is used in this section, Figure 3-1 being only a simple example of a possible layout, no explicit definition of the collocation points is given. As in Section 2.1.3, the collocation points r_m should be spread out over the interval where $\mathbf{A}$ is to be determined, i.e. $0 \leq r \leq R$, with higher concentration of points near the winding edges, and interleaved with the integration limit points r_m^*. The latter must include the winding edges exactly, in order to have the same boundary conditions apply within the range of each interval. The total number of collocation points used in the analysis in this section, including the first and last points, is $K+1$. Thus a total of K constraining equations are required, since the vector potential needs to be determined only to within an additive constant. The last collocation point is at $r_K = R$. The first one does not need to be at the origin, because for $r < r_0$ the potential is fully determined by, and equal to, its value at r_0, for reasons described below.

The next step is expressing the series coefficients of the Bessel function expansion of the magnetic vector potential in terms of its value at the collocation points, in analogy to equation (2.38). The choice of interpolating function in the Cartesian case is a simple line connecting the two neighboring points, which leads to equation (2.30). Using this same function here would be unsuitable, because equation (3.6) yields an integral, namely $\int x J_1(x)\,dx$, that has no closed form solution.* More generally, integrals of the form $\int x^p J_1(x)\,dx$ cannot be solved when p is an odd integer. Conversely, when p is an even integer, closed form solutions are possible, as in the following cases:

$$\int J_1(x)\,dx \quad = -J_0(x) \tag{3.9a}$$

$$\int x^2 J_1(x)\,dx = x^2 J_2(x) \tag{3.9b}$$

Equation (3.9) suggests that a convenient function to be used for interpolation between two consecutive collocation points is:

$$y = c_1 x + \frac{c_2}{x} \qquad\qquad x > 0 \tag{3.10}$$

Specifically, in terms of its values y_1 and y_2 known at two distinct points x_1 and x_2, with

*At least, not a practical closed form solution. This integral may be expressed as a hypergeometric function.

$0 \leq x_1 < x_2$, the value of a function $y(x)$ is given by the following formula:

$$y = \begin{cases} \dfrac{y_2}{x_2} x & x_1 = 0 \text{ and } y_1 = 0 \\ \dfrac{(y_1/x_2 - y_2/x_1)\, x + (x_1 y_2 - x_2 y_1)/x}{x_1/x_2 - x_2/x_1} & \text{otherwise} \end{cases} \tag{3.11}$$

Using this interpolation function, the magnetic vector potential between two collocation points is given by the following expression:

$$A_\varphi(r) = \frac{a_m r_m \left(r_{m+1}^2/r - r\right) + a_{m+1} r_{m+1} \left(r - r_m^2/r\right)}{r_{m+1}^2 - r_m^2} \qquad \begin{matrix} r_m \leq r \leq r_{m+1} \\ m = 0, 1, \ldots, K-1 \end{matrix} \tag{3.12}$$

analogous to equation (2.30). For $0 \leq r \leq r_0$ the magnetic vector potential must be constant and equal to a_0, since its partial derivative with respect to r at $r = 0$ must be zero, or else B_z would be infinite there. Therefore equation (3.10) cannot be used in this interval, since both coefficients would have to be zero. To avoid having to carry out an integral with no closed form over this interval, which would result from constant $A_\varphi(r)$, it is best to set the constant potential there to zero, using the degree of freedom afforded by the arbitrary constant that can be added to the vector potential. Thus

$$A_\varphi(r) = a_0 = 0 \qquad 0 \leq r \leq r_0 \tag{3.13}$$

Letting

$$\beta_n \equiv \frac{\alpha_n}{R} \tag{3.14}$$

the series coefficients are obtained by an integral from zero to $r_K = R$, which can be divided up as:

$$A_n = \frac{1}{Q_n} \sum_{m=0}^{K-1} \int_{r_m}^{r_{m+1}} r A_\varphi(r) J_1(\beta_n r)\, dr \tag{3.15}$$

Substituting equation (3.12) into equation (3.15) and carrying out the integration yields

$$\begin{aligned} A_n Q_n \beta_n = \sum_{m=0}^{K-1} \Bigg(& \frac{1}{r_{m+1}^2 - r_m^2} \times \\ & \times \Big\{ a_{m+1} r_{m+1} \left[r_{m+1}^2 J_2(\beta_n r_{m+1}) - r_m^2 J_2(\beta_n r_m) + r_m^2 J_0(\beta_n r_{m+1}) - r_m^2 J_0(\beta_n r_m) \right] \\ & - a_m r_m \left[r_{m+1}^2 J_2(\beta_n r_{m+1}) - r_m^2 J_2(\beta_n r_m) + r_{m+1}^2 J_0(\beta_n r_{m+1}) - r_{m+1}^2 J_0(\beta_n r_m) \right] \Big\} \Bigg) \end{aligned} \tag{3.16}$$

which, with the help of equation (3.8), is written as

$$\begin{aligned} A_n Q_n \beta_n^2 = 2 \sum_{m=0}^{K-1} \frac{a_{m+1} r_{m+1} - a_m r_m}{r_{m+1}^2 - r_m^2} \Big[r_{m+1} J_1(\beta_n r_{m+1}) - r_m J_1(\beta_n r_m) \Big] \\ - \beta_n \sum_{m=0}^{K-1} \Big[a_{m+1} r_{m+1} J_0(\beta_n r_{m+1}) - a_m r_m J_0(\beta_n r_m) \Big] \end{aligned} \tag{3.17}$$

The second summation in equation (3.17) cancels out on a term by term basis, with the exception of the first and last terms. The other summation can be rewritten as

$$\begin{aligned} A_n = -\frac{4}{\alpha_n^2 J_0^2(\alpha_n)} \Bigg\{ a_K r_K \left[\frac{r_{K-1} J_1(\beta_n r_{K-1})}{r_K^2 - r_{K-1}^2} + \frac{\beta_n}{2} J_0(\beta_n r_K) \right] \\ + \sum_{m=1}^{K-1} a_m r_m \left[\frac{r_{m+1} J_1(\beta_n r_{m+1}) - r_m J_1(\beta_n r_m)}{r_{m+1}^2 - r_m^2} - \frac{r_m J_1(\beta_n r_m) - r_{m-1} J_1(\beta_n r_{m-1})}{r_m^2 - r_{m-1}^2} \right] \Bigg\} \end{aligned} \tag{3.18}$$

similar to equation (2.38). Use has been made of the fact that $a_0 = 0$ and $J_1(\beta_n r_K) = 0$.

3.1.3 Surface reluctance density

As seen in equation (3.3), the z-dependence of the magnetic vector potential is identical to the Cartesian case in equation (2.13), with β substituted for the wavenumber k in the definition of the complex wavenumber γ. Consequently, the concept of defining the surface reluctance density $R_n(z)$ and finding its value at the electrode surface for every spatial mode n via transfer relations across every homogeneous layer is directly applicable here. After substituting β for k, equations (2.39), (2.46), and (2.50) through (2.52) become

$$R_n(z) \equiv \frac{1}{\beta_n} \cdot \frac{H_{r,n}(z)}{A_{\varphi,n}(z)} \tag{3.19}$$

$$R_n(z_0) = \frac{\gamma_n}{\mu^* \beta_n} \tag{3.20}$$

$$R_n(z_0) = \frac{\gamma_n}{\mu^* \beta_n} \cdot \frac{\mu^* \beta_n R_n(z_0 + t) \coth(\gamma_n t) + \gamma_n}{\mu^* \beta_n R_n(z_0 + t) + \gamma_n \coth(\gamma_n t)} \tag{3.21}$$

$$R_n \equiv R_n(0^+) - R_n(0^-) = \frac{1}{\beta_n} \cdot \frac{H_{r,n}(z = 0^+) - H_{r,n}(z = 0^-)}{A_{\varphi,n}(z = 0)} \tag{3.22}$$

$$K_{\mathrm{S}n} = R_n \beta_n A_n \tag{3.23}$$

At the bottom interface ($z = z_0$) of any layer for high mode numbers

$$\lim_{n \to \infty} R_n(z_0) = \frac{1}{\mu^*} \tag{3.24}$$

which means that unless embedded in a magnetizable material,

$$R_\infty = \lim_{n \to \infty} R_n = \frac{2}{\mu_0} \tag{3.25}$$

3.1.4 Boundary conditions

In the gaps between the windings the condition is that the surface current density must be zero, as in equation (2.53):

$$K_{\mathrm{S}}(r) = H_r(r, z = 0^+) - H_r(r, z = 0^-) = 0 \tag{3.26}$$

Similarly, for a single turn winding the contour integral

$$\oint_C \mathbf{E} \cdot d\mathbf{s} = -i\omega \oint_C \mathbf{A} \cdot d\mathbf{s} \tag{3.27}$$

results in a boundary condition of the form

$$v = i\omega(2\pi r)A_\varphi(r) + (2\pi r)\frac{K_{\mathrm{S}}(r)}{\Delta\sigma_{\mathrm{coil}}} \tag{3.28}$$

A complicating factor in equation (3.28) as compared to equation (2.55) is that equation (3.27) involves integration over φ, which introduces a factor of r to the integrand.

Integrating the boundary conditions given by equations (3.26) and (3.28) over an interval, in order to generate a constraining equation for the evaluation of the potential at the collocation points, involves an integral of the surface current density:

$$\begin{aligned}\int_{r_m^*}^{r_{m+1}^*} K_{\mathrm{S}}(r)\,dr &= \sum_{n=1}^{\infty} \int_{r_m^*}^{r_{m+1}^*} R_n A_n \beta_n J_1(\beta_n r)\,dr \\ &= -\sum_{n=1}^{\infty} A_n R_n \left[J_0(\beta_n r_{m+1}^*) - J_0(\beta_n r_m^*)\right] = \sum_{n=1}^{\infty} R_n \sum_{j=1}^{K} M_{m,j}^n a_j\end{aligned} \tag{3.29}$$

The coefficients $M_{m,j}^n$ constitute the contribution to the integral over the mth interval of the vector potential at the jth collocation point for the nth Bessel mode. They can be obtained by substituting equation (3.18) into equation (3.29) yielding

$$\begin{aligned}M_{m,j}^n = \frac{4}{\alpha_n^2 J_0^2(\alpha_n)} &\left[J_0(\beta_n r_{m+1}^*) - J_0(\beta_n r_m^*)\right] \times \\ &\times r_j \left[\frac{r_{j+1}J_1(\beta_n r_{j+1}) - r_j J_1(\beta_n r_j)}{r_{j+1}^2 - r_j^2} - \frac{r_j J_1(\beta_n r_j) - r_{j-1}J_1(\beta_n r_{j-1})}{r_j^2 - r_{j-1}^2}\right] \qquad \text{for } j < K\end{aligned} \tag{3.30a}$$

and

$$M_{m,K}^n = \frac{4}{\alpha_n^2 J_0^2(\alpha_n)} \left[J_0(\beta_n r_{m+1}^*) - J_0(\beta_n r_m^*)\right] r_K \left[\frac{r_{K-1}J_1(\beta_n r_{K-1})}{r_K^2 - r_{K-1}^2} + \frac{\beta_n}{2} J_0(\beta_n r_K)\right] \tag{3.30b}$$

At this point the method diverges somewhat from the Cartesian coordinate method of Section 2.1. The difference comes from the fact that when using Bessel functions there is no analogous closed form of the infinite summation used to define function $f(x)$ in equation (2.61). Consequently, there is no benefit in isolating the R_∞ component and creating a separate M' matrix. This issue is treated with more detail in Appendix B.

Before integrating the boundary condition over the windings, it is convenient to divide

both sides of equation (3.28) by $2\pi r$ first, leading to the following expression for the integral of the left hand side:

$$\int_{r_m^*}^{r_{m+1}^*} \frac{v}{2\pi r}\, dr = \frac{v}{2\pi} \ln\Big(\frac{r_{m+1}^*}{r_m^*}\Big) \tag{3.31}$$

The right hand side of equation (3.28) contains a term with $\int K_S(r)\, dr$, already handled in equation (3.29), and an integral over $A_\varphi(r)$. The latter may be obtained by integrating equation (3.12) directly, but closer scrutiny reveals that this is unnecessarily complicated. The interpolation function in equation (3.11) was chosen in order to make it possible to find a closed form expression for the Bessel series coefficients. Since this function is only an approximation to $A_\varphi(r)$ anyway, it is better for the purpose of this integral to assume a linear interpolation function, similar to equation (2.30):

$$A_\varphi(r) = \frac{a_m(r_{m+1} - r) + a_{m+1}(r - r_m)}{r_{m+1} - r_m} \tag{3.32}$$

yielding

$$\begin{aligned} 2\int_{r_m^*}^{r_{m+1}^*} A_\varphi(r)\, dr = {} & a_{m-1}\frac{(r_m^* - r_m)^2}{r_m - r_{m-1}} + a_{m+1}\frac{(r_{m+1}^* - r_m)^2}{r_{m+1} - r_m} \\ & + a_m\left[\frac{r_m^* - r_m}{r_m - r_{m-1}}(r_m^* + r_m - 2r_{m-1}) + \frac{r_{m+1}^* - r_m}{r_{m+1} - r_m}(2r_{m+1} - r_m - r_{m+1}^*)\right] \\ & r_{m-1} < r_m^* < r_m < r_{m+1}^* < r_{m+1} \end{aligned} \tag{3.33}$$

If written as

$$\int_{r_m^*}^{r_{m+1}^*} A_\varphi(r)\, dr = \sum_{j=1}^{K} M''_{m,j} a_j \tag{3.34}$$

the matrix M'' will have exactly the form given in equation (2.64), with nonzero elements given by

$$\begin{aligned} M''_{m,m} &= \frac{1}{2}\left[\frac{r_{m+1}^* - r_m}{r_{m+1} - r_m}(2r_{m+1} - r_m - r_{m+1}^*) + \frac{r_m^* - r_m}{r_m - r_{m-1}}(r_m^* + r_m - 2r_{m-1})\right] \\ M''_{m,m+1} &= \frac{1}{2}\cdot\frac{(r_{m+1}^* - r_m)^2}{r_{m+1} - r_m} \\ M''_{m+1,m} &= \frac{1}{2}\cdot\frac{(r_m^* - r_m)^2}{r_m - r_{m-1}} \end{aligned} \tag{3.35}$$

3.1.5 Matrix equation and terminal currents

Integrating the boundary conditions over each of the intervals delimited by r_m^* yields equations that may be combined in matrix form to solve for the unknown a_m, which appear in vector a in the matrix equation $Ma = b$. The matrix M can be built from the previously

defined matrices M^n and M'' as follows:

$$M_{m,j} = \begin{cases} \sum_{n=1}^{\infty} R_n M^n_{m,j} & r_m \text{ is in a gap} \\ \frac{1}{\Delta\sigma_{\text{coil}}} \sum_{n=1}^{\infty} R_n M^n_{m,j} + i\omega M''_{m,j} & r_m \text{ is in a winding} \end{cases} \tag{3.36}$$

The right hand side b is determined from equation (3.31), and its nonzero elements are given by:

$$b_{m,p} = \frac{1}{2\pi} \ln\left(\frac{r^*_{m+1}}{r^*_m}\right) \tag{3.37}$$

if $p = 0$ and r_m falls on the primary winding, or if $p = 1$ and r_m falls on the secondary winding.

Solving the matrix equations determines a_m, which in turn determine the magnetic vector potential **A**. The magnetic flux intensity **B** may now be obtained everywhere via equation (3.4).

To determine the terminal currents, the surface current density $K_{\text{S}}(r)$ is integrated across each of the two windings. This can be done by taking advantage of the established matrices by defining the two-port sensor matrix as a product of matrices

$$Y = Fa \tag{3.38}$$

where a is the just calculated set of collocation point vector potential values. The required form for F is

$$F_{p,j} = \sum_m \sum_{n=1}^{\infty} R_n M^n_{m,j} \tag{3.39}$$

with the understanding that the same constraints on the values of m included in the summation hold as for equation (3.37) above.

This concludes the derivation of the formulas necessary to implement the collocation point method of modeling a magnetometer with circular geometry.

3.2 Dielectrometer

This section presents the model of the rotationally symmetric dielectrometer. Although most of the research in this project is focused on magnetic sensors, there are reasons why it is beneficial to consider the electroquasistatic sensor: no one has worked on this model before, and a sensor of this geometry already exists at JENTEK, which makes it easy to test the model experimentally, with the results presented in Section 3.3.

Although the principle of duality provides many parallels between the magnetoquasistatic and electroquasistatic regimes, there is one fundamental difference: there is no equivalent to magnetic diffusion, i.e. the electrostatic potential Φ obeys Laplace's equation. From the point of view of the model, this means that for each spatial mode the decay constant in the z-direction is purely real and equal to the wavenumber k, or β in cylindrical coordinates. It is thus independent of the excitation frequency ω.

In practical terms the lack of the equivalent of magnetic diffusion, already discussed in

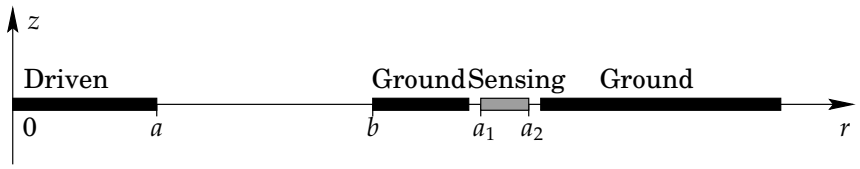

Figure 3-2: Definition of geometry parameters of circular dielectrometer.

Section 2.2, makes dielectric measurements much harder to perform for the following reasons:

1. In the absence of conductivity in the materials, the sensor transadmittance is purely imaginary (capacitive), and therefore there is enough information to determine only a single unknown quantity. Since in practice the sensor lift-off, which is the thickness of the air gap between the sensor electrodes and the material, is almost always unknown, due to surface roughness, sensor electrode thickness, etc., in order to measure even a single unknown material property, data from two sensors with different depths of sensitivity must be combined. Conductivity in the material does not improve matters significantly either, since the extra information present in the phase signal is used up by the extra unknown property, the conductivity. It is usually not possible to assume that this conductivity is known, because in nominally insulating materials, on which these dielectric measurements are performed, the conductivity is a very strong function of temperature, relative humidity, and the presence of contaminants.

2. Since the depth of penetration is independent of frequency,* it is not possible to obtain extra information by operating the same sensor at two or more frequencies.

As a consequence, unless some questionable assumptions are made, two or more sensors need to be used simultaneously, if a meaningful measurement is to be performed.

3.2.1 Sensor geometry

A top view of the sensor considered in this section is shown in Figure 3-5. A cross section of the sensor is shown in Figure 3-2, which also defines the geometrical parameters. In the analysis it is assumed that everywhere for $r \geq b$ the potential at $z = 0$ is forced to zero by the presence of a ground plane. The sensing electrode is formed as a cut-out from this ground plane, with as small a gap as practically possible. It is kept at ground potential via a circuit like the one shown in Figure 2-3. The other side of the sensor substrate is also kept at ground via an electrode over the entire area of the sensor.

The value of the electrostatic potential is known for $0 \leq r \leq a$, where it is equal to the driving voltage, and for $r \geq b$, where it is zero. In the gap, it is determined via a collocation point method. An example of a potential function for a sensor in air is shown in Figure 3-3.

*This is actually strictly true only within a single homogeneous layer, which is the most important case anyway. But in a two-layer structure, a slightly conducting thin layer close to the sensor may let the electric field penetrate and reach to the next layer at high frequencies, while completely shielding the field at low frequencies. At least in theory, in such cases it is possible to obtain extra information by operating at multiple frequencies.

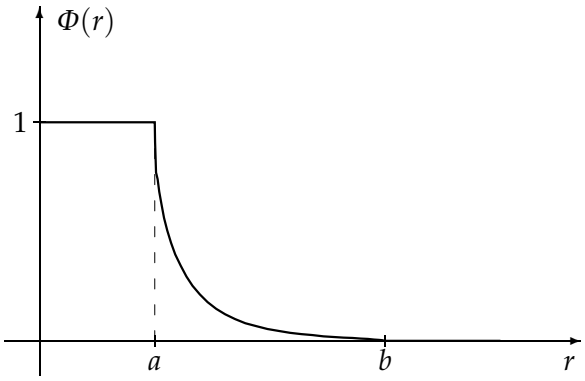

Figure 3-3: Normalized calculated potential at the electrode surface for the circular dielectrometer in air. In this case $a = 0.5$ mm, $b = 1.5$ mm, and the substrate thickness is $h = 0.127$ mm.

3.2.2 Laplace's equation

Due to symmetry, the potential is independent of φ, i.e. $\Phi = \Phi(r,z)$. Laplace's equation assumes the following form:

$$\nabla^2\Phi = \frac{1}{r}\frac{\partial}{\partial r}\left(r\frac{\partial}{\partial r}\Phi\right) + \frac{\partial^2}{\partial z^2}\Phi = 0 \tag{3.40}$$

The relevant solution of this differential equation is:

$$\Phi(r,z) = J_0(\beta r)\left(c_1 e^{-\beta z} + c_2 e^{+\beta z}\right) \tag{3.41}$$

since the Bessel function Y_0 is infinite at $r = 0$. For this solution the electric field is given by:

$$\mathbf{E} = -\nabla\Phi = \beta J_1(\beta r)\left(c_1 e^{-\beta z} + c_2 e^{+\beta z}\right)\hat{\mathbf{r}} + \beta J_0(\beta r)\left(c_1 e^{-\beta z} - c_2 e^{+\beta z}\right)\hat{\mathbf{z}} \tag{3.42}$$

Because of equation (3.41), the Bessel series to use in this case is based on J_0:

$$f(x) = \sum_{n=1}^{\infty} A_n J_0\Big(\frac{\alpha_n}{R}x\Big) \qquad 0 < x < R \tag{3.43}$$

where α_n here are the positive real of J_0. The zeros are numbered from one, i.e. $\alpha_1 = 2.405$. Correspondingly, A_n and Q_n are given by

$$A_n = \frac{1}{Q_n}\int_0^R x\, f(x) J_0\Big(\frac{\alpha_n}{R}x\Big)\, dx \tag{3.44}$$

$$Q_n = \int_0^R x\, J_0^2\Big(\frac{\alpha_n}{R}x\Big)\, dx = \frac{R^2}{2}J_1^2(\alpha_n) \tag{3.45}$$

As in the magnetometer case, the radius R is the outer limit of the interval over which the Bessel series expansion is applied. It is chosen to be several times greater than the outer radius of the sensor, in order to make the effect of any phantom electric fields resulting from the summation of the series terms outside of this radius negligible.

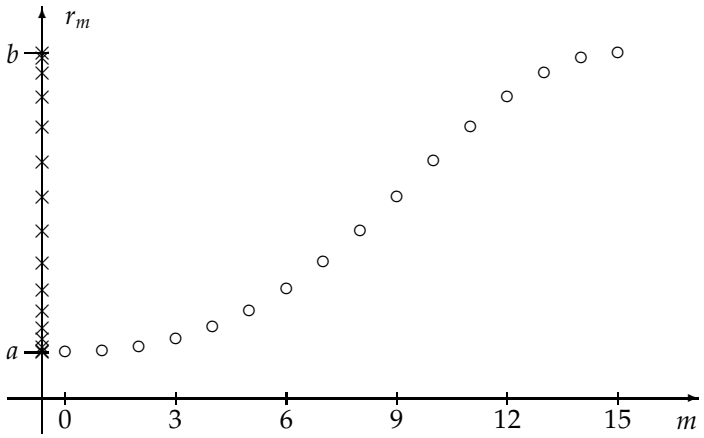

Figure 3-4: Positions of 16 collocation points. The points are concentrated near the electrode edges, where the potential is changing most rapidly. The concentration is skewed toward the driven electrode.

3.2.3 Collocation points

In the sensor gap the electrostatic potential is approximated by an interpolation of its value between a set of $K+2$ collocation points, r_m. The first and last ones are at the electrode edges, and inbetween the points are concentrated near the edges, where the potential is changing the most rapidly as shown in Figure 3-3. The collocation points are more heavily concentrated near the driven electrode, according to the following formula:

$$r_m = a + \frac{b-a}{2}\left\{1 - \cos\left(\frac{m\pi}{K+1}\right) + 0.15\left[\cos\left(\frac{2m\pi}{K+1}\right) - 1\right]\right\} \qquad m = 0, 1, 2, \ldots, K+1 \quad (3.46)$$

A bit of the second harmonic is added to the traditionally used cosinusoidal distribution, in order to skew the points toward the driven electrode. Figure 3-4 shows the resulting positions of the collocation points. The integration intervals, delimited by r_m^*, are positioned half way between the collocation points, except at the two ends:

$$r_m^* = \begin{cases} r_0 & m = 0 \\ r_{K+1} & m = K \\ \dfrac{r_{m+1} + r_m}{2} & m = 1, 2, \ldots, K-1 \end{cases} \quad (3.47)$$

As before, a suitable interpolation function must be chosen to express Φ as a function of its values at the collocation points. Integrals of the form $\int x^p J_0(x)\,dx$ have closed form solutions when p is an odd number. For example:

$$\int x J_0(x)\,dx = x J_1(x) \quad (3.48a)$$

$$\int x^3 J_0(x)\,dx = x^3 J_1(x) - 2x^2 J_2(x) \quad (3.48b)$$

An appropriate interpolation function therefore is

$$y = c_1 + c_2 x^2 \tag{3.49}$$

which results in the following interpolation function $y(x)$ in the interval between x_1 and x_2:

$$y = \frac{y_1(x_2^2 - x^2) + y_2(x^2 - x_1^2)}{x_2^2 - x_1^2} \tag{3.50}$$

Using equation (3.50), the Bessel series coefficients in the expansion of the potential Φ over the period $0 \leq r \leq R$ are given by:

$$\Phi_n = \frac{1}{Q_n}\left[\int_0^a rJ_0(\beta_n r)\,dr + \sum_{m=0}^{K}\int_{r_m}^{r_{m+1}} rJ_0(\beta_n r)\frac{v_m(r_{m+1}^2 - r^2) + v_{m+1}(r^2 - r_m^2)}{r_{m+1}^2 - r_m^2}\,dr\right] \tag{3.51}$$

where the coefficients Q_n are defined in equation (3.45) and $\beta_n = \alpha_n/R$. The first term in equation (3.51) results from integration over the driven electrode, where the potential is forced to the driving voltage and may be set to unity for the computation of the transcapacitance. The potential is zero for $r \geq b$ and therefore this interval is not included. Carrying out the integration yields

$$\begin{aligned}\Phi_n Q_n \beta_n^2 = \beta_n a J_1(\beta_n a) + 2\sum_{m=0}^{K}\frac{v_m - v_{m+1}}{r_{m+1}^2 - r_m^2}\Big[r_{m+1}^2 J_2(\beta_n r_{m+1}) - r_m^2 J_2(\beta_n r_m)\Big] \\ + \beta_n \sum_{m=0}^{K}\Big[v_{m+1} r_{m+1} J_1(\beta_n r_{m+1}) - v_m r_m J_1(\beta_n r_m)\Big]\end{aligned} \tag{3.52}$$

The terms in the second summation of equation (3.52) cancel out on a term by term basis, except for the two end terms multiplying v_0 and v_{K+1}. The latter is at $r_{K+1} = b$, where the potential is zero due to the ground, and can be ignored. The first one contributes a term equal to $-\beta_n a J_1(\beta_n a)$, which exactly cancels the leading term in equation (3.52), since $v_0 = 1$. This results in a much simpler expression:

$$\Phi_n = \frac{4}{\alpha_n^2 J_1^2(\alpha_n)}\sum_{m=0}^{K}\frac{v_m - v_{m+1}}{r_{m+1}^2 - r_m^2}\Big[r_{m+1}^2 J_2(\beta_n r_{m+1}) - r_m^2 J_2(\beta_n r_m)\Big] \tag{3.53}$$

which can be rewritten as

$$\begin{aligned}\Phi_n = \frac{4}{\alpha_n^2 J_1^2(\alpha_n)}\Bigg\{&\frac{r_1^2 J_2(\beta_n r_1) - r_0^2 J_2(\beta_n r_0)}{r_1^2 - r_0^2} \\ &+ \sum_{m=1}^{K} v_m\left[\frac{r_{m+1}^2 J_2(\beta_n r_{m+1}) - r_m^2 J_2(\beta_n r_m)}{r_{m+1}^2 - r_m^2} - \frac{r_m^2 J_2(\beta_n r_m) - r_{m-1}^2 J_2(\beta_n r_{m-1})}{r_m^2 - r_{m-1}^2}\right]\Bigg\}\end{aligned} \tag{3.54}$$

Note than in equation (3.54) the index of the summation starts at $m = 1$. The first term has been written out separately, because $v_0 = 1$ is known, and its coefficient will contribute to the right hand side of the matrix equation.

3.2.4 Surface capacitance density and boundary conditions

All equations derived in Section 2.2.5 directly apply to cylindrical coordinates. The constant term C_0^* is not needed in this case.

In cylindrical coordinates the $\sigma_S^*(r) = 0$ constraint of equation (2.103) takes the following form:

$$\begin{aligned}\int_{r_m^*}^{r_{m+1}^*} \sigma_S^*(r) 2\pi r\, dr &= \sum_{n=1}^{\infty} \int_{r_m^*}^{r_{m+1}^*} C_n^* \Phi_n \beta_n J_0(\beta_n r) 2\pi r\, dr \\ &= 2\pi \sum_{n=1}^{\infty} C_n^* \Phi_n \Big[r_{m+1}^* J_1(\beta_n r_{m+1}^*) - r_m^* J_1(\beta_n r_m^*) \Big] \\ &= \sum_{n=1}^{\infty} C_n^* \sum_{j=0}^{K} M_{m,j}^n v_j = 0\end{aligned} \tag{3.55}$$

After substituting equation (3.54) into equation (3.55), the elements of M^n are determined to be:

$$\begin{aligned}M_{m,j}^n = \frac{8\pi}{\alpha_n^2 J_1^2(\alpha_n)} &\Big[r_{m+1}^* J_1(\beta_n r_{m+1}^*) - r_m^* J_1(\beta_n r_m^*) \Big] \times \\ &\times \left[\frac{r_{j+1}^2 J_2(\beta_n r_{j+1}) - r_j^2 J_2(\beta_n r_j)}{r_{j+1}^2 - r_j^2} - \frac{r_j^2 J_2(\beta_n r_j) - r_{j-1}^2 J_2(\beta_n r_{j-1})}{r_j^2 - r_{j-1}^2} \right]\end{aligned} \tag{3.56}$$

Similarly, the right hand side vector b of the matrix equation is given by

$$b = \sum_{n=1}^{\infty} C_n^* b^n \tag{3.57}$$

where the elements of b^n are

$$b_m^n = -\frac{8\pi}{\alpha_n^2 J_1^2(\alpha_n)} \Big[r_{m+1}^* J_1(\beta_n r_{m+1}^*) - r_m^* J_1(\beta_n r_m^*) \Big] \frac{r_1^2 J_2(\beta_n r_1) - r_0^2 J_2(\beta_n r_0)}{r_1^2 - r_0^2} \tag{3.58}$$

Solving the matrix equation results in full knowledge of the electrostatic potential $\Phi(r)$ at the electrode surface. Figure 3-3 shows this function for a dielectric sensor in air, using straight lines to interpolate between its values at the collocation points.

3.2.5 Calculating transcapacitance

In analogy to Section 2.2.8, the transcapacitance is obtained by integrating σ_S^* over the electrode area:

$$\begin{aligned}C_T &= -\sum_{n=1}^{\infty} \int_{a_1}^{a_2} C_n^* \Phi_n \beta_n J_0(\beta_n r) \theta r\, dr \\ &= -\theta \sum_{n=1}^{\infty} C_n^* \Phi_n \Big[a_2 J_1(\beta_n a_2) - a_1 J_1(\beta_n a_1) \Big]\end{aligned} \tag{3.59}$$

where the electrode extends from a_1 to a_2 radially and has an arc angle of θ, which for practical sensors must be less than 2π. In Figure 3-5 both sensors have $\theta = \pi$, i.e. 180°.

In order to express the transcapacitance C_T in terms of the potential values v calculated

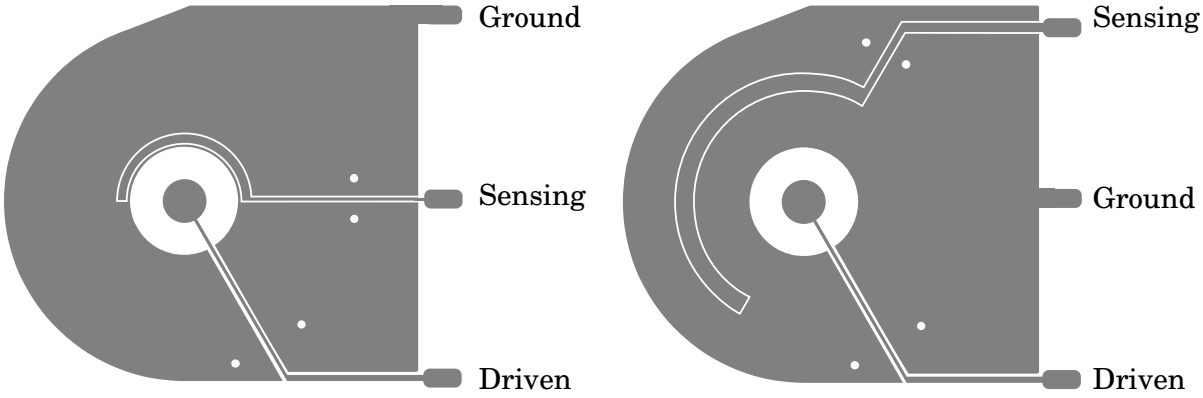

Figure 3-5: Layout of two circular dielectric sensors with different depth of sensitivity. The depth of sensitivity is determined by the position of the sensing electrode. Ignoring the effect of the narrow gap between the virtually grounded sensing electrode and the ground electrode, the electric field is identical for both sensors.

in the last step, equation (3.54) is substituted into equation (3.59), yielding

$$C_T = -4\theta \sum_{n=1}^{\infty} \frac{C_n^*}{\alpha_n^2 J_1^2(\alpha_n)} \Big[a_2 J_1(\beta_n a_2) - a_1 J_1(\beta_n a_1) \Big] \left\{ \frac{r_1^2 J_2(\beta_n r_1) - r_0^2 J_2(\beta_n r_0)}{r_1^2 - r_0^2} + \sum_{m=1}^{K} v_m \left[\frac{r_{m+1}^2 J_2(\beta_n r_{m+1}) - r_m^2 J_2(\beta_n r_m)}{r_{m+1}^2 - r_m^2} - \frac{r_m^2 J_2(\beta_n r_m) - r_{m-1}^2 J_2(\beta_n r_{m-1})}{r_m^2 - r_{m-1}^2} \right] \right\} \quad (3.60)$$

The method described in this section is used to generate the measurement grid shown in the next section.

3.3 Experimental verification of cylindrical coordinate model

This section describes an experiment designed to test the cylindrical geometry methods in this chapter in general, and the dielectric case in particular. The experiment entails measurements with a pair of circular dielectrometers with different depths of sensitivity, shown in Figure 3-5.

At the frequency of operation, 15.8 kHz, all materials used in the experiment can be treated as perfect insulators, i.e. their values of the permittivity ϵ^* are purely real. This means that the sensor transcapacitance is also purely real, and no useful instrument phase data are available. This frequency is chosen primarily as a matter of convenience for use with the standard test instruments at JENTEK. There is no loss of generality by working only with real ϵ, because working with complex ϵ^* results in no changes to the model.

In this experiment two unknown quantities are measured simultaneously, by combining the magnitude of the signal from the two sensors. The two unknown quantities are the permittivity of a dielectric plate positioned above the sensors, and the lift-off, defined as the distance between the bottom surface of the plate and the sensor electrode surface. The thickness of the plate is known, 1.58 mm, and is included in the model used to generate the measurement grid. The entire sensor assembly is contained in a metal chamber, whose cover acts as the ground plane, positioned several centimeters above the sensor and the dielectric plate.

Parameter		Sensor 1	Sensor 2
Driven electrode outer radius	a	1.75 mm	
Ground plane inner radius	b	4.5 mm	
Sensing electrode inner radius	a_1	4.75 mm	9.1875 mm
Sensing electrode outer radius	a_2	5.50 mm	10.625 mm
Sensing electrode segment angle	θ	180°	
Substrate thickness	h	0.254 mm	
Substrate relative permittivity	ϵ_S	2.1	

Table 3.1: Geometric and material parameters of the sensors in Figure 3-5.

The reason for choosing a dielectric sensor with a magnitude/magnitude grid* to test the models is that this configuration is most sensitive to the accuracy of the model, and in particular to the correct treatment of the differences between cylindrical and Cartesian geometry. To understand why this is so, consider the alternatives:

1. For a magnetic sensor the test material would have to be metal, where the conductivity is the dominant material property. Using insulating ferromagnetic materials, such as ferrites, could be an alternative, but these usually have values of the magnetic permeability that are so high as to be essentially infinite. In other words, it is very difficult to differentiate between insulating ferrites of relative permeability of, say, 500 vs. 2000. When using metal, signal phase information has to be considered, which means that in order to have only two degrees of freedom, a single sensor would have to be used. The reason why the dielectric magnitude/magnitude measurement is more sensitive to the correctness of the model is that, since the only difference between the two dielectric magnitude signals stems from the position of the sensing electrode, this difference is extremely sensitive to correct modeling of the sensor geometry, while both magnetic measurement quantities would be affected similarly by an error in the model.

2. Another possibility is to use a single dielectric sensor with a material with non-negligible conductivity. However, as with the magnetic sensor, incorrect modeling of the sensor geometry would tend to affect the two measured quantities similarly, while the difference between two magnitude signals is based entirely on geometrical considerations.

The geometric parameters of the sensors in Figure 3-5 are listed in Table 3.1. Converting the raw sensor magnitude data to estimated parameter data is done with the help of a two dimensional measurement grid. Measurement grids are described in Section 1.4.1. The grid used here is shown in Figure 3-6. A way to understand of the grid qualitatively is to follow two constant lift-off lines, for two different values of the lift-off. When the lift-off is low, the average slope of the line is low, because the signal of the first sensor increases much faster than the second one, since it is closer to the driven electrode. On the other hand, at higher lift-off values the lines become almost vertical, since the dielectric plate is too far from the first sensor to affect its response significantly, while some of the electric field lines that terminate on the second sensor electrode still pass through the plate.

A curious aspect of the grid in Figure 3-6 is that at the highest lift-off values the sensors' magnitudes actually decrease with increasing permittivity, and as a consequence in the figure the $\epsilon = 1$ point on the grid is not at the bottom left corner. This happens because while the

*The concept of magnitude/magnitude grids was developed by Dr. N. J. Goldfine and Dr. A. Washabaugh [54].

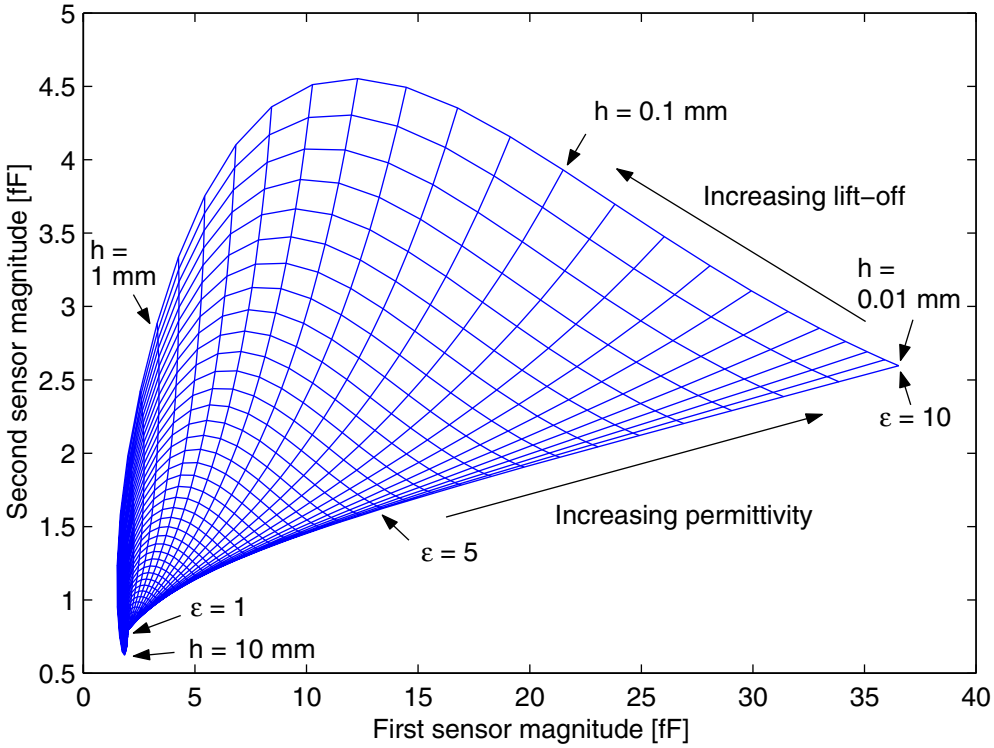

Figure 3-6: Permittivity/lift-off measurement grid for the pair of dielectric sensors in Figure 3-5. The thickness of the dielectric plate is fixed at 1.58 mm (1/16″). The relative permittivity range of the grid is from 1 to 10, and the lift-off range is 0.01 mm to 10 mm, both on a logarithmic scale.

plate is too far from the sensors for any electric field lines that terminate on the sensing electrodes to pass through it, it can still affect the response by redirecting some of the field lines that would otherwise have ended on the electrodes to the grounded back plane, which is the sensor enclosure cover in this setup. This effect would not have been modeled correctly if the back plane had not been considered, which is how the models used to be formulated by others [2, 3]. For further discussion on the effect of the back plane to the collocation point models, refer to Section 2.2.

The measurements are made with two dielectric sheets of equal thickness, 1.58 mm, made of different materials. The first one is made of polycarbonate (Lexan), with a dielectric constant of 3.2. The second one is made of material used in printed circuit boards, with a higher dielectric constant, apparently near 4.8. These two dielectric plates are suspended above the sensors with the aid of spacers at the sides, at lift-offs ranging from intimate contact, which is a few hundredths of a millimeter due to surface roughness, to about three millimeters.

The calibration method used for this set of measurements is two-point reference calibration. For a discussion of the available calibration methods and the circumstances that favor one versus the others, refer to Appendix D. One of the reference points is the air point, $\epsilon = 1$. The other reference point is taken with a polycarbonate plate, whose permittivity is known and equal to 3.2, with an empirically determined value for the reference lift-off, 0.02 mm, which accounts for surface roughness and the nonzero electrode thickness, not otherwise in-

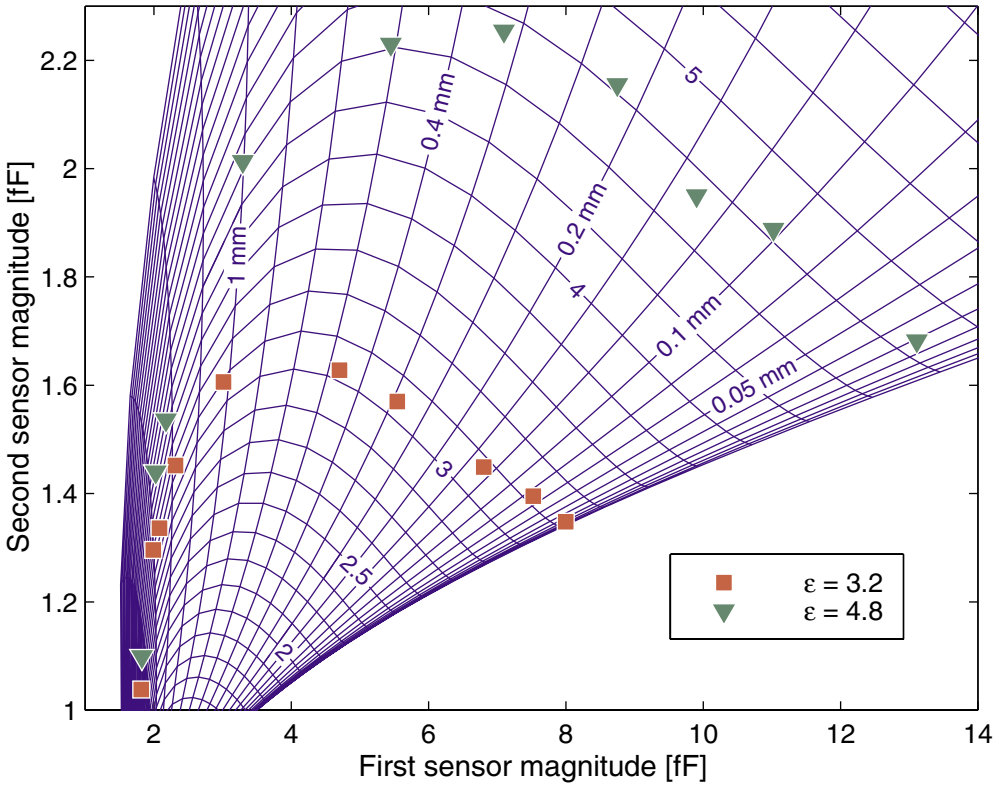

Figure 3-7: Results of measurements with the circular dielectric sensors. Two sets of measurements are shown with materials of different permittivity, taken at a variety of lift-off positions. Each set follows lines of constant permittivity on the measurement grid.

Data set	Permittivity	Lift-off [mm]	Data set	Permittivity	Lift-off [mm]
1	3.20	0.019	11	4.76	0.029
2	3.22	0.070	12	4.83	0.100
3	3.18	0.135	13	4.73	0.139
4	3.15	0.299	14	4.90	0.213
5	3.14	0.458	15	4.84	0.325
6	3.30	1.028	16	4.68	0.497
7	3.46	1.528	17	4.82	0.984
8	3.49	1.845	18	4.48	1.662
9	3.57	1.979	19	4.53	1.865
10	3.60	2.877	20	3.68	2.641

Table 3.2: Results of measurements with the circular dielectric sensors, shown in Figure 3-7. Data sets 1–10 are taken with the polycarbonate plate, with nominal permittivity of 3.2. Data sets 11–20 are taken with the printed circuit board material.

corporated in the model.* For this measurement it is not practical to use one-point air calibration, because with this sensor geometry the parasitic coupling to the sensing electrode leads cannot be neglected. Still, an attempt is made to remain true to the principle of model-based sensor design, where calibration parameters have a valid physical interpretation, by keeping the air point as one of the reference points.

The results of the measurements are listed in Table 3.2 and plotted on the measurement grid in Figure 3-7. The two groups of ten measurement sets correspond to the two different materials. It can be seen right away in the table that the task of independently measuring permittivity and lift-off has succeeded. The measured permittivity is decoupled from the varying lift-off. The accuracy of the measurement decreases significantly at high lift-off values, above approximately 1 mm. This is understandable, since at these separations very few of the electric field lines pass through the material. This can be visualized graphically by noting that the high lift-off points fall on areas of the grid in Figure 3-7 where the grid lines are very dense, which means that small variations of the sensor response result in large variations of the estimated properties.

It can be further observed in Figure 3-7 that the two data sets follow two separate lines of constant permittivity, closely matching the curvature of these lines. This, more than anything else, validates the correctness of the model, since it is very unlikely that a correct relationship that is so highly nonlinear could be accidental.

3.4 Summary of Chapter 3

The semi-analytical collocation point models have been successfully applied to magnetic and dielectric sensors with cylindrical geometry in Sections 3.1 and 3.2 respectively. The dependence of the electromagnetic fields on the z-coordinate exactly parallels the Cartesian case, while the periodic sinusoidal dependence on the x-coordinate is transformed to Bessel functions of the r-coordinate in cylindrical geometry. This requires the use of Fourier-Bessel series. Although there is no periodicity in this geometry, the basic principles of the periodic sensors can still be applied by choosing a domain for the Bessel series that is much larger than the characteristic sensor dimensions.

The validity of the newly developed methods has been confirmed for the capacitive sensor by an experiment, described in Section 3.3, designed to be particularly sensitive to the correct treatment of the sensor geometry.

The new models make it possible to design new families of model-based sensors for a new range of applications. They also provide the basis for the extension of the distributed current drive models, developed in Chapter 4, to cylindrical geometry, adopted for the design of the prototype giant magnetoresistive magnetometer described in Chapter 5.

*Lesieutre *et al.* present a method of incorporating electrode thickness into the semi-analytical models in [37].

Chapter 4

Distributed Current Drive Sensors

In magnetometers where the primary windings are driven in a way that excites a magnetic field with a fundamental spatial wavelength much greater than the distance between neighboring windings, the numerical techniques used to calculate the sensor response are fundamentally different. If the assumption is made that the physical dimensions of the conductors are small with respect to the other relevant length parameters, it becomes possible to analyze each Fourier mode independently, which significantly simplifies the computations, and eliminates the need for iterative techniques or for solving large sets of simultaneous equations. This is a consequence of the fact that with this assumption the current excitation is independent of the resulting magnetic fields, and the constituent Fourier modes are decoupled from each other. It is thus possible to use fast Fourier transforms and related methods to arrive at the magnetic field distribution. These principles are presented in more detail, and with some specific examples, in the rest of this chapter.

Note that these methods may also be applied to the MWM in cases where it is acceptable to assume a current distribution within the windings determined *a priori*. Suitable candidates are: low frequency operation, where the current is uniform across each winding; high frequency operation, where the current is concentrated at the winding edges and may be represented by spatial impulse functions; and cases where the current distribution effects are negligible and can be absorbed in the calibration step.

Three types of sensors are modeled in this chapter:

1. Infinite periodic sensor with a distributed current drive. The simulation results are shown in Section 4.4. This is the simplest case to consider.

2. Rectangular (Cartesian) sensor with a finite width. The finite width of the sensor must be included in the model. Discussed in Section 4.5.

3. Circularly symmetric sensor with a distributed current drive. The methods developed for the other two sensors are combined with some of the ideas from Section 3.1, resulting in the model presented in Sections 4.8 and 4.9. This is the geometry of choice for the giant magnetoresistive sensor in Chapter 5.

Fourier methods are used to compute the sensor response to a material structure that consists of a stack of layers with homogeneous properties. There is no property variation in a direction parallel to the plane of the sensor.

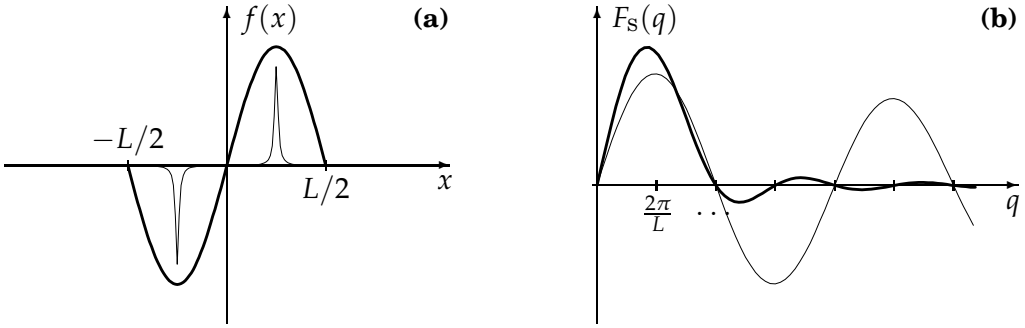

Figure 4-1: Comparison between distributed and concentrated current drives. **(a)** Two possible current profiles exciting a fundamental spatial mode of similar wavelength. **(b)** Corresponding spatial spectra.

4.1 Why use a distributed current drive

The concept of a distributed drive was first proposed by Prof. James R. Melcher [4] and refined by Dr. N. J. Goldfine *et al.* [32, 34, 35]. It is possible to excite a spatial mode of the same fundamental wavelength by using a single current loop of similar dimensions, instead of having several windings that follow a sinusoidal envelope function, which is the case considered in this chapter. Such single-loop implementation would be much simpler than the proposed distributed current drive. Figure 4-1 illustrates why the distributed drive current configuration is to be preferred, by comparing the spatial spectra of the two alternative current excitation schemes.

The applied surface current drive for both cases is shown in Figure 4-1 (a). The discrete nature of the sinusoidal current drive is ignored for the sake of this discussion. If the conductor spacing h is significantly smaller than the sensor width L, this simplification is justified. The single loop is represented by a pair of Lorentzian pulse functions, defined by equation (4.20) with $a = L/100$. Figure 4-1 (b) shows the corresponding spatial spectra.

In the case of the sinusoidal drive the magnitude of the transform falls off quickly for wavenumbers greater than the dominant mode, while the spectrum of the single loop shows substantial energy at wavenumbers much greater than the fundamental. In practice, this means that in the former case the energy is concentrated in the modes that penetrate furthest into the material, which is the desirable characteristic of distributed current drive designs, while in the latter case the sensitivity to material properties away from the surface is substantially reduced.

4.2 Definitions

The following definition for the exponential Fourier transform is used in the rest of this chapter:

$$f(x) = \frac{1}{2\pi} \int_{-\infty}^{\infty} F(q) e^{iqx}\, dq \tag{4.1a}$$

$$F(q) = \int_{-\infty}^{\infty} f(x) e^{-iqx}\, dx \tag{4.1b}$$

Given these definitions, the operation of convolution, denoted by the symbol $\otimes$, is defined

as

$$f(x) \otimes g(x) = \int_{-\infty}^{\infty} f(x')g(x-x')\,dx' \tag{4.2a}$$

$$F(q) \otimes G(q) = \frac{1}{2\pi}\int_{-\infty}^{\infty} F(q')G(q-q')\,dq' \tag{4.2b}$$

Note the factor of $1/(2\pi)$, needed when working in the q-domain. With these definitions, multiplication in one domain corresponds to convolution in the other, if the Fourier transform definition in equation (4.1) is used.

In many cases it is more convenient to work with sine transforms, defined as

$$f(x) = \frac{2}{\pi}\int_0^{\infty} F_{\mathrm{S}}(q)\sin(qx)\,dq \tag{4.3a}$$

$$F_{\mathrm{S}}(q) = \int_0^{\infty} f(x)\sin(qx)\,dx \tag{4.3b}$$

where the assumption is made that both $f(x)$ and $F_{\mathrm{S}}(q)$ are odd functions. The sine transform of an odd function $f(x)$ can be obtained from its exponential Fourier transform as

$$F_{\mathrm{S}}(q) = \frac{i}{2}F(q) \tag{4.4}$$

In this chapter plots of sine transforms are only shown with positive values of q, because they are odd functions. If a function can be represented as a summation of sinusoids as follows:

$$f(x) = \sum_{n=1}^{\infty} A_n \sin(k_n x) \tag{4.5}$$

though ***not*** necessarily as a Fourier series, which requires the wavenumbers k_n to form a harmonic sequence, then its continuous sine transform is

$$F_{\mathrm{S}}(q) = \frac{\pi}{2}\sum_{n=1}^{\infty} A_n u_0(q-k_n) \tag{4.6}$$

where $u_0(x)$ is the unit impulse function, sometimes denoted as $\delta(x)$.

The ***sinc*** function, which appears in many results in this chapter, is defined as

$$\mathrm{sinc}(x) \equiv \begin{cases} \dfrac{\sin(x)}{x} & x \neq 0 \\ 1 & x = 0 \end{cases} \tag{4.7}$$

Appendix A lists most of the symbols and acronyms and their definitions.

4.3 Closed form solutions for the magnetic field

In this section a simple case is considered, with only one infinitely thick layer on one side of the windings, and air, or some other insulating nonmagnetizable material, on the other, as shown in Figure 4-2.

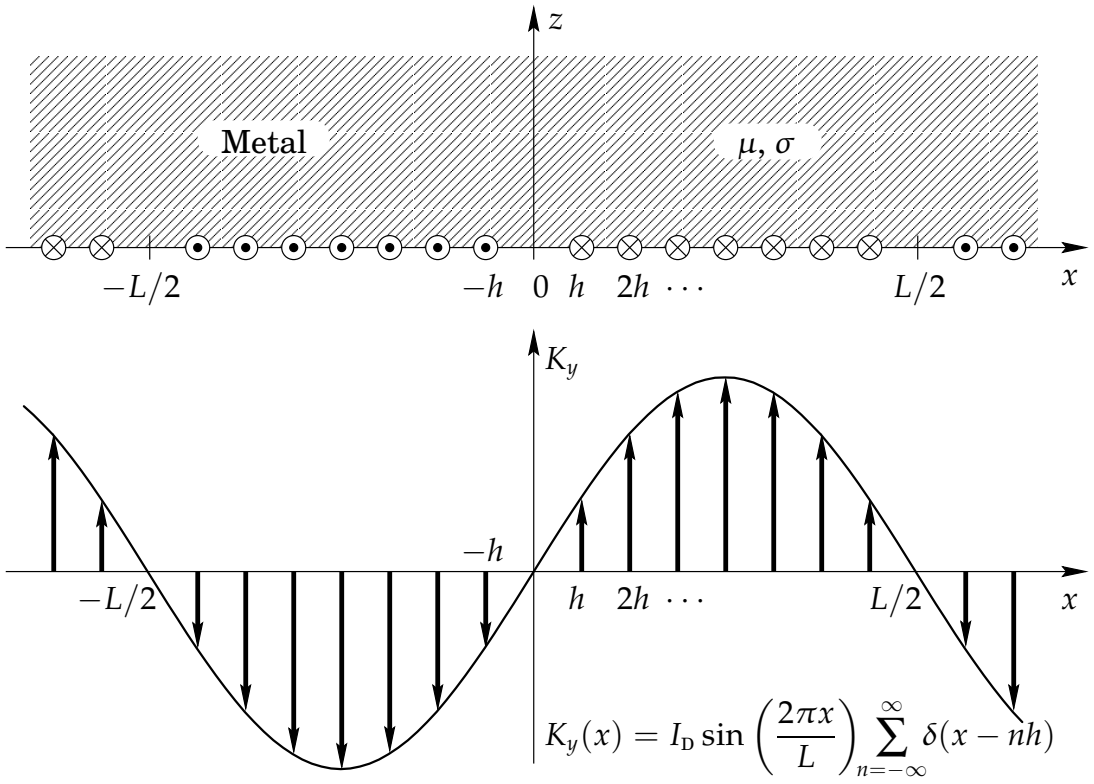

Figure 4-2: Geometry and current drive of the sensor analyzed in Section 4.3. The current drive is implemented as a sequence of conductors oriented in the y-direction, each carrying a current with magnitude determined by a sinusoidal envelope function, as shown in the lower plot. Each conductor is assumed to be infinitely thin, so that the surface current density K_y consists of a series of spatial impulse functions. The structure is assumed to repeat periodically to infinity in the positive and negative x-direction, and to be of infinite extent in the y-direction. The material below the electrodes is air, and above is a material of a given conductivity and magnetic permeability, extending to infinity in the positive z-direction.

If the drive winding pattern is repeated infinitely many times, i.e. sufficiently many on either side of the point of interest so as to appear to the local field as infinite, then the drive current and vector potential may be represented by Fourier series, with each mode decoupled from the rest.

The surface current density, shown in Figure 4-2, can be written as

$$K(x) = I_{\mathrm{D}} \sum_{n=-\infty}^{\infty} u_0(x - nh) \sin\left(\frac{2\pi nh}{L}\right) = I_{\mathrm{D}} \sin\left(\frac{2\pi x}{L}\right) \sum_{n=-\infty}^{\infty} u_0(x - nh) \tag{4.8}$$

where L is the spatial period, and h is the separation between adjacent windings. Figure 4-2, as well as all other figures in this chapter, use $h = L/16$ as the winding spacing. For reasons that will become clear later in this chapter, it is advantageous to design magnetometers with integral values of L/h, preferably a power of two.

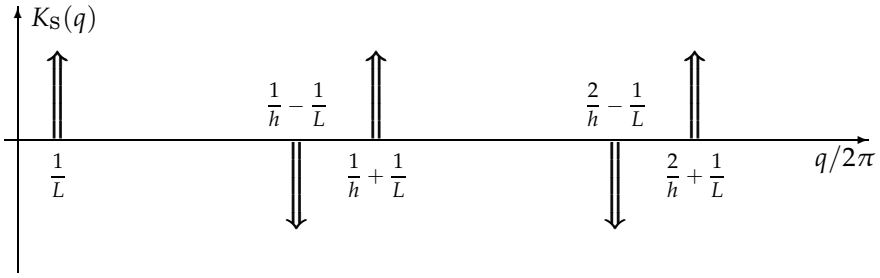

Figure 4-3: Sine transform of the current distribution of the sensor, given by equation (4.10). It is plotted for positive values of q only, because all sine transforms are odd functions.

The Fourier transform of equation (4.8) is

$$\begin{aligned} K(q) &= I_D \frac{2\pi}{2i}\left[u_0\left(q-\frac{2\pi}{L}\right)-u_0\left(q+\frac{2\pi}{L}\right)\right]\otimes\left[\frac{2\pi}{h}\sum_{n=-\infty}^{\infty}u_0\left(q-\frac{2\pi n}{h}\right)\right] \\ &= \frac{I_D}{h}\cdot\frac{2\pi}{2i}\sum_{n=-\infty}^{\infty}\left\{u_0\left(q-2\pi\left[\frac{n}{h}+\frac{1}{L}\right]\right)-u_0\left(q-2\pi\left[\frac{n}{h}-\frac{1}{L}\right]\right)\right\} \end{aligned} \tag{4.9}$$

where the symbol $\otimes$ is used to denote convolution. The corresponding sine transform

$$K_S(q) = \frac{I_D}{h}\cdot\frac{\pi}{2}\sum_{n=-\infty}^{\infty}\left\{u_0\left(q-2\pi\left[\frac{n}{h}+\frac{1}{L}\right]\right)-u_0\left(q-2\pi\left[\frac{n}{h}-\frac{1}{L}\right]\right)\right\} \tag{4.10}$$

obtained from equation (4.9) via equation (4.4), is more useful, because it represents the current distribution as a summation of impulse functions in reciprocal "sine" space, and therefore directly gives the coefficient of every constituent sinusoidal mode. The sine transform function in equation (4.10) is shown in Figure 4-3.

The next step in computing the magnetic fields that result from this current excitation is to calculate the contribution of each constitutive spatial Fourier mode. Let the current density of a mode with wavenumber $q = k$ be

$$K_y(x) = K_0 \sin(kx) \tag{4.11}$$

The solutions of the magnetic diffusion equation, given in equation (2.13), also apply in this geometry. The solutions above and below the sensor are of the form:

$$A_y(x,z) = \begin{cases} A^a \sin(kx)e^{-\gamma z} & z \geq 0 \\ A^b \sin(kx)e^{kz} & z \leq 0 \end{cases} \tag{4.12}$$

with γ defined in equation (2.14). In terms of the two unknown coefficients A^a and A^b, the

magnetic field intensity is

$$\mathbf{H}(x,z) = \begin{cases} \dfrac{A^a}{\mu_0\mu_r}\left[\gamma\sin(kx)\hat{\mathbf{x}} + k\cos(kx)\hat{\mathbf{z}}\right]e^{-\gamma z} & z > 0 \\ \dfrac{A^b}{\mu_0}\left[-k\sin(kx)\hat{\mathbf{x}} + k\cos(kx)\hat{\mathbf{z}}\right]e^{kz} & z < 0 \end{cases} \tag{4.13}$$

where $\mu_r = \mu/\mu_0$ is the relative permeability of the material above the windings.

The boundary conditions at the surface $z = 0$ require that

$$[\![H_x(x,z)]\!] = H_x(x, z=0^+) - H_x(x, z=0^-) = K_y(x) \tag{4.14a}$$

$$\mu_r H_z(x, z=0^+) = H_z(x, z=0^-) \tag{4.14b}$$

The constraint in equation (4.14b) is satisfied if $A^a = A^b$.

Substituting equations (4.11), (4.12) and (4.13) into equation (4.14) yields

$$A^a = A^b = \frac{\mu_0\mu_r K_0}{\gamma + k\mu_r} \tag{4.15}$$

resulting in

$$A_y(x,z) = \begin{cases} \dfrac{\mu_0\mu_r K_0}{\gamma + k\mu_r}\sin(kx)e^{-\gamma z} & z \geq 0 \\ \dfrac{\mu_0\mu_r K_0}{\gamma + k\mu_r}\sin(kx)e^{kz} & z \leq 0 \end{cases} \tag{4.16}$$

The corresponding expressions for the magnetic field intensity are

$$\mathbf{H}(x,z) = \begin{cases} \dfrac{K_0}{\gamma + k\mu_r}\left[\gamma\sin(kx)\hat{\mathbf{x}} + k\cos(kx)\hat{\mathbf{z}}\right]e^{-\gamma z} & z > 0 \\ \dfrac{K_0\mu_r}{\gamma + k\mu_r}\left[-k\sin(kx)\hat{\mathbf{x}} + k\cos(kx)\hat{\mathbf{z}}\right]e^{kz} & z < 0 \end{cases} \tag{4.17}$$

In general, the summation of the above result over all spatial modes must be carried out numerically. In some simple cases it is possible to derive an analytical expression. As an example, consider the magnetic field at the origin ($x = 0$, $z = 0$) when the material under test is air, i.e. $\mu_r = 1$ and $\sigma = 0$, or $\delta = \infty$. In this simplest possible case equation (4.17) degenerates to

$$\mathbf{H}(x=0, z=0) = \frac{K_0}{2}\hat{\mathbf{z}} \tag{4.18}$$

which is independent of the wavenumber k. Summing over all modes that characterize the current distribution in Figure 4-2 presents a problem. As can be seen in equation (4.10), the magnitude of the impulses does not decrease with increasing wavenumber. This is a consequence of neglecting the finite width of the current elements. Attempting to combine equations (4.10) and (4.18) with the help of equation (4.6) yields a summation of the following

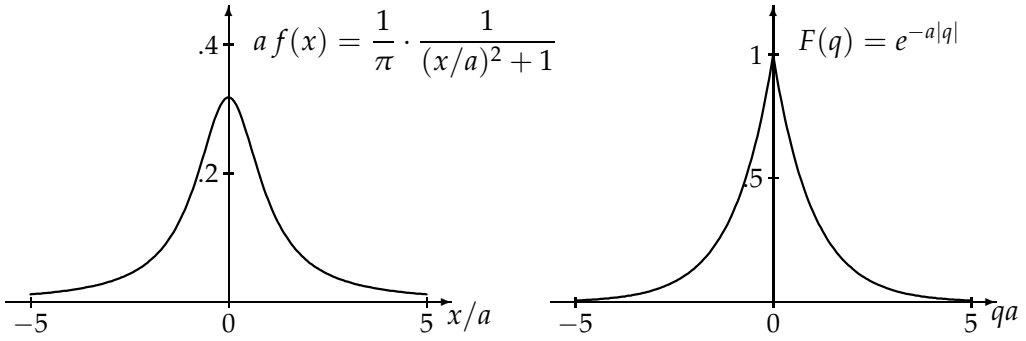

Figure 4-4: The Lorentzian function, defined in equation (4.20), and its Fourier transform, defined in equation (4.21). The area under $f(x)$ is equal to 1, so that $f(x) \to u_0(x)$ when $a \to 0$. The area under the transform is $2\pi f(0) = 2/a$.

form:

$$H_z = \frac{I_D}{2h}\left(1 + \sum 1 - \sum 1\right) \tag{4.19}$$

which does not formally converge. In order to carry out this computation it is necessary initially to give each current element a finite width and then take the limit of the result as this width approaches zero. Any pulse function of area unity can be used in place of the impulse functions in equation (4.8) for this purpose, but it is most convenient to choose one whose Fourier transform will make the summation over modes easy to carry out. For example, a function that has a transform whose positive side is a decaying exponential works well, because the summation becomes a pair of geometric series. This function is the Lorentzian

$$f(x) = \frac{1}{2\pi} \cdot \frac{2a}{x^2 + a^2} \tag{4.20}$$

and it can be used in place of $u_0(x)$. It is plotted in Figure 4-4, together with its Fourier transform

$$F(q) = e^{-a|q|} \tag{4.21}$$

Using equations (4.10), (4.18) and (4.21), it is now possible to write the magnetic field at the origin ($x = 0$, $z = 0$) as

$$H_z = \frac{I_D}{2h}\, S \tag{4.22}$$

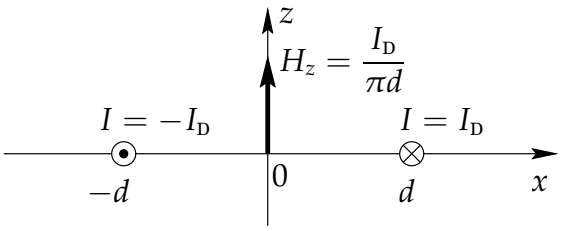

Figure 4-5: Magnetic field at the origin, generated by a pair of conductors positioned at a distance d on either side.

where S is the summation over the Fourier modes and is given by

$$\begin{aligned} S &= \lim_{a\to 0}\left[e^{-2\pi a/L} + \sum_{n=1}^{\infty} e^{-2\pi a(n/h+1/L)} - \sum_{n=1}^{\infty} e^{-2\pi a(n/h-1/L)}\right] \\ &= 1 + \lim_{a'\to 0}\left[\left(e^{-a'/L} - e^{a'/L}\right)\sum_{n=1}^{\infty} e^{-na'/h}\right] \qquad \text{(letting } a' = 2\pi a\text{)} \\ &= 1 - 2\lim_{a'\to 0}\left[\frac{\sinh(a'/L)}{e^{a'/h}-1}\right] = 1 - 2\lim_{a'\to 0}\frac{(1/L)\cosh(a'/L)}{(1/h)e^{a'/h}} \\ &= 1 - 2\frac{h}{L} \end{aligned} \tag{4.23}$$

The magnetic field intensity at the origin ($x = 0$, $z = 0$) is therefore

$$H_z = \frac{I_D}{2h}S = \frac{I_D}{2h}\left(1 - \frac{2h}{L}\right) \tag{4.24}$$

As a way of validating the Fourier series method used to obtain the result in equation (4.24), it is possible to calculate the magnetic field intensity for this simple case using a direct method. The field at the origin generated by a pair of conductors positioned at $x = \pm d$, extending to infinity in the y-direction, and each carrying current I_D as shown in Figure 4-5, is given by

$$H_z = \frac{I_D}{\pi d} \tag{4.25}$$

calculated directly from Ampère's Law. The entire sensor must therefore generate a magnetic field whose magnitude at the origin is

$$H_z = \sum_{n=1}^{\infty}\frac{I_D}{\pi n h}\sin\left(\frac{2\pi n h}{L}\right) = \frac{I_D}{2h}\left(1 - \frac{2h}{L}\right) \tag{4.26}$$

where use has been made of the following formula [52, eq. 1.441]:

$$\sum_{n=1}^{\infty}\frac{\sin(n\pi x)}{n} = \frac{\pi}{2}(1-x) \tag{4.27}$$

Equation (4.26) agrees with equation (4.24), which confirms that the Fourier transform method developed in this section give the correct result.

4.4 Numerical analysis

The analytical method shown above also works if the material above the sensor is magnetizable ($\mu_r > 1$), because in this case equation (4.17) still depends on k only via the sine (or cosine) term, which makes it possible to carry out the summation over modes in closed form. However, if a conducting material with finite skin depth δ is present, the calculations must be carried out numerically.

This can be done with the help of fast Fourier transform (FFT) methods. The algorithm has the following steps:

1. Obtain the sine transform of the current excitation. For the periodic sensor this is given by equation (4.10). For the finite width sensor this step has several substeps, as discussed in Section 4.5.

2. Discretize the spectrum. A property of the FFT algorithm is that the number of sample points in q-space is equal to the number of points in the spatial discretization of the magnetic field in the x-direction. This consideration should determine how many sample points to obtain.

   If the sensor wavelength L, defined in Figure 4-2, is an exact multiple of h, then all impulse functions in Figure 4-3 fall on multiples of $2\pi/h$ in q-space. This means that no information is lost if the discretization step is set to this value. Otherwise a much denser discretization would be necessary to maintain the information in the spectrum. Furthermore, since the FFT algorithm is more efficient if the number of samples is a power of two, it is preferable for L/h also to be a power of two. For the example considered in this chapter, $L = 16h$.

3. Apply a decaying exponential envelope to the discrete spectrum, to give the current elements a finite width. The decay rate should be chosen such that most of the transition has happened by the end of the series of samples. If the exponent decays too fast, then information is unnecessarily being lost, while if the decay is too slow, the resulting field will not be smooth, as a result of the sudden step in the spectrum effectively introduced at the end of the sample sequence. A plot of the resulting discretized spectrum of Figure 4-3 is shown in Figure 4-6.

4. Choose a discretization step in the z-direction. This should most likely be the same as the one in the x-direction, determined in step 2.

5. For every value of z, obtain the spectrum of the vector potential by applying equation (4.16), without the sine term, to the excitation spectrum of step 3.

6. For every value of z, apply inverse FFT to obtain the vector potential as a function of x and z. Standard FFT algorithms perform exponential, not sine, Fourier transforms. As seen in equation (4.4), the sine transform of a function $F_S(q)$, defined for $q > 0$, can be calculated by taking the inverse exponential Fourier transform of the odd function whose positive side is $F_S(q)$, and multiplying the result by $i/2$. Therefore the discrete sine transform can be obtained by first appending a reversed copy of the sample array to itself, and then applying the inverse FFT algorithm to the longer sequence.*

*This procedure introduces a factor of two redundancy in the numerical calculation. The easiest way to take advantage of it is to take the discrete Fourier transform of two functions simultaneously, e.g. for two different values of z, as discussed in [81].

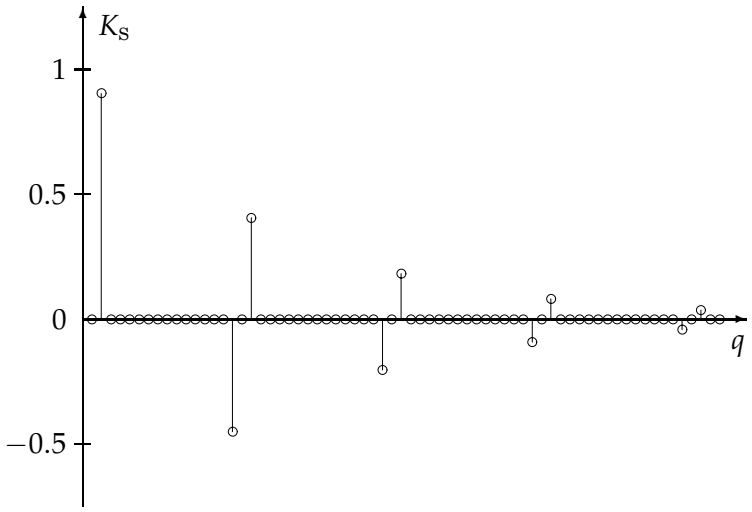

Figure 4-6: Discretized spectrum of the current excitation shown in Figure 4-2, in a decaying exponential envelope.

A contour plot of the vector potential yields the magnetic field lines, since they correspond to lines of constant vector potential. The result of applying this algorithm to the case of the sensor in air is shown in Figure 4-7 (a).

The magnetic fields that result when the material under test has a finite skin depth is shown in Figure 4-7 (b). Unlike the field of Figure 4-7 (a), in this case the temporal phase angle of the vector potential depends on z. The figure shows the real part of the calculated response.

The best way to get the actual magnetic field intensity $\mathbf{H}$ is to avoid calculating the vector potential by carrying out the algorithm as outlined above, but with equation (4.17) used in step 5 instead. The alternative way of calculating it from the vector potential introduces unnecessary numerical imprecision into the result, because it involves taking numeric derivatives.

4.5 Sensor of finite width

When the sensor is not infinitely wide, one must include the finite size as part of the analysis. It is no longer possible to use a quasi* Fourier series representation, where the spectrum consists of a series of impulse functions, as in Figure 4-3. The full Fourier transform of the magnetic field distribution in this case is continuous. The discrete Fourier transform (DFT) methods therefore require a finer discretization of the spectrum. By virtue of the discreteness of the numerical transform methods, the functions represented by DFTs in both domains are always periodic, but this periodicity may be ignored if the period is much larger than the interval of interest. The spacing between samples in reciprocal space in this case is determined as the inverse of the minimum distance that two sensors must be physically separated in

*The word "quasi" used here is meant to convey that the spectrum shown in Figure 4-3 does not necessarily form a harmonic sequence, and therefore is not a Fourier Series, although it is similar to it in that it represents the coefficients of the sinusoidal modes that constitute the original function. On the other hand, a practical implementation of the sensor requires that L be an exact multiple of h, which does in fact make the spectrum a Fourier series, with most coefficients equal to zero.

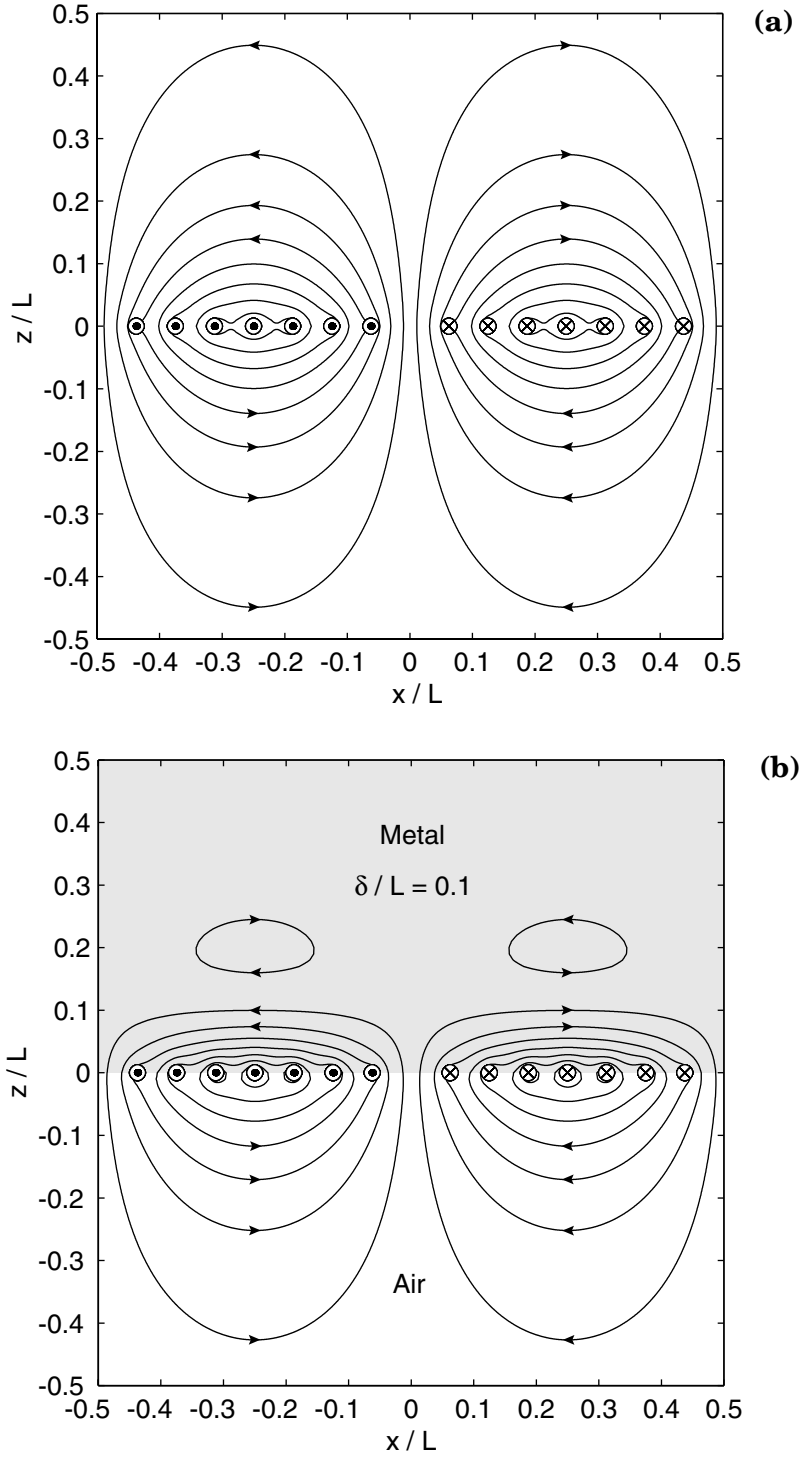

Figure 4-7: Numerically calculated magnetic field of the periodic sensor in air **(a)**, and when the material above it is metal with skin depth $\delta = 0.1L$ **(b)**.

order to influence each other only negligibly, which is usually much greater than the spatial region of interest. This stands in contrast to the periodic case considered in the previous section, where the sample distance in reciprocal space is the inverse of the fundamental sensor wavelength.

The numerical algorithm remains largely the same as before, with the exception of the calculation of the excitation spectrum, which now must consider the finite size of the sensor. The current distribution in this case can be obtained by multiplying the function in equation (4.8) by the square-pulse function

$$f(x) = \begin{cases} 1 & |x| < \dfrac{W}{2} \\ 0 & \text{otherwise} \end{cases} \tag{4.28}$$

where W is the width of the sensor. The Fourier transform of the square-pulse function is

$$F(q) = \frac{\sin(qW/2)}{q/2} = W \operatorname{sinc}\left(\frac{qW}{2}\right) \tag{4.29}$$

which must be convolved with the spectrum of equation (4.9) in order to obtain the Fourier transform of the current excitation of the finite sensor. The resulting sine transform is:

$$K_{\mathrm{S}}(q) = I_{\mathrm{D}} \frac{W}{4h} \sum_{n=-\infty}^{\infty} \left\{ \operatorname{sinc}\left(\frac{W}{2}\left[q - 2\pi\left(\frac{n}{h} + \frac{1}{L} \right) \right] \right) - \operatorname{sinc}\left(\frac{W}{2}\left[q - 2\pi\left(\frac{n}{h} - \frac{1}{L} \right) \right] \right) \right\} \tag{4.30}$$

In practice it is easier to carry out the discretization of the current excitation after the sine transform of the truncated sinusoid is calculated, for reasons presented in step 4 on page 93 later in this section. The spectrum of the nondiscretized single-period surface current density is obtained by taking the convolution of a sinusoid of period L and equation (4.29), and converting it to a sine transform via equation (4.4):

$$\begin{aligned} K_{\mathrm{S}}(q) &= \frac{i}{2} \cdot I_{\mathrm{D}} \frac{2\pi}{2i} \left[u_0\left(q - \frac{2\pi}{L} \right) - u_0\left(q + \frac{2\pi}{L} \right) \right] \otimes W \operatorname{sinc}\left(\frac{qW}{2} \right) \\ &= I_{\mathrm{D}} \frac{W}{4} \left\{ \operatorname{sinc}\left(\frac{W}{2}\left[q - \frac{2\pi}{L} \right] \right) - \operatorname{sinc}\left(\frac{W}{2}\left[q + \frac{2\pi}{L} \right] \right) \right\} \end{aligned} \tag{4.31}$$

The current envelope function for the sensor of finite width, for the case when $W = L$, and its sine transform, given by equation (4.31), are shown in Figure 4-8 with the thick lines. It can be seen in the figure that the peak wavenumber, which is a measure of the effective fundamental wavelength, is not $2\pi/L$, as it would be in the case of the periodic sensor. In order to make this effective wavelength equal to the wavelength L of the current envelope, the width W would have to be increased to $1.210L$ (calculated numerically). The result would be an envelope function that includes the tail of a second period on either side, as shown in Figure 4-8 with thin lines. This is undesirable, because if the sensor ends do not coincide with zeros in the current excitation, the resulting sharp transition at the ends contributes to more energy in the higher wavenumber modes, which have shallower penetration depths. This is clearly visible in Figure 4-8(b). This is the reason why $W = L$ is the optimal choice. On the other hand, extending the current excitation past the end of the period may be necessary for other reasons, as discussed in Section 4.7.

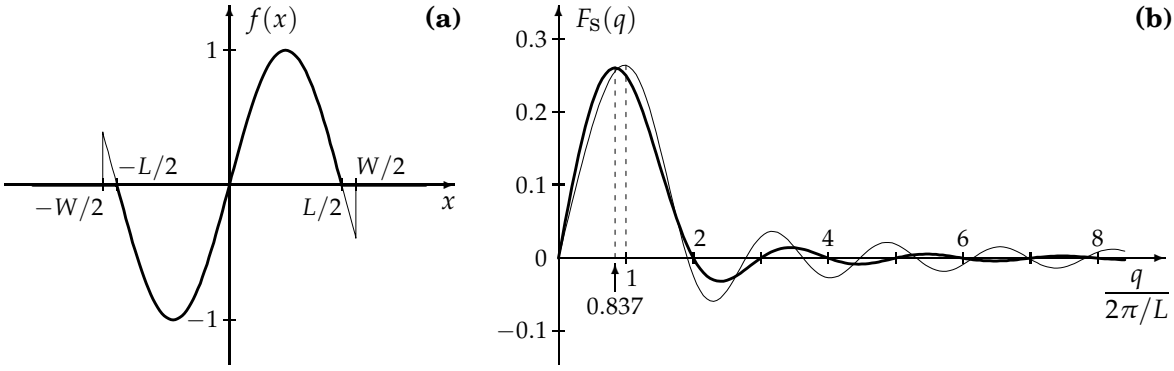

Figure 4-8: Current envelope function for a sensor of finite width **(a)**, and its corresponding sine transform **(b)**. Two cases are shown, for the sensor width W equal to the wavelength L (thick lines), and for $W = 1.210L$, making the effective sensor wavelength equal to the sinusoid wavelength (thin lines).

When using a sensor of finite width, the first two steps in the algorithm outlined on page 89 in Section 4.4 need to be replaced by the following steps:

1. Obtain the sine transform of the current envelope function, as in Figure 4-8 (b).

2. Discretize and truncate the transform. The length of the transform sample to use in this step is determined by the number of current segments in the sensor. For the example used in this chapter, where $W = L = 16h$, the sine transform in Figure 4-8 (b) must be truncated at $q = 8(2\pi/L)$. As before, the sample density is determined by the necessary precision.

3. Append a reversed and negated copy of the sequence to its end, in order to make the FFT algorithm carry out the inverse ***sine*** transform.

   Alternatively, the result of the first three steps may be obtained by taking the FFT of the current profile directly, especially in cases when a closed form of the transform of the profile function is not available.

4. Replicate the resulting sequence a number of times. The resulting sine transform is shown in Figure 4-9. Periodicity in one domain implies discreteness in the other, and therefore the effect of this step is to build into the data the fact that the current distribution is not continuous, but rather generated by discrete current segments. Replication is a simple operation and this is why this method is preferred to discretizing the drive profile function first and convolving with equation (4.29) later. The number of periods is determined by the needed level of detail in close proximity to the current segments. The greater the number of periods, the narrower the implied effective width of the conductors. For example, four periods are used in the calculation of the field distributions shown in Figure 4-10.

5. Proceed with steps 3–6 on page 89.

It is informative to compare the spectrum in Figure 4-9 to that in Figure 4-3. One can see that the effect of limiting the sensor to only one wavelength is to smear out the peaks at the excitation wavenumbers, and as a consequence the magnetic field can no longer be represented as a superposition of individual sinusoidal modes.

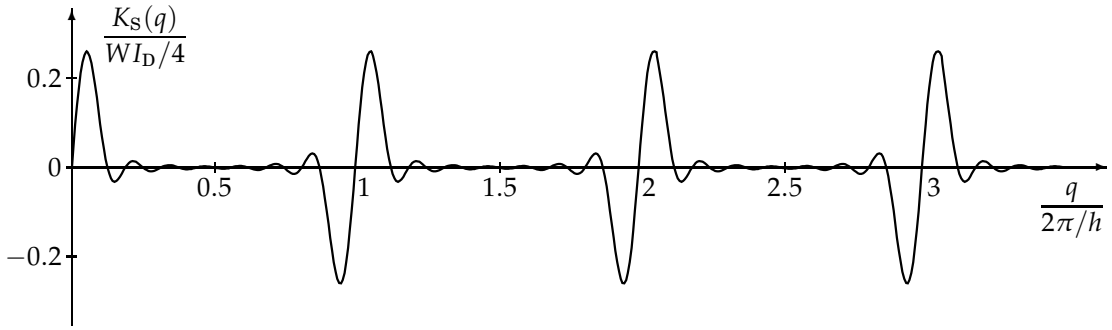

Figure 4-9: Sine transform of the current excitation generated by discrete current elements. It is computed by step 4 on page 93. The discrete nature of the transform is not explicitly shown in the plot. Compare to the spectrum in Figure 4-3.

The magnetic field calculated in this way is shown in Figure 4-10, with the same materials and current excitation as in Figure 4-7, but with no current elements for $|x| > L/2$ (see Figure 4-2). By comparing these sets of figures, the observation may be made that they differ little at the origin, where the sensing elements are positioned, but there is a substantial difference toward the ends of the sensor.

4.6 Multiple homogeneous layers

The models developed so far in this chapter may be extended to apply to material structures that consist of more than one homogeneous layer. Figure 4-11 shows a diagram of such a layered material structure.

The thickness of the top layer in the figure is treated as infinite, which means that it is many times larger than the real part of the characteristic decay rate $1/\gamma$ in that material, so that the properties at the upper surface have no effect on the sensor response. In practice there is always a layer of air, or another nonmagnetic insulating material, between the sensor and the material. This layer, number 4 in the figure, must be included in the model, and its thickness is known as the measurement "lift-off."

The structure in Figure 4-11 may represent a metal coating on a metal substrate, which is a very common situation [26]. Layer number 1 represents the substrate, layer 3 is the coating, and layer 2 is used to model an inter-diffusion zone, whose properties are often quite different from either the coating or the substrate.

The effect of having more than one homogeneous layer of material above the sensor enters the computational method only at step 5 in the method on page 89 in Section 4.4, as a change in equation (4.16), because the invariance of the material structure in the x- and y-directions is maintained. The idea is similar to the method in Section 2.1.5, with the surface reluctance density R_n relating the magnetic vector potential to the normal component of the magnetic field intensity, as in equation (2.51). R_n is derived from the properties of the layers in Figure 4-11, using equations (2.46) and (2.50).

In terms of R_n, for every Fourier mode n equation (4.15) becomes

$$A^a = A^b = \frac{K_n}{k_n R_n} \tag{4.32}$$

where K_n is the Fourier component of order n of the surface current density. This fully deter-

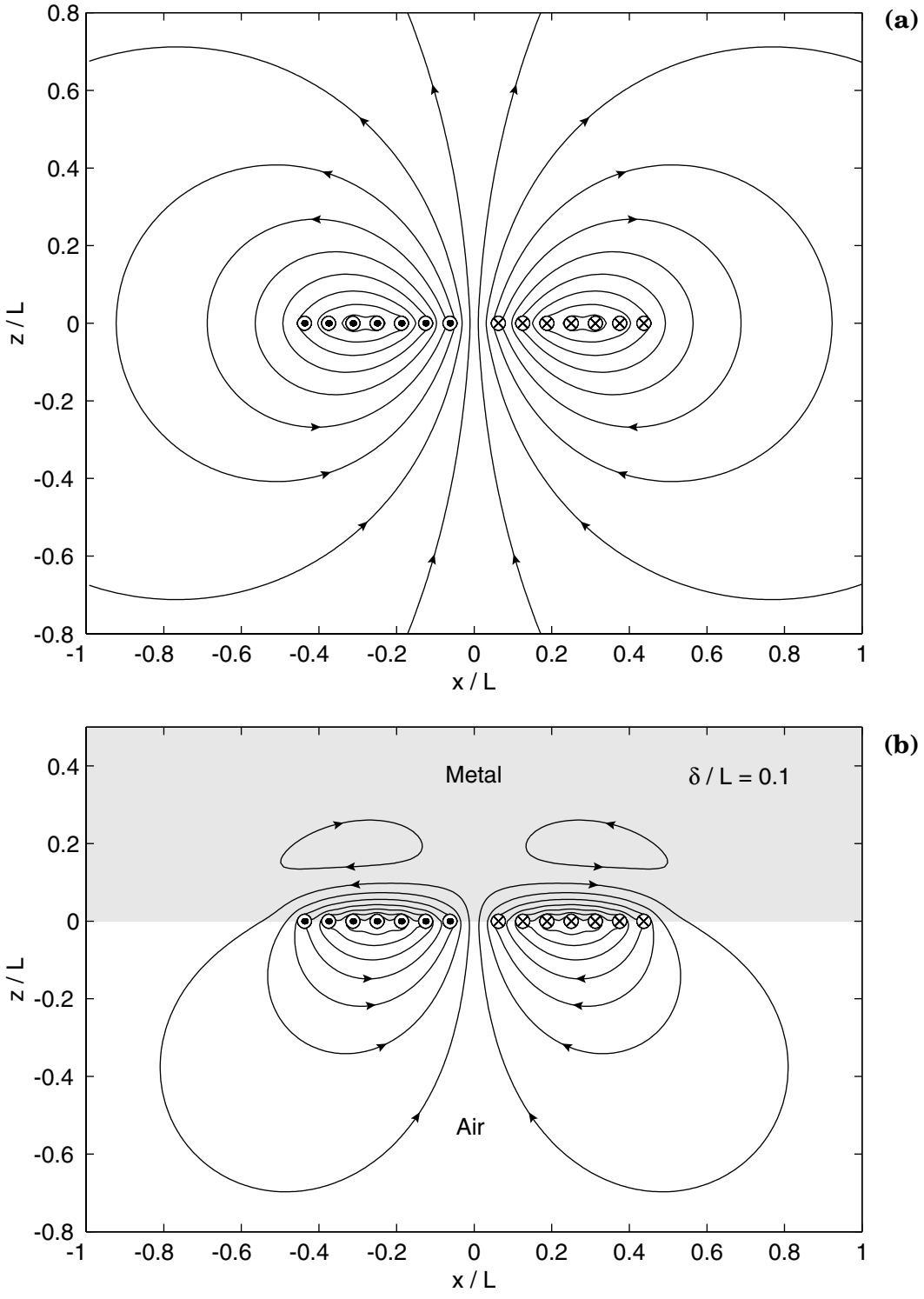

Figure 4-10: Numerically calculated magnetic field of the finite-width sensor in air **(a)**, and when the material above it is metal with skin depth $\delta = 0.1L$ **(b)**.

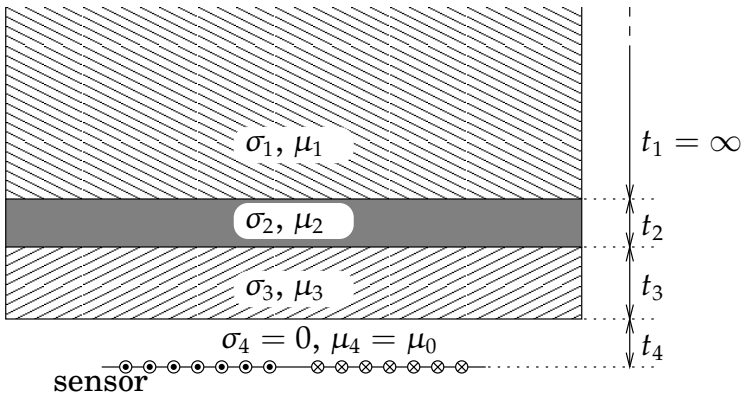

Figure 4-11: Material structure that consists of more than one homogeneous layer. The topmost layer is assumed to extend to infinity. An air layer that models the sensor lift-off is included between the sensor and the material under test. The sensor windings are represented by $\odot$ and $\otimes$.

mines the magnetic field, via equation (4.13).

4.7 Eliminating the net dipole moment

The finite width sensor, described in Section 4.5, has a net dipole moment in the sense that at distances larger than the sensor wavelength the magnetic field approaches the form of a field generated by a magnetic dipole at the origin. It can easily be seen that the net dipole moment is not zero, because each pair of windings, comprising a current segment on either side of the center, together with the return current path, forms a current loop of nonzero area, and the effective magnetic moments of all these loops point in the same direction.

Certainly, close to the sensor windings, at typical measurement distances, the magnetic field is described well by the model of the preceding sections. The reason for addressing the net dipole moment is not to improve the results of this model.

It is important that the sensors have a winding layout which results in no net dipole moment.* This is due to the following reason: At some distance away from the sensor, the assumptions of the model no longer hold. The sensor is finite in the y-direction, which cannot be ignored at distances comparable to the sensor length. Furthermore, the discrete Fourier transform does have an implied periodicity, determined by the reciprocal domain sample frequency, so that the finite width sensor model only holds at distances much smaller than the distance between the sensor and its first phantom image. For example, the magnetic field lines shown in Figure 4-10 have a phantom image period sixteen times greater than the sensor width W.

These unmodeled effects in general do not affect the accuracy of a measurement, because all practical measurement procedures include a calibration step, designed to compensate for such imperfections of the model, which do not change with time or experimental conditions. Calibration methods are discussed in more detail in Appendix D.

The difficulty comes from the rate at which the sensor loses sensitivity with distance. Near the sensor surface the magnetic field decays essentially exponentially, at a rate determined

*This issue was first discovered and addressed by Darrell E. Schlicker in connection with the standard MWM. It led to a redesign of the MWM with two separate layers for the primary and secondary windings.

by its spatial wavelength and the skin depth in the medium, given in equation (2.14). Far from the sensor the fields fall off at a rate determined by the lowest order multi-pole moment excited by the sensor. This should be a high order moment, since it is important for the sensor to lose sensitivity quickly with distance. Otherwise its response would be slightly affected by the presence of magnetizable and/or conducting objects in its vicinity, even if they are much farther than the material under test. Whereas this effect may be small, even compared to other unmodeled effects, the problem is that it can change with time, as objects near the sensor are moved, or when the sensor is moved to inspect a new location. This means that it cannot be eliminated via calibration, ultimately leading to lack of reproducibility.

Sometimes very small changes in the material properties must be measured, e.g. conductivity variations related to shotpeen intensity or cold work quality [18, 24]. In cases like that the accuracy of the measurement may be substantially degraded by the presence of a net dipole moment. It is desirable for the sensor to lose sensitivity far from its active region as quickly as possible. This is why the goal is to create a winding pattern with no net dipole moment.

The analysis of the sensor in the far field, i.e. at distances much greater than the sensor dimensions, is most conveniently formulated in spherical coordinates with the use of the magnetic scalar potential. This is because at large distances all windings and conducting media may be represented by a singularity at the origin, since there is no interest in the magnetic field details near the sensor. This makes it possible to write the magnetic field intensity in the current-free region as a gradient of a scalar potential Ψ, defined everywhere except at $r = 0$:

$$\mathbf{H} = -\nabla\Psi \tag{4.33}$$

The magnetic scalar potential must obey Laplace's equation, because the divergence of the magnetic flux density is zero: $\nabla^2\Psi = 0$. In spherical coordinates it becomes

$$\frac{1}{r^2}\frac{\partial}{\partial r}\left(r^2\frac{\partial}{\partial r}\Psi\right) + \frac{1}{r^2\sin\theta}\cdot\frac{\partial}{\partial\theta}\left(\sin\theta\frac{\partial}{\partial\theta}\Psi\right) + \frac{1}{r^2\sin^2\theta}\cdot\frac{\partial^2}{\partial\varphi^2}\Psi = 0 \tag{4.34}$$

which, letting $\Psi(r,\theta,\varphi) = R(r)Y(\theta,\varphi)$, separates into

$$\frac{d}{dr}\left(r^2\frac{d}{dr}R\right) - \ell(\ell+1)R = 0 \tag{4.35}$$

and

$$\frac{1}{\sin\theta}\cdot\frac{\partial}{\partial\theta}\left(\sin\theta\frac{\partial}{\partial\theta}Y\right) + \frac{1}{\sin^2\theta}\cdot\frac{\partial^2}{\partial\varphi^2}Y + \ell(\ell+1)Y = 0 \tag{4.36}$$

The solutions of equation (4.35) are r^ℓ and $r^{-\ell-1}$, and the solutions to equation (4.36) are [55]:

$$Y_{\ell m}(\theta,\varphi) = \sqrt{\frac{2\ell+1}{4\pi}\cdot\frac{(\ell-m)!}{(\ell+m)!}}\,P_\ell^m\big(\cos\theta\big)\,e^{-im\varphi} \qquad m = -\ell,\dots,\ell \tag{4.37}$$

where P_ℓ^m are the Associated Legendre functions. The series of functions $Y_{\ell m}$ are the spherical harmonic functions. They are written out for the first several values of ℓ in Table 4.1.

For magnetic fields the lowest order possible is the dipole moment, whose scalar magnetic potential decays as r^{-2}. Figure 4-12 shows the equipotential surfaces of the scalar magnetic

$$\ell = 0 \qquad Y_{00} = \sqrt{\frac{1}{4\pi}}$$

$$\ell = 1 \quad \begin{cases} Y_{11} = -\frac{1}{2}\sqrt{\frac{3}{2\pi}}\sin\theta\, e^{i\varphi} \\ Y_{10} = \sqrt{\frac{3}{4\pi}}\cos\theta \end{cases}$$

$$\ell = 2 \quad \begin{cases} Y_{22} = \frac{1}{4}\sqrt{\frac{15}{2\pi}}\sin^2\theta\, e^{2i\varphi} \\ Y_{21} = -\frac{1}{2}\sqrt{\frac{15}{2\pi}}\sin\theta\cos\theta\, e^{i\varphi} \\ Y_{20} = \sqrt{\frac{5}{4\pi}}\left(\frac{3}{2}\cos^2\theta - \frac{1}{2}\right) \end{cases}$$

$$\ell = 3 \quad \begin{cases} Y_{33} = -\frac{1}{4}\sqrt{\frac{35}{4\pi}}\sin^3\theta\, e^{3i\varphi} \\ Y_{32} = \frac{1}{4}\sqrt{\frac{105}{2\pi}}\sin^2\theta\cos\theta\, e^{2i\varphi} \\ Y_{31} = -\frac{1}{4}\sqrt{\frac{21}{4\pi}}\sin\theta\big(5\cos^2\theta - 1\big)e^{i\varphi} \\ Y_{30} = \sqrt{\frac{7}{4\pi}}\left(\frac{5}{2}\cos^3\theta - \frac{3}{2}\cos\theta\right) \end{cases}$$

$$\ell = 4 \quad \begin{cases} Y_{44} = \frac{3}{16}\sqrt{\frac{35}{2\pi}}\sin^4\theta\, e^{4i\varphi} \\ Y_{43} = -\frac{3}{4}\sqrt{\frac{35}{4\pi}}\sin^3\theta\cos\theta\, e^{3i\varphi} \\ Y_{42} = \frac{3}{8}\sqrt{\frac{5}{2\pi}}\sin^2\theta\big(7\cos^2\theta - 1\big)e^{2i\varphi} \\ Y_{41} = -\frac{3}{4}\sqrt{\frac{5}{4\pi}}\sin\theta\big(7\cos^3\theta - 3\cos\theta\big)e^{i\varphi} \\ Y_{40} = \sqrt{\frac{9}{4\pi}}\left(\frac{35}{8}\cos^4\theta - \frac{30}{8}\cos^2\theta + \frac{3}{8}\right) \end{cases}$$

Table 4.1: Spherical harmonic functions defined in equation (4.37).

potential for the three lowest order rotationally symmetric multipole modes. The requirement for rotational symmetry is due to the fact that the sensor windings are confined to the x-y plane, and applies both to the rectangular sensor and to the circular sensor of Section 4.8. Of the spherical harmonic functions $Y_{\ell m}$ in Table 4.1, only those with $m = 0$ have this symmetry, i.e. are independent of φ. The "quadrupole" mode, $\ell = 2$, cannot be excited by these magnetic sensors, since it is even with respect to z, whereas flipping the sensor upside down reverses the current direction in all windings, changing the sense of all magnetic fields.

If the dipole moment is eliminated, the next dominant mode is the "octupole," or $\ell = 3$ moment, whose magnetic field lines are shown in Figure 4-13. The potential of this mode has a r^{-4} dependence, which means that the magnetic field intensity falls off as r^{-5}. In practice this is fast enough that canceling out the dipole moment is all that is required to eliminate unwanted long range sensitivity.

Instead of driving each current segment of the sensor independently, it is much easier to set the correct current profile by changing the number of windings in each segment. As a consequence, the relative values of the segment current must be ratios of integer numbers. Since the sensor length is constant, the dipole moment of each loop made up of windings at $x = \pm jh$ is proportional to the number of windings w_j and to j:

$$\mathbf{p} \propto j w_j \tag{4.38}$$

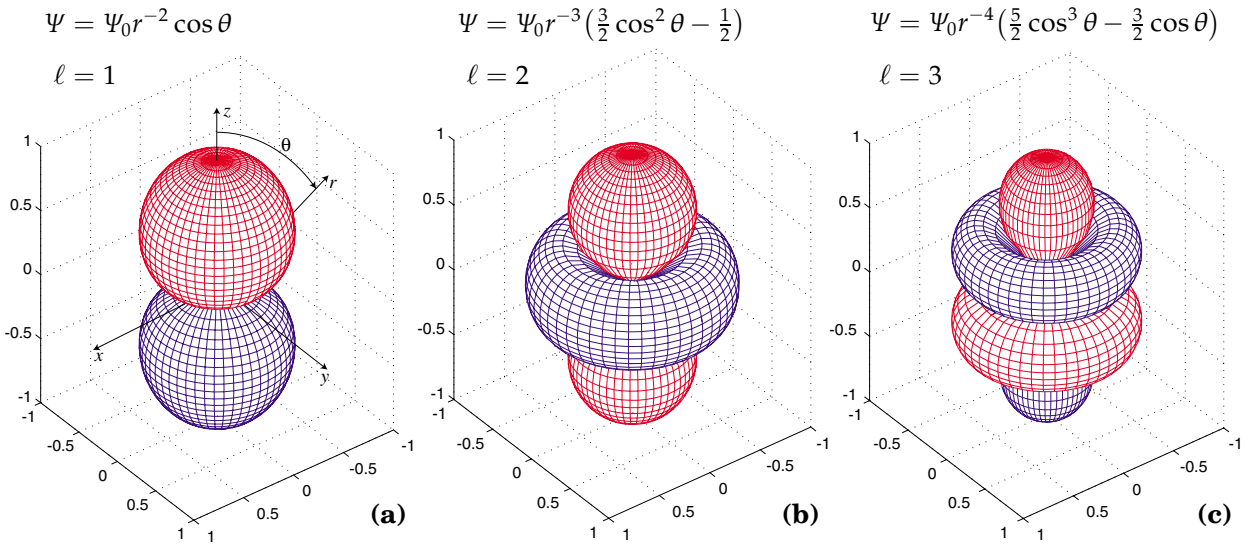

Figure 4-12: Equipotential surfaces, $\Psi(r,\theta,\varphi) = \Psi_0$, of the magnetic scalar potential for multipole moments with no φ-dependence. These three cases correspond to the spherical harmonic functions Y_{10} **(a)**, Y_{20} **(b)**, and Y_{30} **(c)** respectively. If the dipole ($\ell = 1$) moment is zero, then the lowest order moment remaining for the magnetometer is $\ell = 3$, since the $\ell = 2$ moment is not allowed, due to its symmetry.

which means that in order to cancel out the net dipole moment, these individual contributions must sum up to zero:

$$\sum_{j=1}^{N} j w_j = 0 \tag{4.39}$$

where N is the total number of current segments in one half of the sensor.

To satisfy equation (4.39), the sensor must include a fraction of a wavelength past the end of the single period, where the current flow is in the opposite direction (see Figure 4-2). Since both j and w_j are integers, it is impossible to satisfy equation (4.39) exactly while at the same time strictly following the sinusoidal envelope function. A compromise is shown in Table 4.2, which lists a winding pattern resulting in no net dipole moment. The winding turns are also plotted in Figure 4-14. The current in the last two segments deviates from the sinusoid. Another consideration in choosing the numbers in this table is to taper off the current towards the ends of the sensor, in order to avoid rapid changes in the primary current distribution, which would result in more energy in higher Fourier modes. This matter was previously discussed in Section 4.5.

$j = x/h$	0	1	2	3	4	5	6	7	8	9	10	11	12
Winding turns w_j	0	5	9	12	13	12	9	5	0	−5	−9	−7	−4

Table 4.2: Number of winding turns w_j for the finite sensor with no net dipole moment. Negative number of turns means that the winding is wound in the opposite direction (clockwise). Only the windings for $x \geq 0$ are given, because the sensor is symmetric.

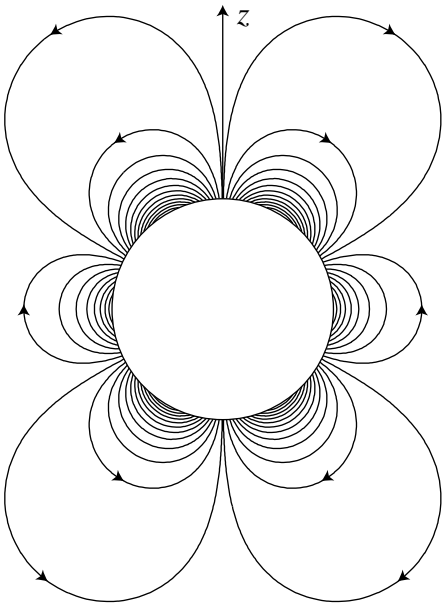

Figure 4-13: Magnetic field lines for $\ell = 3$ "octupole" moment potential. The central region is left blank, because the density of lines increases very rapidly, due to the r^{-5} dependence of the magnetic field intensity.

4.8 Sensor with rotational symmetry

This section describes a circular magnetometer with a distributed current drive, applying the ideas and methods of Chapter 3 to the sensors in this chapter.

When designing distributed current drive sensors, the reasons for preferring a circular geometry are even more compelling. Since the sensor width is the same as, or similar to, the spatial wavelength, the edge effects due to the finite length in the y-direction are much more pronounced. Even worse, the total amount of current that flows in this return path is equal to the total of all windings, making it several times higher than the winding with the highest current. To make the edge effects negligible, it would be necessary to make the sensor width in the y-direction perhaps a factor of ten larger than its length, defeating the purpose of having a distributed drive in the first place, which is to create a relatively large spatial wavelength

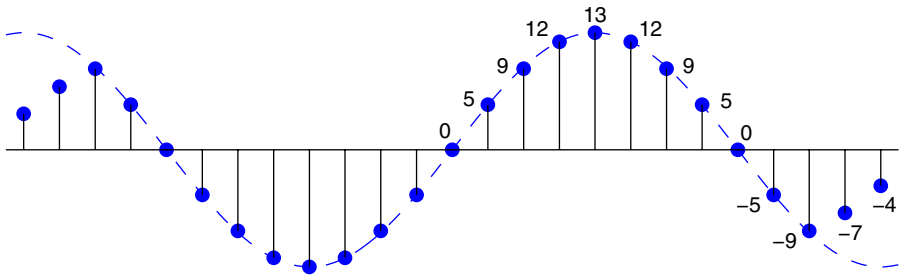

Figure 4-14: Number of winding turns for the finite sensor with no net dipole moment, according to Table 4.2. The sinusoidal envelope function is shown with a dashed line. The number of turns do not fall exactly on the curve, since they need to be integers. The number of turns in the last two windings on either side are tapered off in order to avoid rapid changes in the primary current distribution, which would result in more energy in higher order Fourier modes.

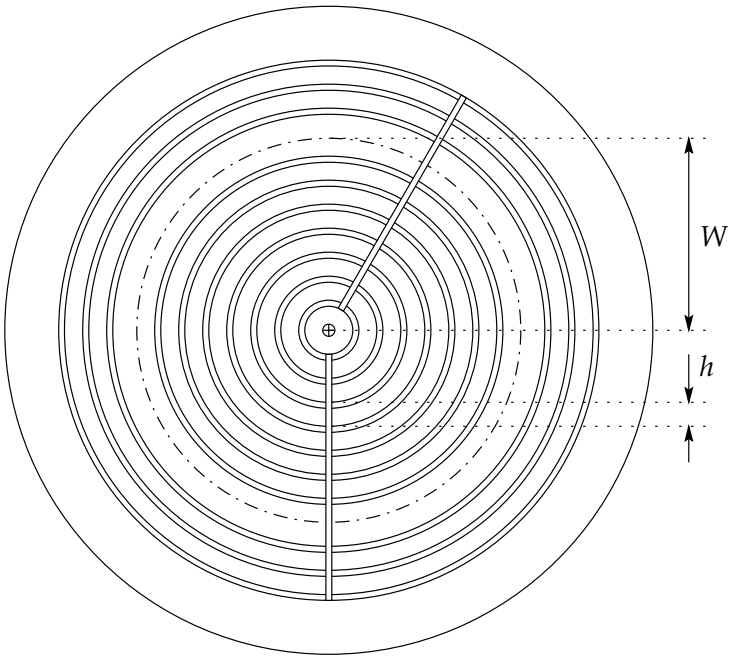

Figure 4-15: Structure of the circular magnetometer with distributed current drive. There is a set of concentric grooves, equally spaced h apart, to hold the primary windings. The number of turns in each winding follows a first order Bessel function envelope, according to Table 4.3. There is no groove at $r = W$, since this point corresponds to a zero in the envelope function.

excitation with a small footprint. Employing a circular geometry altogether eliminates the unmodeled edge effects.

This section discusses a sensor with this geometry and the changes needed to adapt the modeling techniques developed so far in this chapter to cylindrical coordinates.

4.8.1 Sensor description

A circularly symmetric sensor with distributed primary current drive has been created. Its structure is shown in Figure 4-15. The sensor substrate is made of a 0.5 inch thick polypropylene plate with 3 mm wide concentric grooves used to hold the windings. The grooves are spaced $h = 1$ cm apart, machined at an angle directed radially inward to keep the windings in place at the correct radius. The two straight radial grooves are used to hold wires connecting the windings.

The current drive follows a Bessel function envelope, $J_1(\alpha_1 r/W)$, where $\alpha_1 \approx 3.832$ is the first zero of J_1. There is no groove at $r = W = 8$ cm, because this point corresponds to the zero in the Bessel function. Windings are present past the first zero, in order to allow for net dipole moment cancellation, as discussed in Section 4.7. Unlike the rectangular sensor, whose windings have a fixed length, here the dipole moment of each winding is proportional to the square of the radius, which changes the requirement for dipole cancellation to

$$\sum_{j=1}^{N} j^2 w_j = 0 \tag{4.40}$$

The number of windings chosen for this sensor prototype are given in Table 4.3 and in Fig-

$j = r/h$	1	2	3	4	5	6	7	8	9	10	11
Winding turns w_j	5	9	11	12	11	8	4	0	-4	-4	-3

Table 4.3: Number of turns per winding w_j for the circular magnetometer.

ure 4-19.

This sensor is built with a single sensing element, located in the center. Since a magnetoresistive sensor is used, details and experimental measurement results are presented in Chapter 5. This section focuses on the mathematical models of the sensor response, used to generate appropriate measurement grids.

4.8.2 Sensor modeling

The surface current density of a sensor with N concentric windings is

$$K_{\mathrm{S}}(r) = I_{\mathrm{D}} J_1\Big(\frac{\alpha_1}{W} r\Big) \sum_{j=1}^{N} u_0(r - jh) = I_{\mathrm{D}} \sum_{j=1}^{N} u_0(r - jh) J_1\Big(\frac{\alpha_1}{W} jh\Big) \tag{4.41}$$

where h is the radial spacing of the windings, and W is the position of the first zero of the current distribution. This envelope function is chosen to match the solutions of the magnetic diffusion equation in cylindrical coordinates, shown in equation (3.3). Using the definition of the Fourier-Bessel Series from Section 3.1.1, the series coefficients of the surface current density are

$$K_n = \frac{1}{Q_n} \int_0^R r K_{\mathrm{S}}(r) J_1(\beta_n r)\, dr = \frac{2 I_{\mathrm{D}}}{R^2 J_0^2(\alpha_n)} \sum_{j=1}^{N} J_1\Big(\frac{\alpha_1}{W} jh\Big) J_1(\beta_n jh)\, jh \tag{4.42}$$

where $\beta_n = \alpha_n / R$, and the radius R, over which the series is defined, is chosen large compared to W.

The counterpart of equations (4.12) and (4.13) of Section 4.3 in cylindrical coordinates are

$$A_\varphi(r, z) = \begin{cases} A^a J_1(\beta r) e^{-\gamma z} & z \geq 0 \\ A^b J_1(\beta r) e^{\beta z} & z \leq 0 \end{cases} \tag{4.43}$$

and

$$\mathbf{H}(r, z) = \begin{cases} \dfrac{A^a}{\mu_0 \mu_{\mathrm{r}}} \big[\gamma J_1(\beta r) \hat{\mathbf{r}} + \beta J_0(\beta r) \hat{\mathbf{z}}\big] e^{-\gamma z} & z > 0 \\ \dfrac{A^b}{\mu_0} \big[-\beta J_1(\beta r) \hat{\mathbf{r}} + \beta J_0(\beta r) \hat{\mathbf{z}}\big] e^{\beta z} & z < 0 \end{cases} \tag{4.44}$$

Application of the boundary conditions then yields

$$A^a = A^b = \frac{\mu_0 \mu_{\mathrm{r}} I_{\mathrm{D}}}{\gamma + \beta \mu_{\mathrm{r}}} \tag{4.45}$$

exactly analogous to equation (4.15).

The method of incorporating multiple layers in the model, developed in Section 4.6, is also directly applicable in this case. Combining the results in equations (4.44), (4.32), and (4.42),

and summing over all Fourier-Bessel modes, yields the following result for the magnetic flux density at the origin:

$$B_z(r=0,z=0) = I_{\mathrm{D}} \sum_{n=1}^{\infty} \frac{2}{R^2 J_0^2(\alpha_n)} \cdot \frac{1}{R_n} \sum_{j=1}^{N} J_1\Big(\frac{\alpha_1}{W} jh\Big) J_1(\beta_n jh)\, jh \tag{4.46}$$

So far the ideal value of the drive current density in equation (4.41) has been used. In the practical implementation of the sensor, the shape of the current density is achieved by adjusting the number of turns in each segment of the winding, to approximate the ideal envelope function. As a consequence, the total effective current in each segment is an integral multiple of the driving current. The approximation can be made arbitrarily close by increasing the number of turns, but from a practical perspective a compromise must be made between the coarseness of the quantization and the increasing inductance and parasitic capacitance of the primary winding, as the total number of turns increases. The winding turns in Table 4.3 are the result of such a compromise. Figure 4-19 plots the actual number of turns and the corresponding ideal envelope function for two different winding patterns.

To use the actual current density that results from the winding pattern in Table 4.3, equation (4.41) must be replaced with

$$K_{\mathrm{S}}(r) = I_{\mathrm{D}} \sum_{j=1}^{N} w_j u_0(r - jh) \tag{4.47}$$

where the value of the driving current I_{D} is not necessarily the same. As discussed in Chapter 5 and Appendix D, such multiplicative factors in the magnitude of the sensor response can be ignored in the simulations, since they are absorbed in the sensor calibration step. Equations (4.42) and (4.46) must similarly be altered as follows:

$$K_n = \frac{2 I_{\mathrm{D}}}{R^2 J_0^2(\alpha_n)} \sum_{j=1}^{N} w_j J_1(\beta_n jh)\, jh \tag{4.48}$$

$$B_z(r=0,z=0) = I_{\mathrm{D}} \sum_{n=1}^{\infty} \frac{2}{R^2 J_0^2(\alpha_n)} \cdot \frac{1}{R_n} \sum_{j=1}^{N} w_j J_1(\beta_n jh)\, jh \tag{4.49}$$

Equations (4.44), (4.45), and (4.48) are used to calculate the magnetic field lines of the sensor in this section for air and metal, in analogy to the results shown in Figure 4-10. The results are shown in Figure 4-16.

The measurement grids used in Chapter 5, shown in Figures 5-8, 5-10, 5-13, and 5-15, are generated using a version of this method, described in Section 5.3.

One may visually confirm that the field far from the windings in Figure 4-16(a) has no dipole moment by comparing it to the pattern in Figure 4-13, observing that the dominant multi-pole moment appears to be the "octupole" ($\ell = 3$) moment.

4.9 Fast Hankel transform

Methods similar to the FFT methods in Section 4.4 may be used to model sensors with rotational symmetry, such as the one described in Section 4.8. The magnetic vector potential in this case is represented as a Fourier-Bessel series, applied over the interval $0 < r \leq R$, where

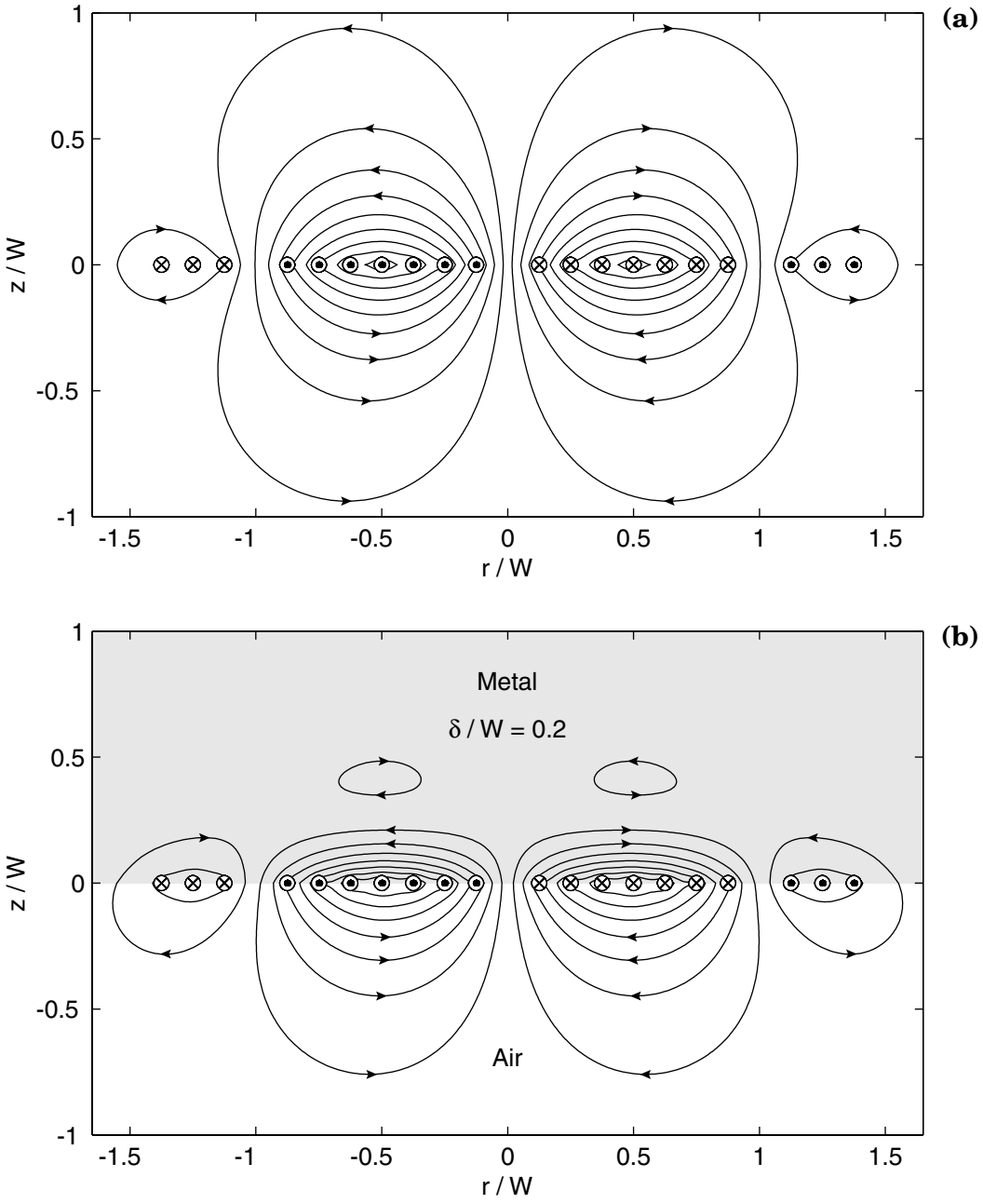

Figure 4-16: Numerically calculated magnetic field of the circular magnetometer in air **(a)**, and when the material above it is metal with skin depth $\delta = 0.2W$ **(b)**, where W is the radius where the first order Bessel function has its first zero.

the radius R is chosen to be large compared to the relevant length scale.

Calculating the Bessel series coefficients and then summing over the spatial modes, as done in Section 4.8, can be a very computationally intensive task. The Cartesian geometry case took advantage of the FFT methods, which unfortunately have no direct analog for the Bessel series.

The continuous Fourier-Bessel transform is better known as the Hankel transform. A method of Hankel transform evaluation using FFT methods is described in [56]. There the Hankel transform is carried out in two FFT steps. This section presents an implementation of this ***Fast Hankel Transform*** (FHT), as an alternative to the direct method of Section 4.8.

4.9.1 Definition and derivation

The Hankel transform can be based on Bessel functions of any order. Here the relevant transform is based on J_1. It is defined as follows:

$$g(u) = \int_0^\infty f(r) J_1(ur) r \, dr \tag{4.50}$$

If the following substitutions are made:

$$r = r_0 e^{\alpha x} \tag{4.51}$$

$$u = u_0 e^{\alpha y} \tag{4.52}$$

$$\hat{f}(x) = r f(r) = r_0 e^{\alpha x} f\left(r_0 e^{\alpha x}\right) \tag{4.53}$$

$$\hat{g}(y) = u g(u) = u_0 e^{\alpha y} g\left(u_0 e^{\alpha y}\right) \tag{4.54}$$

then equation (4.50) transforms to the following correlation integral:

$$\hat{g}(y) = \int_{-\infty}^\infty \hat{f}(x) \hat{\jmath}(x+y) \, dx \tag{4.55}$$

where the kernel $\hat{\jmath}(x)$ is defined as

$$\hat{\jmath}(x) = \alpha r_0 u_0 e^{\alpha x} \tag{4.56}$$

Taking the Fourier transform, defined in equation (4.1b), of both sides of equation (4.55), the following relationship is derived:

$$\begin{aligned} \mathcal{F}\left\{\hat{g}\right\} &= \int_{-\infty}^\infty \hat{g}(y) e^{-iky} \, dy = \int_{-\infty}^\infty \hat{f}(x) \, dx \int_{-\infty}^\infty \hat{\jmath}(x+y) e^{-iky} \, dy \\ &= \int_{-\infty}^\infty \hat{f}(x) e^{+ikx} \, dx \int_{-\infty}^\infty \hat{\jmath}(y') e^{-iky'} \, dy' = \mathcal{F}\left\{\hat{\jmath}\right\} \cdot 2\pi \mathcal{F}^{-1}\left\{\hat{f}\right\} \end{aligned} \tag{4.57}$$

where the substitution $y' = y + x$ was used.

It is therefore possible to compute the Hankel transform by applying the Fourier transform twice. It is important to realize that the Fourier transform of the kernel $\hat{\jmath}$ does not depend on the original function $f(r)$, and therefore needs to be computed only once for multiple Hankel transform evaluations. This step is also the only one which involves evaluating Bessel functions. These features of the fast Hankel transform give it its computational advantage.

4.9.2 Discretization

The Fourier transform steps can be carried out using fast Fourier transform methods, where x and y assume integer values between zero and $N-1$. The necessity for discrete sampling raises several considerations:

Exponential point distribution

If the sample points are spaced evenly in the x-domain, as required by the FFT, their distribution in the r-domain is exponential. This necessarily results in oversampling for low values of r, if a minimal sampling frequency is to be maintained at the upper end of the range.

Due to the exponential distribution of the sample points, one cannot take advantage of the impulse-train structure of the current drive, given in equation (4.41). As discussed previously in Section 4.4 for the rectangular sensor, the sample frequency does not need to be higher than the spatial frequency of the primary windings, which results in very fast computation. In this case there is no particular advantage to the even spacing of the primary windings.

Furthermore, the transition from the continuous representation, where the surface current density is given as a sum of impulse functions, to the discrete domain, is no longer accomplished simply by using the impulse function magnitudes as the values at the sample points. Due to the nonuniform spacing of the sample points, a finite spatial width must be given to each winding, with many sample points falling inside it, in order to capture the magnitude of the current in each segment correctly. For example, in Figure 4-17, discussed later in this section, Gaussian pulses are used to represent the surface current density of the circular sensor in place of impulse functions. The surface current density in equation (4.47) in this case is changed to

$$K_{\mathrm{S}}(r) = I_{\mathrm{D}} \sum_{j=1}^{N} \frac{w_j}{\Delta\sqrt{2\pi}}\, e^{-(r-jh)^2/2\Delta^2} \tag{4.58}$$

where Δ is the width of the Gaussian pulse.

Padding with zeros

The use of a discrete Fourier transform representation automatically implies that both the function and its transform are periodic, with a period equal to the range over which the functions are sampled. It can be inferred from equation (4.55) that if $\hat{f}$ and $\hat{g}$ are defined at N points, then $N+N=2N$ points are needed for $\hat{\jmath}$. Therefore, in order to calculate the transform correctly, $\hat{f}$ needs to be first padded by appending additional N zeros, and after $\hat{g}$ is calculated via the FHT, the last N points must be ignored, since they are meaningless and represent aliasing effects.

Choosing appropriate values for α, r_0, and u_0

Given the spatial extent $r_{\max}$, maximum spatial frequency $u_{\max}$, and number of points N, chosen to be a power of 2 for computational efficiency, the parameters α, r_0, and u_0 need to be determined. The point spacing, $\alpha r_0 e^{\alpha n}$ at its rarest point, $n=N$, as well as the minimum value r_0 itself, should be roughly equal to each other and to the inverse of the highest "frequency"

Parameter	Value
N	$2^{10} = 1024$
α	0.00515
r_0	0.0154
$r_{\max}$	3.00
q_0	0.946
$q_{\max}$	184

Table 4.4: Fast Hankel transform normalized parameter values.

value in the reciprocal domain. This results in the following equation for α:

$$\alpha e^{\alpha N} = 1 \tag{4.59}$$

This in turn determines r_0 and u_0:

$$r_0 = r_{\max} e^{-\alpha N} \tag{4.60}$$

$$u_0 = u_{\max} e^{-\alpha N} \tag{4.61}$$

Whether or not the resulting values of r_0 and u_0 are small enough to be able to represent the discretized functions with adequate accuracy depends on the original choice of N. It is also possible to pick r_0 and u_0 first, and let this determine α and N, as was done in [56].

4.9.3 Application of the fast Hankel transform to the circular magnetometer

The first step in applying the FHT to calculate the response of the circular magnetometer is to verify that the values of the various FHT parameters are appropriate, to ensure that the transform represents the sensor with adequate precision, while keeping the computational burden at a minimum.

Figure 4-17 (a) is a plot of the surface current density in equation (4.58). The FHT is applied to obtain the transform of the surface current density, with the result shown in Figure 4-17 (b). The FHT parameters used are given in Table 4.4. This transform is similar in structure to the spectrum shown in Figure 4-9. Here the magnitude decreases with increasing q because of the nonzero width of the current pulses in the r-domain. A similar amplitude envelope was used in the computations in Section 4.5, although not explicitly shown in Figure 4-9. In that case the exponential decay was imposed on the spectrum after it was computed, while here it occurs naturally, because the initial current function already includes the nonzero pulse width.

Applying the FHT for a second time to the transform restores the original function, because the Hankel transform is its own inverse. The result is shown in Figure 4-17 (c). It can be seen in the figure that the twice-transformed function $f'(r)$ is a very close match to $f(r)$, with the exception of the ripples that result from the finite length of the spectrum, the ripple frequency being dominated by the first nontrivial component past the truncated end of the spectrum, somewhere near $qW = 190$ in this case.

Thus the correctness of the FHT developed in this section is confirmed. This method can now be applied to generate the same magnetic field line diagrams as Figure 4-16 in Sec-

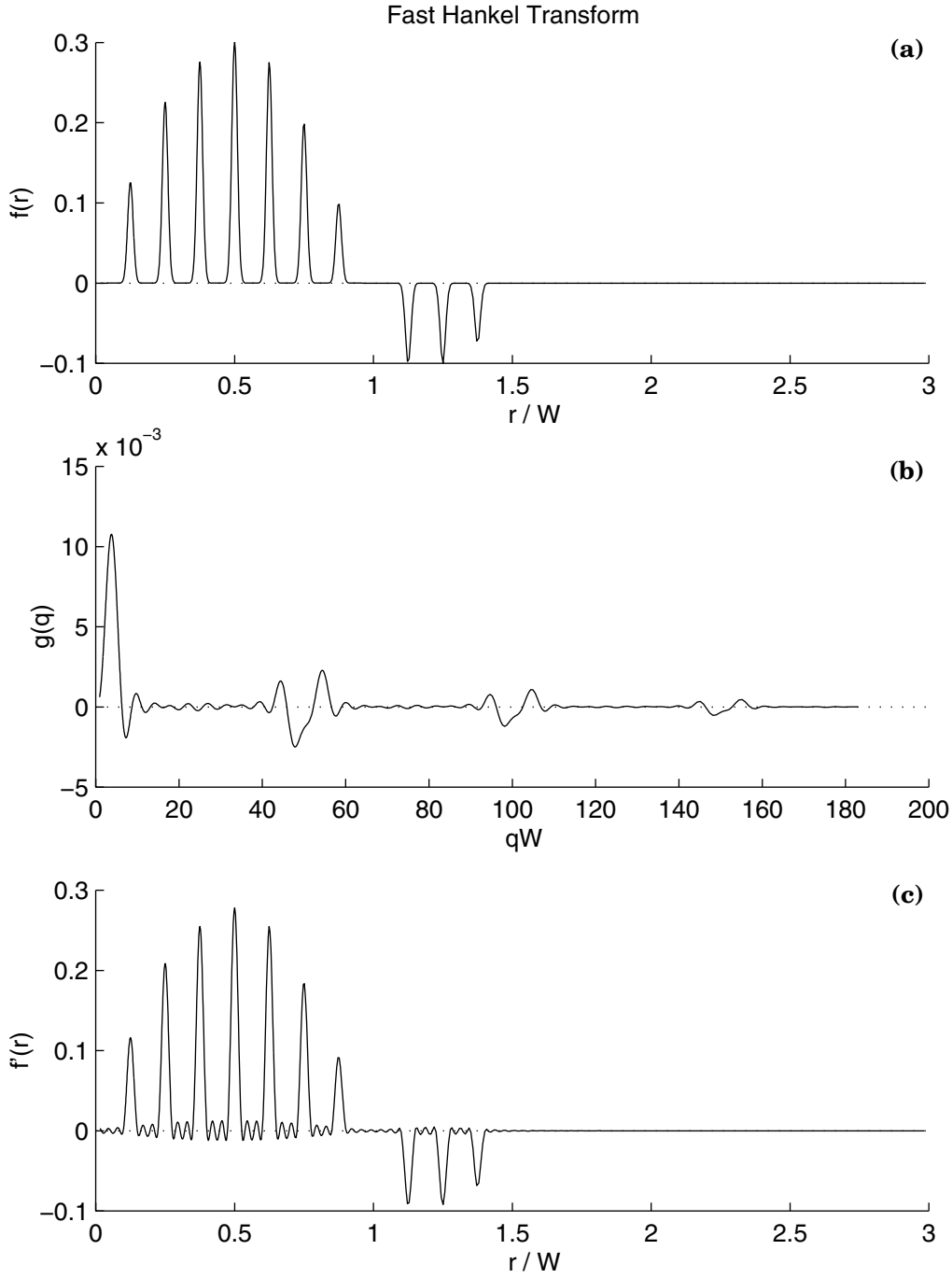

Figure 4-17: Results of the application of the fast Hankel transform. The FHT parameters used are given in Table 4.4. **(a)** The function used to represent the surface current density $K_{\mathrm{S}}(r)$ of the primary winding. **(b)** The fast Hankel transform of this function. **(c)** The original function restored with another application of the FHT. The high frequency ripples are well understood, and are due to the truncation of the Hankel transform.

A	0	14	22	21	13	3	−4	−4	0	1	−2	−7	−4
B	0	−4	−4	3	13	21	22	14	0	−11	−16	−7	−4
$A+B$	0	10	18	24	26	24	18	10	0	−10	−18	−14	−8
$A-B$	0	18	26	18	0	−18	−26	−18	0	12	14	0	0

Table 4.5: Winding pattern for the rectangular magnetometer, enabling two different fundamental wavelengths, determined by the polarity of the connection.

A	13	21	21	15	7	1	−1	0	1	−4	−3
B	−3	−3	1	9	15	15	9	0	−9	−4	−3
$A+B$	10	18	22	24	22	16	8	0	−8	−8	−6
$A-B$	16	24	20	6	−8	−14	−10	0	10	0	0

Table 4.6: Winding pattern for the circular magnetometer, enabling two different fundamental wavelengths, determined by the polarity of the connection.

tion 4.8, by using the numerical techniques of Sections 4.4 and 4.5, using the FHT in place of the FFT. The results are shown in Figure 4-18. The two sets of figures appear identical.

4.10 Different wavelength modes with the same sensor

It is possible to change the fundamental wavelength of the current excitation without changing the geometry of the sensor, by changing the current distribution in the primary winding segments. This may be accomplished by supplying an independent current drive for each segment, and changing the relative magnitudes of these drives to follow an appropriate envelope function with the needed spatial wavelength.

Another possibility, which avoids the need for multiple drives, is to use two or more independent winding circuits, and to switch the relative current direction between them. As an example, consider the winding pattern in Table 4.5, meant for the rectangular sensor.

Two windings, A and B, and the number of turns each has in every winding segment, are shown in this table. As before, negative turns indicate that they are wound in the opposite direction. When the two windings are driven with the same polarity, the resulting current distribution is proportional to the one in Table 4.2, exciting a mode with a fundamental wavelength equal to the length of the sensor. If, on the other hand, the two windings are driven with opposite polarities, the resulting excitation has a fundamental wavelength equal to one-half of the sensor length.

The depth of sensitivity of the sensor depends on the imposed spatial wavelength. Therefore, the use of more than one excitation wavelength provides some information on how the material properties change with depth. Furthermore, the use of more than one wavelength within the same footprint has the advantage that the lift-off, defined as the distance between sensor and material, is the same for both modes of operation. This is very useful when there are more than two unknown parameters, and measurements under two different applied magnetic field distributions are necessary to determine all unknowns uniquely.

A similar idea can be applied to the circular sensor, where the higher mode uses $\alpha_2 \approx 7.016$ in the current envelope function, so that W is the radius where it has its second zero. The winding pattern, including the dipole cancellation windings for both modes, is given in Table 4.6, and is plotted in Figure 4-19. This is the winding pattern actually used in the sensor

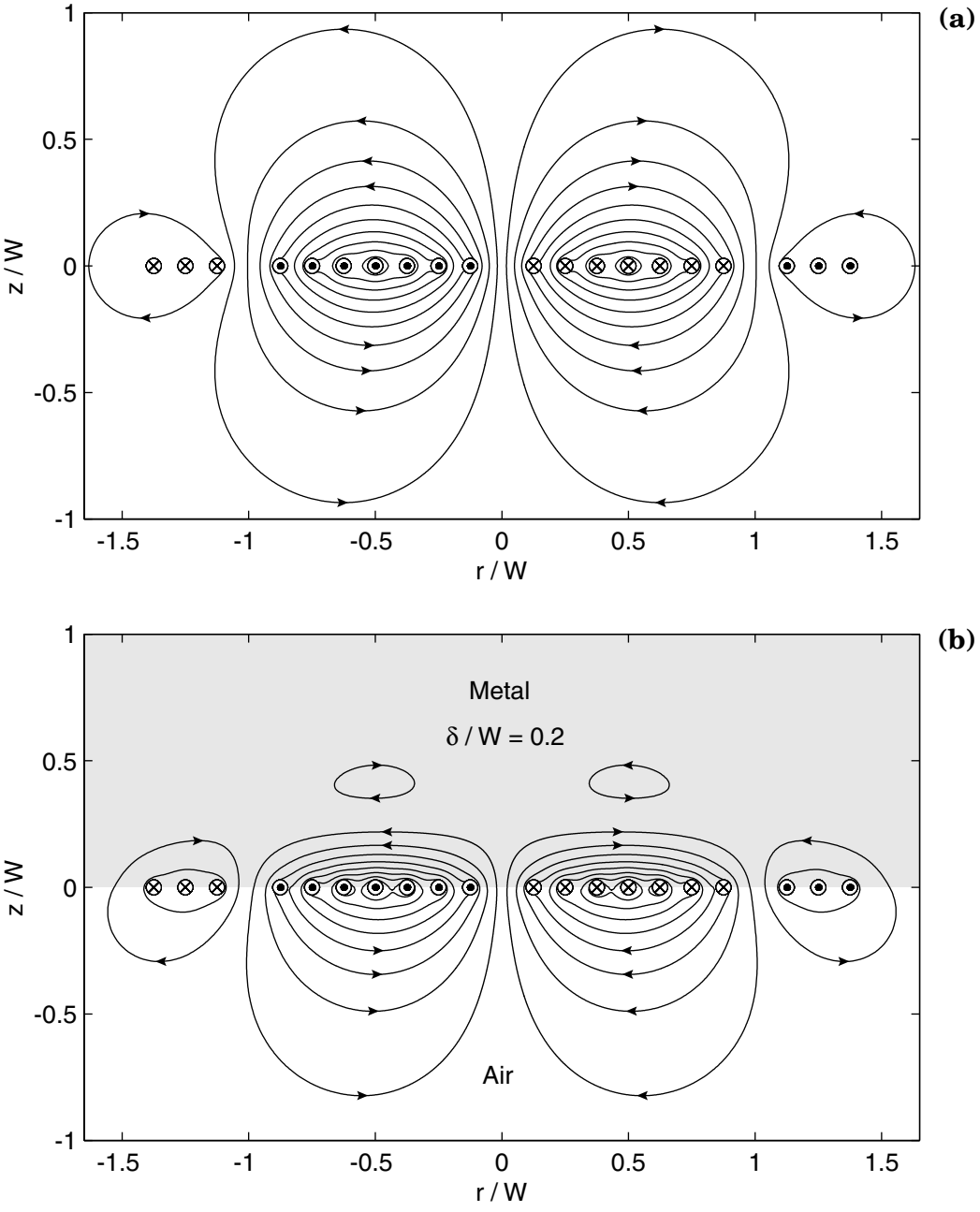

Figure 4-18: Magnetic field lines of the circular magnetometer, calculated with the fast Hankel transform: in air **(a)**, and when the material above it is metal with skin depth $\delta = 0.2W$ **(b)**, where W is the radius where the first order Bessel function has its first zero.

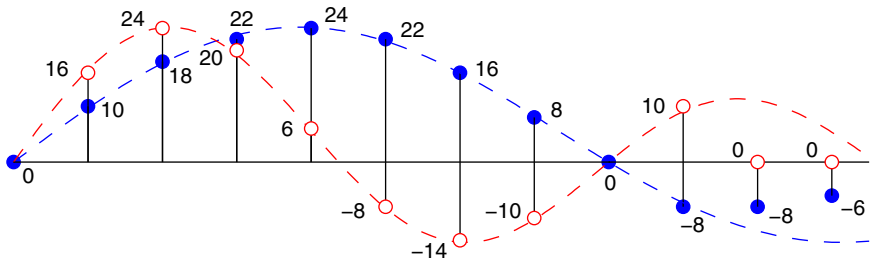

Figure 4-19: Winding pattern for the circular magnetometer that enables two different fundamental wavelengths, determined by the polarity of the connection, according to Table 4.6. The filled circles correspond to the $A + B$ connection, and the hollow circles correspond to $A - B$. Because the number of turns result from the combination of two separate windings, the numbers are two times greater than the ones listed in Table 4.3. The first order Bessel envelope function is shown with dashed lines for both configurations. The number of turns do not fall exactly on the curves, since they need to be integers. The number of turns in the last two windings are tapered off in order to avoid rapid changes in the primary current distribution, which would result in more energy in higher order Fourier-Bessel modes.

built for experimentation. Results of two-wavelength measurements carried out using this approach are presented in Section 5.5.

4.11 Summary of Chapter 4

In this chapter an analysis has been carried out of the unique characteristics of magnetometers with a distributed current drive. For such sensors it may be assumed that the drive current distribution is known, which makes them suitable for very efficient discrete Fourier transform methods. To illustrate the power of such methods, the magnetic field lines have been computed for the three basic magnetometer geometries considered, shown in Figures 4-7, 4-10, and 4-16.

The effort in this chapter has focused on addressing considerations of the practical design of a circular magnetometer with a distributed primary winding. The Bessel series approach, introduced in Chapter 3, is applied to developing a method for modeling this new magnetometer design. Other important factors have also been considered, such as the elimination of the net dipole moment for improved measurement repeatability (Section 4.7), and layout of the primary winding that permits sensor operation at two distinct effective spatial wavelengths (Section 4.10). A methodology has also been presented in Section 4.9 for extending the highly efficient Cartesian fast Fourier transform method to the computation of the Fourier-Bessel (Hankel) transform, required by the cylindrical geometry.

In summary, many important theoretical tools have been developed that are needed for the design of the high performance magnetometer, described in Chapter 5, capable of absolute property measurement without the need for calibration standards.

Chapter 5

Deep Penetration Magnetoresistive Magnetometer: Structure and Measurement Results

This chapter describes the design of a circularly symmetric, distributed current drive magnetometer with a secondary sensor based on the giant magnetoresistive (GMR) effect. It is an implementation of the ideas and models presented in the previous chapters.

As discussed in Chapter 1, the use of a magnetoresistive sensor allows the magnetometer to be operated at frequencies lower than currently possible with existing MWM and other eddy current sensors. Indeed, it is possible to operate this magnetometer with temporally constant magnetic field excitation, confirmed experimentally with measurements shown in Section 5.5. Low frequency operation is needed to increase the depth of sensitivity of the magnetometer, which is determined by the skin depth $\delta \propto 1/\sqrt{\omega}$, and by the imposed spatial period via equation (2.14). The latter can be made large by using a distributed current drive, as discussed in Chapter 4.

The principles of operation of the magnetoresistive and giant magnetoresistive sensors are described in Section 5.1.

A photograph of the prototype sensor used in the experiments in this chapter is shown in Figure 5-1. It is built according to the diagram in Figure 4-15, with $W = 8$ cm and $h = 1$ cm. There are two overlapping windings, with the number of turns in each groove determined by the A and B rows in Table 4.6. These two windings are connected in series, and the polarity of the connection determines which of the two current drive patterns, given in Table 4.6 and Figure 4-19, are excited. The two excitation modes have different effective fundamental spatial wavelengths.

A secondary sensor assembly, consisting of a giant magnetoresistive sensor and a secondary solenoidal coil, is positioned at the center of the magnetometer. They are connected in a feedback loop, as described in Section 5.2. A circuit board that hosts the GMR sensor buffer amplifier, not visible in the photograph, is positioned near the center below the magnetometer base. The primary windings and the sensor assembly are connected to a circuit board that contains the secondary coil driver, compensation amplifier, and interface electronics. It does not need to be in very close proximity to the sensor. The interface circuitry is connected to the impedance analyzer instrumentation used to measure the magnetometer's transfer function magnitude and phase angle.

Section 5.2 describes the reasons for placing the GMR sensor in a feedback loop with

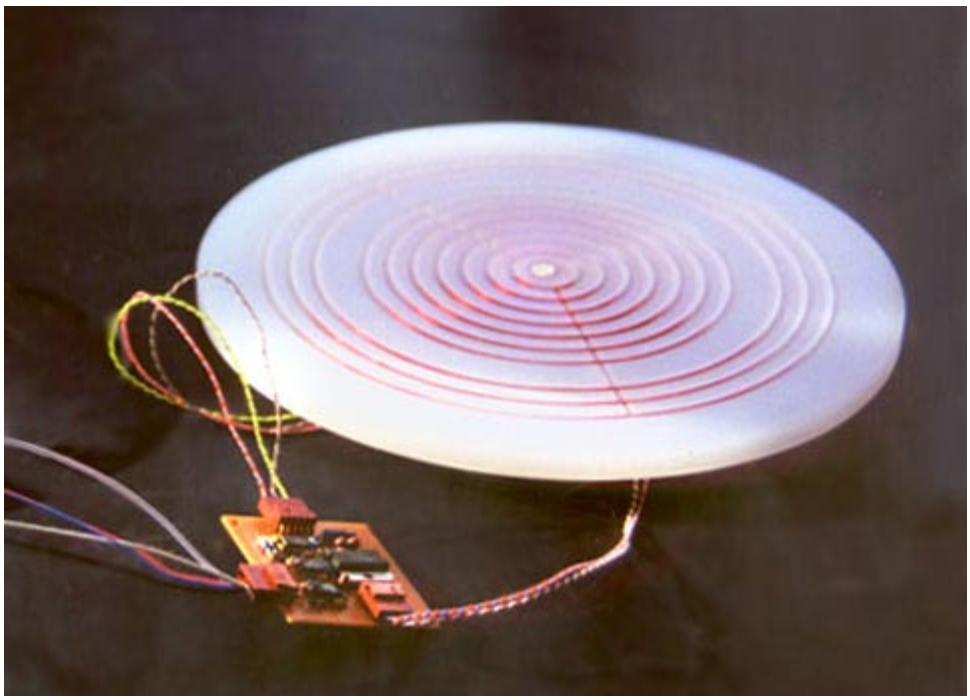

Figure 5-1: Photograph of the prototype sensor used in all experiments shown in Chapter 5. The sensor base is built according to Figure 4-15, and the number of turns in each segment of the primary winding are specified in Table 4.6 and Figure 4-19. A secondary sensor assembly, consisting of a giant magnetoresistive sensor and a secondary solenoidal coil, connected in a feedback loop as described in Section 5.2, is positioned at the center of the magnetometer. Below the base, not visible in the photograph, is a circuit board hosting a buffer amplifier stage. The visible detached circuit board contains the secondary coil driver, compensation amplifier, and interface electronics.

a secondary driven winding. The design of the supporting electronic circuit is shown, and questions associated with the dynamic behavior of the feedback loop are addressed. The presence of the secondary driven coil needs to be incorporated in the model developed in Chapter 4. This expansion of the model is described in Section 5.3.

Sections 5.4 and beyond are dedicated to reporting the results of a variety of measurements, chosen to illustrate the useful new unique features of this magnetometer, including ultra low frequency, and DC two-wavelength measurements on magnetizable materials, evaluation of thick metallic coatings, thickness measurement of thick metal plates, used for corrosion mapping of metal components via measurements through the opposite surface, detection of deeply buried flaws in metals, and measurements of the magnetic permeability of ferrofluids.

5.1 Theory of the magnetoresistive and giant magnetoresistive effects

This section describes magnetoresistance, magnetoresistive anisotropy in ferromagnetic metals, and giant magnetoresistance in metallic magnetic superlattices. This is a qualitative discussion, since these are complex quantum effects, and the actual physics behind the operation

of the sensors based on these phenomena does not affect the modeling of the magnetometer response. Furthermore, as shown in Section 5.2, the sensor is connected in a way that eliminates the effect of the transfer function of the magnetoresistive sensor on the magnetometer response.

5.1.1 Magnetoresistance

In general magnetoresistance is an effect which results when the carrier trajectories in a material are curved due to the Lorentz force which acts in a direction orthogonal to their motion. If an electron undergoes no scattering, then in the presence of a magnetic field it follows a helical orbit with angular frequency

$$\omega_{\mathrm{C}} = \frac{eB}{m^*} \tag{5.1}$$

(the cyclotron frequency), where e is the charge of the electron, B is the magnetic flux density, and m^* is the cyclotron effective mass. When scattering is present, the carriers experience a drag force characterized by a decay time constant τ, related to the conductivity as

$$\sigma = \frac{ne^2\tau}{m^*} \tag{5.2}$$

where n is the carrier density. The dimensionless product

$$\omega_{\mathrm{C}}\tau = \frac{B\sigma}{ne} \tag{5.3}$$

is a measure of how significant the magnetoresistance is under the specified conditions. It represents the mean angular deflection that a carrier undergoes between collisions. If this number is much less than one, then the trajectory radius is much greater than the mean free path and consequently the resistivity is not affected. To make an observable difference, $\omega_{\mathrm{C}}\tau$ must be of order unity or greater [57].

In practice, to meet this condition it is necessary to use very pure materials at cryogenic temperatures, in order to make τ large, and subject the sample to an extremely strong magnetic field, > 1T, to make ω_{C} large.

It can be shown that the curved trajectories themselves do not necessarily lead to magnetoresistance, so that the condition $\omega_{\mathrm{C}}\tau > 1$ is a necessary, but not sufficient condition for magnetoresistance. In materials with only one type of carrier that has a spherical Fermi surface, like the alkali metals, the diagonal elements of the resistivity tensor remain unchanged, and no magnetoresistance is observed. A the other extreme, in materials such as the noble metals, which have highly irregular interconnected Fermi surfaces, the magnetoresistance is rather strong and very much dependent on the orientation of the magnetic field with respect to the crystal lattice axes. Alternatively, materials like the semimetal bismuth, which have an equal number of electrons and holes as carriers, also exhibit high magnetoresistance [57]. The resistivity $\rho = 1/\sigma$ of the material along the magnetic field direction is unaffected, as carriers moving in this direction experience no Lorentz force, while it is increased in the orthogonal direction, i.e. $\rho_{\parallel} < \rho_{\perp}$.

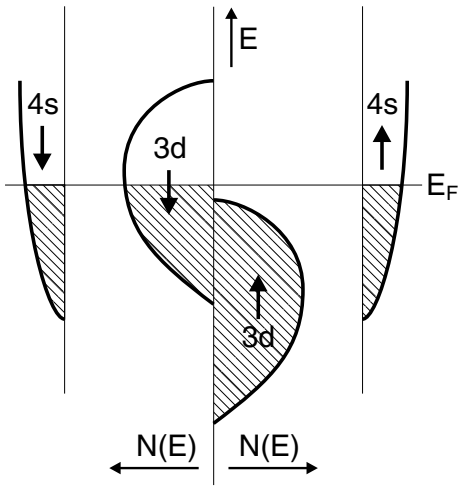

Figure 5-2: Fermi diagram of conduction states in a ferromagnetic metal. At low temperatures the spin-up $3d$ states are almost completely filled, and due to the magnetization, the holes in this band are not evenly distributed between the five d-orbitals. This results in anisotropy in the scattering rates of conduction electrons, leading to magnetoresistive anisotropy in such materials.

Magnetoresistive anisotropy

In the following discussion it is assumed that anisotropic behavior due to crystal lattice symmetries is negligible, which is true for amorphous or polycrystalline materials. In this case the direction of the magnetic field determines the resistive anisotropy axis in the material.

A stronger magnetoresistive effect of a different nature, also known as magnetoresistive anisotropy, is observed in thin films of ferromagnetic metals and alloys [58]. The trends observed in these materials are in some respects opposite to those described so far. In ferromagnetic thin films the magnetoresistive effect is strongest in alloys, such as Ni-Fe, while the large number of crystalline defects in alloys tends to make τ shorter. Furthermore, the lower resistivity is observed in the orthogonal direction, i.e. $\rho_{\parallel} > \rho_{\perp}$, also in contradiction to ordinary magnetoresistance.

Clearly, a different mechanism is responsible for this effect. One theory that presents an explanation for this behavior is given in [58]. According to this explanation, the conductivity is largely determined by s-electrons scattering into and out of d-orbitals, with the scattering caused by lattice vibration and lattice imperfections, much higher in alloys than in pure metals. The current may be divided in two branches, corresponding to spin-up and spin-down electrons. This is known as the two-current, or two-band, model, and is commonly used to model transport phenomena in ferromagnetic transition metals [59, 60]. Ignoring spin exchange between the s-electrons keeps the two bands independent, and the total resistivity is

$$\rho = \frac{\rho_{\uparrow}\rho_{\downarrow}}{\rho_{\uparrow} + \rho_{\downarrow}} \tag{5.4}$$

where $\rho_{\uparrow}$ and $\rho_{\downarrow}$ are the resistivities of the spin-up and spin-down branches respectively. At low temperatures the $3d$ spin-up states are almost completely occupied, allowing only $4s$ to $4s$ transitions, resulting in less scattering and lower resistivity for the spin-up band. This condition is graphically illustrated in Figure 5-2.

This in itself does not introduce any anisotropy. However, when the spin-orbit interaction is considered, some mixing of parallel and antiparallel states occurs, and as a consequence there are some unoccupied parallel $3d$ states (holes) even at absolute zero. These holes are not equally distributed between the five d-orbitals, with a deficit of holes in orbitals perpendicular to the magnetization. The $4s$ to $3d$ transition probability is smallest if the s-electron moves perpendicular to the orbit. Thus an electron moving in the direction of magnetization has a higher than average probability of being trapped in a $3d$ state, resulting in higher resistivity in this direction, i.e. $\rho_{\parallel} > \rho_{\perp}$.

Results shown in [58] indicate that magnetoresistive anisotropy is strongest in Fe/Co/Ni alloys with an average atomic magnetic moment of one Bohr magneton μ_B, independent of the actual alloy composition. The Bohr magneton $\mu_B = e\hbar/(2m_e)$ is the magnetic moment of an electron, where m_e is the electron rest mass, and $\hbar = h/(2\pi)$ is the normalized Planck's constant. This effect has yet to be explained theoretically.

One of the earlier practical magnetoresistive sensors based on this effect was proposed by R. P. Hunt in 1971 [61], and since then they have enjoyed popularity for many practical applications, some of which are listed in Table 1.1 [40, 62–64].

5.1.2 Giant magnetoresistance

The magnetoresistive effect is generally on the order of a few percent, perhaps as much as 5% at low temperature. ***Giant magnetoresistance*** refers to magnetoresistive changes of 20% or more [65], observed in certain metallic magnetic superlattices, also called magnetic multilayers. It was first described in 1988 [66] and has since then been an area of very active research [67–73, and many papers in 74].

The definition used in the literature for reporting the magnitude of the giant magnetoresistive (GMR) effect is not consistent in whether the change in resistivity is referenced to its highest value, which occurs with no external field, or its lowest value, which occurs in saturation. This can lead to large disparity in the reported values. One must be aware which convention is used when comparing the performance of different structures. The definition used here expresses the magnitude as a percent change of the resistivity with respect to its value with no external field, i.e. $\Delta\rho/\rho_{\max}$.

Giant magnetoresistance was first observed in Fe/Cr magnetic superlattices [66], where a drop of as much as 45% of the resistivity was measured at liquid helium temperature (4.2 K). At room temperature the magnitude of the effect was reduced to about 12%. Other material systems have been tested since then, with the Co/Cu magnetic superlattice emerging as the system of choice in the development of practical sensors. It exhibits resistivity drops of up to 55% at liquid helium temperature and 40% at room temperature [69].

The magnetic superlattices have alternating layers of a nonferromagnetic and ferromagnetic metal. The thickness of the nonferromagnetic layers is chosen such that in the absence of applied external magnetic field the moments of consecutive ferromagnetic layers are arranged antiparallel to each other. This antiferromagnetic coupling between these layers has been ascribed to indirect exchange interactions through the nonferromagnetic layers [66]. The presence of an external field acts to align the moments of all ferromagnetic layers, resulting in reduction of the electric resistivity. This is schematically illustrated in Figure 5-3. The magnetoresistance is thus defined as [61]

$$\frac{\Delta\rho}{\rho_{\max}} = \frac{\rho_{\uparrow\downarrow} - \rho_{\uparrow\uparrow}}{\rho_{\uparrow\downarrow}} \tag{5.5}$$

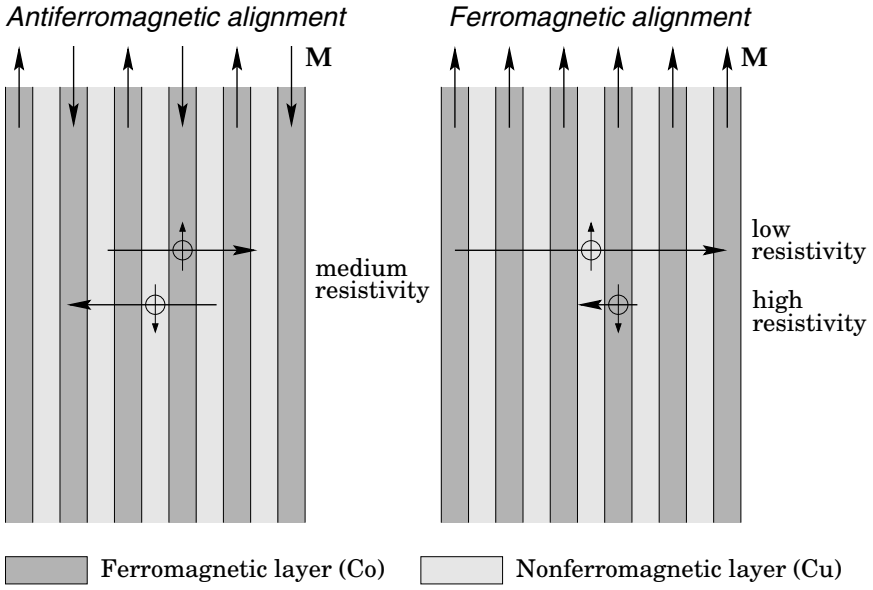

Figure 5-3: Diagram illustrating the giant magnetoresistive effect. GMR is the result of differences in the scattering of spin-up and spin-down electrons at the layer interfaces. In the absence of external magnetic fields the moments of adjacent ferromagnetic layers are antiparallel, resulting in medium resistivity for both spin bands. In the presence of an externally applied magnetic field the ferromagnetic layers are aligned, drastically reducing the scattering of spin-up electrons, which acts to reduce the overall resistivity of the superlattice.

where $\rho_{\uparrow\uparrow}$ and $\rho_{\uparrow\downarrow}$ are the resistivities in the parallel and antiparallel states respectively.

The physical explanation for this phenomenon, as initially suggested in [66], hinges on the spin-dependent scattering characteristic of ferromagnetic metals. As before, the current is divided into two branches, for spin-up electrons and spin-down electrons [59, 60]. In the antiferromagnetic state, on average both types of electrons experience the same set of scattering potentials, resulting in the two branches having equal resistivity of intermediate value, $2\rho_{\uparrow\downarrow} = \rho_{\uparrow} = \rho_{\downarrow}$ (see equation (5.4)). In the aligned state, the spin-up electrons are scattered much less effectively, resulting in low resistivity for this current branch and an overall lower resistivity for the entire structure, $\rho_{\uparrow\uparrow} \approx \rho_{\uparrow} \ll \rho_{\downarrow}$.

Several publications offer explanations and theoretical models for the difference of scattering for spin-up and spin-down electrons [65, 68]. Two distinct processes can lead to such difference. The first is spin-flip scattering. As illustrated in Figure 5-2, in ferromagnetic metals there is a difference in the number of available states at the Fermi level for spin-up and spin-down electrons. Thus an electron spin-polarized in one ferromagnetic layer may experience spin reversal when it enters the next one [67]. Such scattering events are caused by spin-orbit effects, by impurities with a localized magnetic moment, or by magnons (spin waves).

The other process leading to scattering differences between the two electron bands is spin-dependent scattering at the layer interfaces, which is the only effect considered by the Boltzmann transport equation model in [68]. As pointed out in that publication, there would be no magnetoresistance effect for perfect interfaces, and as the surface roughness increases, so does the scattering. The scattering rates for the two types of electrons can differ by a factor of six or more [66, 68], leading to the needed difference in resistivity in the two branches of the current.

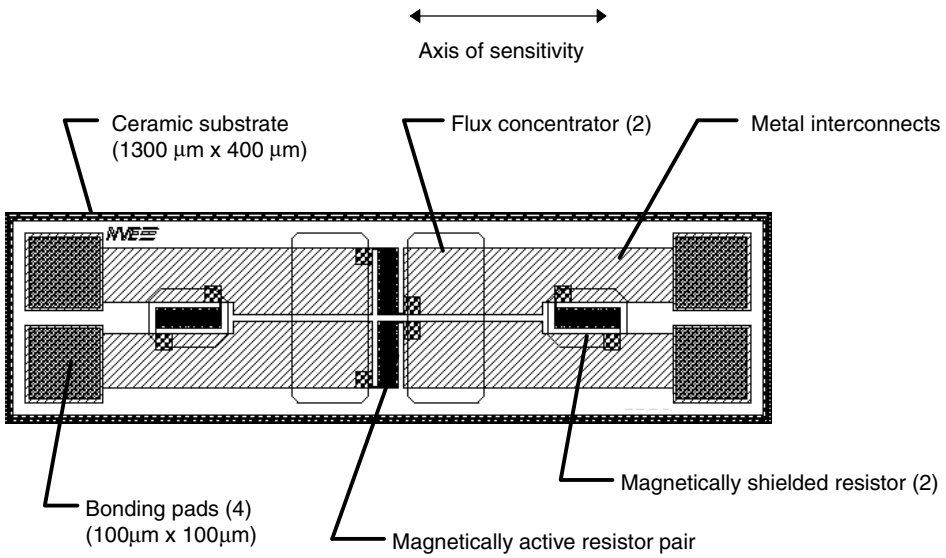

Figure 5-4: Typical GMR magnetic field sensor layout [75]. Four magnetic superlattice resistors are formed on a common ceramic substrate and connected in a bridge configuration. Two of the resistors are shielded from external fields. Ferromagnetic flux concentrators are used to increase the effect of the magnetic field on the other two resistors. If a voltage is applied across a pair of diagonally opposed terminals, a differential voltage is developed across the other pair in the presence of magnetic field.

Due to the spin alignment in a ferromagnetic metal, the spin-up and spin-down electrons have different band structure, Fermi surface, effective mass, etc. This is why the scattering rates for the different spin electrons can be different for the same scatterer. A. Fert and I. A. Campbell apply the two-band model to resistivity data in Ni and Fe based alloys to obtain a consistent set of parameters for the scattering within each spin band for various impurities [59, 60]. The large differences in scattering rates have been confirmed experimentally.

On the whole, the best quantitative physical model of the giant magnetoresistive effect appears to be the one developed by R. Q. Hood and L. M. Falicov [65]. One of the conclusions drawn in this work is that spin-flip scattering can account for no more than a few percent of magnetoresistance, and a large difference in interface scattering for the different spins is needed to explain the observed large GMR values.

5.2 Operation of the secondary GMR sensor assembly

5.2.1 GMR sensor characteristics

A commercially available magnetic sensor, based on the giant magnetoresistive effect, is used as the secondary element of the magnetometer. The sensor is manufactured by Nonvolatile Electronics, Inc. It consists of four magnetic superlattice resistors, deposited on a common ceramic substrate, and connected in a bridge configuration, as shown in Figure 5-4 [75]. Two of the resistors are shielded from external magnetic fields. Ferromagnetic flux concentrators are used to increase the effect of the magnetic field on the other two resistors. If a voltage is applied across a pair of diagonally opposed terminals, a potential difference appears between the other terminal pair in the presence of an externally applied magnetic field.

Figure 5-5 is a plot of the transfer characteristic of this magnetic sensor [75]. Several

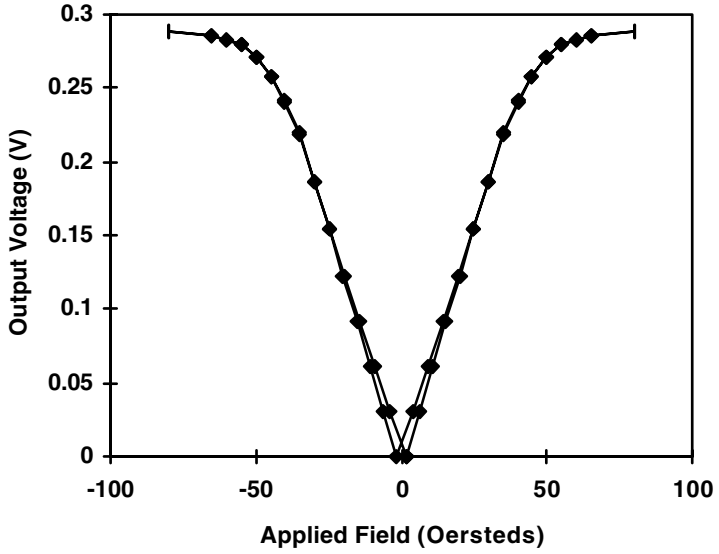

Figure 5-5: Transfer characteristic of the GMR magnetic sensor biased at 5 V [75]. This curve illustrates some of the features of the giant magnetoresistive effect: the output voltage is independent of the field polarity, saturates at high fields, and displays some hysteresis.

features of the giant magnetoresistive effect are evident in this figure. The differential output voltage is independent of the polarity of the applied field, because either polarity leads to a departure from the fully antiparallel alignment. At a certain field magnitude, about 50 Oe for this sensor, the output reaches a saturation value, corresponding to complete alignment of the ferromagnetic layers. Finally, the response shows some hysteresis.

The highly nonlinear nature of the transfer characteristic, especially near zero, makes it necessary to operate the sensor with a certain DC field bias, moving the operating point to the linear region of the characteristic, at approximately 25 Oe and 0.15 V. The biasing may be accomplished with the help of a permanent magnet, but a magnet will perturb the surrounding magnetic flux density, more than just adding its constant field. Alternatively, the sensor may be biased with an electromagnet.

5.2.2 Feedback loop

While DC biasing addresses the nonlinearity and hysteresis problems, a severe limitation still remains: satisfactory operation is maintained only for fields with magnitudes that are small compared to the DC bias field. As the field magnitude increases, the response becomes more and more nonlinear, and for amplitudes on the order of the bias field, saturation and polarity reversal come into effect.

To address these limitations, it is beneficial to place the sensor in a feedback configuration with a secondary winding, as shown in Figure 5-6. In this way the magnetic field at the GMR sensor remains constant during operation, eliminating the effect of the nonlinear transfer characteristic, while maintaining sensitivity at low frequencies. The magnitude of the current in the secondary winding is taken as the output signal, and since the relationship between this current and the magnetic field for an air-core winding is perfectly linear, so is the transfer characteristic of the entire hybrid sensor structure.

Another benefit of the feedback configuration is temperature stability. Since the measured quantities are currents in the windings, which are directly related to the magnetic fields,

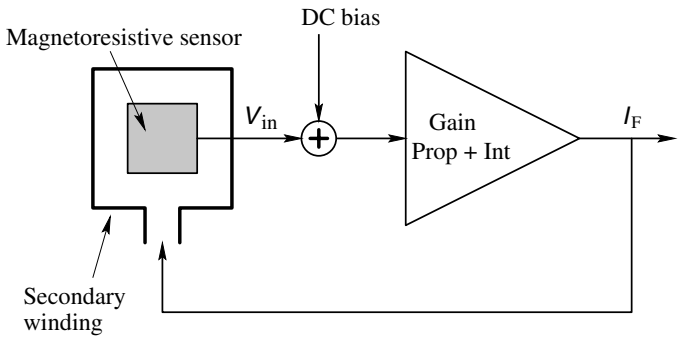

Figure 5-6: Structure of the hybrid sensor feedback loop. The secondary winding maintains a constant magnetic field at the GMR sensor, determined by the value of the DC bias. This allows for high dynamic range and linearity, while retaining low frequency sensitivity. In addition to gain, the forward stage of the loop includes an integral term, which ensures zero error at DC.

temperature dependence of the GMR sensor or winding resistance, etc. has no effect on the magnetometer response.

The magnetic field magnitude that this hybrid sensor can measure is limited only by the magnitude of the field that the secondary winding can produce, which can be orders of magnitude higher than the saturation field of the GMR sensor. There is a further advantage of the feedback connection: biasing the GMR sensor to the appropriate operating point is accomplished simply by adding an appropriate DC voltage offset at the input of the gain stage. This is much better than the biasing methods described so far, because correct biasing is maintained even if the position of the GMR sensor with respect to the bias source changes, which would not be true for biasing with a constant field source. This eliminates the need for complex alignment methods, since biasing at the correct level is automatic with the appropriate choice of circuit components.

There can be situations where this kind of feedback configuration may be inappropriate. The bandwidth of the hybrid sensor is limited by the dynamics of the feedback loop, and is always narrower than open-loop operation. Therefore, at high frequencies the sensor may need to be operated open-loop, although it is still possible to keep the loop closed for low frequencies at the same time, in order to maintain the proper DC bias. This is not a severe limitation, since this magnetometer is not designed for high frequency operation, where it may be more appropriate to use a standard MWM, or simply the induced voltage in a secondary winding. An additional limitation of the feedback loop configuration is that in an array setup, the feedback windings of adjacent elements will be coupled to each other, leading to interchannel cross talk. It is in general possible to compensate for this in the models, but it is better to avoid such situations by appropriate shielding or by open-loop operation.

5.2.3 Electronics

A full schematic of the electronic circuit used to implement the feedback loop, biasing, and interface is shown in Figure 5-7. The resistor bridge of the GMR sensor is shown as U_1. The output impedance of the sensor is relatively high, on the order of $40\ \mathrm{k}\Omega$, and in order to avoid parasitic signal and noise pick-up, as well as extra phase shift due to cable capacitance, a buffer amplifier is placed in close proximity to the sensor. The entire buffer stage assembly, which also implements the sensor DC biasing scheme, is enclosed in a dashed box in the figure. The buffering is accomplished with a high bandwidth instrumentation amplifier U_2.

The voltage regulator U_3 is needed to ensure constant sensor voltage and field biasing. The DC operating point is set by the voltage divider implemented with R_1 and R_2. This first amplifier stage has a gain of ten.

The loop gain and compensation, described later, are implemented with the U_4 amplifier stage. The secondary winding is driven by the high power video amplifier U_5, connected as a unity gain follower. Since U_5 is a current feedback operational amplifier, it is necessary to include R_9, which is also used to set the bandwidth of the stage.

The current I_F through the secondary feedback winding is measured as the voltage across a precision zero-inductance power resistor R_{10}, connected in series. The last stage, implemented with U_6, is used as a coaxial cable driver. It also eliminates the DC component of the signal, and brings the output magnitude to the optimal input levels of the JENTEK impedance analyzer equipment. For constant field measurements, which do not require an impedance analyzer, the output signal is taken at test point 3.

5.2.4 DC stability

Because of the rectifying effect of the GMR sensor, the overall polarity of the feedback loop depends on the direction of the magnetic field, which means that as the circuit is initially powered up, it may enter a positive feedback mode, which is unstable, and leads to the output of U_5 saturating at the positive supply voltage level, rendering the system inoperable. On the other hand, once the correct operating point is established, then the feedback is negative, and the loop remains stable from then on, unless the magnetic field reaches such magnitude that the driver of the secondary winding cannot keep up, in which case the loop may again become unstable.

This complication is a direct consequence of the GMR sensor transfer characteristic, and cannot be avoided. It is therefore necessary to implement some external mechanism that detects the faulty condition and resets the loop by forcing the output to be near the operating point. A much simpler remedy, used in this implementation, is to ensure that the current through the secondary winding is always negative, by connecting a diode D_1 in series with it. This does resolve the stability problem, and ensures that the feedback loop always recovers to the proper operating point. However, it also introduces a limitation. While the magnitude of the measured field is unlimited in the positive direction, in the negative direction its magnitude may not exceed that of the bias field. Although this compromise is acceptable for the prototype magnetometer, in a more general setting it may be necessary to incorporate an auxiliary “watch dog” circuit of the kind described above.

5.2.5 AC stability and loop bandwidth

Ignoring for the moment the U_4 stage, the ideal open-loop transfer characteristic consists of a single pole at $\omega = R_{10}/L$, introduced by the relationship between driver output voltage and secondary winding current I_F. In the ideal case where this is the only pole, the loop is always stable, and its bandwidth can be increased indefinitely by increasing the loop gain. In practice all operational amplifiers have a limited bandwidth, plus parasitic capacitances always introduce extra phase.

The approach taken here to find the optimal loop gain is to measure the open-loop transfer function experimentally. This is done by shorting out R_6 and C_1, which turns U_4 into a voltage follower, applying a signal at test point 2, and measuring the relative magnitude and phase of the voltage at test point 1. The input signal must include an appropriate DC offset, needed

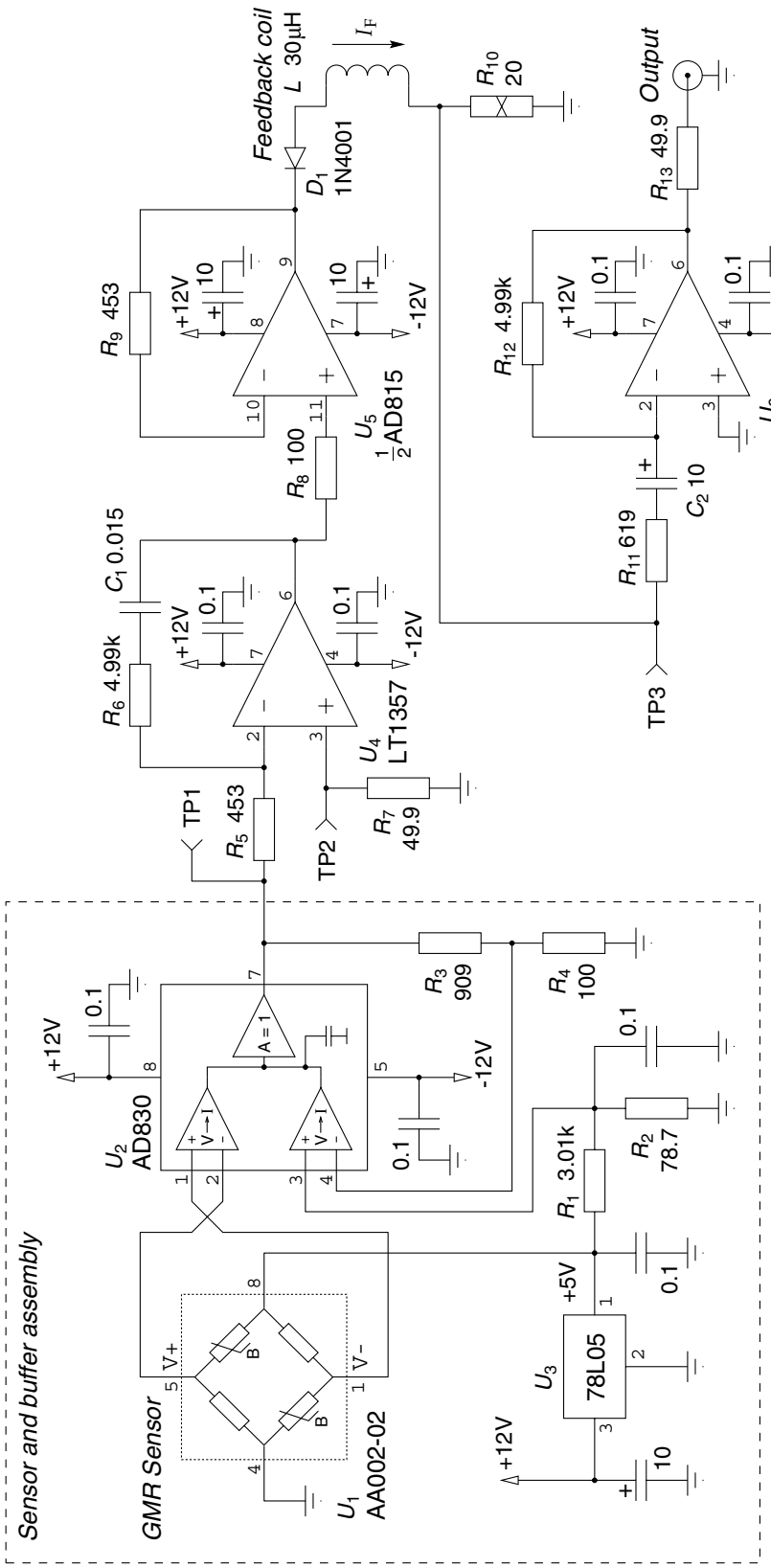

Figure 5-7: Feedback and interface circuit schematic. Resistor values are in ohms, and capacitor values are in microfarads. The components enclosed with a dashed box are mounted on a separate circuit board, located in close proximity to the GMR sensor.

for proper biasing of the GMR sensor.

As expected, the phase angle reaches -45° at about 100 kHz, the frequency of the pole. The phase angle reaches -90° at about 350 kHz, which is chosen as the loop bandwidth, allowing for plenty of phase margin, 90° [76]. This is accomplished by choosing R_6 so that the gain of the U_4 amplifier stage is equal to the inverse of the open-loop magnitude at this frequency.

The presence of C_1 in series with R_6 is useful, though not required, because it introduces a pole at $\omega = 0$ and a zero at $\omega = 1/(R_6 C_1)$, near 2 kHz. As a consequence, the feedback loop error, given by the voltage at test point 1, is zero at DC, and small at low frequencies.

5.3 Incorporating the effects of the feedback loop into the sensor model

Initially the measurement grids used in the experiments in this chapter had been generated via equation (4.49). The results were less than satisfactory, and complex two-point reference-part calibration methods, described in Appendix D, had to be employed to bring the data near the correct place in the grid, and even then the results were poor for points far from the two reference calibration points. It became apparent that there was a large unmodeled effect that had to be taken in consideration.

This unmodeled effect is the dependence of the relationship between the feedback winding current I_{F} and the magnetic flux intensity at the origin $B_z(x = 0, z = 0)$ on the material under test. The previous section assumed that the output signal I_{F}, is directly proportional to the imposed field at the origin, since the secondary winding is a solenoid tightly wound around the GMR sensor. The experiments show that that this assumption is not justified.

A different way of looking at this is that while equation (4.49) gives B_z/I_{D}, where I_{D} is the primary current, the impedance analyzer measures $I_{\mathrm{F}}/I_{\mathrm{D}}$. It is therefore necessary to develop a method of calculating B_z/I_{F} as a function of the material structure and sensor parameters.

This turns out to be a very easy task, because it can be done by applying the method of Section 4.8 directly to the special case of a single concentric winding. Thus, if the feedback coil's radius is r_{F}, and it has w_{F} turns, then the surface current density is

$$K_{\mathrm{S}}(r) = I_{\mathrm{F}} w_{\mathrm{F}} u_0(r - r_{\mathrm{F}}) \tag{5.6}$$

whose Fourier-Bessel series components, derived from equation (4.42), are

$$K_n = \frac{2 I_{\mathrm{F}} w_{\mathrm{F}}}{R^2 J_0^2(\alpha_n)} J_1(\beta_n r_{\mathrm{F}}) r_{\mathrm{F}} \tag{5.7}$$

leading to the required relationship

$$B_z(r = 0, z = 0) = I_{\mathrm{F}} w_{\mathrm{F}} \sum_{n=1}^{\infty} \frac{2}{R^2 J_0^2(\alpha_n)} \cdot \frac{1}{R_n} J_1(\beta_n r_{\mathrm{F}}) r_{\mathrm{F}} \tag{5.8}$$

Taking the ratio of equations (4.49) and (5.8) yields the expression of the complex transfer

function magnitude, measured by the impedance analyzer:

$$\frac{I_F}{I_D} = \frac{\sum_{n=1}^{\infty} \frac{2}{R^2 J_0^2(\alpha_n)} \cdot \frac{1}{R_n} \sum_{j=1}^{N} w_j J_1(\beta_n jh)\, jh}{\sum_{n=1}^{\infty} \frac{2}{R^2 J_0^2(\alpha_n)} \cdot \frac{1}{R_n} w_F J_1(\beta_n r_F) r_F} \tag{5.9}$$

The measurement grids in this chapter have been generated using equation (5.9), and normalized to the magnitude in air, so that the air point on a grid always has unity magnitude and zero phase. For all grid plots in this chapter, the normalized magnitude is the magnitude of the ratio I_F/I_D divided by the magnitude of this ratio for the magnetometer in air.

The magnitude/magnitude grid in Figure 5-10 did not acquire its characteristic spiral shape until the correction described in this section was applied to the model. The spiral curve followed by the experimental data in Section 5.5 was what first suggested the need for the change, and once applied, it significantly improved the results of all other measurements as well.

5.4 Conductivity / lift-off measurements at 12.6 kHz

The first set of measurements with the GMR magnetometer consists of conductivity/lift-off measurements with three different materials, at a range of lift-off values. The measurement grid used is generated via equation (5.9). It is shown in Figure 5-8. Since both the conductivity and the lift-off parameters vary over a relatively wide range, the parameter values for this grid are chosen on a logarithmic scale. As discussed in Section 1.4.1, the grid cell area is a measure of the sensitivity of the measurement in that region of the grid. For the grid in Figure 5-8, it should be noted that for high conductivity and lift-off values the grid cells would have been even narrower, if the parameter values had been equally spaced on a linear scale.

This pair of estimated properties is chosen because it is the most common type of measurement made with the MWM family of magnetometers and magnetometer arrays. The measurements are carried out at 12.6 kHz, which is the lowest frequency supported by the JENTEK impedance analyzer instruments, in order to illustrate the low frequency capability of this magnetometer. A simple one-point air calibration method is used for this measurement and for all other measurements in this chapter. Calibration methods and their effect on measurement error are described in Appendix D.

The lift-off is changed by placing plastic sheet shims between the sensor and the metal plates. A set of five shims, whose thicknesses are approximately related as consecutive powers of two, makes it possible to take many data points at closely spaced values of the lift-off. The results are shown in Figure 5-9 and listed in Table 5.1.

The first observation to make in Figure 5-9 is that the three data sets follow lines of constant conductivity very closely. Since the sensitivity of the measurement decreases at higher lift-off, only the first twelve out of the twenty data sets are listed in the table. The last column in the table lists the nominal values of the lift-off, calculated by adding the thicknesses of the shims used, measured with a caliper. The estimated lift-off values are in excellent agreement with the nominal values. The conductivity data in Table 5.1 are also in good agreement with the numbers reported in the literature [77, 78]. Table 5.2 lists typical values of the conductivity for the metals used in this chapter. The magnitude, nature, and source of

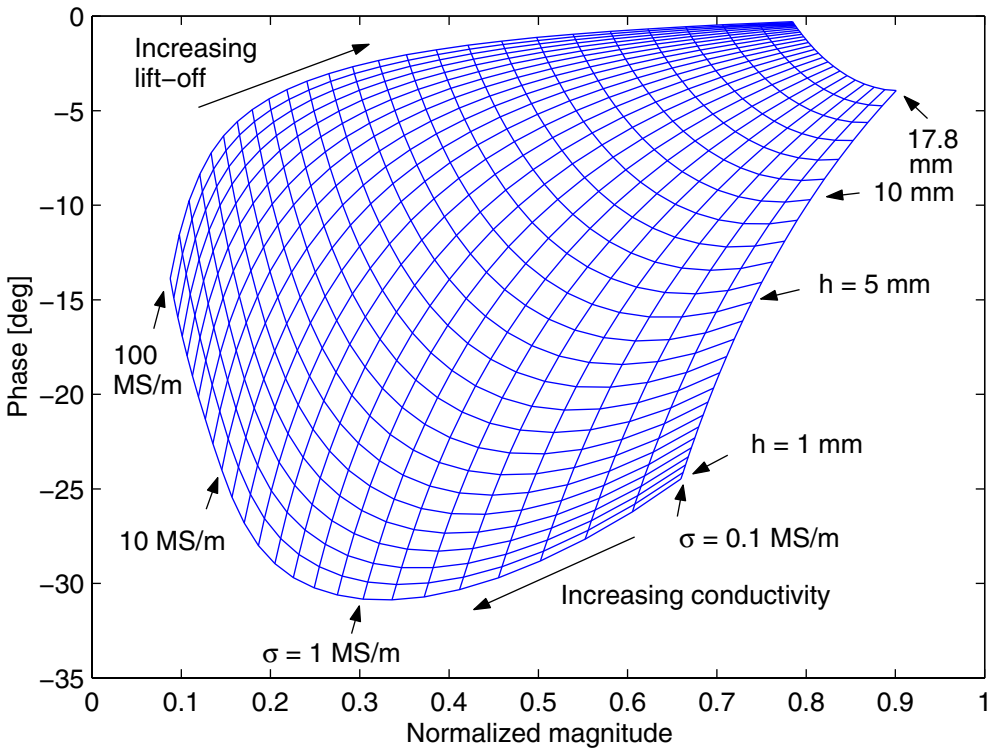

Figure 5-8: Conductivity/lift-off measurement grid for circular sensor at 12.6 kHz. The two coordinate axes are the magnitude and phase of the ratio I_F/I_D, normalized by its value in air.

the measurement errors are discussed in more detail in Appendix C.

The lowest value of the lift-off, 3.3 mm, corresponds to carrying out the measurement with no shim, and is equal to the effective depth of the windings below the surface. This amount has been added to the data in the last column, after having been estimated by taking the average of the difference between the magnetometer estimated values and the measured shim thicknesses. This number is quite reasonable, given that the average depth of the grooves is on the order of 3 mm, and that the winding thickness, about 2 mm, is not considered by the model.

As discussed in Appendix C, there appears to be an optimal range of the lift-off, 5–7 mm, where the estimated conductivity is most accurate. This is to be expected, since sensitivity to the material's conductivity is lost as it is positioned further from the sensor surface. Being too close to the sensor windings also reduces the accuracy, since the effects of the nonzero winding thickness become stronger in close proximity.

It may appear at first that there is too much spread in the conductivity data in Table 5.1. Given that this measurement was carried out with no calibration standards and with a single air calibration point, the simplicity of the model used, and the fact that no empirical data have been used to compute the grid, we consider these measurement results to be remarkably good. It has taken years of effort to improve the MWM design to the point where with one point air calibration it can produce results as accurate as these.

If it is necessary to perform a very exact conductivity measurement, then a two-point reference part calibration is recommended, with the properties of the two reference parts, or the same part at two lift-off values, closely bracketing the properties of the unknown part. A comparison of the measurement error and other performance criteria of the different calibration

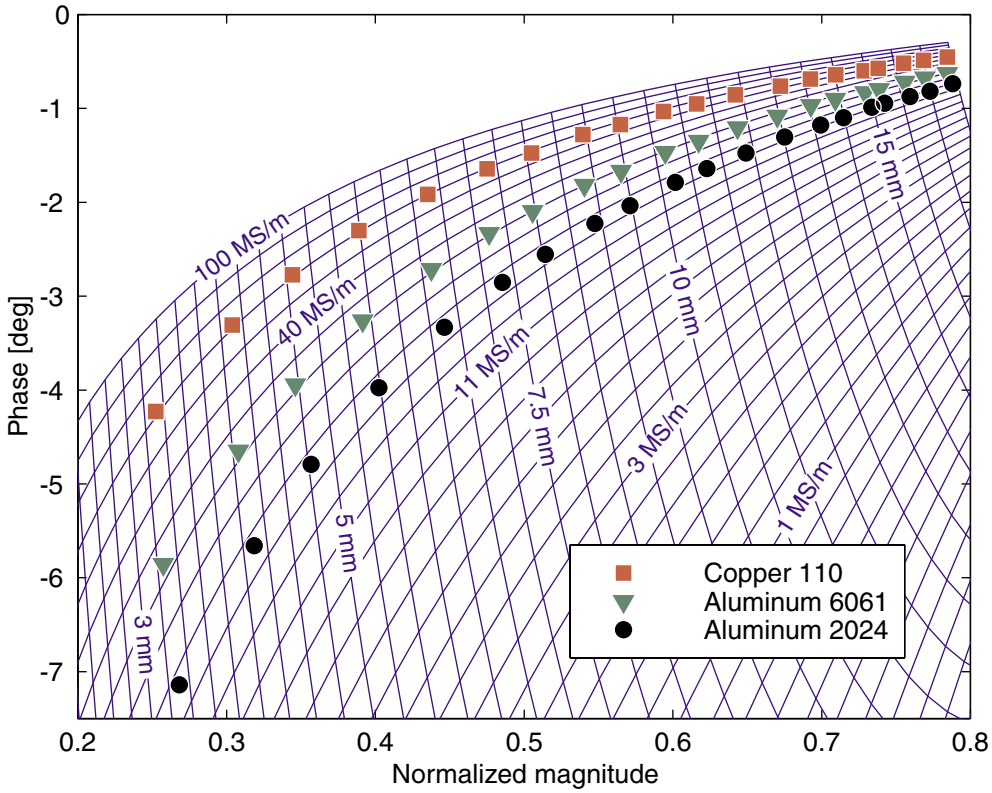

Figure 5-9: Results of conductivity/lift-off measurements with the circular magnetometer. Three sets of measurements are shown with metal plates of different conductivity, taken at a variety of lift-off positions. Each set follows a line of constant conductivity on the measurement grid, which is an expanded view of the grid in Figure 5-8.

Data set	*Cu 110*		*Al 6061*		*Al 2024*		Nominal lift-off [mm]
	Cond. [MS/m]	Lift. [mm]	Cond. [MS/m]	Lift. [mm]	Cond. [MS/m]	Lift. [mm]	
1	59.2	3.3	29.5	3.2	18.0	3.3	3.3
2	59.2	4.1	28.9	4.0	17.8	4.1	4.1
3	58.7	4.8	28.7	4.7	17.8	4.8	4.8
4	58.3	5.6	28.6	5.5	17.6	5.6	5.6
5	57.8	6.5	28.3	6.4	17.6	6.5	6.5
6	57.1	7.4	28.1	7.3	17.5	7.3	7.3
7	55.7	8.0	27.4	7.9	17.3	8.0	8.0
8	56.1	8.9	27.5	8.7	17.4	8.8	8.8
9	54.3	9.5	26.8	9.4	17.1	9.4	9.4
10	55.2	10.3	27.0	10.2	17.2	10.3	10.2
11	53.5	10.9	26.4	10.8	17.0	10.9	10.9
12	53.0	11.7	26.3	11.7	16.7	11.7	11.7

Table 5.1: Results of conductivity/lift-off measurements with the circular magnetometer, shown in Figure 5-9. Only the first twelve sets of the twenty shown in the figure are listed, due to the lack of sensitivity at higher lift-off values, as illustrated by the narrowing grid cells at the top right corner of Figure 5-9.

Material	Conductivity [MS/m]
Copper 110	58
Aluminum 6061	27.3
Aluminum 2024	17.5
Stainless steel 304	1.39

Table 5.2: Conductivity of metal alloys used in experiments. The data for aluminum alloys have been obtained from [78], and the others are from [77].

techniques are discussed in Appendix D.

The results presented in this section confirm the validity of the model developed in Chapter 4. The remaining measurements in this chapter are chosen to illustrate the unique advantages of the GMR magnetometer, by using frequencies and material thicknesses out of bounds of the standard MWM sensors.

5.5 Permeability / lift-off measurements at DC

The measurement described in this section combines the signal magnitudes of the magnetometer at two different imposed spatial wavelengths with DC excitation, to determine the magnetic permeability of a layer of known thickness and its lift-off from the sensor surface. This type of measurement is unique in three important ways: (1) no other quasistatic sensor has ever been operated in the fully static regime at DC; (2) two-wavelength magnetometry has never been tried before; and (3) the wavelength of the sensor can be changed dynamically, with the material under test still in place. These are all useful capabilities, especially in measuring magnetizable materials without the limitation caused by the skin depth effect.

With DC operation, the time-varying term in the diffusion differential equation (2.11) disappears, and the problem becomes completely parallel to dielectrometry measurements on insulating materials. All amplitudes in the model are now real numbers, and one measurement provides only one degree of freedom.

Measurements at two different spatial wavelengths are carried out by changing the polarity of the series connection of the two overlapping primary windings, whose winding patterns are determined by the A and B rows in Table 4.6. As shown in Figure 4-19, the resulting current drive profiles follow a first order Bessel function J_1, with the $r = W = 8$ cm radius corresponding to its first and second zeros respectively. In cylindrical geometry the current drive and other physical quantities are not periodic, so there is no spatial "period" or "wavelength" to speak of. In this case the radius at the first zero of the Bessel function profile is the counterpart of the spatial period in Cartesian geometry, which determines the rate of Laplacian decay in the z-direction of the fundamental spatial wavenumber mode, according to the solutions in equation (3.3). If this radius is named the effective spatial wavelength, then the long and short wavelengths are $W = 8$ cm and $W\alpha_1/\alpha_2 = 4.4$ cm.

The magnitude/magnitude measurement grid [54] used for parameter estimation is shown in Figure 5-10. As with the grid in Figure 5-8, the values of the two parameters, relative permeability and lift-off, are equally spaced on a logarithmic scale. The spiral nature of the grid, not shared by its dielectric counterpart in Figure 3-6, is due to the influence of the material under test on the feedback loop transfer function, and can only be modeled correctly if the changes in the model, described in Section 5.3, are applied. The physical explanation

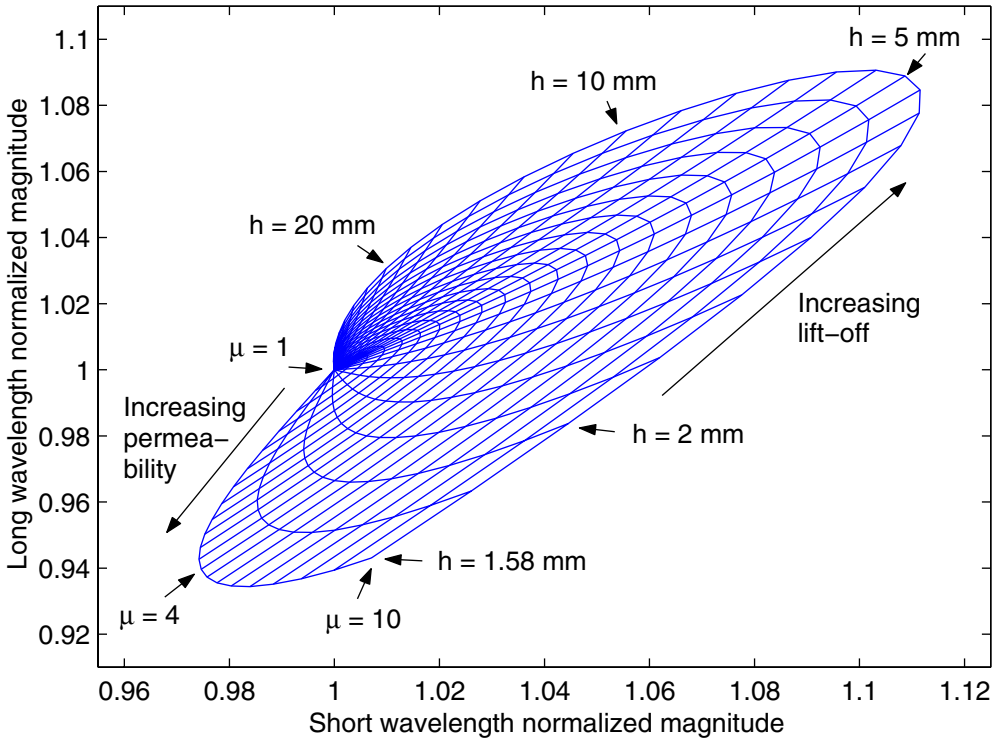

Figure 5-10: Two wavelength magnitude/magnitude permeability/lift-off grid for the circular magnetometer with DC excitation. The short and long wavelength current drive patterns are excited by appropriate connection of the two overlapping primary windings, and correspond to effective spatial wavelengths of 4.4 cm and 8 cm respectively. The thickness of the magnetizable layer is fixed at 1 mm.

of this spiral behavior is as follows: In general, as a magnetizable material is brought closer to the sensor windings, the magnitude of the signal increases, because the material tends to concentrate the magnetic flux. However, as the lift-off is reduced even further, this field concentration effect begins to affect the secondary feedback winding too, and since its radius is much smaller than the radii of the segments of the primary winding, this effect begins to dominate the overall magnetometer transfer function, bringing the magnitude back down. This effect is easy to observe in the grid in Figure 5-10.

This measurement is completely analogous to the dielectrometer measurements described in Section 3.3. Both types of measurements use the signal magnitudes at two different spatial wavelengths to estimate the dielectric permittivity or magnetic permeability of a sample with known thickness and its distance from the sensor electrodes or windings. The magnetizable layer consists of 1 mm thick polymer that contains ferromagnetic particles suspended in the polymer foam. The sensor lift-off is controlled with the same set of plastic shims as in Section 5.4. The results of the measurement are shown in Figure 5-11, and listed in Table 5.3.

The measurement procedure at DC presents some challenges. On the one hand, the only equipment necessary are a power supply and a voltmeter, making the measurement simpler. On the other hand, the accuracy of the measurement is lower than that possible with AC excitation. When operating the sensor at a certain frequency, the magnitude of this frequency component in the output signal can be measured very accurately by mixing it with a signal at the same frequency from the same source, and passing the resulting signal through a low pass filter to obtain the DC component. The signal can be integrated over many cycles, resulting

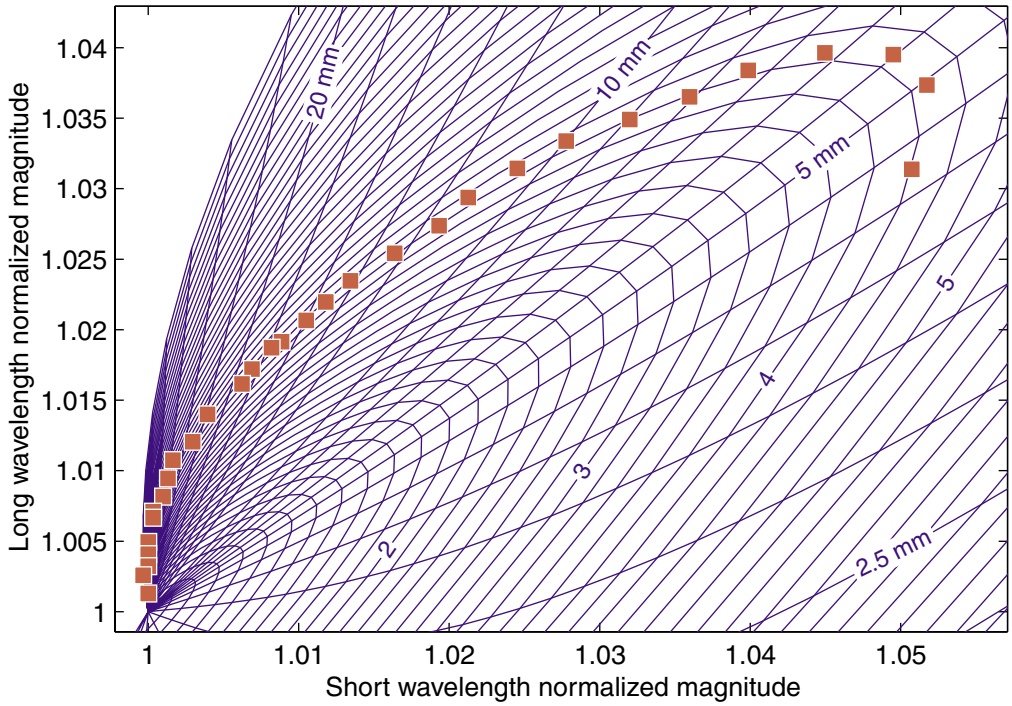

Figure 5-11: Permeability/lift-off measurement results with the circular GMR magnetometer of 1 mm thick magnetizable foam layer. The data points follow a spiral line of constant permeability. The grid is an expanded view of the grid in Figure 5-10.

Data set	Relative permeability	Lift-off [mm]	Nominal Lift-off [mm]
1	4.23	4.2	4.2
2	4.30	5.0	5.0
3	4.30	5.7	5.7
4	4.29	6.6	6.5
5	4.28	7.5	7.4
6	4.19	8.1	8.2
7	4.21	8.9	8.9
8	4.36	10.0	9.7
9	4.37	10.8	10.3
10	4.39	11.7	11.1
11	4.21	12.0	11.8
12	4.28	13.1	12.6
13	4.43	14.4	13.5
14	4.44	15.2	14.3
15	4.41	15.8	15.0
16	4.50	17.0	15.8

Table 5.3: Experiment results of the permeability/lift-off measurements at DC, shown in Figure 5-11. Only the first sixteen out of the thirty-one sets shown in the figure are listed, due to the lack of sensitivity at higher lift-off values, as illustrated by the narrowing grid cells in the lower left of Figure 5-11.

in a very accurate measurement of the transfer function at this frequency.

With DC operation this frequency mixing technique is not available. Furthermore, it is not practical to average the signal over a long time, because outside factors affecting the measurement may change during that time. For example, the output voltage of the power supply used to drive the primary winding may be not perfectly stable, and the primary current is also affected by changing contact resistance in the leads and the changing resistance of the primary winding itself, as its equilibrium temperature varies based on the thermal insulation caused by the material under test. Finally, changes in the physical position of the sensor can alter its output due to the presence of magnetically active objects in the vicinity, and as a result of changes of its position relative to the direction of the earth's magnetic field.

The approach taken in this measurement to eliminate the signal noise introduced by all these factors is to measure the sensor response in air not just once before the measurement, as is done with the other measurements in this chapter, but before every data point, with as little time in between as possible. In this way every measurement data point has its own air calibration reference. Air calibration and other calibration techniques are described in Appendix D.

Bearing in mind that in general DC data are less accurate, the results in Table 5.3 are still very good, even if the lift-off does not track its nominal value as well as the data in Section 5.4. The relative permeability of the polymer layer is measured to be about 4.3. As in the conductivity/lift-off measurements of the previous section, the measurement results are most accurate for lift-off values in the 5–7 mm range.

The data follow a constant permeability curve quite well. An interesting phenomenon that may be observed in Figure 5-11 is that at the highest lift-off values, there is a range where the magnitude of the short wavelength signal is lower than its value in air. The grid lines confirm that this effect is physical. It is due to the fact that this far from the surface the magnetizable layer is too far to intercept any magnetic field lines going through the center, but is still close enough to attract some of the field lines away from the surface. An exact dual of this effect is observed in the dielectrometer grids in the presence of a ground plane behind the material sample. This can be seen in Figure 3-6, where at the high lift-off with nonunity relative permittivity the magnitudes dip slightly below the air point.

5.6 Thickness / lift-off measurements with a multi-layer structure

Thickness/lift-off measurements most often arise in applications where it is necessary to measure the thickness of a metallic coating on a metal substrate. The multi-layer structure that needs to be modeled has at least three layers, two metal layers and an air layer, where the conductivity and magnetic permeability of the two metal layers are known. A diagram of this structure is shown in Figure 5-12. Low frequency operation, made possible by the GMR magnetometer, allows measurement of much higher coating thicknesses. The measurements described in this section illustrate this type of measurement by determining the thickness of a stainless steel layer, backed by a copper layer. The upper limit of the thickness of a stainless steel layer that can be measured at 12.6 kHz is approximately 5 mm.

The measurement grid used in this application is shown in Figure 5-13. It assumes operation at 12.6 kHz. The conductivities of stainless steel 304 and copper 110, used for generating the grid, are taken from Table 5.2. Unlike the measurement grids used in the previous two

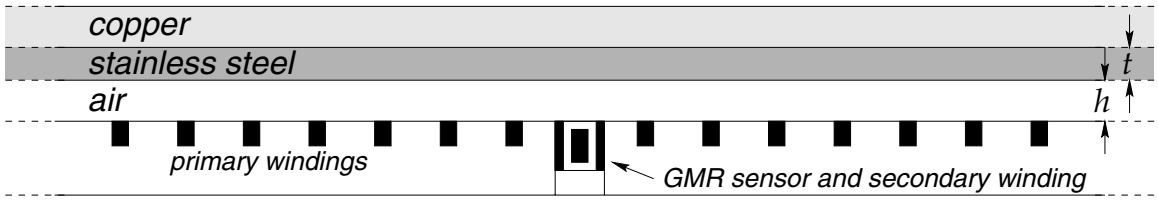

Figure 5-12: Three layer structure used in thickness/lift-off measurements. The two properties being estimated are the thickness t of the first metal layer and the thickness h of the air layer, called the lift-off. The thickness of the second metal layer is considered to be infinite, since it is much greater than the skin depth in this material.

sections, the parameter values for this grid are chosen on a linear scale.

The copper plate is 3.2 mm thick, but its thickness is modeled as being infinite, because it is several times greater than the value of the skin depth δ in copper at this frequency, 0.59 mm, calculated using equation (2.15). This is typical of coating characterization applications, where the substrate is much thicker than the depth of sensitivity of the magnetometer. In comparison, due to its much lower conductivity, the skin depth in the stainless steel layer is 3.8 mm, several times greater than that of the copper layer, and comparable to the plate thicknesses. By considering the size of the grid cells in Figure 5-13, it can be observed that the thickness measurement, but not the lift-off, loses sensitivity for thickness values below about 0.5 mm and above 5 mm. This is explained by comparing these values to the skin depth of 3.8 mm. At the lower thickness values the stainless steel layer has little influence on the magnetic fields, since its conductivity is much lower than that of the copper layer, which dominates the sensor response. At the high end of the thickness range the exponential decay of the magnetic field intensity makes the magnetometer insensitive to the position of the material interface. For these two limits the grid lines approach two constant lift-off lines of the infinite-half-space conductivity/lift-off grid in Figure 5-8, corresponding to the conductivities of copper and stainless steel. This can be confirmed visually by comparing the two grids.

Optimal sensitivity, corresponding to the biggest and most orthogonal grid cells, is achieved for thicknesses on the order of 3 mm, approximately equal to $(\pi/4)\delta$. This is to be expected, as explained in the next section, and illustrated by the curve in Figure 5-17. If the values of the thickness parameter in the grid extend past the $(\pi/2)\delta = 6$ mm point, the grid would develop a curl, also described in Section 5.7.

The thickness of the stainless steel layer in this set of measurements is changed by stacking up to four plates of various thicknesses in different combinations. As with the plastic plates used for changing the lift-off, the thicknesses of the metal sheets are chosen to allow for a wide range of possible total thickness values. Twelve sets of data are taken at each one of five different lift-off values. The results are shown in Figure 5-14 and listed in Table 5.4.

As in all other measurements in this chapter, the calibration of the sensor and equipment is done with a single point in air. Therefore any deviation of the actual material conductivities from the quoted values used for the generation of the grid would lead to errors in the estimated properties. This is particularly true at the lower thickness values, where the grid cells are very narrow. This explains the negative thickness values reported in the first row in Table 5.4, which lists data taken with no steel layer. Nevertheless, it can be seen in Figure 5-14 that these five points fall exactly on the grid edge, as they should. If an application requires better accuracy at such low thickness values, a two-point calibration method, including calibration on the copper layer, would eliminate the effect of any disparity between the conductivity value used in generating the grid and the actual conductivity of the part. Also, higher frequency

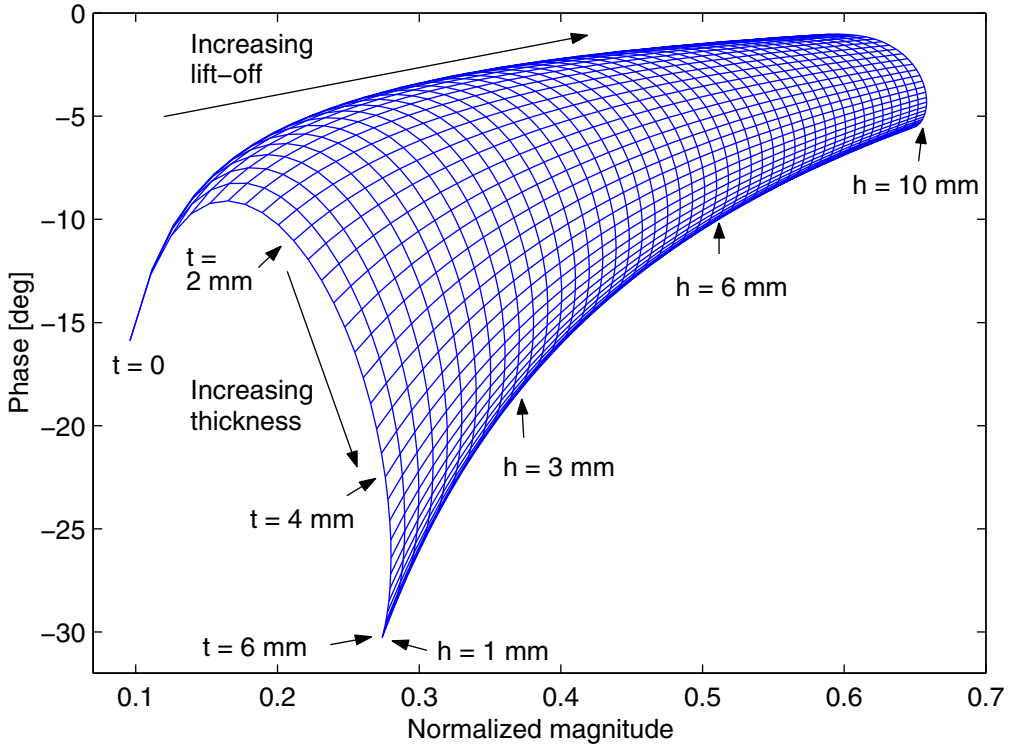

Figure 5-13: Thickness/lift-off measurement grid for the circular magnetometer at 12.6 kHz. The thickness is of a stainless steel layer on an infinitely thick copper substrate.

would improve sensitivity to thinner coatings by reducing the skin depth. The choice not to take this approach here is made in order to emphasize the high level of agreement between the simulated and measured results, as evidenced in the rest of the table, by avoiding the use of empirical measurements with a calibration standard.

The excellent agreement between the nominal and estimated values of the thickness and lift-off in Table 5.4 is further confirmation of the validity of the analytical model, applied to a more complex material structure that incorporates more than one conducting metal layer.

5.7 Low frequency (100 Hz) thickness measurements

This section describes another type of measurement, not possible with previous magnetometers, namely thickness measurement of quarter inch or thicker aluminum plates. In order to make the skin depth large enough, the magnetometer is operated at 100 Hz, which yields a skin depth of 9.5 mm for the more conducting aluminum alloy 6061 tested.

One important application of this type of measurement is in corrosion mapping, where the side that experiences corrosion is not accessible for direct measurement. Since the other material property being measured is conductivity, an area scan of this type simultaneously detects cracks and other flaws in the metal, as illustrated in the next section.

The conductivity/thickness grid used in this set of measurements is shown in Figure 5-15. Unlike all other grids considered, this one does not have lift-off as one of the two estimated parameters. The lift-off is assumed to be known and equal to 3.3 mm, the intrinsic magnetometer value obtained from the measurements in Section 5.4. There are two reasons why

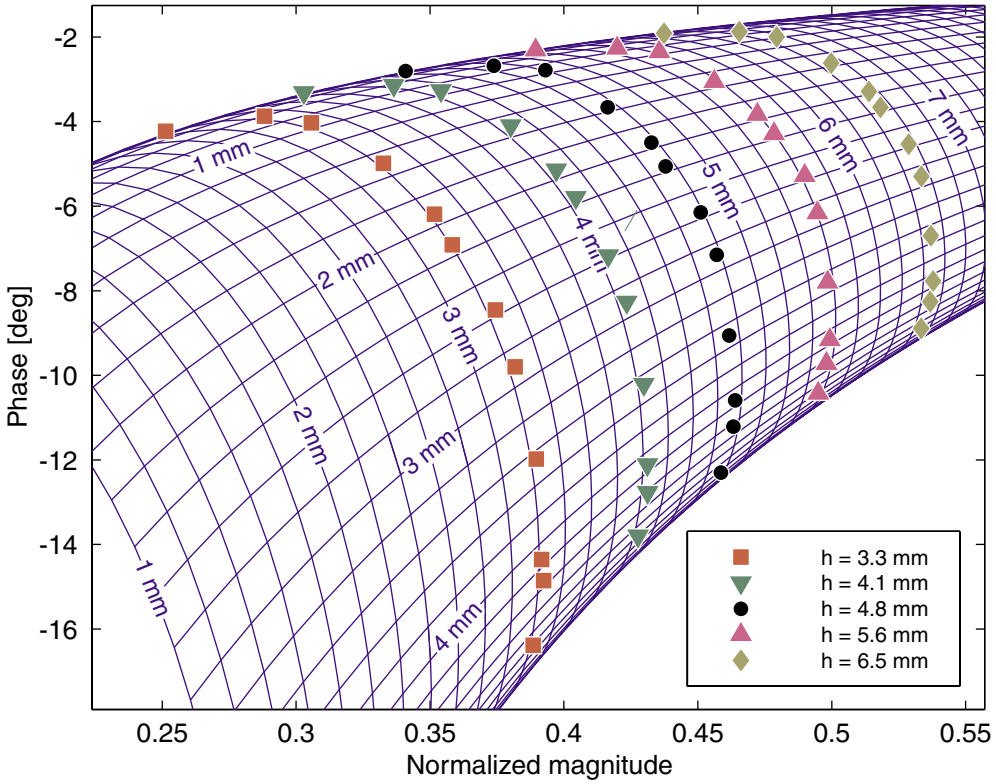

Figure 5-14: Stainless steel layer thickness measurements at five different lift-offs. Each data set follows a line of constant lift-off. The data are listed in Table 5.4.

Data	$h = 3.3$ mm		$h = 4.1$ mm		$h = 4.8$ mm		$h = 5.6$ mm		$h = 6.5$ mm		Nominal
set	Thk.	Lift.	Thk.	Lift.	Thk.	Lift.	Thk.	Lift.	Thk.	Lift.	thickness
1	−0.33	3.57	−0.33	4.40	−0.33	5.05	0.02	5.60	0.24	6.33	0.00
2	0.61	3.26	0.63	4.06	0.63	4.72	0.71	5.54	0.69	6.49	0.60
3	0.92	3.26	0.93	4.09	0.94	4.81	0.94	5.64	0.97	6.54	0.96
4	1.49	3.23	1.50	4.08	1.56	4.73	1.53	5.57	1.55	6.51	1.50
5	1.93	3.23	1.94	4.07	1.95	4.76	1.95	5.60	1.97	6.53	1.89
6	2.14	3.21	2.16	4.06	2.16	4.73	2.15	5.60	2.16	6.51	2.10
7	2.57	3.25	2.58	4.06	2.56	4.78	2.56	5.63	2.57	6.54	2.49
8	2.90	3.24	2.90	4.06	2.88	4.77	2.89	5.60	2.90	6.53	2.85
9	3.45	3.24	3.47	4.05	3.50	4.72	3.50	5.55	3.52	6.49	3.39
10	4.13	3.22	4.12	4.04	4.13	4.75	4.13	5.55	4.10	6.50	3.99
11	4.33	3.24	4.43	4.06	4.46	4.75	4.46	5.55	4.44	6.49	4.35
12	5.03	3.23	5.01	4.05	5.30	4.76	5.04	5.55	5.04	6.49	4.95

Table 5.4: Stainless steel layer thickness estimation results for various lift-offs h. Each of the five sets of twelve measurements is taken at a different value of the lift-off.

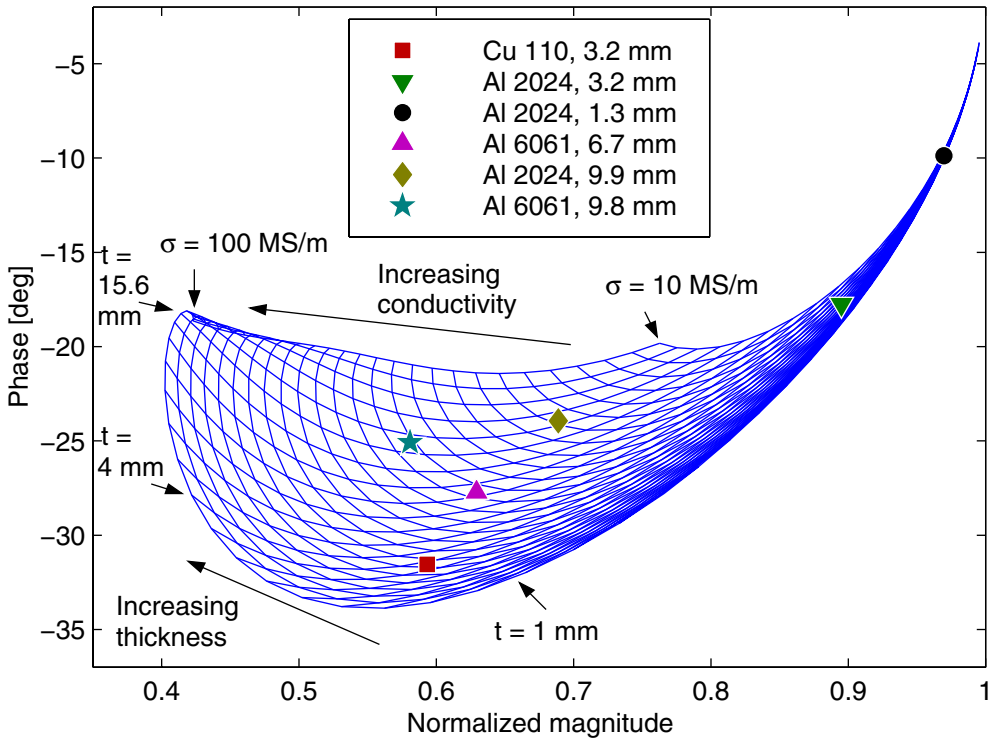

Figure 5-15: Low frequency (100 Hz) conductivity/thickness measurement grid and results for six different metal plates. The data are listed in Table 5.5. The grid is built assuming a constant lift-off of 3.3 mm.

lift-off is almost always one of the unknown properties to be estimated in magnetometer measurements: (1) at the lower thickness scales typical of MWM sensors dust particles and surface roughness make a non-negligible contribution to the lift-off; and (2) grids including lift-off have more closely "orthogonal" cells, and thus better selectivity, as other material properties are less independent of each other when they enter the model. The relatively large minimum lift-off value for this sensor reduces the importance of the first consideration. The second one still remains an issue, as can be observed in the upper right corner of Figure 5-15, where the grid cells collapse and approach zero area, as their edges become almost parallel to each other, making it impossible to measure conductivity and thickness independently. Grid look-ups in such an area of the grid are naturally unreliable. Nonetheless, there is a large region of the grid where the two unknown properties are sufficiently independent of each other.

Another interesting property displayed by this grid is that near the upper left corner lines of constant conductivity form spirals, as they approach the limiting point, which corresponds to infinite thickness. As a result the grid folds in on itself, sometimes several times for a large enough range of thicknesses. This means that for certain values of the complex sensor magnitude there can be two or more solutions, all physically valid. Expanded views of this region of the grid are shown in Figure 5-16.

This kind of behavior can be manifested by magnetometer grids where one of the unknown parameters is the thickness of a metal layer [13]. This is caused by the fact that in the presence of magnetic diffusion, the exponent γ of the z-dependent term is a complex number, as shown in equation (2.14). If the decay is dominated by the skin depth, as is the case here, the real and imaginary components of γ are approximately equal. The resulting exponential decay is shown in Figure 5-17, which is a plot of $\Re\{e^{-(1+i)z/\delta}\} = e^{-z/\delta}\cos(z/\delta)$.

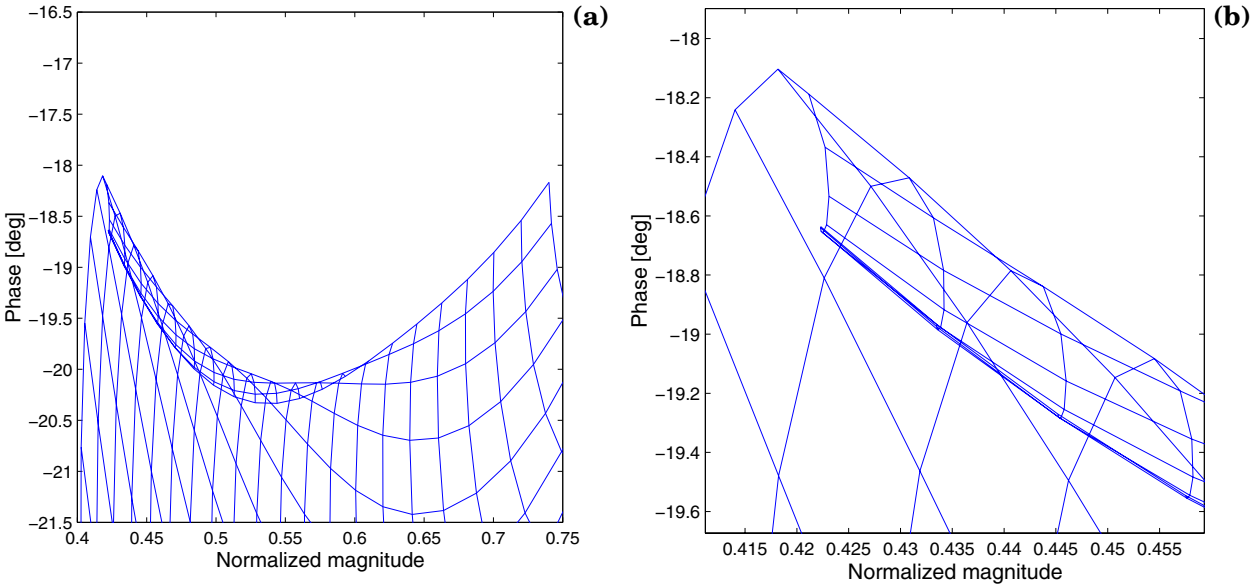

Figure 5-16: Expanded views of the upper left corner of the grid in Figure 5-15, showing the curl in the grid.

Due to the imaginary part of the exponent, the phase of the induced eddy currents changes with depth, so that the effect of the missing tail of the exponent, due to the finite width of the layer, can alternatively enhance or reduce the fields at the secondary sensor, leading to the spiral grid effect. Exactly the same phenomenon is responsible for the sign reversal of the crack signature in Figure 5-22 in the next section, compared to the other two scans taken at shallower depths.

Since 100 Hz is outside the range of frequencies available with the JENTEK impedance analyzer equipment, an HP 4263A instrument is used to carry out measurements shown in Figure 5-15 and Table 5.5. This has certain disadvantages, because the JENTEK software environment provides some useful features, such as data averaging, filtering, and real time grid look-up, unavailable here.

The data in Table 5.5 are in good agreement with the conductivity values in Table 5.2 and the nominal thicknesses, measured with a caliper. One notable exception is the 1.3 mm thick aluminum plate. It is simply out of the range of sensitivity for this measurement. This can be seen visually in Figure 5-15, with this point falling in a very narrow region of the grid.

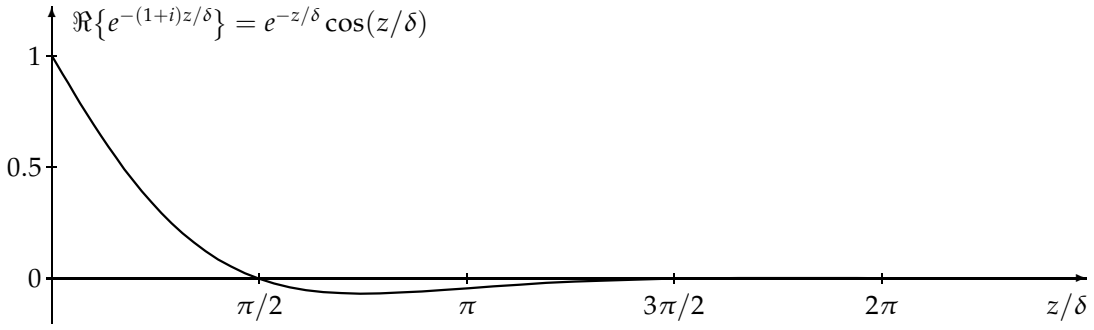

Figure 5-17: A plot of the real part of complex exponential decay, characteristic of magnetic diffusion.

Data set	Material	Nominal thickness [mm]	Measured conductivity [MS/m]	Measured thickness [mm]
1	Cu 110	3.2	56.2	3.39
2	Al 2024	3.2	17.5	3.34
3	Al 2024	1.3	12.5	2.19
4	Al 6061	6.7	29.1	6.53
5	Al 2024	9.9	17.1	10.38
6	Al 6061	9.8	28.1	9.52

Table 5.5: Low frequency (100 Hz) conductivity/thickness measurement results for six metal plates.

Given how narrow the grid is at this point, and that only one point air calibration is used, it is fortunate that the point does not fall outside of the grid. Similarly, given that the Al 2024 3.2 mm point is also in a very narrow region, it is surprising that the values estimated for this case are as good as they are. This loss of sensitivity for metal layers with thicknesses much less than the skin depth is exactly analogous to the measurement of thin coatings in Section 5.6.

5.8 Crack detection through 1/4 inch stainless steel plate

The last set of experiments with the prototype GMR sensor magnetometer illustrate its ability to detect material flaws hidden behind a thick layer of metal. They are carried out by performing area scans of a set of stainless steel plates, into one of which a one inch long slot has been milled out to simulate a crack. The geometry of the plate and slot are shown in Figure 5-18.

The grid used for this measurement is the conductivity/lift-off grid in Figure 5-8. The crack is not modeled explicitly, but its presence is usually manifested by a local reduction in the value of the measured effective conductivity. In some cases, depending on its depth and

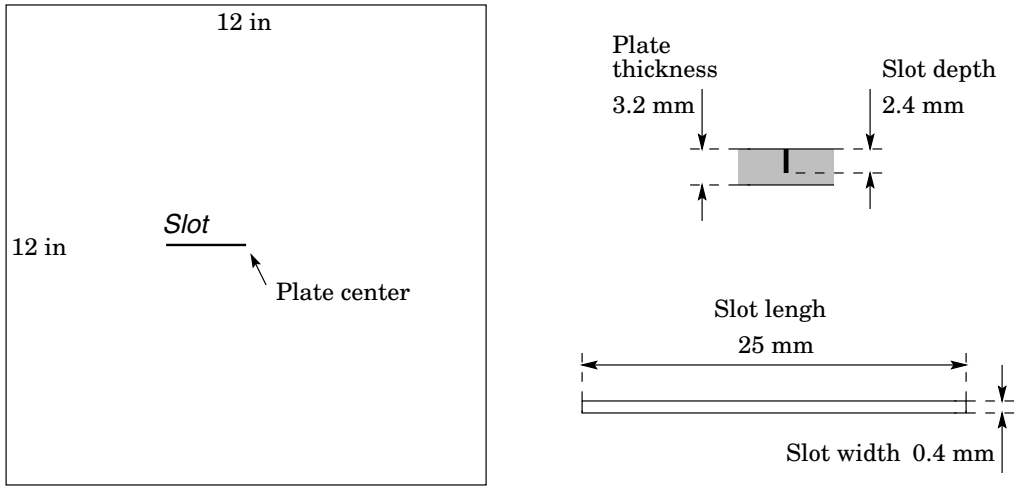

Figure 5-18: Geometry of stainless steel plate with a slot simulating a crack.

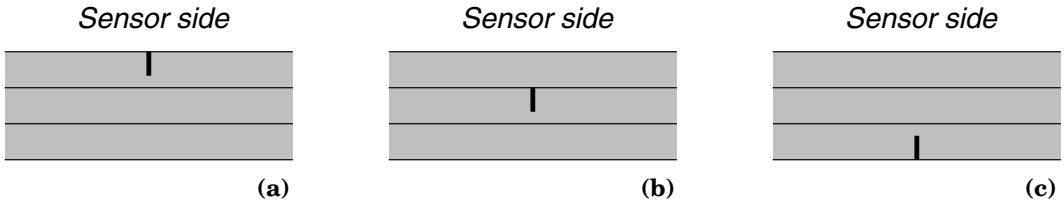

Figure 5-19: Stainless steel plate configuration for three area scans. The three arrangements position the simulated crack at the upper surface **(a)**, 3.2 mm below the upper surface **(b)**, and 7.2 mm below the upper surface **(c)**.

position below the surface, it may appear as a local change in the lift-off, as explained later in this section.

The scans are carried out by attaching a linear encoder to the magnetometer base, and sliding it down the length of the plates, using a ruler as a guide. The instrument takes data continuously and records it together with the encoder position. The position of the ruler is changed in small increments in the x-direction, for a total of thirty-nine linear scans, combined into one two-dimensional area scan. The number of points in the y-direction is typically between 500 and 1000 and the data are processed in a way that averages and interpolates the points, giving a value for every 0.1 inch increment in the y-direction. The excitation frequency is 12.6 kHz.

Due to the relatively large diameter of the magnetometer, $\approx 11''$, relative to the plates' dimensions, $12'' \times 12''$, the area scanned is limited to less than $6'' \times 6''$. Even so, near the edges of the scan area some of the sensor windings fall past the end of the plates. The magnetometer always has its inner windings, contained in a circle with radius equal to $W = 8$ cm, corresponding to the first zero of the Bessel function current distribution, over the metal plates.

Three scans are taken, with the stainless steel plates arranged as shown in Figure 5-19. The image generated by the first scan, with the slot at the surface, is shown in Figure 5-20. The image shows the conductivity, normalized by its value far away from the crack, by assigning color according to the scale shown on the right side of the figure. The crack signal is very strong, with the effective conductivity decreasing more than 3% near the crack position.

The double hump signature of the crack is characteristic of the effect cracks have on the signal of spatially periodic magnetometers. The crack alters the magnetic fields by causing an interruption in the path of the eddy currents induced in the metal. The induced current density tends to mirror the current density of the drive, and as a consequence the disruption caused by the crack is greatest when it is directly below the primary winding nearest to the sensing element, and is oriented perpendicular to the direction of the current. This explains the nature of the signature seen in Figure 5-20.

The image generated with the crack positioned 3.2 mm below the surface is shown in Figure 5-21. The change of the effective conductivity is approximately 2.5% in this case.

The most important area scan is done with the crack 7.2 mm below the surface. The image is shown in Figure 5-22. In this case the conductivity change is less than 0.5%, which is barely greater than the noise level with this setup. This is to be expected, since the skin depth of the stainless steel at the excitation frequency is 3.8 mm, calculated earlier in Section 5.6. The quality of the image at this depth can be improved by measuring at a lower frequency, with the skin depth becoming correspondingly larger. This experiment confirms that this type of magnetometer can detect deeply buried cracks by operating at sufficiently low frequency.

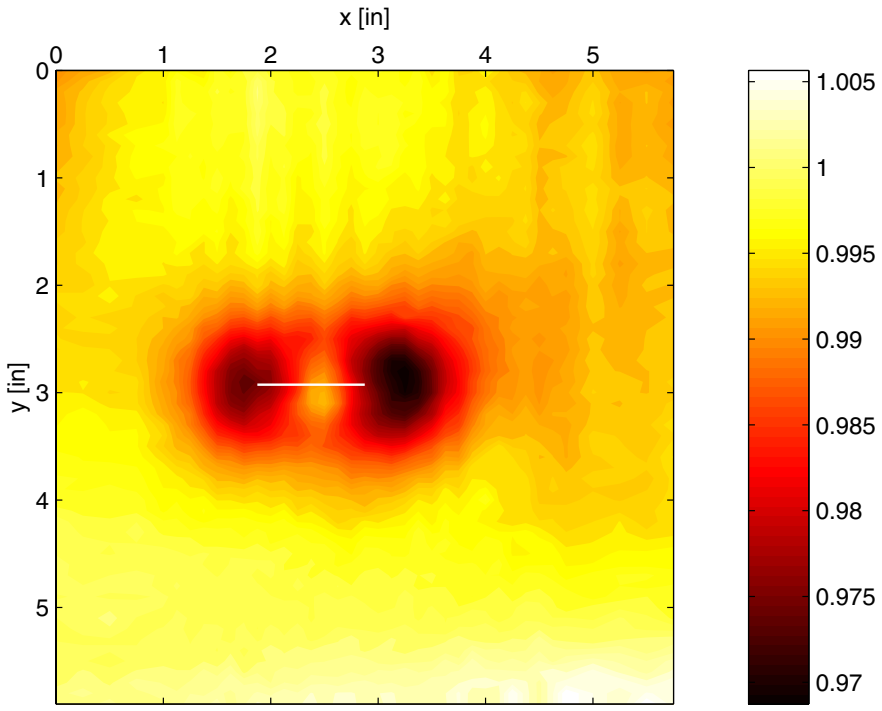

Figure 5-20: Area scan of stainless steel plate with the crack at the surface. The position of the crack is indicated with a white line. The color in the image represents the value of the conductivity, normalized by its average value far away from the crack, according to the scale on the right side of the figure.

It is important to understand that the depth of sensitivity to flaws cannot be extended indefinitely by making the frequency of excitation arbitrarily low. There are two factors that contribute to the eventual loss of sensitivity at lower frequencies. The first one is that since the flaws affect the measurement by altering the eddy current path, and are thus manifested as a change in the effective conductivity, if the frequency is lowered to the point where the Laplacian decay term in equation (2.14) begins to dominate, the measurement loses sensitivity to the presence of the flaw and to the conductivity in general. The second factor is that as the skin depth becomes larger, in order to reach a flaw buried deeper, the flaw's signature becomes more diluted by the averaging of the conductivity over a greater volume of metal. Consequently, the size of the smallest crack that can be detected increases. Nevertheless, since the GMR sensor overcomes the previously described loss of sensitivity experienced by standard eddy current sensors at low frequencies, the depth of sensitivity is much greater than what can be achieved with the MWM and other magnetometers, as confirmed by the data in this section.

An interesting feature to be observed in Figure 5-22 is that the effective conductivity change is in the opposite direction, i.e. near the crack the measured effective conductivity is actually higher. The cause of this effect is the same as what causes the grid in Figure 5-15 to curl in. As illustrated in Figure 5-17, the phase of the induced eddy currents changes with depth. With the crack positioned 7.2 mm below the surface, which is 0.6π skin depths into the metal, falling in the negative region in Figure 5-17, it interrupts eddy currents that are flowing in a direction opposite to the surface eddy currents, thereby increasing the magnetic flux at the sensor. This reversal of the eddy current direction and associated magnetic field

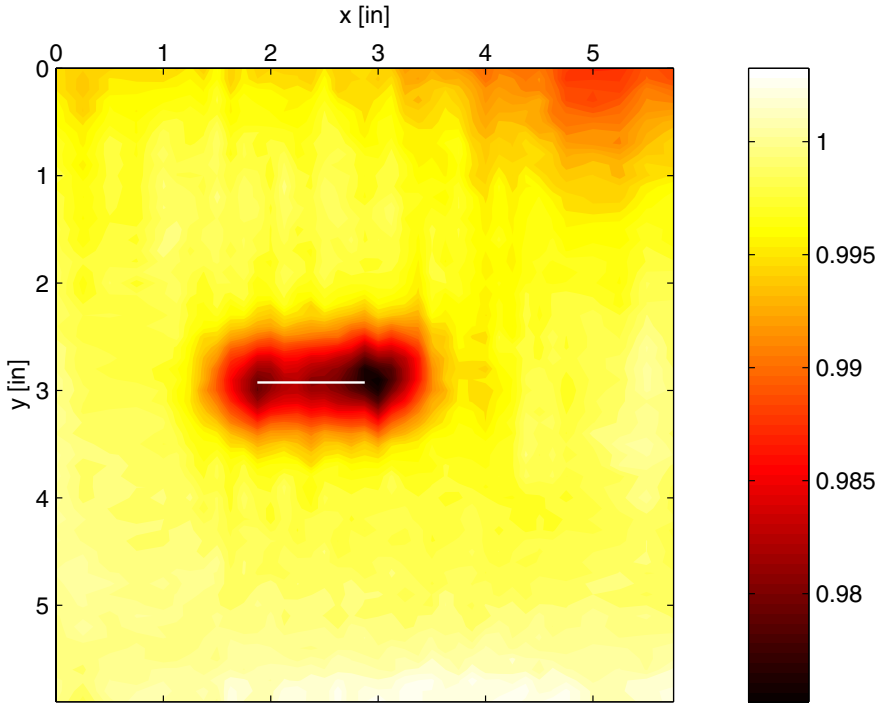

Figure 5-21: Area scan of stainless steel plate with the crack 3.2 mm below the surface. The position of the crack is indicated with a white line.

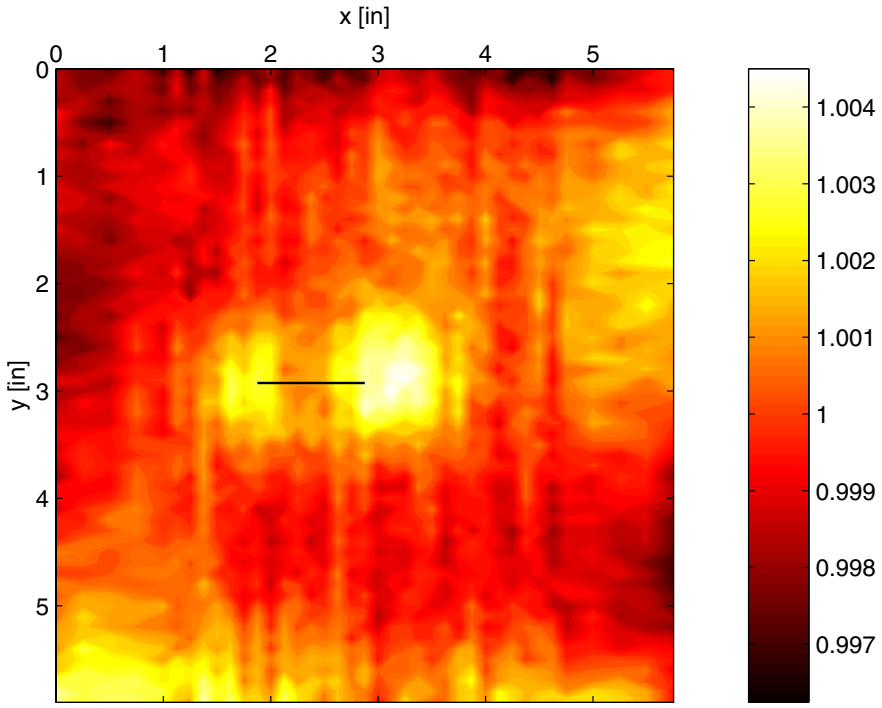

Figure 5-22: Area scan of stainless steel plate with the crack 7.2 mm below the surface. The position of the crack is indicated with a black line. Because of the change in phase of the induced current, at this depth the polarity of the crack signature is reversed.

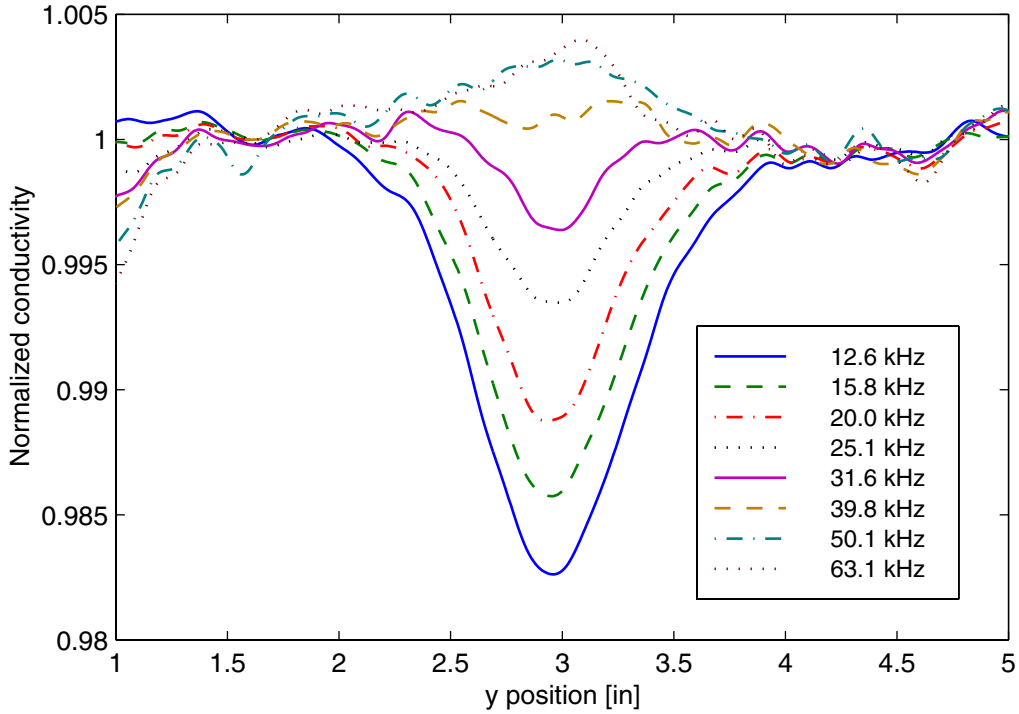

Figure 5-23: Linear scan of simulated crack taken at multiple frequencies. The slot is 3.2 mm below the surface, according to Figure 5-19 (b). The motion is in the y-direction, with the slot oriented perpendicular to the scan direction at a position just before the 3 inch point. The x-position of the scan corresponds to the right end point of the slot in Figure 5-20. The conductivity is normalized by its value far away from the slot. As the frequency of excitation is increased, decreasing the skin depth, the polarity of the crack signature is reversed.

can also be observed in Figure 4-16 (b), where the magnetic field lines reverse direction deeper into the metal.

An interesting consequence of this effect is that there is a characteristic depth, near $\pi/2$ skin depths, where a crack causes no change in the effective conductivity. Figure 5-23 shows one of the constitutive linear scans used to generate the area scan in Figure 5-21, taken at eight different frequencies, with the slot 3.2 mm below the surface. It can be seen that at 40 kHz the crack cannot be detected. At this frequency the skin depth is 2.1 mm, so that the slot extends from $1.5\,\delta$ to $2.6\,\delta$ in the z-direction, and it straddles the $\pi/2$ point in Figure 5-17 in just the right proportion to cancel out its effect on the measured effective conductivity. As expected, at higher frequencies and corresponding lower skin depths the polarity on the signature is reversed.

To avoid the risk of missing a flaw in this way, it is common practice to test at more than one frequency. In addition, while the real part of the exponent may average out to zero, the imaginary component in that case does not, and consequently the crack signature is present in a plot of the effective lift-off. This is also evident in the grid in Figure 5-15, where a constant conductivity line may change its direction along a spiral, but never crosses itself.

5.9 Magnetic permeability measurements of ferromagnetic fluids

The circular magnetometer is also used to measure the magnetic permeability of a set of samples of different ferrofluids. Ferromagnetic fluids, or ferrofluids, are highly paramagnetic materials synthesized by introducing a colloidal suspension of permanently magnetized single domain particles, typically magnetite, of order 10 nm diameter in a carrier fluid [79, 80] [49, §12.2.4]. A surfactant, such as oleic acid, is needed to keep the particles from agglomerating from attractive magnetic and van der Waals forces, by using steric repulsion with a molecular monolayer coating around each particle. Typical ferrofluids can thus remain gravitationally and magnetically stable indefinitely. The particle density of a typical ferrofluid is on the order of 10^{23} m^{-3}.

Since ferrofluids are typically electrical insulators, in the absence of other materials the phase of the magnetometer transfer function is zero. The imaginary component μ'' of the complex magnetic permeability μ^* is defined by

$$\mu^* = \mu' - i\mu'' \tag{5.10}$$

The imaginary component μ'' reflects energy loss due to magnetization. At excitation frequencies of several megahertz or higher, μ'' can become significant, in which case the magnetometer phase is not zero, and the information contained in it can be used to estimate its value. Typical power loss mechanisms are associated with the change in magnetization direction due to particle rotation in the carrier liquid, called Brownian relaxation, or by rotation of the magnetization within the particle, called Néel relaxation.

Neither one of these processes can be observed with the magnetometer used in this set of experiments, because it is not designed to be operated at the high frequency range needed to observe the loss spectrum of the fluids. Whatever contribution to the phase the imaginary component of the permeability may have is overwhelmed by the parasitic phase shift due to the self-capacitance of the primary winding. Consequently, at a given excitation spatial wavelength only one degree of freedom is available, making it possible to estimate only one unknown parameter. Unlike measurements on conducting media, operation at different frequencies does not provide independent information, which is also the case with dielectrometer measurements.

The type of measurement carried out with the ferromagnetic fluids estimates their magnetic permeability, assuming that the lift-off and the thickness of the magnetic layer are known. The thickness is calculated by dividing the measured volume of fluid by the surface area of the flat-bottomed glass vessel used to contain the liquid during measurement. The lift-off is the sum of the intrinsic lift-off of the sensor and the thickness of the bottom of the glass container. It is best to measure this lift-off experimentally, using the conductivity/lift-off method described in Section 5.4, with several thick sheets of copper positioned at the bottom of the glass beaker. In this way any nonuniformity in the lift-off due to glass thickness variation and/or curvature is absorbed into a single average effective lift-off value.

The results of measurements with six ferrofluid samples are shown in Table 5.6. The inner diameter of the circular beaker is 18.5 cm, corresponding to a surface area of 269 cm^2. The first four tests use 50 cm^3 fluid samples, yielding a layer thickness of $t = 1.87$ mm. The volume in sets 5 and 6 is increased by 50 and 100 cm^3 respectively, by adding water to the water-based fluid in set 4, yielding layer thicknesses of 3.74 mm and 5.61 mm. The measured

Data set	Type of ferrofluid	Saturation magnetization	Measured relative permeability μ_r
	Ferrofluidics Corporation Isopar-m (similar to kerosene) ferrofluids		
1	Lot no. 1634	400 Gauss	1.95
2	NF 1848	400 Gauss	1.62
3	NF 1680	250 Gauss	1.26
	Georgia Pacific Lignosite water-based ferromagnetic liquid		
4	Concentrated	150 Gauss	1.39
5	Diluted with one part water	75 Gauss	1.22
6	Diluted with two parts water	50 Gauss	1.18

Table 5.6: Measured ferrofluid magnetic permeability. This is a single unknown measurement at 12.6 kHz. The thickness of the fluid and the lift-off are known and included in the generation of the measurement grid.

average lift-off value is $h = 6.5$ mm. The measurements are carried out at 12.6 kHz.

For a given type and size of ferromagnetic particles, the magnetic susceptibility χ_m in a ferrofluid is expected to be proportional to the density of the particles. The permeability is expressed in terms of the susceptibility as

$$\mu = \mu_0 \mu_r = \mu_0 (1 + \chi_m) \tag{5.11}$$

Therefore the susceptibilities of the three different concentrations of water-based ferrofluid, given as sets 4, 5, and 6 in Table 5.6, should be expected to be related in proportion as $1 : 1/2 : 1/3$. The actual measured susceptibility values are 0.39, 0.22, and 0.18, in the ratio $1 : 0.56 : 0.46$. Thus the diluted samples have susceptibilities higher than expected. This is due to the fact that when water is added to the vessel, even after stirring, the concentration of ferromagnetic particles remains higher closer to the bottom, resulting in property averaging biased toward overestimating the permeability, since the exponential magnetic field profile places higher weight on the properties of material closest to the sensor.

In principle, the magnitudes of two fundamental wavelength modes can be combined to estimate two unknown properties simultaneously, as described in Section 5.5. For the measurements in this section, given that both the thickness and lift-off are known and well controlled, better accuracy of the permeability measurement is achieved by limiting the estimation process to a single unknown property.

5.10 Summary of Chapter 5

This chapter has described a magnetometer that incorporates all of the new ideas in its design: a giant magnetoresistive secondary element, a distributed primary winding, and cylindrical geometry. The correct treatment and analysis of all of these features is necessary for the successful operation of the new magnetometer, along with the improvements in grid look-up methods that are described in Section 6.2.

A solution has been found for the problems that result from the highly nonlinear and limited response of the GMR sensor, which is to place it in a feedback loop with a secondary

winding (Section 5.2). The transfer characteristics of the loop also depend on the material under test, and this has made it necessary to expand the distributed current drive model, developed in Chapter 4, to incorporate these effects (Section 5.3). Having addressed all of these issues, the magnetometer has been tested in a range of applications:

1. Conductivity/lift-off measurements on nonmagnetic metals (Section 5.4).
2. Two-wavelength permeability/lift-off measurements on magnetizable nonconducting materials (Section 5.5).
3. Thickness/lift-off measurements for a metal layer in a two-metal test structure (Section 5.6).
4. Thickness/conductivity measurements for thick metal plates at ultralow frequency and high skin depth (Section 5.7).
5. Detection of cracks buried beneath a thick layer of metal (Section 5.8).
6. Magnetic permeability measurements of ferromagnetic fluids (Section 5.9).

All of these are absolute property measurements that have been performed using a one-point air calibration method, i.e. without the use of calibration standards. The excellent agreement between the property values obtained with the magnetometer and data from other sources demonstrates the success of the most important new contribution to existing NDE technology, which is the ability to perform low-frequency deep-penetration absolute property measurements without the need for calibration standards.

Chapter 6

Further Extensions of the Sensor Models

Each of the two sections in this chapter is an extension of the semi-analytical models described in previous chapters. Section 6.1 introduces motion to the model of the MWM sensor, which can be useful in scanning applications at low frequencies and high scanning speeds, if the distance traveled by the sensor in one temporal cycle period is not negligible compared to the effective spatial wavelength. Section 6.2 describes improvements to the grid look-up and inverse interpolation methods.

6.1 Mathematical model of the MWM sensor in the presence of convection

In order to scan a material for flaws, a sensor array can be moved so that the one-dimensional property profile, provided by the row of sensing elements, can be used to generate a two-dimensional image. Most often the time interval determined by the scanning speed and the characteristic length scale of the sensor is much greater than the time period of the imposed AC field, and in this case the effects of the motion become negligible.

However, as the excitation frequency is lowered, in order to overcome the depth of penetration limitation due to the skin depth effect, it may become important to incorporate sensor motion into the mathematical models. This section shows the changes to the model of Section 2.1 that result from convection, and shows the results of simulations based on this modified model.

6.1.1 Changes to the diffusion equation

The most convenient way of incorporating motion in magnetoquasistatic systems is to replace $\mathbf{E}$ by $\mathbf{E} + \mathbf{v} \times \mathbf{B}$ [49, 50], so that the current density is written as

$$\mathbf{J} = \sigma\big(\mathbf{E} + \mathbf{v} \times \mathbf{B}\big) \tag{6.1}$$

and equation (2.6) becomes

$$\nabla \times \mathbf{H} = -\sigma\big(i\omega\mathbf{A} + \nabla\Phi - \mathbf{v} \times \mathbf{B}\big) \tag{6.2}$$

Using the same gauge condition in equation (2.10) and the other manipulations in Section 2.1.1, equation (6.2) leads to the following equation for the magnetic vector potential:

$$\nabla^2\mathbf{A} = i\omega\sigma\mu\mathbf{A} - \sigma\mu\mathbf{v}\times\big(\nabla\times\mathbf{A}\big) = i\omega\sigma\mu\mathbf{A} + \sigma\mu\big(\mathbf{v}\cdot\nabla\big)\mathbf{A} \tag{6.3}$$

As before, current flows only in the y-direction, and all quantities are independent of y, so that the y-component of the velocity has no effect on the sensor response. The velocity can thus be assumed to be only in the x-direction. Consequently

$$\mathbf{A} = A_y(x,z)\hat{\mathbf{y}} \qquad\qquad \mathbf{v} = u\hat{\mathbf{x}} \tag{6.4}$$

and the partial differential equation for A_y becomes

$$\frac{\partial^2}{\partial x^2}A_y + \frac{\partial^2}{\partial z^2}A_y = i\omega\sigma\mu A_y + \sigma\mu u\frac{\partial}{\partial x}A_y \tag{6.5}$$

As will be discussed in more detail later in this section, the presence of convection breaks the symmetry that allows the solutions of equation (6.5) to be written only in terms of cosines, as was done in Section 2.1. The full exponential form must be used here:

$$A_y = A_0 e^{-ikx}e^{\pm\gamma z} \tag{6.6}$$

The sign of k in the exponent is arbitrary, because both positive and negative spatial wavenumbers will be considered. After substitution in equation (6.5), equation (6.6) leads to the following constraint on γ:

$$\gamma = \sqrt{k^2 + i\sigma\mu(\omega - uk)} \tag{6.7}$$

Comparing equation (6.7) to equation (2.14) shows that the way convection enters the collocation point model is that if a homogeneous layer is moving with a velocity u with respect to the sensor, and it is possible for each layer to have a different velocity, then the frequency ω in that layer is replaced with $\omega - uk$, analogous to induction motors. As a consequence,

$$\gamma_n \neq \gamma_{-n} \tag{6.8}$$

which means that positive and negative wavenumber modes must be considered separately, and the full exponential form of the Fourier series must be retained.

The magnetometer geometry is shown in Figure 2-1. All definitions are the same as in Section 2.1. As was done in that section, all physical quantities are normalized according to the equations in Section 2.1.2. Given the normalization of σ and k, the velocity must be normalized as

$$\bar{u} = \frac{u}{\omega\lambda} \tag{6.9}$$

leading to the following expression for the normalized $\bar{\gamma}$ in terms of the other normalized quantities:

$$\bar{\gamma}_n = \sqrt{(2\pi n)^2 + i\bar{\sigma}\bar{\mu}^*(1 - 2\pi n\bar{u})} \tag{6.10}$$

6.1.2 Symmetry

The presence of convection changes the symmetry constraints of equation (2.27) to

$$\left.\frac{\partial A_y}{\partial x}\right|_{x} \neq \left.\frac{\partial A_y}{\partial x}\right|_{-x} \tag{6.11a}$$

$$A_y(x) = -A_y\left(x + \frac{1}{2}\right) \tag{6.11b}$$

Comparing equation (6.11) to equation (2.27) shows that the even symmetry with respect to $x = 0$ is broken, because $\mathbf{v}$ changes direction when reflected across the y-z plane. The negative symmetry of translation by $1/2$ still holds because, the presence of motion does not invalidate the fact that half a period to the right all current flows in the opposite direction, changing the sense of most other physical quantities as well.

The effect of the broken symmetry is to require the use of the full exponential Fourier series, instead of the even cosine series. Furthermore, a full half period must be included in the model, to determine the magnetic vector potential everywhere.

As before, only odd-numbered Fourier modes are needed, due to the translational symmetry conditions, and, as in Section 2.1, all summations over Fourier modes use only odd values of n.

6.1.3 Collocation points

Since the interval of interest now contains one half wavelength, the number of regions modeled separately increases to seven, with the addition of the return leg of the secondary winding, another gap, and half of the return leg of the primary.

This number may be reduced to six by shifting the origin from the center of the primary winding to its left edge. This change does not violate the built-in symmetry assumptions in equation (6.11), since the odd symmetry with respect to the origin is already broken.

If K collocation points are still placed in each interval, the total number becomes $6K$. The distribution of the points is made cosinusoidal in every interval. It is still necessary for the integration interval limits to include the winding edges, and in analogy to equation (2.33) they are defined as

$$\left.\begin{aligned}
x^*_m &= ct_m \\
x^*_{K+m} &= c + gt_m \\
x^*_{2K+m} &= c + g + dt_m \\
x^*_{3K+m} &= c + g + d + \left(\frac{1}{2} - c - 2d - 2g\right) t_m \\
x^*_{4K+m} &= \frac{1}{2} - g - (1 - t_m)d \\
x^*_{5K+m} &= \frac{1}{2} - (1 - t_m)g
\end{aligned}\right\} \quad 0 \leq m \leq K \tag{6.12}$$

where t_m is defined as

$$t_m = \frac{1 - \cos(\pi m/K)}{2} \tag{6.13}$$

The geometrical parameters c, d, and g are defined in Figure 2-1, and all length parameters are normalized by the wavelength λ. As in equation (2.34), the collocation points x_m are situated in the middle of the integration intervals, except at the two ends:

$$x_m = \begin{cases} x_m^* & m = 0, 6K \\ \dfrac{x_{m+1}^* + x_m^*}{2} & m = 1, 2, \ldots, 6K-1 \end{cases} \tag{6.14}$$

The collocation points span half a period, so that $x_{6K} - x_0 = 1/2$. Equation (6.11) requires that

$$a_{6K} = -a_0 \tag{6.15}$$

where a_m are the values of A_y at the points x_m. Equation (6.15) is the extra constraint needed to make the number of independent unknowns equal to the number of integration intervals. The corresponding constraint in Section 2.1 is equation (2.32).

6.1.4 Fourier series representation

The magnetic vector potential is represented as an exponential Fourier series:

$$A_y(x) = \sum_{\substack{n=-\infty \\ n \text{ odd}}}^{\infty} A_n e^{-ik_n x} \tag{6.16}$$

Only odd-numbered modes are necessary, because of the constraint given in equation (6.11). To obtain the Fourier coefficients A_n in terms of the values at the collocation points, the following integral must be solved:

$$\begin{aligned} A_n &= 2\int_0^{1/2} A_y(x) e^{ik_n x} dx \\ &= 2\sum_{m=0}^{6K-1} \int_{x_m}^{x_{m+1}} \frac{(x_{m+1}-x)a_m + (x-x_m)a_{m+1}}{x_{m+1}-x_m} e^{ik_n x} dx \\ &= \frac{2}{k_n^2} \sum_{m=0}^{6K-1} \frac{e^{ik_n x_{m+1}} - e^{ik_n x_m}}{x_{m+1}-x_m} \left(a_{m+1} - a_m\right) + \frac{2}{ik_n} \sum_{m=0}^{6K-1} \left[a_{m+1} e^{ik_n x_{m+1}} - a_m e^{ik_n x_m} \right] \end{aligned} \tag{6.17}$$

The summation in the last term of equation (6.17) cancels out on a term by term basis, with the first and last terms also canceling each other due to the wrap-around effect:

$$a_{6K} e^{ik_n x_{6K}} = -a_0 e^{ik_n \left(x_0 + \frac{1}{2}\right)} = -a_0 e^{ik_n x_0} e^{i\pi n} = a_0 e^{ik_n x_0} \tag{6.18}$$

where n is an odd number, and use has been made of the previously established relationships $a_0 = -a_{6K}$ and $x_{6K} - x_0 = 1/2$. The remaining summation in equation (6.17) can be rewritten as

$$A_n = -\frac{2}{k_n^2} \sum_{m=1}^{6K} a_m \left[\frac{e^{ik_n x_{m+1}} - e^{ik_n x_m}}{x_{m+1}-x_m} - \frac{e^{ik_n x_m} - e^{ik_n x_{m-1}}}{x_m - x_{m-1}} \right] \tag{6.19}$$

if, for convenience, an extra collocation point is defined:

$$x_{6K+1} = x_1 + \frac{1}{2} \tag{6.20}$$

This works because

$$-a_0 \frac{e^{ik_n x_1} - e^{ik_n x_0}}{x_1 - x_0} = a_{6K} \frac{-e^{ik_n x_{6K+1}} + e^{ik_n x_{6K}}}{x_{6K+1} - x_{6K}} \tag{6.21}$$

having used the same method as in equation (6.18).

6.1.5 Normalized surface reluctance density

Equations (2.39) through (2.52) apply without any changes, as long as negative values for the mode number n are allowed, and the definition of γ_n used in each layer is obtained via equation (6.7).

6.1.6 Boundary conditions

As before, the surface current must be zero in the gaps, requiring no changes to equation (2.53). Equation (2.56) also applies, but there is one complication: whereas over the primary winding the terminal voltage is still v_1, it is not known ahead of time how v_2 is divided between the two legs of the secondary winding, since the symmetry is broken and the voltage is not divided equally.

If $-v'$ is the terminal voltage in equation (2.56) applied over the second leg of the secondary winding, then for the first leg $v_2 - v'$ must be used. The extra unknown v' requires an additional constraint, in order to determine the vector potential uniquely. The extra equation comes from the restriction that the total current in both legs of the secondary winding must be equal in magnitude.

The integral over K_S remains in a similar form:

$$\begin{aligned}
\int_{x_m^*}^{x_{m+1}^*} K_S(x)\,dx &= \sum_{\substack{n=-\infty \\ n \text{ odd}}}^{\infty} R_n k_n \int_{x_m^*}^{x_{m+1}^*} A_n e^{-ik_n x}\,dx \\
&= -\sum_{\substack{n=-\infty \\ n \text{ odd}}}^{\infty} iR_n \left[e^{-ik_n x_{m+1}^*} - e^{-ik_n x_m^*} \right] \frac{2}{k_n^2} \sum_{j=1}^{6K} a_j \left[\frac{e^{ik_n x_{j+1}} - e^{ik_n x_j}}{x_{j+1} - x_j} - \frac{e^{ik_n x_j} - e^{ik_n x_{j-1}}}{x_j - x_{j-1}} \right] \\
&= \sum_{\substack{n=-\infty \\ n \text{ odd}}}^{\infty} R_n \sum_{j=1}^{6K} M_{m,j}^n a_j
\end{aligned} \tag{6.22}$$

which leads to the following definition of $M^n_{m,j}$:

$$\begin{aligned} M^n_{m,j} = \frac{2i}{k_n^2}\Bigg\{ &- \frac{1}{x_{j+1}-x_j}\left[e^{ik_n(x_{j+1}-x^*_{m+1})} - e^{ik_n(x_{j+1}-x^*_m)}\right] \\ &+ \left[\frac{1}{x_{j+1}-x_j} + \frac{1}{x_j - x_{j-1}}\right] \cdot \left[e^{ik_n(x_j-x^*_{m+1})} - e^{ik_n(x_j-x^*_m)}\right] \\ &- \frac{1}{x_j - x_{j-1}}\left[e^{ik_n(x_{j-1}-x^*_{m+1})} - e^{ik_n(x_{j-1}-x^*_m)}\right]\Bigg\} \end{aligned} \tag{6.23}$$

It is still possible to use the shortcut implemented in Section 2.1.6 via R_∞ and $M'_{m,j}$. If N is large enough, so that $R_n \approx R_\infty$ for $n > N$ ***and*** $R_n \approx -R_\infty$ for $n < -N$, then the modes with positive and negative indices may be paired up as

$$\sum_{\substack{n=1 \\ n \text{ odd}}}^{\infty} \frac{2i}{k_n^2}\left(e^{ik_n x} - e^{-ik_n x}\right) = -4\sum_{\substack{n=1 \\ n \text{ odd}}}^{\infty} \frac{\sin(k_n x)}{k_n^2} = -\frac{1}{\pi^2} f(x) \tag{6.24}$$

where $f(x)$ is the function defined in equation (2.61). The integral over $K_\mathrm{S}(x)$ in equation (6.22) can then be written as:

$$\int_{x^*_m}^{x^*_{m+1}} K_\mathrm{S}(x)\,dx \approx \sum_{\substack{n=-N \\ n \text{ odd}}}^{N} (R_n - R_\infty)\sum_{j=1}^{6K} M^n_{m,j} a_j + R_\infty \sum_{j=1}^{6K} M'_{m,j} a_j \tag{6.25}$$

where the coefficients $M'_{m,j}$ are given by:

$$\begin{aligned} M'_{m,j} = \sum_{\substack{n=-\infty \\ n \text{ odd}}}^{\infty} M^n_{m,j} = -\frac{1}{\pi^2}\Bigg\{ &- \frac{1}{x_{j+1}-x_j}\left[f\left(x_{j+1}-x^*_{m+1}\right) - f\left(x_{j+1}-x^*_m\right)\right] \\ &+ \left[\frac{1}{x_{j+1}-x_j} + \frac{1}{x_j - x_{j-1}}\right] \cdot \left[f\left(x_j-x^*_{m+1}\right) - f\left(x_j-x^*_m\right)\right] \\ &- \frac{1}{x_j - x_{j-1}}\left[f\left(x_{j-1}-x^*_{m+1}\right) - f\left(x_{j-1}-x^*_m\right)\right]\Bigg\} \end{aligned} \tag{6.26}$$

The computation of the integral over $A(x)$ does not depend on the Fourier representation, which means that equations (2.63), (2.64), and (2.65) remain valid in the presence of motion.

6.1.7 Setting up the matrix equation

As explained in the previous section, there is an extra unknown, v', and an extra equation which must be considered when setting up the matrix equation. If v' is appended to the end of the vector a, then the matrix M in $Ma = b$ has one extra row and one extra column, compared to the matrices M^n, M', and M'', which are $6K \times 6K$ matrices. This results in the following

definition for the elements of M:

$$M_{m,j} = \begin{cases} \displaystyle\sum_{\substack{n=-\infty \\ n \text{ odd}}}^{N} \left(R_n - R_\infty\right) M^n_{m,j} + R_\infty M'_{m,j} & \begin{cases} K \le m < 2K \\ 3K \le m < 4K \\ 5K \le m < 6K \end{cases} \quad 0 \le j \le 6K \\ \displaystyle\sum_{\substack{n=-\infty \\ n \text{ odd}}}^{N} \left(R_n - R_\infty\right) M^n_{m,j} + R_\infty M'_{m,j} + i\sigma_{\text{coil}} M''_{m,j} & \begin{cases} 0 \le m < K \\ 2K \le m < 3K \\ 4K \le m < 5K \end{cases} \quad 0 \le j \le 6K \\ \sigma_{\text{coil}}\left(x^*_{m+1} - x^*_m\right) & \begin{cases} 2K \le m < 3K \\ 4K \le m < 5K \end{cases} \quad j = 6K \\ \left\{ \displaystyle\sum_{\ell=2K}^{3K-1} - \sum_{\ell=4K}^{5K-1} \right\} \left[\displaystyle\sum_{\substack{n=-\infty \\ n \text{ odd}}}^{N} \left(R_n - R_\infty\right) M^n_{\ell,j} + R_\infty M'_{\ell,j} \right] & m = 6K \quad 0 \le j \le 6K \\ 0 & m = 6K \quad j = 6K \end{cases} \tag{6.27}$$

where the definition of the last row, $m = 6K$, which implements the constraint that the total of the current in the two legs of the secondary winding must be zero, is derived from equation (2.69). The following short hand notation was used in equation (6.27):

$$\left\{ \sum\nolimits_1 - \sum\nolimits_2 \right\} [\,] \equiv \sum\nolimits_1 [\,] - \sum\nolimits_2 [\,] \tag{6.28}$$

The definition of b in equation (2.68) remains unchanged, with the addition of an extra row of zeros at the bottom.

A minor change in equation (2.69) requires the removal of the factor of two, since the entire primary is in the half period, and the addition of a column of zeros:

$$F_{m,j} = \begin{cases} \displaystyle\sum_{\ell=0}^{K-1} \left[\sum_{\substack{n=-\infty \\ n \text{ odd}}}^{N} \left(R_n - R_\infty\right) M^n_{\ell,j} + R_\infty M'_{\ell,j} \right] & m = 0 \quad j < 6K \\ \displaystyle\sum_{\ell=2K}^{3K-1} \left[\sum_{\substack{n=-\infty \\ n \text{ odd}}}^{N} \left(R_n - R_\infty\right) M^n_{\ell,j} + R_\infty M'_{\ell,j} \right] & m = 1 \quad j < 6K \\ 0 & j = 6K \end{cases} \tag{6.29}$$

6.1.8 Effect of convection on sensor response

The implementation of the changes to the model shown in this section makes it possible to study how the sensor response changes with increasing velocity. Figure 6-1 shows the trajectory of the sensor transinductance in magnitude/phase space, as the velocity of the material is increased.

An interesting phenomenon to observe in Figure 6-1 is that for a certain range of values the phase of the transinductance becomes positive, corresponding to impedance with a negative real component. Whereas this may appear nonphysical at first, one must bear in mind that this is a two-port transinductance of a continuum system and cannot be thought of as a single lumped component. A somewhat similar phenomenon of negative transconductance and transcapacitance can occur in the IDED [10].

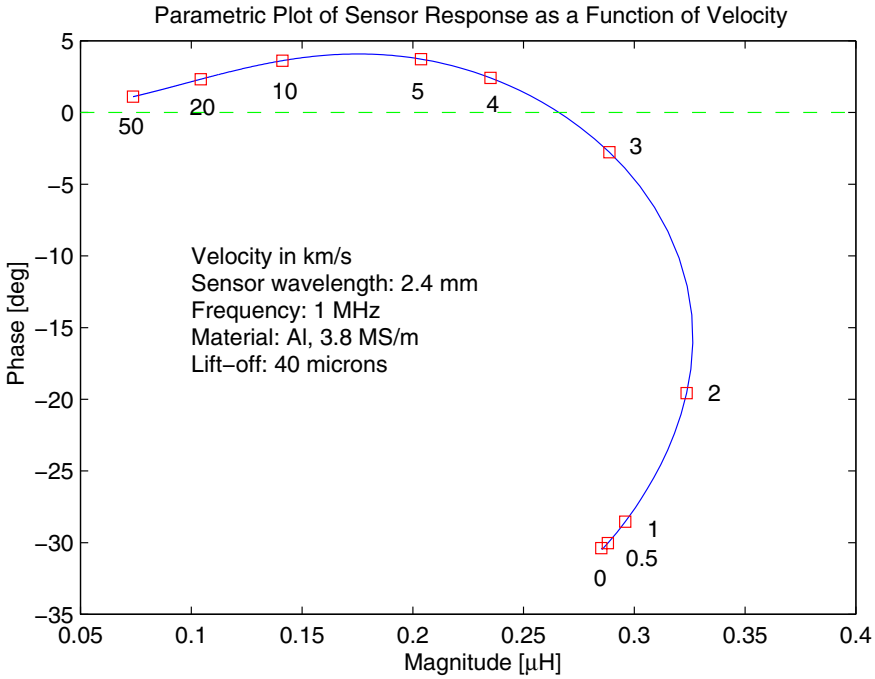

Figure 6-1: Locus of the transinductance of an MWM in magnitude/phase space as the convection velocity increases.

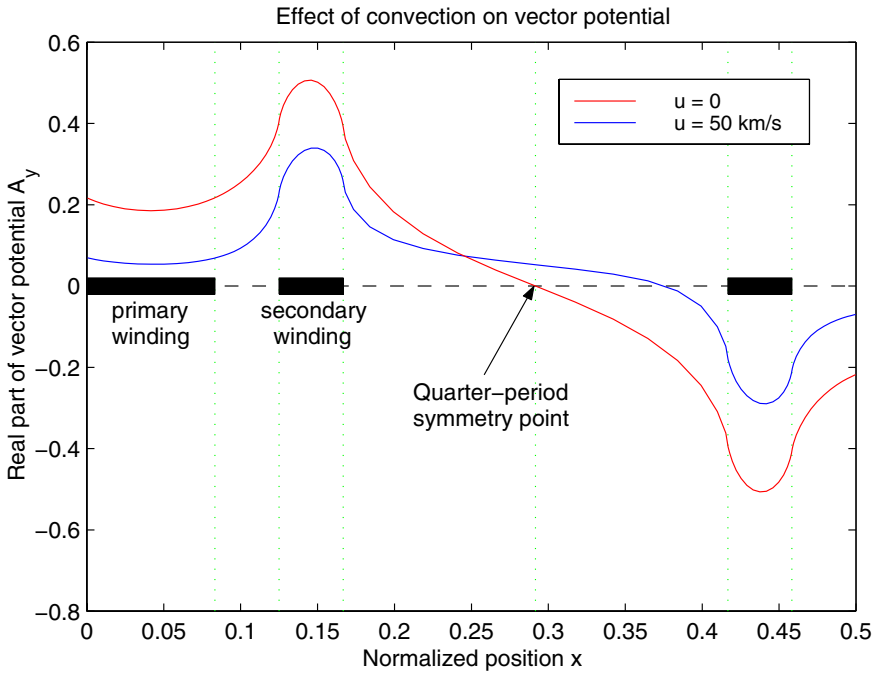

Figure 6-2: Real part of the magnetic vector potential A_y, shown for stationary and moving media. It can be seen that the odd symmetry with respect to the quarter-period point is broken while the translational symmetry still holds, as implied by equation (6.11). The potential in this figure corresponds to driving the secondary winding, which is the opposite of typical operation, but the effect is easier to observe in this case.

Figure 6-2 shows a comparison between a moving and stationary metal layer. In addition to breaking the symmetry with respect to the quarter-period point, clearly visible in the figure, the motion also acts to decrease the magnitude of the potential. The ability of the conducting material to counteract the imposed magnetic field improves at higher speed, a behavior also observable in Figure 6-1.

6.1.9 Summary

This section has illustrated how to incorporate material motion into the semi-analytical collocation point model of the magnetometers with Cartesian geometry. Although the analysis has focused on the MWM, the same methods are also directly applicable to modeling Cartesian geometry magnetometers with distributed current drives, of the type described in Chapter 4. Most magnetometer arrays, used for generating two-dimensional scans of a material, for example the one shown in Figure 1-2, fall in the latter category.

Use of magnetoresistive secondary elements, as described in Chapter 5, makes it possible to operate magnetometers and magnetometer arrays at very low excitation frequencies, and in such cases the scanning velocity may begin to have an appreciable effect on the sensor response, and will have to be incorporated in the simulation methods.

6.2 Grid look-up and interpolation algorithms

This section describes the most recent implementation of the two-dimensional grid look-up algorithm. The purpose of this algorithm is to convert the value of the measured transimpedance of a sensor to material properties, i.e. parameter estimation, by interpolating between the points of a look-up table of pre-computed sensor responses, known as a measurement grid. The concept of using measurement grids for parameter estimation is described in Section 1.4.

The type of interpolation that needs to be carried out for a grid look-up is not what is done in typical look-up table algorithms, which are forward interpolation algorithms. This is a critical distinction and deserves some more explanation. Interpolation methods of this nature are discussed in [81], though the subject of two-dimensional inverse interpolation algorithms is not discussed at all.

6.2.1 Two-dimensional inverse interpolation

The concept of inverse interpolation is best illustrated with an example. Suppose there is a function $y(x)$, whose values y_n are known at a set of points x_n. The independent variable is x, and x_n are chosen by the designer of the look-up table to span the anticipated function domain. The most common task is finding a value for y at a given value of x. This is one-dimensional forward interpolation and is very easy to carry out, since it is known from the start which x_n is closest to x, etc.

Finding a value of x that corresponds to a given value of y in the table described above is what is known as inverse interpolation. It is a much more difficult operation, especially if $y(x)$ is not a monotonic function. Furthermore, the values of y may be repeated, and are not evenly spaced, unless the function is a straight line.

In two dimensions, forward interpolation entails finding the value of a function $y(x_1, x_2)$ from x_1 and x_2 by interpolating in a two-dimensional table that lists the values of y at a set of predetermined values of the two independent variables. This can be done via bilinear interpolation or its higher order variants. The key feature is that, as in the one-dimensional

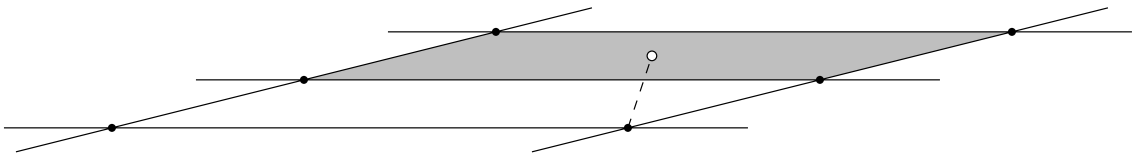

Figure 6-3: Example of a situation where the closest grid point to a target point is not one of the corners of the grid cell enclosing the target point.

case, it is known from the outset which is the closest point in the table to the target point, and which of the table's points to use for the interpolation. The actual interpolation is also easy, since when plotted in x_1-x_2 space the table forms a rectangular grid.

Two-dimensional inverse interpolation comes about when there is a table that lists the values of two functions, $y_1(x_1, x_2)$ and $y_2(x_1, x_2)$, at a set of predetermined values of the independent variables, which form a rectangular grid. The goal is to find the appropriate values for x_1 and x_2 where the functions y_1 and y_2 attain a pair of known values. This task is orders of magnitude more complicated. Here are some of the complications:

- Even when both target y_1 and y_2 fall inside the ranges of the corresponding functions, there is no guarantee that a solution exists.
- It is not known at the outset what the indices of x_1 and x_2 are for the point closest to the target.
- Even if the first two difficulties are overcome, and it is established which cell in the table should be used for interpolation, in general in y_1-y_2 space this cell is not rectangular, or even a parallelogram, and no standard interpolation formula can be applied.

The grid methods implement this kind of two-dimensional inverse interpolation to convert the sensor measurement's magnitude and phase data to real physical quantities, such as conductivity and lift-off. The measurement grids are generated by applying the forward models, described in Chapters 2–4, at a set of values for the two parameters, giving the magnitude and phase at each combination. The two measurement parameters do not need to be magnitude and phase, it is possible to have magnitude/magnitude grids for two sensors, or two spatial wavelengths inside the same sensor, for example the grids used in Section 3.3 and Section 5.5.

Previously the method of identifying the closest grid point, used to establish which cell to use in the interpolation, was to calculate the distance to each point on the grid and pick the shortest one. This is clearly very inefficient, and can also give the wrong result in some cases, as seen in Figure 6-3. The cell that contains the target point is shaded in the figure. The closest grid point to the target is clearly not one of its four corners.

The actual interpolation step was also deficient in many respects for nonrectangular grid cells, giving discontinuous interpolation not only at cell boundaries, but sometimes even inside the same cell, in addition to sometimes manifesting bias toward some of the grid cells that cannot be justified geometrically.

This section describes methods that successfully overcome all of these limitations. It is divided into three subsections: the search algorithm, which aims to find the grid cell inside which the target point is located; and two interpolation methods of increasing performance and complexity.

6.2.2 Search algorithm

The function of this algorithm is to locate quickly the grid cell that contains the target point. It can be roughly divided into four steps:

1. ***Choose a starting point.*** Initiating the search close to the target point can significantly improve the efficiency of the search. In general, this should be the cell used in the last look-up, because it is very likely that consecutive measurements lie close together on the grid. In fact, in most cases the last cell used contains the current target point, so that this step often concludes the search. If this is the first look-up in the current session, a rough interpolation is done based on the four corners of the grid to estimate the indices of the starting point, using a method similar to the one described in Section 6.2.3.

2. ***Zoom out.*** If the target point is not inside the current cell, increase the size of the area tested to 2×2, 4×4, etc., until either the current grid "square" (collection of cells being considered) contains the target point, or it reaches a predefined limit or the size of the entire grid.

3. ***Move the grid square.*** If the grid square currently under consideration does not contain the target point, move to the next grid square of the current size in the direction toward the target point. Keep moving until one of the following three conditions occurs:

   (a) The target point falls inside the current square.

   (b) The square reaches the edge of the grid.

   (c) It cannot be determined which the correct direction to move is. This last condition can occur in special cases near singular points, near grid folds, or if the current grid square is not a convex quadrangle.

4. ***Zoom in.*** If the size of the current grid square is greater than a single grid cell, reduce it by a factor of two and go back to step 3. Otherwise, end the search.

If in the end the current grid cell contains the target point, the search was successful. Otherwise, the target point is most likely off the grid.

There can be cases when the search fails even if the target point is on the grid. This can happen if the grid is so curved that moving in a direction toward the target in the plane of the grid, i.e. in magnitude/phase space, moves away from the correct cell in parameter space. These cases are handled by reverting to the "brute force" method of computing the distance to every point on the grid and finding the closest grid point to the target point. It is then used as the starting cell for a second run through the search algorithm. If, in fact, the target point is on the grid, this will find the correct cell with a very high likelihood. Most often, however, if the first run fails, it is because the point is off the grid, so that if used every time a point off the grid is encountered, this second search step takes a disproportionately long time to run, which can create problems, especially when performing real-time estimation. Whether to give up after the first try or attempt the long search method depends on the particular application.

In order to determine the direction to move in step 3 above, a formula (equation (6.31)) is applied that calculates the area of the triangles formed by each of the four sides of the grid square and the target point, and the sign of the result is used to determine whether the target point lies inside the square, or else in which direction the square is to be moved. For example, if the target point is to the "right" of both the "left" and "right" sides of the square, it must be moved one over to the right, etc. The directions here are put in quotations, because the

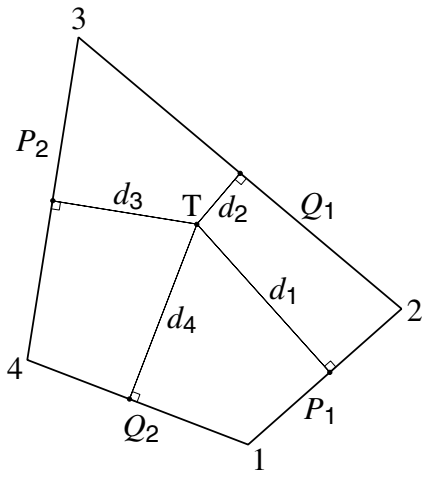

Figure 6-4: Schematic diagram of the two-dimensional inverse interpolation in a grid cell. Each pair of opposing sides is associated with two values of a parameter being estimated, P or Q. d_1 through d_4 are the distances from the target point T to the four grid edges.

meanings of "right", "left", "top", and "bottom" depend on the direction of increasing parameter index number, and on whether the grid is "right-handed" or "left-handed", i.e. whether the axes in magnitude/phase space and parameter space have the same or opposite sense.

6.2.3 Simple inverse two-dimensional interpolation

This interpolation method is based on the distances between the target point and the lines of constant parameter, P or Q, as shown in Figure 6-4:

$$P = \frac{d_3 P_1 - d_1 P_2}{d_3 - d_1} \qquad Q = \frac{d_4 Q_1 - d_2 Q_2}{d_4 - d_2} \tag{6.30}$$

The distances d_1 through d_4 are calculated by dividing the area of the triangle with vertices at the two corners and the target point by the length of the cell side, and then dividing by two. The following formula is used to find the triangle area:

$$A_{ijk} = x_i(y_k - y_j) + x_j(y_i - y_k) + x_k(y_j - y_i) \tag{6.31}$$

The sign of A_{ijk} can be positive or negative, depending on whether the motion is in a positive (counterclockwise) or negative (clockwise) direction along the circumscribed circle when going from i to j to k. Therefore this formula retains directionality information, although it calculates area. If all three points lie on a line, the result is zero.

It is important to realize that the distances d_1 through d_4 in equation (6.30) are signed quantities, so that when the target point lies inside the cell, d_1 and d_3 have opposite signs, as do d_2 and d_4. The order of the area indices in equation (6.31) is important. The advantage of maintaining the polarity information is that the correct result will be obtained even if the target point lies outside the grid cell used for interpolation.

The problem with the "simple" method in this section is continuity across cell boundaries. The value of the parameter associated with the cell wall being crossed, e.g. P when crossing line 1–2 in Figure 6-4, is continuous, because it is equal to the value of the parameter on that line, P_1. However, the value of the other parameter, e.g. Q, when crossing line 1–2,

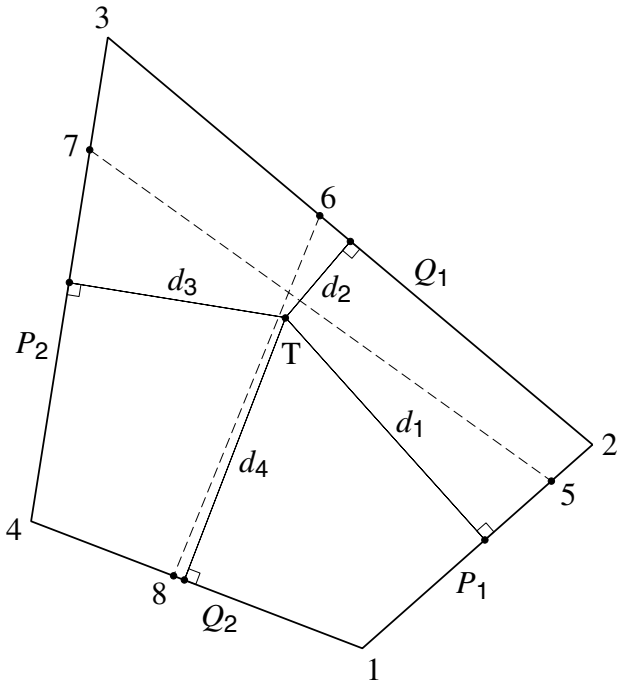

Figure 6-5: Diagram of a grid cell showing the points used by the complex inverse two-dimensional interpolation algorithm. Points 5–8 are positioned on the grid cell edges according to equation (6.32). Instead of being associated with line segments, the four parameter values P_1, Q_1, P_2, and Q_2 are now associated with points 5–8 respectively.

in general makes a discontinuous jump as the grid cell being used for interpolation changes. This is usually a very small jump, since in most grids the edges of neighboring cells are nearly parallel.

The practical implications of this discontinuous behaviour are most pronounced when using iterative techniques, e.g. in coating characterization applications where three unknowns are measured simultaneously [26], or other multiple-unknown measurements, where it could lead to lack of convergence. It is also possible to observe the effect when scanning along a part with continuously varying properties using a coarser grid, where the measured property may appear to change in steps.

6.2.4 Complex inverse two-dimensional interpolation

To solve the discontinuity problem, given a target point on a grid cell wall, both of the estimated parameters, P and Q, must depend only on the coordinates of the target point and the two end points of the edge being crossed, common to both cells. For example, when the target point lies on line 1–2, both P and Q must depend only on the coordinates of points 1, 2, and T. With the simple method this is true only for P.

This is accomplished in the following way. Instead of using equation (6.30) to calculate P and Q directly, it is used to find the coordinates of four new points, 5–8, one on each of the

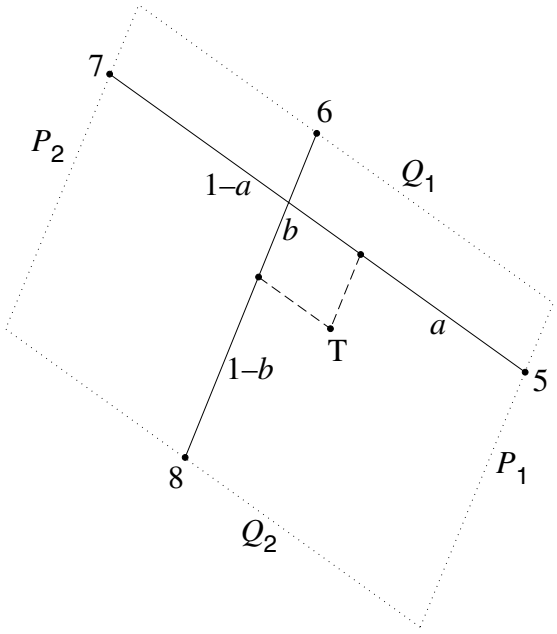

Figure 6-6: Grid cell transformed into a parallelogram via points 5–8. The interpolation becomes the simple linear operation given in equation (6.33). The ratios a and b are determined by the lengths of the sections into which the line segments 5–7 and 6–8 are divided by lines through the target point T and parallel to the two segments.

four sides of the cell, as shown in Figure 6-5. This is done via the following equations:

$$x_5 = \frac{d_4 x_2 - d_2 x_1}{d_4 - d_2} \qquad y_5 = \frac{d_4 y_2 - d_2 y_1}{d_4 - d_2} \tag{6.32a}$$

$$x_6 = \frac{d_3 x_2 - d_1 x_3}{d_3 - d_1} \qquad y_6 = \frac{d_3 y_2 - d_1 y_3}{d_3 - d_1} \tag{6.32b}$$

$$x_7 = \frac{d_4 x_3 - d_2 x_4}{d_4 - d_2} \qquad y_7 = \frac{d_4 y_3 - d_2 y_4}{d_4 - d_2} \tag{6.32c}$$

$$x_8 = \frac{d_3 x_1 - d_1 x_4}{d_3 - d_1} \qquad y_8 = \frac{d_3 y_1 - d_1 y_4}{d_3 - d_1} \tag{6.32d}$$

Now instead of being associated with a line segment, each of the two pairs of grid parameters is associated with a pair of points, as shown in Figure 6-6. If, for example, the target point lies on cell side 1–2, points 8 and 6 will coincide with 1 and 2 respectively, making Q dependent only on these two points, as required. If P and Q are expressed in terms of the coefficients a and b, using

$$P = (1-a)P_1 + aP_2 \qquad Q = (1-b)Q_1 + bQ_2 \tag{6.33}$$

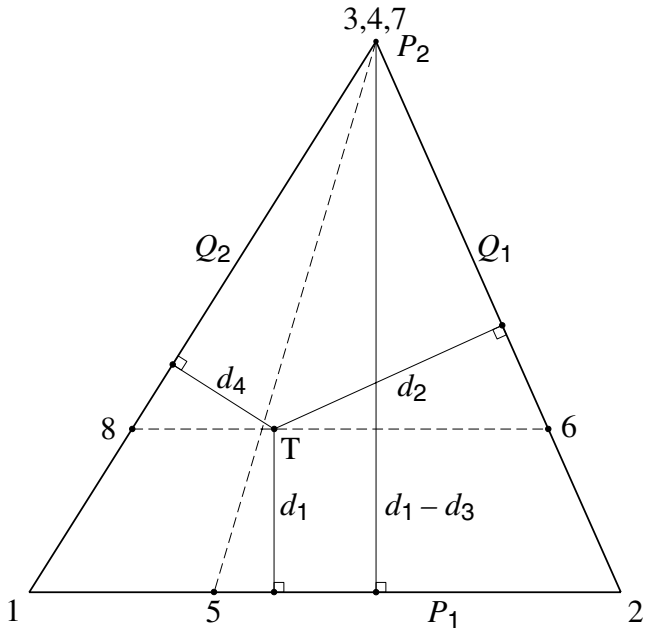

Figure 6-7: Point and segment definitions for a triangular grid cell. Corners 3 and 4 of the cell coincide. The distance d_3 is not well defined, because the line through points 3 and 4 is not unique. A solution is to pick the line parallel to segment 1–2. The distance d_3 is then equal to the difference between d_1 and the distance from point 3 to segment 1–2, keeping in mind that the distances are signed quantities, and in this example d_3 is negative.

then standard bilinear interpolation leads to the following expressions for these coefficients:

$$a = \frac{(x_8 - x_6)(y - y_5) - (x - x_5)(y_8 - y_6)}{(x_8 - x_6)(y_7 - y_5) - (x_7 - x_5)(y_8 - y_6)} \tag{6.34a}$$

$$b = \frac{(x - x_6)(y_7 - y_5) - (x_7 - x_5)(y - y_6)}{(x_8 - x_6)(y_7 - y_5) - (x_7 - x_5)(y_8 - y_6)} \tag{6.34b}$$

Using this procedure, the grid cell has effectively been transformed from an arbitrary quadrangle to a parallelogram, outlined with dotted lines in Figure 6-6, although the shape of this parallelogram depends on the coordinates of the target point.

6.2.5 Handling triangular grid cells

In the past the grid look-up algorithms could not handle cases when two adjacent corners of a grid cell coincided, as in the grid cell in Figure 6-7. This can be a serious impediment, since grids with some triangular cells appear to be quite common. Most often this type of measurement grid arises when the “air” point, which is the sensor response in air, is included in the grid, at which point the sensor response does not change with lift-off, and the entire edge of a grid collapses into a single point. Often the air point is used as a reference for sensor calibration, as described in Appendix D, necessitating its inclusion in the grids to avoid the need for special treatment.

As a working example consider the case where points 3 and 4 coincide, as shown in Figure 6-7. The main problem with applying the method outlined in the previous section directly is that the distance d_3 is not well defined, because points 3 and 4 do not uniquely define a line.

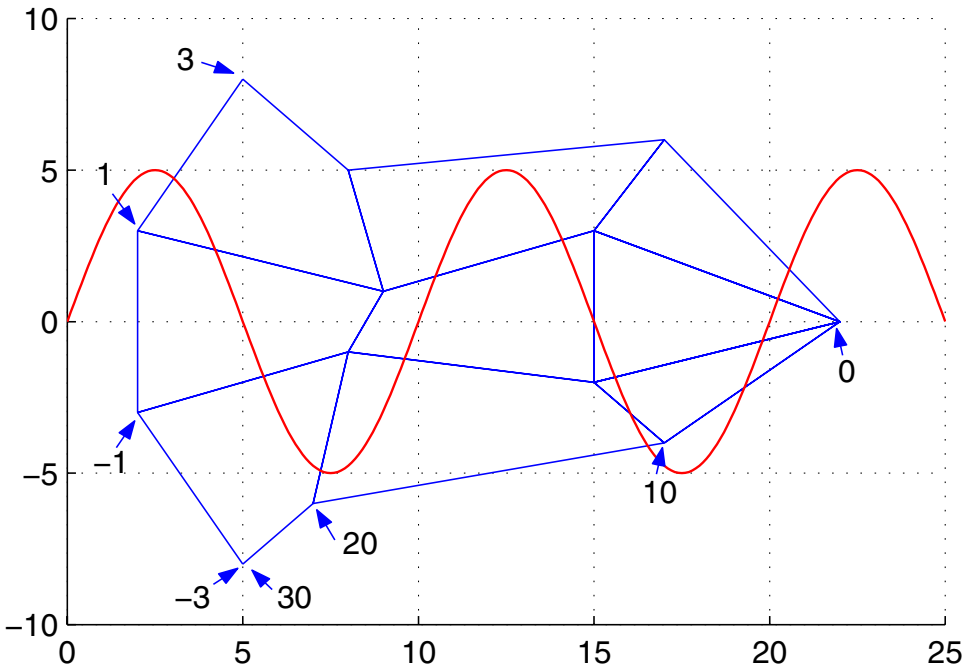

Figure 6-8: Pathological test grid and path through the grid followed by the target point. The new algorithm makes sure that the estimated values of the two properties remain continuous at cell edge crossings inside the grid, and that proper parameter estimation is possible inside the triangular cells near the grid singularity at $(22, 0)$.

It is not possible simply to use the distance between the target point T and point 3, because the polarity information is lost in this case, among other things, and the results would be very wrong indeed, especially if the target is outside the cell, which we hope to handle with at least some grace. The solution is to take the direction of the line through 3 and 4 to be parallel to the line through 1 and 2. A consequence of this is that the line through 6 and 8 is always parallel to 1–2 and passes through the target point T. The undefined distance d_3 needs to be redefined via the segments as shown in the figure.

6.2.6 Comparison between the new and the old interpolation methods

A test grid is used to compare the performance of the two interpolation methods, shown in Figure 6-8. It is crooked by design, so that the discontinuity of the estimated properties is more pronounced. The grid also includes three triangular grid cells. The values of the parameters are shown with arrows in the figure. The range of the "radial," or perhaps "horizontal," property is from 30 to 0 and the range of the "azimuthal," or "vertical," property is from -3 to 3. The figure also shows the continuous path followed by the target point through the grid, which would ideally result in a continuous estimate of the two properties.

The results of using the two look-up methods are shown in the plots in Figures 6-9 and 6-10. A number of discontinuous steps are visible at grid line crossings with the simple method, while the new complex method remains continuous. As seen in the plot of the radial property, the complex method can also be discontinuous, but only ***outside*** the grid. Whereas an attempt has been made to treat off-grid cases reasonably, in general continuity cannot be guaranteed, because it is not possible to determine uniquely which grid cell should be used for the interpolation. Nonetheless, one can see that as long as the target point remains near the

grid, the results of the complex method are still quite reasonable. It is only in the azimuthal property near the singular point at $(22, 0)$ that the estimated property attains extreme values, but this is to be expected, since several segments with different parameter values merge to a single point there. Following the air point example, this is the equivalent of attempting to estimate the lift-off of a material made of air, which is clearly meaningless.

It can be seen in the plots of the estimated properties that the old method curves end prematurely. This is because the old method could not effectively handle nonstandard, e.g. triangular, grid cells, which it encounters in the process of locating the bounding grid cell.

6.2.7 Handling multi-valued grids

There are cases when a grid folds in on itself, as described and illustrated in Section 5.7. This look-up algorithm also attempts to handle this kind of grid, at least in the simplest cases when there is no more than one "fold" or "twist". The main difficulty is that the searching stage of the algorithm may become confused near the fold line. For example, at the fold many grid cells are quadrangles whose opposite edges cross. It is not possible to determine whether the target point is to the "left" or "right" of a cell whose left and right edges intersect. In fact, it is not possible to decide whether the target point falls inside the cell at all.

The approach taken in such cases is to try four different runs of the search algorithm described in Section 6.2.2, starting at the four corners of the grid. Practice has shown that this approach is quite effective at handling most cases, providing even for the possibility of finding two solutions in the areas where the grid surface overlaps itself. No attempt is made to determine which one of the two solutions is to be considered the "correct" one, as such decisions need to be made at a higher level, using other information.

6.2.8 Summary

This section has described changes to the existing grid look-up algorithms that result in substantial improvements of the efficiency and accuracy of these methods. In particular, the numerical search algorithm that locates the grid cell that encloses the target point has been made very efficient and capable of handling unconventional or singular grids. The inverse interpolation step is formulated in a way that ensures continuity of both estimated properties throughout the range of the grid. In addition to better accuracy and efficiency, the new grid look-up is much more robust in its ability to treat unusual cases, such as target points that lie outside the grid or near grid singularities, in a reasonable way.

High performance of the grid look-up algorithm is essential for obtaining the full benefits of the model-based sensor methodology. The algorithm enhancements described in this section have already led to great improvements in the quality of data taken with the MWM, IDED, and their derivatives. Furthermore, the continuity property is very important in algorithms that include grid look-ups as an intermediate step in an iterative process, as is the case with several algorithms used to estimate more than two unknowns simultaneously. The robustness is also very valuable in such cases.

In addition to its application in measurements with the magnetic and dielectric sensors, this method has independent value as a generic numerical tool for two-dimensional inverse interpolation.

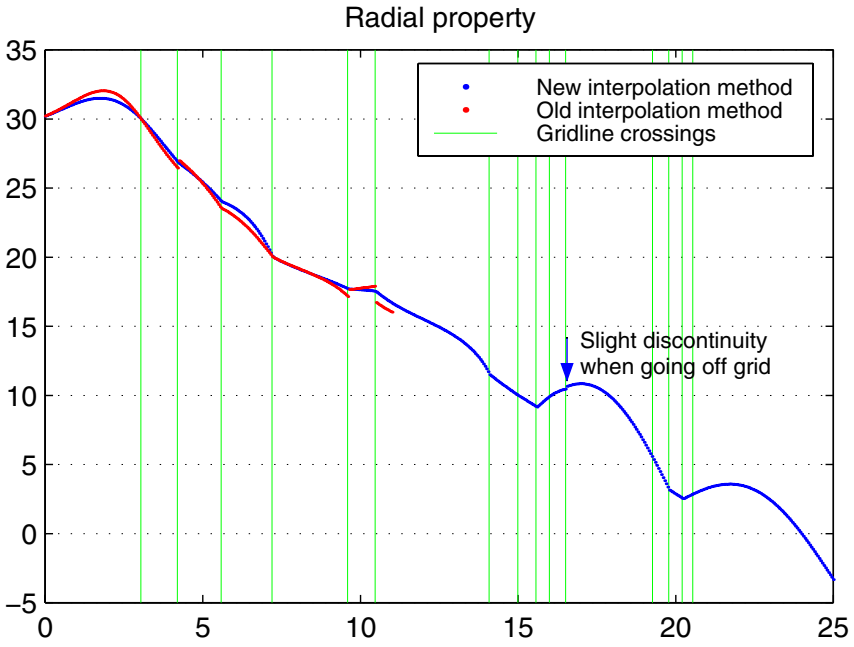

Figure 6-9: Results with both interpolation methods for the radial property of the grid in Figure 6-8. The values estimated with the new complex method are continuous across internal cell boundaries. The line of the simple method ends prematurely because it cannot handle triangular grid cells.

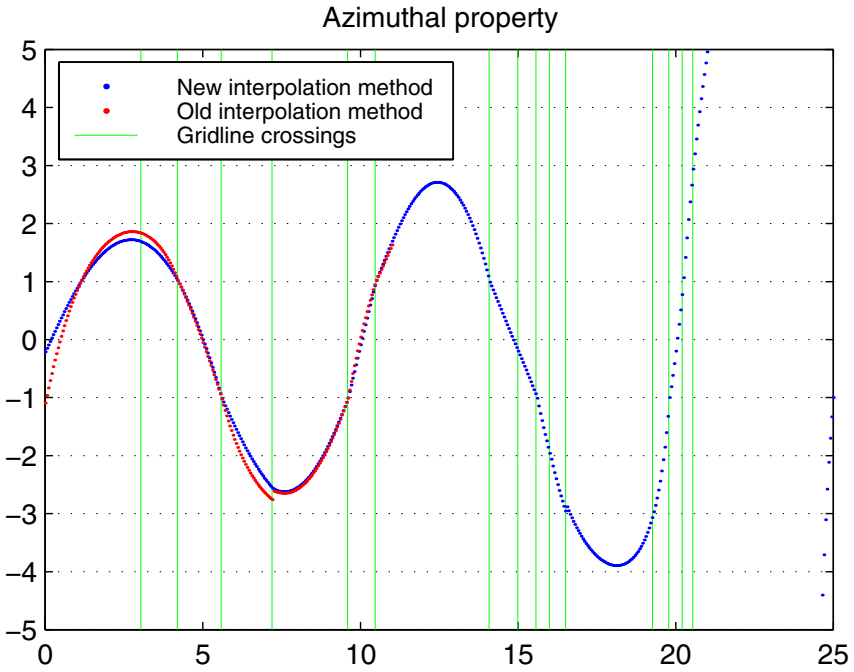

Figure 6-10: Results with both interpolation methods for the azimuthal property of the grid in Figure 6-8. The values estimated with the new complex method are continuous across internal cell boundaries. The extreme values attained near the end of the path are due to the fact that they correspond to target points outside the grid, near a grid singularity, where grid lines with different values of the azimuthal parameter converge to a single point.

Chapter 7

Summary, Conclusions, and Suggestions for Continuing Work

7.1 Summary

The main focus of the research effort has been to extend the depth of sensitivity of the periodic-field quasistatic magnetometers, in order to allow them to detect flaws, such as cracks, voids, and inclusions, buried deep in a metallic component, or hidden behind a metal layer. This type of measurement is difficult with the MWM and traditional eddy current magnetometers, because in the frequency range of sensitivity of these devices, the depth of penetration is limited by the skin depth of the magnetic field in the metal. In order to overcome this limitation, it is necessary to make the skin depth on the order of, or larger than, the thickness of metal between the flaw and the sensor. This may be accomplished by lowering the frequency of operation, since the skin depth is related to frequency as $\delta \propto 1/\sqrt{\omega}$.

The output of traditional eddy current magnetometers is the induced voltage in a secondary winding. Since it is proportional to the rate of change of the magnetic flux, the sensitivity of the measurement decreases with decreasing frequency, which makes such sensors unsuitable for low frequency operation. In order to overcome this limitation, the approach taken here is to replace the secondary winding with a giant magnetoresistive magnetic field sensor, which responds to the magnitude of the magnetic flux density, and consequently has no lower bound on its frequency of operation.

A prototype magnetometer that uses this idea has been built and tested. Its deep penetration and low frequency operation capabilities have been used for a range of measurement applications:

1. Conductivity/lift-off measurements on nonmagnetic metals.
2. Two-wavelength permeability/lift-off measurements on magnetizable nonconducting materials.
3. Thickness/lift-off measurements for a metal layer in a two-metal test structure.
4. Thickness/conductivity measurements for thick metal plates at ultralow frequency and high skin depth.
5. Detection of cracks buried beneath a thick layer of metal.
6. Magnetic permeability measurements of ferromagnetic fluids.

Successful operation of the GMR-based magnetometer has required that solutions be found to a number of design problems. Magnetic sensors based on the giant magnetoresistive effect are passive components, with a highly nonlinear transfer characteristic and limited dynamic range. These limitations have been overcome by appropriate biasing, and by placing the sensor in a feedback loop configuration with a secondary winding that maintains the magnetic flux density at the sensor constant.

The imposed spatial wavelength of the magnetometer is the other factor, together with skin depth, that can potentially limit its depth of sensitivity. It must therefore also be long compared to the required depth of penetration. Generating a magnetic field pattern with a long effective spatial wavelength, while avoiding the need to increase the magnetometer footprint to impractical dimensions, is accomplished by shaping the current in each segment of the primary winding to follow an appropriate envelope function.

An important necessary requirement for GMR magnetometer operation is the development of good mathematical and physical models, needed for the interpretation of data, and for parameter estimation of absolute properties. Such models must address the nature of the distributed current drive primary winding, and must be developed in cylindrical coordinates, because of the circular symmetry chosen for the sensor prototype.

Efficient simulation methods based on the fast Fourier transform have been developed for distributed current drive magnetometers, with versions available for both Cartesian and cylindrical geometry. The validity of the simulation results has been demonstrated by showing the close agreement between a variety of experimental data and corresponding sensor simulations.

In addition to the many stages of the project that have had to be completed before a GMR magnetometer could be tested successfully, the capabilities of the spatially periodic sensor family have been extended in a number of other areas:

1. The existing semi-analytical collocation point methods, used to model magnetometers and dielectrometers, have been reformulated in a way that offers several advantages:

   (a) The magnetometer and dielectrometer models, previously developed by different earlier research teams, now use a formulation that maintains the direct parallels between the magnetoquasistatic and electroquasistatic regimes, afforded by the principle of duality. Unifying the two models is beneficial in that improvements in one can be directly incorporated in the other with little extra effort.

   (b) The electroquasistatic model has corrected earlier errors by incorporating the zero order spatial Fourier mode properly. This makes a particularly noticeable improvement in cases where a ground plane is present behind the material under test.

   (c) Perhaps with greatest significance, the equations are written in a way that cleanly separates the computation of intermediate results that depend only on the sensor geometry, and which constitute the greatest computational burden, from those that depend on the material under test. In almost all practical cases, the former need to be carried out only once per session, and as a consequence the tasks of generating measurement grids for a given sensor, or running parameter estimation based on a minimization algorithm, have been rendered many times more efficient.

2. The semi-analytical collocation point methods have been extended to cylindrical geometry. New practical applications have required the development of analogs of the standard magnetometers and dielectrometers that have rotational symmetry, suitable for

measurements on circularly symmetric components or in cases where it is important to avoid the dependence of sensitivity on orientation. These extended models have been successfully applied to this new type of sensor. Experimental data have been presented that confirm the validity of these models by showing the close agreement between simulated and measured dielectrometer behavior.

3. The highly efficient FFT methods, used to simulate sensors with distributed current drive, can also be applied for modeling of magnetometers that traditionally use the collocation point technique, in cases when the exact distribution of the current density inside the windings is not important.

4. The magnetometer collocation point models have also been extended to accommodate relative motion between the magnetometer and the material under test. This effect may become important in scanning applications at low frequencies, if the distance traveled by the sensor in one temporal cycle period is not negligible compared to the effective spatial wavelength.

Several improvements to the measurement grid look-up method, which is the most common approach to two-dimensional parameter estimation, have also been presented. Superior performance has been demonstrated in both aspects of the look-up process:

1. The numerical search algorithm has been made much more efficient and more reliable. In addition to being able to find the needed target cell quickly, the new method is also capable of responding appropriately to unusual cases, which arise in the presence of topological anomalies in the grid, such as folds, twists, curls, or triangular grid cells. This capability has become very important recently, as new practical applications have introduced whole new classes of nonstandard measurement grids, like magnitude/magnitude, or higher-dimensional grids that involve three or more unknowns.

2. The inverse two-dimensional interpolation stage has been formulated in a way that guarantees continuity in both of the estimated properties across grid cell boundaries. This avoids the problem of introducing artificial "features" to a sensitive property scan, and also improves convergence of iterative algorithms that use grid look-up as an intermediate step. Furthermore, compared to previous interpolation methods, on the whole the improvement in the algorithm's performance for grid cells whose opposite sides are appreciably nonparallel makes it possible to use coarser grids with the same level of accuracy, leading to further improvement in efficiency, as well as conservation of computer memory resources.

7.2 Conclusions

The combination of the various enhancements and innovations in this work has resulted in the design of a whole new magnetometer sensor structure, capable of absolute property measurement of conductivity, magnetic permeability, and layer thickness at metal depths previously unattainable with the periodic-field eddy current magnetometers. It has been successfully demonstrated in the following deep-penetration measurements:

1. Detection of a crack hidden behind a $0.25''$ steel plate.

2. Thickness of aluminum plates on the order of $0.4''$.

3. Thickness of a steel layer approximately $0.2''$ thick in a two-metal structure.

These thickness values are at least a factor of ten higher than the current thickness upper limits of the MWM with the same materials, and are nowhere near the outer bound of the depth of sensitivity of the magnetoresistive magnetometer. Rather, they are the result of the choice of convenient frequencies and materials used to show feasibility. The depth of penetration limits of this sensor design have yet to be determined, and by operating at very low frequencies can in principle be extended to any material thickness.

Another important conclusion is that it has been possible to create a deep penetration magnetometer that matches the models so well that it can measure absolute physical properties without the need for calibration standards. The excellent results of a range of different measurements with the prototype magnetometer that rely only on a single calibration point in air demonstrate that the models used to simulate the sensor response, based on Fourier-Bessel analysis and the magnetic diffusion equation, are valid and accurate.

While there are other (nonperiodic) types of eddy-current sensors that use sensing coils with high number of turns for increased sensitivity at frequencies as low as 1 kHz, they are not capable of air calibration, and thus always require calibration standards and empirical calibration curves.

In addition to validating the simulation techniques, the experiments also confirm that the circuits that implement the feedback loop are operating correctly, and that the errors due to unmodeled parasitic effects can be neglected.

The data taken with the circular capacitive sensors in Chapter 3 demonstrate that the cylindrical geometry formulation of the collocation point methods is correct, and that this is an acceptable layout for dielectric sensors.

Altogether this thesis has demonstrated the feasibility of the new sensing technology concepts, and has opened up several possibilities for further improvements of existing time and space periodic sensor technology and design of new types of magnetometers and dielectrometers that belong to this class of sensors.

7.3 Suggestions for continuing work

The validity of the semi-analytical models and numerical methods has been confirmed, and the feasibility of creating a deep penetration magnetometer has been demonstrated. Now the research and design effort can focus on the adaptation of the principles established in the construction of the prototype to specific practical applications. A few of the potential areas of further research are suggested in this section.

7.3.1 Scaled down GMR magnetometer

The dimensions of the prototype magnetometer analyzed here have been chosen to make construction and experimentation easier. The relatively large size has made it possible to use prepackaged off-the-shelf components, and has relaxed the requirements on the connections, circuits, windings, etc., that are needed to minimize the performance deterioration due to parasitic and unmodeled effects. It has also facilitated the implementation of the multiple-wavelength idea, which requires double the number of turns in the primary winding. One of the first questions that needs to be investigated is how miniaturization will affect the magnetometer's performance, and what new engineering challenges will arise from its smaller size.

In general, a smaller magnetometer footprint is desirable because it increases its versatility in being able to inspect components with smaller dimensions. In addition, reducing the size of the secondary winding of a magnetometer or a magnetometer array improves sensitivity, because the signal is less diluted by averaging over a large area. Nevertheless, the minimal size of the magnetometer footprint will be limited by the minimal spatial wavelength requirement, determined by the necessary depth of penetration. For example, if one is to be able to see through $1/4''$ of aluminum, the imposed spatial wavelength needs to be on the order of an inch.

Another aspect of the practical design of a smaller version of the GMR magnetometer is making its base flexible, which is a property of the standard MWM. If a similar flexible circuit technology is to be used, one must address the question of how the distributed current drive primary winding is to be designed. Multiple turn windings are difficult to implement in a planar two-dimensional topology, so that in this case it would possibly be more appropriate to shape the surface current density by controlling the current, not the number of turns, of each winding segment.

Regardless of the exact implementation details, it is almost certain that the next stage in the process of adapting GMR magnetometer technology to practical applications is the design and implementation of a smaller, perhaps by a factor of a hundred in area, version of the GMR magnetometer prototype.

7.3.2 GMR magnetometer arrays

The ultimate goal of the GMR magnetometer effort is to be able to design analogs of the existing MWM sensor arrays to use GMR secondary elements, rather than secondary windings. In principle, this may be as simple as adapting an existing MWM array geometry by replacing the individual secondary elements with pre-manufactured GMR sensor chips. One of the questions that arises is whether it will be practical in this case to maintain the feedback loop configuration. While offering many advantages, the feedback connection does increase the size requirements on each array element, in addition to introducing unwanted cross-coupling between the individual array elements. Therefore in an array configuration the preferred mode of operation may be open-loop, in which case an alternative biasing method must be designed. For example, it may be possible to set the operating point by adding a DC offset to the primary current drive. Most likely, though, this would lead to impractically large current requirements for the primary, so that the preferred biasing method may be to place a suitable permanently magnetized flexible ferromagnetic polymer layer behind the sensor array. Ferromagnetic polymers are made by a suspension of small ferromagnetic particles. A further advantage of this approach is that it is relatively easy to incorporate the effect of a magnetizable layer in the model, due to its spatial uniformity. The presence of a magnetizable layer will concentrate the magnetic field intensity on the active side of the magnetometer array, but it has not yet been established whether this will lead to improvement or deterioration of the sensitivity to material faults.

With low frequency operation in scanning applications it may be necessary to incorporate some of the model changes that include media motion into the methods used to simulate such sensor arrays.

With the present homogeneous layer models, as the depth of the flaw's position is increased, the relative effect a material flaw has on the effective measured conductivity of the metal is reduced in magnitude, and is spread over a wider area. Therefore, in deep penetration applications it may be necessary to apply data filtering and transformations that combine

the signal from many individual pixels to reconstruct the original position of the flaw.

7.3.3 Applying the cylindrical geometry collocation point method to Rosette sensors

The cylindrical coordinate magnetometer method described in Chapter 3 has not yet been applied to practical magnetometers, although JENTEK's Rosette sensor arrays, which have the appropriate geometry, are already in use in a number of crack detection and fatigue monitoring applications. It is interesting to determine whether use of the cylindrical geometry model will lead to a performance improvement for these magnetometers. The validity of the dielectric equivalent of the model has already been confirmed by measurements with the circular dielectrometer in Chapter 3.

Appendix A

Definition of Symbols, Abbreviations, and Acronyms

Most of the mathematical symbols used in this document are shown in Table A.2. Symbols used only locally, and not meaningful outside of the paragraph that defines them, are usually not listed here. Not listed are also summation indices, such as j, ℓ, m, or n.

Bold upright Roman letters are used for vectors. Unit vectors are denoted by a hat accent '^' over the lowercase symbol. Subscripts in italics denote array or matrix indices and coordinate components, while upright Roman subscripts are considered part of the symbol's name. The coordinates used are: Cartesian (x, y, z), cylindrical (r, φ, z), and spherical (r, θ, φ).

Abbreviations and acronyms are listed in Table A.1.

Table A.1: Abbreviations and acronyms in alphabetical order.

DFT	Discrete Fourier Transform
EQS	Electroquasistatic
FFT	Fast Fourier Transform
FHT	Fast Hankel Transform
GMR	Giant Magnetoresistive
IDED*	Interdigitated Electrode Dielectrometer
MQS	Magnetoquasistatic
MUT	Material Under Test
MWM*	Meandering Winding Magnetometer
NDE	Non-Destructive Evaluation
SQUID	Superconducting Quantum Interference Device

Table A.2: Definition of symbols

Symbol	(Eq.) / Fig.	Page	Description
$\bar{}$ accent	(2.18), etc.	37	Normalized quantity

continued on next page

*MWM and IDED are trademarks of JENTEK Sensors, Inc.

continued from previous page

Symbol	(Eq.) / Fig.	Page	Description
$\hat{}$ accent	(2.1)	33	Complex amplitude. Also used for unit vectors and in the definition of the FHT
$\tilde{}$ accent	(2.40)	41	Implied $\cos(k_n x)$ factor
$\otimes$	(4.2)	83	Convolution
$[\![f(z)]\!]$			Discontinuous change in $f(z)$ across a boundary, usually at $z = 0$
$\mathbf{A}$, $A_y(x)$, $A_\varphi(r)$	(2.3)	34	Magnetic vector potential
A_n	(2.35), (3.15)	40, 65	Fourier component of A
a_m	(2.30)	39	Values of A at collocation points
a	(2.66)	47	a_m as a vector
a	3-2	70	Driven electrode radius
a_1, a_2	3-2	70	Inner and outer radii of sensing electrode
α_n	(3.5), (3.43)	63, 71	Zeros of $J_1(r)$ or $J_0(r)$
$\mathbf{B}$			Magnetic flux density
B_n	(2.61), (2.108)	45, 58	Bernoulli numbers
b	3-2	70	Inner radius of guard ring
b	(2.66)	47	Right hand side vector for matrix equation
b^n, b^0	(2.110)	58	Fourier components of the vector b
β, β_n	(3.14)	65	"Wavenumber" in cylindrical coordinates
$C_n^*(z)$	(2.89)	53	Complex surface capacitance density
C_n^*, C_0^*	(2.100)	55	Jump in the surface capacitance density across the electrode plane
C_∞^*	(2.106)	57	Asymptotic limit of C_n^* for high values of n
C_T	(2.112), (3.59)	59, 74	Transcapacitance of dielectric sensors
c	2-1, 2-4	37, 50	Primary winding width; driven electrode width
χ_m	(5.11)	143	Magnetic susceptibility $\chi_\mathrm{m} = \mu_\mathrm{r} - 1$
d	2-1, 2-4	37, 50	Secondary winding width; sensing electrode width

continued on next page

continued from previous page

Symbol	(Eq.) / Fig.	Page	Description
Δ	2-1	37	Winding thickness
δ	(2.15)	35	Skin depth
E			Electric field intensity
e			Base of natural logarithms
ϵ	(2.85)	53	Dielectric permittivity
ϵ_0			Dielectric permittivity of vacuum
ϵ^*	(2.87)	53	Complex dielectric permittivity, including conduction loss
ϵ_S	2-6	55	Dielectric permittivity of sensor substrate
$\mathcal{F}\{\}$			Fourier transform
F	(2.70), (3.38)	48, 69	Matrix used to compute transimpedance matrix from magnetic vector potential
$F(q)$	(4.1b)	82	Fourier transform function of $f(x)$
$F_S(q)$	(4.3b)	83	Sine transform function of $f(x)$
$f(x)$			Used to denote a generic function
$f(x)$	(2.61), (B.1), B-2	45, 175, 177	Infinite summation function for MWM
g	2-1	37	Gap between windings
$g(x)$	(2.108), (B.2), B-2	58, 175, 177	Infinite summation function for IDED
γ, γ_n	(2.14)	35	Magnetic diffusion complex wavenumber
H			Magnetic field intensity
h	4-2, 4-15	84, 101	Spacing between windings of distributed current drive
h	2-6	55	Dielectrometer substrate thickness
h	5-8	126	Sensor lift-off
I_D	1-1	20	Magnetometer drive current
I_S	1-4	22	Dielectrometer sense current
I_F	(5.6)	124	Secondary feedback winding current
i			Imaginary unit

continued on next page

continued from previous page

Symbol	(Eq.) / Fig.	Page	Description
i_1, i_2	(2.26)	38	Two-port terminal currents
$\mathbf{J}$			Electric current density
J_0, J_1, J_2			Bessel functions of the first kind
K	(2.30), (2.78)	39, 51	Number of collocation points per region
$K_\mathrm{S}(x), K_\mathrm{S}(r)$	(2.53), (3.26)	43, 67	Surface current density
$K_{\mathrm{S}n}$	(2.52), (3.23)	43, 66	Fourier component of $K_\mathrm{S}(x)$ or $K_\mathrm{S}(r)$
k, k_n	(2.24)	38	Wavenumber, $k_n = 2\pi n/\lambda$
L	4-2	84	Period (wavelength) of current drive envelope function
λ	2-1, 2-4	37, 50	Periodic sensor wavelength
M	(2.66)	47	Matrix of collocation point constraints
M^n, M^0, M', M''	(2.67), (2.104)	47, 56	Fourier components and other submatrices of M
M_L			Meander length, total length of windings/electrodes
μ			Magnetic permeability
μ_0			Magnetic permeability of vacuum
μ_r			Relative magnetic permeability $\mu_\mathrm{r} = \mu/\mu_0$
μ^*			Complex magnetic permeability, including magnetic, but not conduction, loss
N	(2.59)	45	Upper limit of needed Fourier modes
ω			Angular frequency of excitation
$\mathbf{p}$	(2.59)	45	Magnetic dipole moment
$\Phi(x), \Phi(r)$	(2.72), (3.41)	49, 71	Electric potential
Φ_n	(2.81), (3.51)	51, 73	Fourier components of $\Phi(x)$ or $\Phi(r)$
Ψ	(4.33)	97	Magnetic scalar potential
Q_n	(3.7), (3.45)	63, 71	Bessel series normalization coefficients

continued on next page

continued from previous page

Symbol	(Eq.) / Fig.	Page	Description
R	(3.5), (3.43), (4.42)	63, 71, 102	Bessel series expansion radius, chosen much greater than sensor dimensions
$R_n(z)$	(2.39)	41	Surface reluctance density
R_n	(2.51)	43	Jump in the surface reluctance density across the winding plane
R_∞	(2.59)	45	Asymptotic limit of R_n for high values of n
r_m	(3.46)	72	Collocation points in cylindrical coordinates
r_m^*	(3.47)	72	Integration interval limits in cylindrical coordinates
r_{F}	(5.6)	124	Radius of secondary feedback coil
ρ			Resistivity $\rho = 1/\sigma$
$\rho_\parallel, \rho_\perp$	Section 5.1.1		Directional resistivity, parallel and perpendicular to direction of magnetization
$\rho_\uparrow, \rho_\downarrow$	(5.4)	116	Ferromagnetic metal resistivities due to spin-up and spin-down electrons
$\rho_{\uparrow\uparrow}, \rho_{\uparrow\downarrow}$	(5.5)	117	Resistivity in parallel and antiparallel states of GMR superlattice
$\mathrm{sinc}(x)$	(4.7)	83	$\mathrm{sinc}(x) = \sin(x)/x,\ x \neq 0;\ \mathrm{sinc}(0) = 1$
σ			Electric conductivity, $\mathbf{J} = \sigma\mathbf{E}$
σ_{coil}			Conductivity of the MWM windings
$\sigma_{\mathrm{S}}^*(x), \sigma_{\mathrm{S}}^*(r)$	(2.98)	55	Jump in $\epsilon^*\mathbf{E}$ across $z = 0$ boundary
$\sigma_{\mathrm{S}}^* n$	(2.101)	55	Fourier components of $\sigma_{\mathrm{S}}^*(x)$ or $\sigma_{\mathrm{S}}^*(r)$
t	(2-6), (4-11)	55, 96	Material layer thicknesses
θ	(3.59)	74	Arc angle of the sensing electrode of the circular dielectrometer
u	(6.4)	146	x-component of the convection velocity
$u_0(x)$			Unit impulse functional
V_{D}	1-4	22	Dielectrometer driven electrode voltage
$V_{\mathrm{S}}, V_{\mathrm{S1}}, V_{\mathrm{S2}}$	1-1	20	Magnetometer secondary winding voltages

continued on next page

continued from previous page

Symbol	(Eq.) / Fig.	Page	Description
$\mathbf{v}$	(6.1)	145	Convection velocity
v_m	(2.78)	51	Values of the electric potential Φ at the collocation points
v		56	v_m as a vector
v_1, v_2	(2.26)	38	Two-port terminal voltages
v'	Section 6.1.6		Part of the secondary winding terminal voltage, associated with one of its legs
W	4-8	93	Distributed current drive magnetometer width
W	4-15	101	Radius where the first order Bessel function has its first zero
w_j	Tbl. 4.2, 4.3	99, 102	Turns per winding for distributed current drive
w_F	(5.6)	124	Number of turns in secondary feedback coil
x_m	(2.34), (2.79)	40, 51	Collocation points in Cartesian coordinates
x_m^*	(2.33), (2.80)	40, 51	Integration interval limits in Cartesian coordinates
Y, Y_{11}, etc.	(2.26)	38	Two-port admittance matrix and its elements
$Y_{\ell m}(\theta, \varphi)$	(4.37), Tbl. 4.1	97, 98	Spherical harmonic functions
Y_0, Y_1			Bessel functions of the second kind
Z, Z_{11}, etc.	(2.26)	38	Two-port impedance matrix and its elements

Appendix B

Infinite Sums over Fourier Modes

This appendix discusses in some detail the properties of the infinite summation functions that arise in the collocation point methods, discussed in Chapters 2 and 3.

As illustrated in Section 2.1, while summing over the Fourier modes, past a certain mode it is possible to carry out the summation over the remaining modes in a single operation, using equations (2.59) and (2.60). Equation (2.61), repeated here for convenience, defines a function $f(x)$, which results from the evaluation of the Fourier series:

$$f\Big(\frac{x}{2\pi}\Big) = \sum_{n=0}^{\infty} \frac{\sin(2n+1)x}{(2n+1)^2} = -\frac{1}{2}\int_0^x \ln\Big(\tan\frac{t}{2}\Big)\,dt \tag{B.1}$$

This function, given by the integral $\int \ln(\tan x)\,dx$, appears often enough in Fourier series analyses that perhaps it deserves to be given its own name. A relative of this function also appears in the collocation point methods used to model the IDED in Section 2.2:

$$g\Big(\frac{x}{2\pi}\Big) = \sum_{n=1}^{\infty} \frac{\sin(nx)}{n^2} = -\int_0^x \ln\Big(2\sin\frac{t}{2}\Big)\,dt \tag{B.2}$$

Several aspects of these Fourier series are discussed in this appendix. Section B.1 presents the infinite sums for both Cartesian and cylindrical coordinate systems, some of their properties, and methods of computing them. Section B.2 presents a way of altogether eliminating the need for evaluating the sum in equation (B.1). No computational advantage is achieved via this alternative method, because in the end it appears again as $\int \ln(\tan x)\,dx$, but this alternative formulation suggests a way to approach the cylindrical coordinate case, where the sum cannot be evaluated in closed form.

B.1 Overview

The values of the magnetic vector potential at the collocation points are determined by applying the appropriate boundary conditions over a set of intervals, each containing one collocation point, as described in Section 2.1. After carrying out the integration over these intervals, the

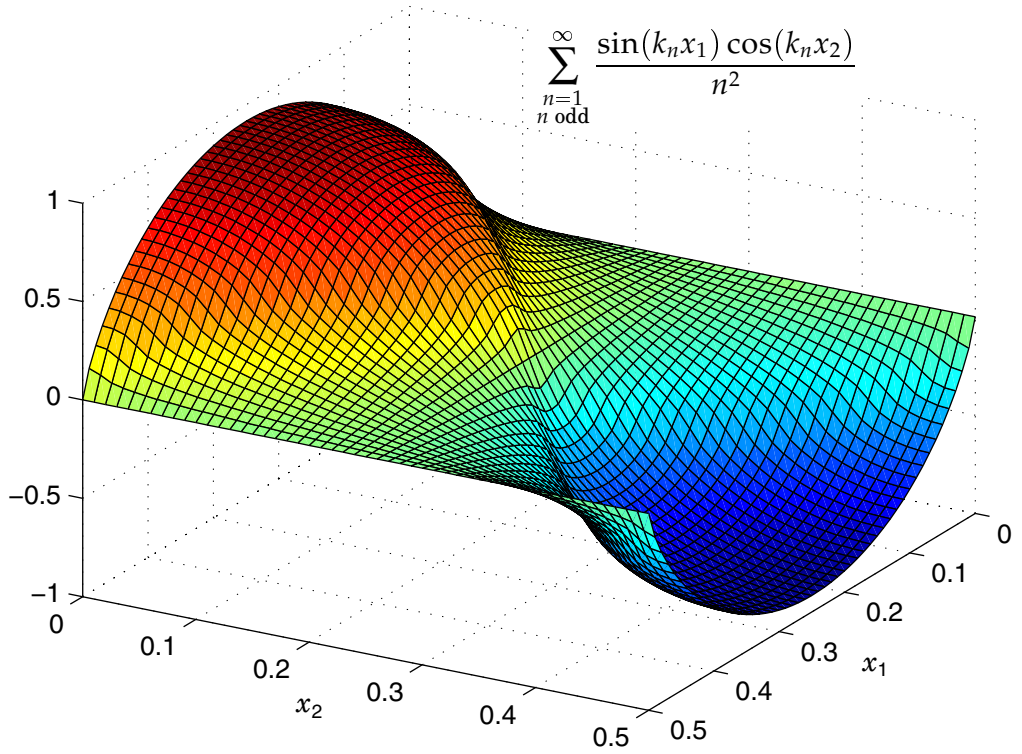

Figure B-1: Three-dimensional plot of the infinite summation function in equation (B.3).

need arises to evaluate the following function:

$$f(x_1, x_2) = \sum_{\substack{n=1 \\ n \text{ odd}}}^{\infty} \frac{\sin(k_n x_1)\cos(k_n x_2)}{n^2} \tag{B.3}$$

where x_1 is one of the integration interval limits x_m^*, and x_2 is one of the collocation points x_m. In fact, all such combinations need to be evaluated. The surface plot of this function is shown in Figure B-1.

Equation (B.3) can be simplified using a product formula, so that it is evaluated via two applications of the single variable function in equation (B.1). The surface plot is shown as a comparison to the cylindrical case, where no such product formula exists.

The function $f(x)$ in equation (B.1) is plotted in Figure B-2. One interesting characteristic of this function is that its derivative at its zeros is infinite. This can be seen by taking the derivative in its definition, which results in a sum of the form $\sum(1/n)$. This turns out to be of practical significance, because when used in the collocation point methods, often differences of its values are taken for arguments very near zero. An attempt was made once to evaluate this function via interpolation in a look-up table, but significant errors arose no matter how dense the interpolation points near zero were. Interpolation cannot handle infinite derivatives adequately, since that requires the interpolation points to be infinitely dense in this vicinity. Consequently, it is always necessary to use the Bernoulli number series given in equation (2.62) to evaluate the function.

The function $g(x)$, defined in equation (B.2), is also shown in Figure B-2. It includes the

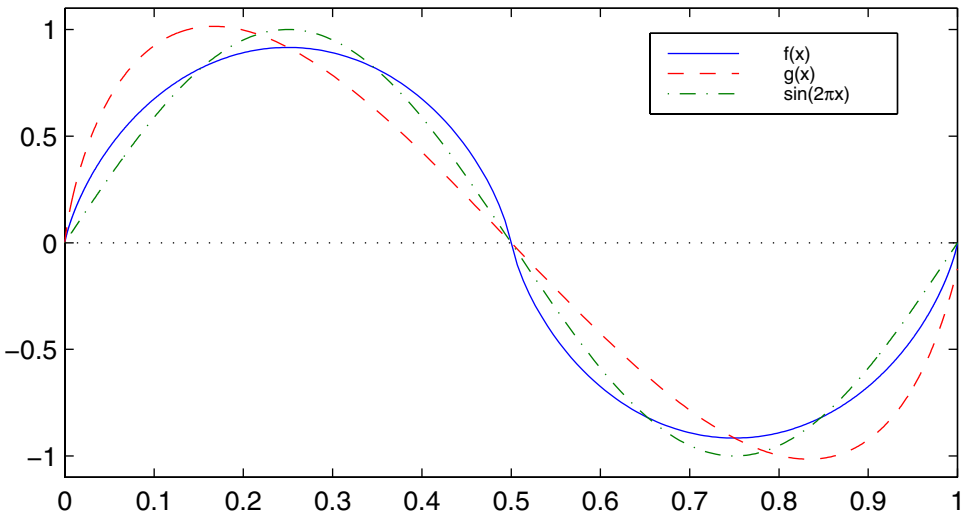

Figure B-2: Plot of the functions $f(x)$ and $g(x)$. A sinusoid with the same period is shown for comparison.

even Fourier modes, manifested as a skew toward zero. Its derivative is also infinite at $x = 0$, but not at $x = 1/2$.

As seen in equations equation (3.30) and equation (3.56), analogous infinite summation series arise in cylindrical coordinates:

$$f(r_1, r_2) = \sum_{n=1}^{\infty} \frac{J_1(\alpha_n r_1) J_0(\alpha_n r_2)}{\alpha_n^2 J_0^2(\alpha_n)} \qquad \alpha_n : \; J_1(\alpha_n) = 0 \tag{B.4}$$

and

$$g(r_1, r_2) = \sum_{n=1}^{\infty} \frac{J_2(\alpha_n r_1) J_1(\alpha_n r_2)}{\alpha_n^2 J_1^2(\alpha_n)} \qquad \alpha_n : \; J_0(\alpha_n) = 0 \tag{B.5}$$

A surface plot of $f(r_1, r_2)$ in equation (B.4) is shown in Figure B-3. At this time there appears to be no efficient method of calculating it, other than carrying out the summation itself up to a sufficiently high number of terms. Its derivative with respect to r_1 is also infinite at $r_1 = r_2 = 0$.

The lack of an efficient method of calculating the sum in equations (B.4) and (B.5) [82] is what motivated the search for an alternative approach to setting up the constraining equations for the collocation points, which avoids the infinite sums.

B.2 Alternative formulation

The magnetoquasistatic case is considered in this section. The infinite summation arises from the need to express the surface current density K_S in terms of the magnetic vector potential A_y, which in turn is expressed in terms of its values a_m at the collocation points x_m. The boundary conditions of the surface current density, now a function of a_m, can be integrated over a set of intervals to create the constraints needed to solve for the unknowns a_m. In the Fourier domain, equation (2.52), repeated here for convenience, expresses the surface current

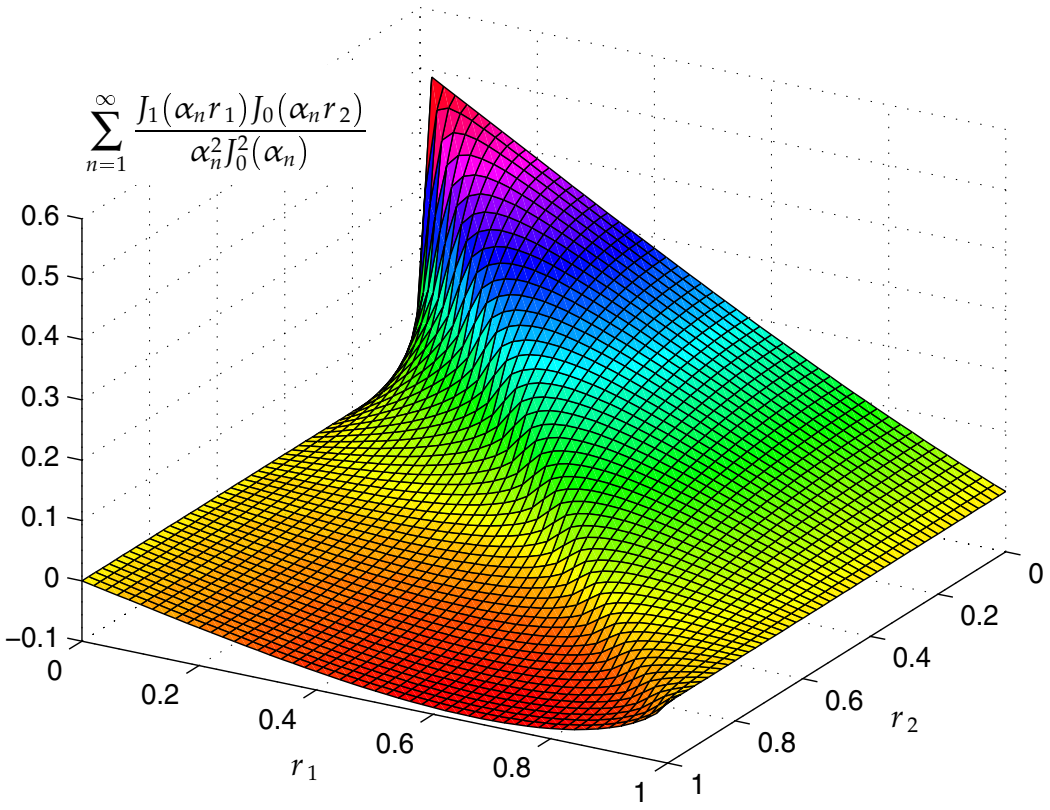

Figure B-3: Three-dimensional plot of the infinite summation function in equation (B.4).

density in terms of the vector potential:

$$K_{Sn} = R_n k_n A_n \tag{B.6}$$

As discussed in Section 2.1.6, at high values of n the surface reluctance density R_n approaches a common value, R_∞, which is used for all n in equation (B.6), allowing the summation of all modes to be carried out in a single step.

The new idea here is to find an expression of $K_S(x)$ in terms of $A_y(x)$ ***in the x-domain***, fully bypassing the Fourier series operations. The question that needs to be answered is this: If the sine series coefficients of a function $F(x)$ are A_n, then which is the function $G(x)$ whose sine series coefficients are $k_n A_n$? In other words, given that

$$F(x) = \sum_{n=1}^{\infty} A_n \sin(k_n x) \qquad\qquad k_n = \frac{2\pi n}{\lambda} \tag{B.7}$$

and

$$G(x) = \sum_{n=1}^{\infty} A_n k_n \sin(k_n x) \tag{B.8}$$

how is $G(x)$ expressed in terms of $F(x)$?

Multiplication by the transform variable in one domain corresponds to differentiation in

the other. Therefore, since

$$A_n = \frac{2}{\lambda}\int_{-\lambda/2}^{\lambda/2} F(x)\sin(k_n x)dx \tag{B.9}$$

then via integration by parts

$$A_n k_n = \frac{2}{\lambda}\int_{-\lambda/2}^{\lambda/2} F'(x)\cos(k_n x)dx \tag{B.10}$$

While differentiation does yield the necessary factor of k_n, it also changes all sines to cosines, so that another operation is necessary to reach $G(x)$, derived later in this section.

There is another way of thinking about this problem. Consider the full exponential Fourier series:

$$F(x) = \sum_{n=-\infty}^{\infty} A_n e^{-ik_n x} \qquad\qquad k_n = \frac{2\pi n}{\lambda} \tag{B.11}$$

In this formulation the function $G(x)$ must be expressed as:

$$G(x) = \sum_{n=-\infty}^{\infty} |k_n| A_n e^{-ik_n x} \tag{B.12}$$

When considering the full exponential series, the operation in the Fourier domain that transforms A_y to K_S is multiplication by ***the absolute value of*** k_n. From a physical perspective, this comes about from the fact that the exponential component $e^{\pm\gamma z}$ of the solutions in equation (2.13) must have a negative real part for $z > 0$, for both positive and negative values of the wavenumber k_n, to make sure that the field decays to zero at infinity. With negative values of k_n the solution with the opposite sign in the exponent must be taken.* This is equivalent to multiplication by the sign function in reciprocal space, effectively converting the cosines resulting from the differentiation back to sines. Another example of the use of the full exponential Fourier series in the collocation point model is given in Section 6.1.

For the continuous Fourier transform, multiplication by the sign function in the reciprocal domain corresponds to convolution with its transform in the real domain. The equivalent in the discrete series case turns out to be circular convolution with the cotangent function. To show this, substitute equation (B.10) in equation (B.8), having returned to the original sine

*For the purpose of this discussion, the definition of γ, given by equation (2.14), is altered so that γ incorporates the sign of k, i.e. $\gamma = \mathrm{sgn}(k)\sqrt{k^2 + i\omega\sigma\mu}$. This is unlike the convention used in Section 6.1, where the change of sign discussed in this paragraph is implicit in the definition of γ in equation (6.7), where it has a positive real part for both positive and negative values of k.

series form:

$$\begin{aligned} G(x) &= \sum_{n=1}^{\infty} \sin(k_n x) \frac{2}{\lambda} \int_{-\lambda/2}^{\lambda/2} F'(t) \cos(k_n t) dt = \frac{2}{\lambda} \int_{-\lambda/2}^{\lambda/2} F'(t) dt \sum_{n=1}^{\infty} \sin(k_n x) \cos(k_n t) \\ &= \frac{1}{\lambda} \left\{ \int_{-\lambda/2}^{\lambda/2} F'(t) dt \sum_{n=1}^{\infty} \sin k_n (x-t) + \int_{-\lambda/2}^{\lambda/2} F'(t) dt \sum_{n=1}^{\infty} \sin k_n (x+t) \right\} \\ &= \frac{2}{\lambda} \int_{-\lambda/2}^{\lambda/2} F'(t) dt \sum_{n=1}^{\infty} \sin k_n (x-t) \\ &= \frac{1}{\lambda} \int_{-\lambda/2}^{\lambda/2} F'(t) \cot \frac{\pi}{\lambda} (x-t)\, dt \end{aligned} \tag{B.13}$$

Equation (B.13) makes it possible to get an expression of $K_S(x)$ in terms of a_m directly from equation (2.30). Taking the derivative of the vector potential function

$$A'_y(x) = \frac{a_{m+1} - a_m}{x_{m+1} - x_m} \qquad\qquad x_m < x < x_{m+1} \tag{B.14}$$

and switching to normalized quantities (i.e. $\lambda \to 1$), the following expression for $K_S(x)$ is obtained:

$$\begin{aligned} K_S(x) &= R_\infty \int_{-1/2}^{1/2} A'_y(t) \cot \pi(x-t)\, dt \\ &= R_\infty \sum_{m=1}^{4K-1} \frac{a_{m+1} - a_m}{x_{m+1} - x_m} \left\{ - \int_{x_m - 1/2}^{x_{m+1}-1/2} \cot \pi(x-t)\, dt - \int_{-x_{m+1}}^{-x_m} \cot \pi(x-t)\, dt \right. \\ &\qquad \left. + \int_{x_m}^{x_{m+1}} \cot \pi(x-t)\, dt + \int_{1/2-x_{m+1}}^{1/2-x_m} \cot \pi(x-t)\, dt \right\} \end{aligned} \tag{B.15}$$

where all four quarter periods are considered separately, since the cotangent function does not have the same symmetry. It has also been taken into consideration that $A'_y(x)$ is odd with respect to the $x = 0$ point, and even with respect to $x = 1/2$, which is a consequence of the symmetry properties of $A_y(x)$ given in equation (2.29). Carrying out the integration,

$$\begin{aligned} K_S(x) = \frac{R_\infty}{\pi} \sum_{m=1}^{4K-1} \frac{a_{m+1} - a_m}{x_{m+1} - x_m} \Bigg\{ &- \ln \left| \sin \left[\pi(x - x_m) + \frac{\pi}{2} \right] \right| + \ln \left| \sin \left[\pi(x - x_{m+1}) + \frac{\pi}{2} \right] \right| \\ &- \ln \left| \sin \left[\pi(x + x_{m+1}) \right] \right| + \ln \left| \sin \left[\pi(x + x_m) \right] \right| + \ln \left| \sin \left[\pi(x - x_m) \right] \right| - \ln \left| \sin \left[\pi(x - x_{m+1}) \right] \right| \\ &+ \ln \left| \sin \left[\pi(x + x_{m+1}) - \frac{\pi}{2} \right] \right| - \ln \left| \sin \left[\pi(x + x_m) - \frac{\pi}{2} \right] \right| \Bigg\} \end{aligned} \tag{B.16}$$

Converting the terms containing $\pi/2$ to cosines and combining them with the corresponding

sine terms finally yields

$$K_{\mathrm{S}}(x) = \frac{R_\infty}{\pi} \sum_{m=1}^{4K-1} \frac{a_{m+1} - a_m}{x_{m+1} - x_m} \Big[\ln\big|\tan \pi(x - x_m)\big| + \ln\big|\tan \pi(x + x_m)\big| \\ - \ln\big|\tan \pi(x - x_{m+1})\big| - \ln\big|\tan \pi(x + x_{m+1})\big| \Big] \tag{B.17}$$

It can be seen in equation (B.17) that building the matrix M' of Section 2.1.6 involves taking the integral $\int \ln(\tan x)\, dx$, which, as seen in equation (B.1), is the same as evaluating the function $f(x)$, defined by the infinite sum. In other words, while completely avoiding the infinite sum, no direct benefit has been achieved, except for deriving a proof for equation (B.1). The indirect benefit is that an alternative approach is now available for handling the analogous problem in cylindrical coordinates.

Following the same steps, if the Bessel series expansion of a function $F(r)$ is given by

$$F(r) = \sum_{n=1}^{\infty} A_n J_1\Big(\frac{\alpha_n}{R} r\Big) \qquad 0 < r < R \qquad \alpha_n :\ J_1(\alpha_n) = 0 \tag{B.18}$$

then how can the function $G(r)$, defined by

$$G(r) = \sum_{n=1}^{\infty} \frac{\alpha_n}{R} A_n J_1\Big(\frac{\alpha_n}{R} r\Big) \tag{B.19}$$

be expressed in terms of $F(r)$ in the r-domain? As in the Cartesian case, differentiation with respect to r yields the necessary factor of α_n/R, but it also changes J_1 to J_0. Therefore it is necessary to derive the operation that would change J_0 back to J_1, analogous to the circular convolution with the cotangent in the Cartesian case.

Because of the lack of (finite) product formulas for Bessel functions [82], the last step appears to be a very difficult task, and is still open for further study. Should this problem be solved, it would lead to tremendous improvement of the computational efficiency of the collocation point method in cylindrical coordinates.

Appendix C

Error analysis

Although at this stage of the development of the new GMR sensor-based magnetometer technology the goal is to establish the basic principles of operation and to demonstrate feasibility, it is important to consider the magnitude, nature, and source of the measurement errors in one representative experiment. The conductivity/lift-off measurements described in Section 5.4 are a good choice, because they are the most common type of measurement made with the MWM family of magnetometers and magnetometer arrays.

The results of the measurements in Section 5.4, previously listed in Table 5.1, are repeated in Table C.1, for all twenty sets, accompanied by the percent deviation of the estimated properties from the reference values. For the lift-off, the latter are obtained from the caliper thicknesses of the plastic shims, and are listed in the last column of the table. These nominal lift-off values are listed with only one digit after the decimal point, because of local variations of the shim thickness, and because dust and surface roughness affect the total lift-off when several shims are used. The reference metal conductivities are taken from Table 5.2, and are repeated in Table C.1 at the top of the columns for each of the three metal samples.

It may be observed in the data in Table C.1 that the lift-off errors are much smaller than the conductivity errors. This is a known characteristic of all model-based magnetometer measurements. It is due to the much higher sensitivity of the sensor response to lift-off, compared to other properties of the test structure. The sensitivity and selectivity of a measurement to a physical property may be determined by analysis based on singular value decomposition of the corresponding Jacobian matrix [1, 13]. The high sensitivity to lift-off is also the main reason why it is chosen to be one of the unknown properties in most measurement grids, because if a grid is built with an assumed lift-off value, there is a danger that a small difference in the actual physical lift-off, possibly due to surface roughness or dust, would lead to large errors in the estimated properties.

Each data point in Table C.1 is the average of seven sequential measurements. The averaging is carried out ***after*** the grid look-up has been performed, because in this way the data are compensated for actual lift-off differences among the seven individual measurements, which may be due, for example, to varying pressure applied by the operator to the material/sensor interface. The availability of more than one measurement per data point makes it possible to compute standard deviations, as a measure of the noise. It is unnecessary to list these standard deviations for every data point in Table C.1, because there is little variation among them for the different data points in this measurement. The averages of the standard deviations of the conductivity and lift-off estimates are 0.43% and 0.046% respectively.

The measurement noise, characterized by the standard deviation values listed above, is

Data set	***Cu 110***, $\sigma = 58$ MS/m				***Al 6061***, $\sigma = 27.3$ MS/m				***Al 2024***, $\sigma = 17.5$ MS/m				Nominal
	cond. [MS/m]	% error	lift-off [mm]	% error	cond. [MS/m]	% error	lift-off [mm]	% error	cond. [MS/m]	% error	lift-off [mm]	% error	lift-off [mm]
1	59.2	+2.1	3.27	+0.8	29.5	+8.1	3.22	−2.5	18.0	+2.9	3.26	−1.3	3.3
2	59.2	+2.0	4.11	+0.2	28.9	+5.9	4.04	−1.5	17.8	+2.0	4.09	−0.2	4.1
3	58.7	+1.3	4.80	+0.0	28.7	+5.0	4.70	−2.2	17.8	+1.5	4.76	−0.8	4.8
4	58.3	+0.5	5.61	+0.2	28.6	+4.6	5.52	−1.3	17.6	+0.6	5.61	+0.1	5.6
5	57.8	−0.3	6.52	+0.3	28.3	+3.7	6.43	−1.1	17.6	+0.3	6.49	−0.2	6.5
6	57.1	−1.5	7.36	+0.8	28.1	+2.9	7.25	−0.7	17.5	+0.0	7.33	+0.4	7.3
7	55.7	−4.0	8.02	+0.3	27.4	+0.4	7.91	−1.2	17.3	−1.3	7.99	−0.2	8.0
8	56.1	−3.3	8.86	+0.6	27.5	+0.9	8.75	−0.6	17.4	−0.5	8.80	+0.0	8.8
9	54.3	−6.4	9.50	+1.0	26.8	−2.0	9.37	−0.3	17.1	−2.1	9.41	+0.1	9.4
10	55.2	−4.8	10.29	+0.9	27.0	−1.1	10.19	−0.1	17.2	−1.5	10.27	+0.6	10.2
11	53.5	−7.8	10.94	+0.3	26.4	−3.3	10.84	−0.5	17.0	−2.6	10.89	−0.1	10.9
12	53.0	−8.7	11.74	+0.4	26.3	−3.8	11.66	−0.4	16.7	−4.5	11.72	+0.2	11.7
13	50.3	−13.3	12.76	+1.3	25.6	−6.3	12.55	−0.4	16.7	−4.3	12.61	+0.1	12.6
14	51.1	−11.9	13.50	+0.7	25.7	−5.9	13.37	−0.2	16.4	−6.3	13.51	+0.8	13.4
15	49.5	−14.6	14.15	+0.4	25.1	−8.0	14.01	−0.6	16.1	−8.2	14.11	+0.1	14.1
16	46.6	−19.6	14.94	+0.3	24.2	−11.5	14.83	−0.5	16.3	−6.8	14.92	+0.1	14.9
17	46.3	−20.2	15.36	−0.9	23.7	−13.0	15.25	−1.6	16.2	−7.3	15.31	−1.2	15.5
18	46.6	−19.6	16.15	−0.9	24.1	−11.8	16.06	−1.5	15.7	−10.3	16.11	−1.2	16.3
19	45.1	−22.3	16.80	−1.2	23.4	−14.1	16.71	−1.7	15.4	−12.1	16.77	−1.3	17.0
20	43.2	−25.5	17.64	−5.7	22.6	−17.3	17.52	−6.3	15.6	−10.6	17.61	−5.8	18.7
Average error magnitude, sets 1–12:		**3.6**		**0.5**		**3.5**		**1.0**		**1.7**		**0.4**	

Table C.1: Results of the conductivity/lift-off measurements of Section 5.4, including all twenty sets, and showing percentage errors. The lift-off data are referred to the nominal lift-off values, listed in the last column. The conductivity errors are calculated with respect to the values reported in the literature for these alloys, listed in the first line of the table. The percentage errors shown in bold type in the bottom line are the average of the absolute values of the errors of the first twelve data sets.

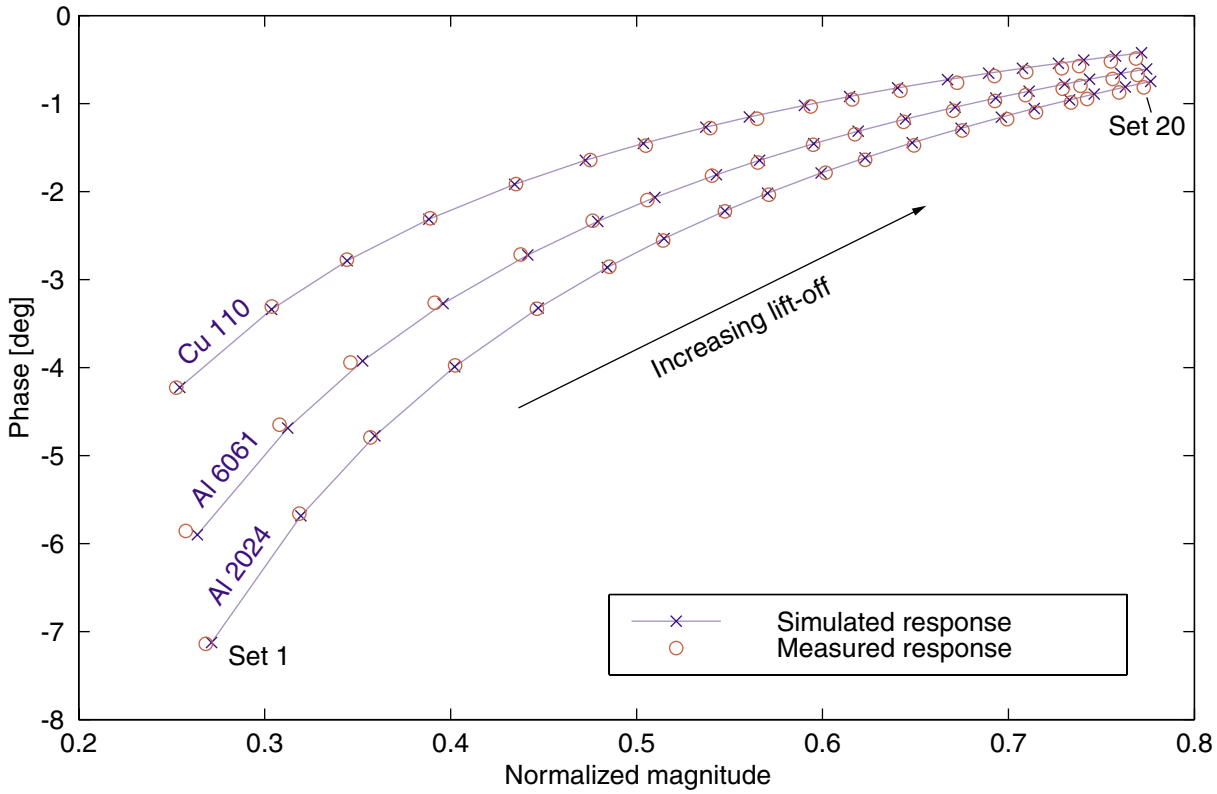

Figure C-1: Comparison between simulated and measured response of the magnetometer in the conductivity/lift-off measurements. A systematic error is evident at higher lift-offs that results in an offset of every measurement point toward the lower left of the corresponding simulated point. This is attributed to unmodeled changes in the primary winding current, due to the parasitic inter-winding capacitance.

clearly not enough to account for the magnitude of the errors reported in Table C.1. The errors due to instrumentation noise, etc. are not directly relevant to this research effort, whose focus is on the validity of the semi-analytical models, and on the demonstration of the principle of operation. Furthermore, the deviations from the reference values in Table C.1 manifest a clear bias, which is in the same direction and increases in magnitude as the lift-off increases. They are clearly due not to noise, which would result in uncorrelated random errors, but to the effects of unmodeled or parasitic magnetometer behavior.

To investigate the latter point further, it is useful to move from considering errors in property space to magnetometer magnitude/phase space. The data are shown in a magnitude/phase plot in Figure C-1, which also shows the simulated sensor response for the three samples, using the conductivity values from Table 5.2 and the measured lift-off values in Tables 5.1 and C.1.

The data in Figure C-1 clearly demonstrate the presence of systematic error that results in an offset of every measurement point toward the lower left of the corresponding simulated point at higher lift-offs. This error is most likely due to the parasitic self-capacitance of the primary winding. The instrumentation only measures the primary winding current at the magnetometer terminals, which means that the effect of parasitic cable and inter-winding capacitance is not eliminated. Although the frequency at which the data was taken, 12.6 kHz, is far below the self-resonant frequency of the primary winding, which is on the order of a

megahertz, the resulting negative phase shift and magnitude decrease are nonetheless non-negligible. Although this difference in measured and actual drive current is compensated for in the calibration step, as described in Appendix D, it is quite sensitive to the loss factor of the resonance, which changes in the presence of materials with finite conductivity, and is therefore dependent on the lift-off. As magnetometers with smaller dimensions and fewer winding turns are designed, this source of error will be greatly diminished.

Although all errors in the figure are small, the corresponding errors of the estimated properties at higher lift-offs can be large. For example, the copper conductivity for set 20 is more than 25% off. This is due to the loss of sensitivity of the measurement as the material is moved farther away from the magnetometer. This loss of sensitivity can be observed on the grid in Figure 5-8, where the density of grid lines is high in the upper right corner of the grid. When the grid cells are narrow, small changes in signal magnitude or phase result in large changes of the estimated properties.

It can also be observed in Table C.1 that the error increases somewhat at the lowest lift-off values, so that there is an optimal range of the lift-off, approximately 5–7 mm, where the estimated conductivity is most accurate. Being too close to the sensor windings also reduces the accuracy, since the effects of the nonzero winding thickness become stronger as the separation between the windings and the metal samples becomes smaller and comparable to the thickness of the windings.

Although it is expected that the errors due to parasitic and unmodeled effects will become less significant as the magnetometer design is improved and its size is reduced, it is also possible to improve the accuracy of a particular measurement significantly by performing a two-point reference calibration instead of the air calibration used in Section 5.4. In this approach the calibration parameters are chosen to ensure that the measured response matches the simulated response at two points in magnitude/phase space that are closely spaced and positioned on either side of the expected data point. Thus the precision of the estimated properties in this range can be made arbitrarily high, at the expense of precision in other areas of the grid. The trade-offs of the different calibration methods are discussed in more detail in Appendix D, which also compares the measurement errors associated with them. The average percentage error magnitudes reported in the bottom line of Table C.1 are used for a quantitative comparison between the two methods.

This appendix has described the measurement errors of the conductivity/lift-off measurements and has discussed the source and nature of these errors. As the new technology and numerical techniques mature, more research will be needed to analyze the performance of the magnetometers and to develop sensor improvements that minimize such measurement errors.

Appendix D

Calibration methods

In this context calibration refers to the processing step applied to raw impedance analyzer data before they are passed through the measurement grid for parameter estimation, and to the methods used in obtaining the parameters used in this step. The methods described in this appendix have been developed at JENTEK Sensors, Inc., and are an integral component of JENTEK's copyrighted GridStation™ software environment [83].

The calibration step is in general necessary because of the presence of unmodeled parasitic effects of a physical nature, and because the instrumentation itself can introduce magnitude and phase errors. The raw data transformation is a very simple linear operation of the form

$$\overline{Z} = K \cdot Z - Z_{\text{off}} \tag{D.1}$$

where Z is the raw complex measurement magnitude, and $\overline{Z}$ is the complex magnitude used for parameter estimation. The two coefficients K and Z_{off} are also complex numbers.

Both K and Z_{off} have a physical interpretation. The constant offset term Z_{off} represents the parasitic coupling of the primary drive to the secondary signal, which can be due to cable capacitance and inductive pick-up, unmodeled sensor interconnect traces, etc.

The phase angle of the complex parameter K compensates for phase offsets, usually introduced by the interface electronics and the impedance analyzer. For the magnetometer in Chapter 5, there is another source of phase error. Due to its relatively high total number of turns, the primary winding has a large inductance, typically on the order of 1 mH. This in itself is not a problem, since all measurements are referred to the current in the primary. The unknown phase offset is introduced by the self-capacitance of the winding, which cannot be eliminated from the overall sensor transfer function, because the primary current is measured at its terminals, while the capacitance is distributed across the windings. This introduces phase angle that is dependent on the frequency of excitation, on the resistance of the winding, which can change with temperature, etc.

The absolute value of K scales the magnitude of the sensor signal to match the corresponding magnitude on the measurement grid. In general it is not practical to attempt to obtain the exact magnitude in the models, for several reasons: Various stages of the equipment have amplification that is not known with high precision. Furthermore, preamplifier gain stages in JENTEK instruments may have variable gain, used to tune the instrument to the dynamic range with optimal signal to noise ratio. Sometimes a new sensor is designed that has exactly the same parameters as an existing sensor, such as wavelength, gap, etc., but which has a larger or smaller footprint. In such cases the same measurement grids may be used, with the extra scale factor absorbed in the calibration step. Finally, from a practical point of view, it is

easier not to have to keep track of the numerous scale factors introduced at various stages of the measurement process.

Based on the arguments outlined so far, it is clear that the complex scale factor K is always needed. On the other hand, under ideal conditions Z_{off} may be taken to be zero. Use of a calibration step makes it possible to normalize all grids in Chapter 5 to the simulated sensor response in air, which makes grid visualization and interpretation easier.

The rest of the appendix describes specific methods for obtaining the calibration parameters, K and Z_{off}, used in a particular measurement.

D.1 Single point air calibration

This is the simplest calibration method. It involves making a measurement with the sensor in air, and taking K to be the ratio of the simulated sensor complex magnitude in air and the measured complex magnitude. This method assumes that there is no parasitic coupling, i.e. $Z_{\text{off}} = 0$.

The advantages of this method are its simplicity and that it does not involve measurement standards. Unlike calibration on standard parts, whose properties may not be known exactly and may shift with aging, the electromagnetic properties of air are known and universal. As discussed later in Section D.3, where the two methods are compared, an additional positive aspect of air calibration is that it does not bias the measurement accuracy to be better for a particular range of estimated property values.

Air calibration gives good results only if the sensors' parasitic coupling is negligible. For example, it is not a good choice for the experiment in Section 3.3, because the circular dielectric sensors have non-negligible parasitic coupling of the driven electrode to the sensing electrode traces and to the leads that connect the dielectrometer to the buffer amplifier. On the other hand, the success with which this method has been applied to the GMR magnetometer in Chapter 5 implies that the parasitic coupling in that type of magnetometer is indeed negligible.

D.2 Air and shunt calibration

In general, two data points are needed to determine both K and Z_{off} uniquely. This method takes the point of view that Z_{off} is a measurable physical quantity. It is obtained by shunting, or disconnecting if appropriate, the secondary sensing element while driving the primary, and measuring the resulting signal level. This signal is due entirely to parasitic coupling.

The value of K is then determined by an air measurement, as with the single point air calibration method, after having subtracted the measured offset Z_{off} from the instrument complex magnitude in air.

While this method is very useful for MWM measurements, it cannot be applied to the GMR magnetometer, since with the secondary in a feedback loop it is not possible to shunt or disconnect it in a meaningful way: disconnecting at the output of the loop would ignore parasitic pickup by the loop components, which is most likely the dominant source, while disconnecting the GMR sensor itself prevents loop operation altogether.

D.3 Two point reference part calibration

The two complex calibration parameters may alternatively be obtained from measurements at any two points on the grid, by solving the resulting system of two linear equations. This method is very useful in a number of different cases.

If a property is to be measured with very high precision, and it is known ahead of time what its value is likely to be approximately, then by choosing two points on the grid in close proximity to the unknown, it is possible to guarantee that this region of the grid is in very good agreement with the standard used for the measurement. For example, this occurs in situations where the purpose of the measurement is not to obtain the absolute value of a physical property of the material, which may be known, but to capture with high precision local variations in this property. The most common example of this is in conductivity/lift-off measurements, where the sensor is calibrated on a sample of known conductivity, with and without a plastic shim.

Another situation where reference point calibration may be needed is when the value of a material property is built into the grid. For example, the thickness/lift-off grid in Section 5.6 incorporates the conductivity of the copper and steel layers. In such cases reference calibration on the actual substrate material eliminates errors that are introduced into the thickness estimation by a difference between the actual conductivity of the copper layer and the value assumed in the generation of the grid. Such differences may be due to variation between different parts.

There is a danger associated with the use of this method. Since it guarantees that measurements at the two reference points produce the prescribed parameter values, it is possible to force a measurement to match any region of any grid. If the reference points are chosen to fall on either side of the unknown property, then with this method practically any grid will produce results which, while being wrong, are not far out of the expected range, so that the user is not aware that there is problem with the measurement. Similarly, this method makes it possible to "calibrate out" errors due to hardware failure, improper connection, etc., or to hide real discrepancies between simulated and measured sensor behavior.

On a more fundamental level, by treating the calibration step simply as a linear transformation, with the two point reference part method the two calibration parameters are determined empirically, and lose their physical meaning, which is in discord with the principle of model-based sensor design. Relying on sound physical models, as opposed to empirical calibration, is what sets apart the spatially periodic quasistatic sensors from other eddy current and similar technologies. Still, as discussed earlier, there are many applications where use of this method is beneficial.

As a way of comparing the air and reference part calibration methods, consider the data in Table D.1. The table shows the results of using two point reference calibration with the measurements in Section 5.4. It has the same format as Table C.1. The two reference points chosen are with Aluminum 6061, which is the intermediate conductivity material, with no shim and with a 6.1 mm shim, corresponding to data sets 1 and 9 respectively. The reference conductivity used is 27.3 MS/m, taken from Table 5.2.

As expected, the results for Al 6061 are markedly better than those in Table C.1, with the average errors of the first twelve sets reduced by more than a factor of three for both the conductivity and lift-off estimates. In fact, the lift-off values for this material match the nominal values perfectly if listed with one digit after the decimal point. However, the improved performance for this material comes at the expense of measurement accuracy for other materials. While the estimated conductivity for copper and Al 2024 may be only a

Data set	***Cu 110***, $\sigma = 58$ MS/m				***Al 6061***, $\sigma = 27.3$ MS/m				***Al 2024***, $\sigma = 17.5$ MS/m				Nominal
	cond. [MS/m]	% error	lift-off [mm]	% error	cond. [MS/m]	% error	lift-off [mm]	% error	cond. [MS/m]	% error	lift-off [mm]	% error	lift-off [mm]
1	52.7	−9.2	3.35	+1.6	**27.3**	+0.1	**3.30**	+0.0	17.0	−2.6	3.34	+1.2	3.3
2	53.4	−7.9	4.18	+2.0	27.1	−0.8	4.11	+0.4	17.0	−2.6	4.17	+1.6	4.1
3	53.8	−7.3	4.87	+1.4	27.1	−0.8	4.77	−0.7	17.1	−2.2	4.83	+0.7	4.8
4	54.2	−6.5	5.68	+1.4	27.3	−0.1	5.59	−0.2	17.1	−2.2	5.67	+1.3	5.6
5	54.8	−5.6	6.57	+1.1	27.4	+0.4	6.49	−0.2	17.2	−1.5	6.55	+0.7	6.5
6	55.1	−5.0	7.40	+1.4	27.6	+1.0	7.30	+0.0	17.4	−0.7	7.38	+1.0	7.3
7	54.6	−5.8	8.07	+0.8	27.2	−0.2	7.95	−0.6	17.3	−1.0	8.03	+0.4	8.0
8	56.1	−3.2	8.89	+1.0	27.8	+1.8	8.78	−0.2	17.7	+1.1	8.84	+0.4	8.8
9	55.3	−4.6	9.53	+1.3	**27.3**	+0.1	**9.40**	+0.0	17.6	+0.4	9.44	+0.5	9.4
10	57.5	−0.9	10.31	+1.1	28.1	+2.9	10.21	+0.1	18.0	+2.7	10.29	+0.9	10.2
11	56.8	−2.0	10.95	+0.5	27.8	+1.9	10.86	−0.4	18.0	+2.7	10.91	+0.1	10.9
12	57.8	−0.3	11.74	+0.4	28.2	+3.4	11.66	−0.3	17.9	+2.3	11.73	+0.2	11.7
13	56.8	−2.1	12.75	+1.2	28.2	+3.2	12.54	−0.5	18.3	+4.6	12.61	+0.1	12.6
14	59.5	+2.6	13.48	+0.6	29.0	+6.1	13.35	−0.4	18.3	+4.5	13.49	+0.7	13.4
15	59.1	+2.0	14.12	+0.2	28.9	+5.8	13.98	−0.8	18.2	+4.0	14.09	−0.1	14.1
16	57.4	−1.0	14.90	+0.0	28.4	+4.2	14.79	−0.7	18.9	+7.9	14.88	−0.1	14.9
17	58.0	+0.1	15.30	−1.3	28.3	+3.7	15.20	−1.9	19.0	+8.5	15.27	−1.5	15.5
18	60.9	+5.0	16.08	−1.3	29.6	+8.4	16.00	−1.9	18.8	+7.5	16.05	−1.5	16.3
19	60.8	+4.8	16.73	−1.6	29.5	+8.1	16.64	−2.1	18.8	+7.4	16.70	−1.7	17.0
20	60.8	+4.9	17.55	−6.1	29.3	+7.2	17.43	−6.8	19.7	+12.8	17.52	−6.3	18.7
Average error magnitude, sets 1–12:		**4.9**		**1.2**		**1.1**		**0.3**		**1.8**		**0.7**	

Table D.1: Data from Table C.1, re-calibrated using the two point reference part method. The two reference points are set 1 and set 9 with the Al 6061 plate, printed in bold type in the table. As compared to the results in Table C.1, the average percent error for the reference material in the bracketed lift-off range is reduced by more than a factor of three, while the errors for the other two materials are higher than the errors of the measurements done with the one point air calibration method.

little worse in this case as compared to air calibration, a definite offset is apparent in the estimated lift-off for these materials, leading to much larger average errors. Thus the two-point reference calibration has introduced an accuracy bias towards Al 6061 samples with 3.3 to 9.4 mm lift-off.

D.4 Other calibration methods

There are other methods of obtaining the two calibration parameters, usually tailored to specific applications. For example, it is possible to use more than two reference points. In this case the system of equations for K and Z_{off} is over-determined, and can be solved in the least squares sense. In other applications these calibration methods may be combined in a multiple-step algorithm.

In all cases, the goal is to improve sensor design and models to the point where single point air calibration would provide adequate performance for most applications.

Bibliography

[1] N. J. Goldfine, "Uncalibrated, Absolute Property Estimation and Measurement Optimization for Conducting and Magnetic Media Using Imposed ω-k Magnetometry," Sc.D. thesis, Department of Mechanical Engineering, Massachusetts Institute of Technology, September, 1990.

[2] M. C. Zaretsky, L. Mouayad, J. R. Melcher, "Continuum Properties from Interdigital Electrode Dielectrometry," ***IEEE Transactions on Electrical Insulation***, vol. 23, no. 6, pp. 897–917, December 1988.

[3] M. C. Zaretsky, "Parameter Estimation Using Microdielectrometry with Application to Transformer Monitoring," Ph.D. thesis, Department of Electrical Engineering and Computer Science, Massachusetts Institute of Technology, Cambridge, MA, November 1987.

[4] J. R. Melcher, M. C. Zaretsky, "Apparatus and Methods for Measuring Permittivity in Materials," US patent number 4,814,690, March 21, 1989.

[5] P. Li, "Low Frequency, Millimeter Wavelength, Interdigital Dielectrometry of Insulating Media in a Transformer Environment," M.S. thesis, Department of Electrical Engineering and Computer Science, Massachusetts Institute of Technology, Cambridge, MA, May 1987.

[6] P. A. von Guggenberg, "Applications of Interdigital Dielectrometry to Moisture and Double Layer Measurements in Transformer Insulation," Ph.D. thesis, Department of Electrical Engineering and Computer Science, Massachusetts Institute of Technology, Cambridge, MA, June 1993.

[7] Y. Sheiretov, "Dielectrometry Measurements of Moisture Dynamics in Oil-Impregnated Pressboard," M.S. thesis, Department of Electrical Engineering and Computer Science, Massachusetts Institute of Technology, Cambridge, MA, May 1994.

[8] Y. Sheiretov, M. Zahn, "Dielectrometry Measurements of Moisture Dynamics in Oil-Impregnated Pressboard," ***IEEE Transactions on Dielectrics and Electrical Insulation***, vol. 2, pp. 329–351, June 1995.

[9] N. J. Goldfine, A. Washabaugh, J. V. Dearlove, P. A. von Guggenberg, "Imposed ω-k Magnetometer and Dielectrometer Applications," ***Review of Progress in Quantitative Nondestructive Evaluation***, vol. 12A, pp. 1115-1122, 1993.

[10] A. V. Mamishev, "Interdigital Dielectrometry Sensor Design and Parameter Estimation Algorithms for Non-Destructive Materials Evaluation," Ph.D. thesis, Department of Electrical Engineering and Computer Science, Massachusetts Institute of Technology, Cambridge, MA, May 1999.

[11] Y. Du, "Measurements and Modeling of Moisture Diffusion Processes in Transformer Insulation Using Interdigital Dielectrometry Sensors," Ph.D. thesis, Department of Electrical Engineering and Computer Science, Massachusetts Institute of Technology, Cambridge, MA, May 1999.

[12] J. R. Melcher, "Apparatus and Methods for Measuring Permeability and Conductivity in Materials Using Multiple Wavelength Interrogations," US patent number 5,015,951, May 14, 1991.

[13] N. J. Goldfine, "Magnetometers for Improved Materials Characterization in Aerospace Applications," ***Materials Evaluation***, 51 (3), pp. 396, March 1993.

[14] N. J. Goldfine, J. R. Melcher, "Magnetometer Having Periodic Winding Structure and Material Property Estimator," US patent number 5,453,689, September 26, 1995.

[15] N. J. Goldfine, D. Clark, H. Eckhardt, "Apparatus and Methods for Measuring Bulk Materials and Surface Condition for Flat and Curved Parts," US patent pending, ser. no. 60/002,804.

[16] N. J. Goldfine, D. Clark, T. Lovett, "Materials Characterization Using Model-based MWET," EPRI Topical Workshop: Electromagnetic NDE Applications in the Electric Power Industry, Charlotte, NC, 1995.

[17] N. J. Goldfine, D. E. Schlicker, W. M. Chepolis, "Robust, Absolute Property Measurements for Aerospace System Health Monitoring and Manufacturing Quality Control," Proceedings of BiNDT Conference "NDT '98," September 1998.

[18] J. M. Fisher, N. J. Goldfine, V. Zilberstein, "Cold Work Quality Assessment and Fatigue Characterization Using Conformable MWM™ Eddy-Current Sensors," 49th Defense Working Group on NDT, Biloxi, Mississippi, November 2000.

[19] V. Zilberstein, D. E. Schlicker, K. Walrath, V. Weiss, N. J. Goldfine, "MWM™ Eddy Current Sensors for Monitoring of Crack Initiation and Growth during Fatigue Tests and in Service," International Conference of Fatigue Damage in Structural Materials III, Hyannis, MA, September 2000.

[20] V. Weiss, N. J. Goldfine, M. Natishan, "Early Stage Fatigue Damage Characterization in Aluminum Alloys and Stainless Steels with Meandering Winding Magnetometer Technology," ASTM 30th National Symposium on Fatigue and Fracture Mechanics at Washington University, St. Louis, MO, June 1998.

[21] N. J. Goldfine, D. E. Schlicker, A. Washabaugh, "Surface-Mounted Eddy-Current Sensors for On-Line Monitoring of Fatigue Tests and for Aircraft Health Monitoring," Second Joint NASA/FAA/DoD Conference on Aging Aircraft, August 1998.

[22] N. J. Goldfine, "Conformable Meandering Winding Magnetometer (MWM) for Flaw and Materials Characterization in Ferrous and Nonferrous Metals," ***NDE Performance Demonstration, Planning and Research***, American Society of Mechanical Engineers, Pressure Vessels and Piping Division, PVP, vol. 352 1997. ASM. New York, NY, 1997.

[23] N. J. Goldfine, A. Washabaugh, V. Zilberstein, D. E. Schlicker, M. Fisher, T. Lovett, T. Yentzer, R. Pittman, "Scanning and Permanently Mounted Conformable MWM Eddy

Current Arrays for Fatigue/Corrosion Imaging and Fatigue Monitoring," USAF ASIP Conference, San Antonio, TX, December 2000.

[24] T. Yentzer, V. Zilberstein, N. Goldfine, D. Schlicker, D. Clark, "Anisotropic Conductivity Measurements for Quality Control of C-130/P-3 Propeller Blades Using MWM™ Sensors with Grid Methods," Fourth DoD/FAA/NASA Conference on Aging Aircraft, St. Louis, MO, May 2000.

[25] N. J. Goldfine, Y. Sheiretov, A. Washabaugh, V. Zilberstein, "Materials Characterization and Flaw Detection for Metallic Coating Repairs," ***Insight: Non-Destructive Testing and Condition Monitoring***, vol. 42, no. 12, December 2000.

[26] N. J. Goldfine, D. E. Schlicker, Y. Sheiretov, A. Washabaugh, V. Zilberstein, "Conformable Eddy-Current Sensors and Arrays for Fleet-Wide Gas Turbine Component Quality Assessment," ASME Turbo Expo Land, Sea, & Air, New Orleans, LA, 2001.

[27] V. Zilberstein, Y. Sheiretov, A. Washabaugh, Y. Chen, N. J. Goldfine, "Applications of Spatially Periodic Field Eddy Current Sensors for Surface Layer Characterization in Metallic Alloys," 27th Annual Review of Progress in QNDE, Iowa State University, Ames, Iowa, July 2000.

[28] N. J. Goldfine, T. Lovett, Y. Sheiretov, P. J. Zombo, "Dielectrometers and Magnetometers, Suitable for In-situ Inspection of Ceramic and Metallic Coated Components," SPIE proceedings, vol. 2459, pp. 164–174, 1995.

[29] N. J. Goldfine, V. Zilberstein, "Recent Applications of Meandering Winding Magnetometers to Materials Characterization," ***Insight: Non-Destructive Testing and Condition Monitoring***, vol. 42, no. 1, 2000.

[30] N. J. Goldfine, J. T. Lovett, Y. J. Zhao, "A New Eddy-Current Based Technology for Repeatable Residual Stress and Age Degradation Monitoring," ASNT International Chemical and Petroleum Industry Inspection Technology, IV Topical Conference, Houston, TX, June 1995.

[31] N. J. Goldfine, D. E. Schlicker, K. Walrath, A. Washabaugh, V. Zilberstein, "Applications of MWM-Array Eddy Current Sensors to Corrosion Mapping," 4th International Aircraft Corrosion Workshop, Naval Air Warfare Center, Patuxent River, MD, August 2000.

[32] N. J. Goldfine, A. Washabaugh, D. E. Schlicker, "High Resolution Inductive Array Imaging of Buried Objects," SPIE AeroSense 2000, Orlando, FL, April 2000.

[33] N. J. Goldfine, D. E. Schlicker, A. Washabaugh, D. Clark, M. Zahn, "New Quasistatic Magnetic and Electric Field Imaging Arrays and Algorithms for Object Detection, Identification, and Discrimination," ***Proceedings of SPIE, the International Society for Optical Engineers***, vol. 3710, no. 1, pp. 89–100, 1999.

[34] N. J. Goldfine, D. E. Schlicker, "Magnetometer with Waveform Shaping," US patent number 6,144,206, November 2000.

[35] N. J. Goldfine, D. E. Schlicker, M. Zahn, W. D. Ryan, Y. Sheiretov, A. Washabaugh, "Magnetometer and Dielectrometer Detection of Subsurface Objects," US patent pending, ser. no. 09/488,241.

[36] A. Washabaugh, Y. Sheiretov, D. E. Schlicker, N. J. Goldfine, "Non-Contact Capacitive Sensing Dielectrometers for Characterization of Adhesives and Epoxies," ASNT Fall Conference 2000, Indianapolis, IN, November 2000.

[37] B. C. Lesieutre, A. V. Mamishev, Y. Du, E. Keskiner, M. Zahn, G. C. Verghese, "Forward and Inverse Parameter Estimation Algorithms of Interdigital Dielectrometry Sensors," ***IEEE Transactions on Dielectrics and Electrical Insulation***, 2001.

[38] N. J. Goldfine, J. R. Melcher, "Apparatus and Methods for Obtaining Increased Sensitivity, Selectivity, and Dynamic Range in Property Measurements Using Magnetometers," US patent number 5,629,621, May 13, 1997.

[39] James E. Lenz, "A Review of Magnetic Sensors," ***Proceedings of the IEEE***, vol. 78, no. 6, June 1990.

[40] D. J. Mapps, "Magnetoresistive sensors," ***Sensors and Actuators***, A 59 (1997), pp. 9–19.

[41] D. J. Mapps, "Non Linear Magnetoresistance," ***Nonlinear Electromagnetic Systems***, IOS Press, 1996.

[42] M. Uesaka, T. Nakanishi, K. Miya, H. Komatsu, K. Aoki, K. Kasai, "Micro Eddy Current Testing by Micro Magnetic Sensor Array," ***IEEE Transactions on Magnetics***, vol. 31, no. 1, January 1995.

[43] D. J. Staton, Y. P. Ma, N. G. Sepulveda, J. P. Wikswo Jr., "High-resolution magnetic mapping using a squid magnetometer array," ***IEEE Transactions on Magnetics***, vol. 27, no. 2, March 1991.

[44] S. S. Tinchev, J. H. Hinken, M. Stiller, A. Baranyak, D. Hartmann, "High-T_C RF SQUID magnetometer system for high-resolution magnetic imaging," ***IEEE Transactions on Applied Superconductivity***, vol. 3, no. 1, pt. 4, March 1993, pp. 2469–71.

[45] J. H. Hinken, Y. Tavrin, "Detection of Segregation in Aero Engine Turbine Disks with the Thermoelectric SQUID Method," ASNT Fall Conference and Quality Testing Show, Phoenix, Arizona, October 1999.

[46] W. G. Jenks, S. S. H. Sadeghi, J. P. Wikswo Jr., "SQUIDs for nondestructive evaluation," ***Journal of Physics D: Applied Physics***, vol. 30, no. 3, pp. 293–323, 7 February 1997.

[47] Y. Sheiretov, "Continuum Modeling of the Flexible Interdigitated Electroquasistatic Sensor: Numerical Methods for Parameter Estimation," Technical Report, Laboratory for Electromagnetic and Electronic Systems, Massachusetts Institute of Technology, Cambridge, MA, November 1997.

[48] H. A. Haus, J. R. Melcher, "Electromagnetic fields and energy," Prentice-Hall, Inc., New Jersey, 1989.

[49] H. H. Woodson, J. R. Melcher, "Electromechanical Dynamics," John Wiley & Sons, New York, 1968.

[50] J. R. Melcher, "Continuum Electromechanics," The MIT Press, Cambridge, MA, 1981.

[51] F. Oberhettinger, "Fourier Expansions, A Collection of Formulas," Academic Press, 1973.

[52] I. S. Gradshteyn, I. M. Ryzhik, "Table of Integrals, Series, and Products," Fifth edition, Academic Press, 1994.

[53] F. B. Hildebrand, "Advanced Calculus for Applications," 2nd Edition, Prentice-Hall, Inc., Englewood Cliffs, NJ, 1976.

[54] N. J. Goldfine, M. Zahn, A. V. Mamishev, D. E. Schlicker, A. P. Washabaugh, "Methods for Processing, Optimization, Calibration, and Display of Measured Dielectrometry Signals Using Property Estimation Grids," US patent pending, ser. no. 09/310,507.

[55] J. D. Jackson, "Classical Electrodynamics," Second edition, John Wiley & Sons, New York, 1975.

[56] A. E. Siegman, "Quasi fast Hankel transform," ***Optics Letters***, vol. 1, no. 1, pp. 13–15, July 1977.

[57] A. B. Pippard, "Magnetoresistance in Metals," ***Cambridge University Press***, 1989.

[58] J. Smit, "Magnetoresistance of Ferromagnetic Metals and Alloys at Low Temperatures," ***Physica XVI***, no. 6, pp. 612, June 1951.

[59] A. Fert, I. A. Campbell, "Electrical resistivity of ferromagnetic nickel and iron based alloys," ***Journal of Physics F: Metal Physics***, vol. 6, no. 5, pp. 849, 1976.

[60] I. A. Campbell, A. Fert, in "Ferromagnetic Materials," edited by E. P. Wohlfarth (Amsterdam, Holland, 1982), vol. 3, pp. 769.

[61] R. P. Hunt, "A magnetoresistive Readout Transducer," ***IEEE Transactions on Magnetics***, vol. MAG-7, no. 1, March 1971

[62] D. J. Mapps, "Magnetoresistance," ***Applied Magnetism***, pp. 377–403, 1994.

[63] T. Kawai, T. Sagara, Y. Syonowaki, A. Tanaka, "Magnetoresistive Sensors," ***IEEE Translation Journal on Magnetics in Japan***, vol. 8, no. 6, pp. 381, June 1993.

[64] N. Smith, F. Jeffers, J. Freeman, "A High-Sensitivity Magnetoresistive Magnetometer," ***Journal of Applied Physics***, 69 (8), 15 April 1991.

[65] R. Hood, L. M. Falicov, "Theory of the negative magnetoresistance in magnetic metallic multilayers," ***Materials Research Society Symposium Proceedings***, vol. 313, San Francisco, California, April 12–16, 1993.

[66] M. N. Baibich, J. M. Broto, A. Fert, F. Nguyen Van Dau, F. Petroff, P. Eitenne, G. Creuzet, A. Friedrich, J. Chazelas, "Giant Magnetoresistance of (001)Fe/(001)Cr Magnetic Superlattices," ***Physical Review Letters***, vol. 61, no. 21, pp. 2472, November 1988.

[67] G. Binasch, P. Grünberg, F. Saurenbach, W. Zinn, "Enhanced magnetoresistance in layered magnetic structures with antiferromagnetic interlayer exchange," ***Physical Review B***, vol. 39, no. 7, pp. 4828, March 1989.

[68] R. E. Camley, J. Barnaś, "Theory of Giant Magnetoresistance Effects in Magnetic Layered Structures with Antiferromagnetic Coupling," ***Physical Review Letters***, vol. 63, no. 6, pp. 664, August 1989.

[69] S. S. P. Parkin, Z. G. Li, D. J. Smith, "Giant magnetoresistance in antiferromagnetic Co/Cu multilayers," ***Applied Physics Letters***, vol. 58 (23), pp. 2720, June 1991.

[70] S. S. P. Parkin, "Oscillations in giant magnetoresistance and antiferromagnetic coupling in $[Ni_{81}Fe_{19}/Cu]_N$ multilayers," ***Applied Physics Letters***, vol. 60 (4), pp. 512, January 1992.

[71] L. M. Falicov, "Metallic magnetic superlattices," ***Physics Today***, October 1992.

[72] S. S. P. Parkin, R. F. Marks, R. F. C. Farrow, G. R. Harp, Q. H. Lam, R. J. Savoy, "Giant magnetoresistance and enhanced antiferromagnetic coupling in highly oriented Co/Cu (111) superlattices," ***Physical Review B***, vol. 46, no. 14, pp. 9262, October 1992.

[73] S.-F. Lee, W. P. Pratt Jr., Q. Yang, P. Halody, R. Loloee, P. A. Schroeder, J. Bass, "Two-channel analysis of CPP-MR data for Ag/Co and AgSn/Co multilayers," ***Journal of Magnetism and Magnetic Materials***, 118, pp. L1, 1993.

[74] "Magnetic Ultrathin Films," ***Materials Research Society Symposium Proceedings***, vol. 313, San Francisco, California, April 12–16, 1993.

[75] "NVE Sensor Engineering and Application Notes," revision 9/10/98, Nonvolatile Electronics, Inc., Eden Prairie, MN, *http://www.nve.com*.

[76] J. Van de Vegte, "Feedback control systems," Prentice-Hall, Inc., New Jersey, 1990.

[77] "CRC Handbook of Chemistry and Physics," 76th edition, CRC Press, Inc., Boca Raton, FL, 33431, 1996.

[78] "Electrical and Magnetic Properties of Metals," ASM Ready Reference, ASM International, Materials Park, OH 44073, 2000, Table 2.1.

[79] R. E. Rosensweig, "Magnetic Fluids," ***International Science and Technology***, 55, pp. 48–66, July 1966.

[80] R. E. Rosensweig, "Ferrohydrodynamics," Cambridge University Press, Cambridge, 1985.

[81] W. H. Press, B. P. Flannery, S. A. Teukolsky, W. T. Vetterling, "Numerical Recipes; The Art of Scientific Computing," 2nd Edition, Cambridge University Press, 1992.

[82] G. N. Watson, "A Treatise on the Theory of Bessel Functions," Cambridge University Press, 1966.

[83] N. J. Goldfine, D. E. Schlicker, A. Washabaugh, "Absolute Property Measurement with Air Calibration," US patent number 6,188,218, February 13, 2001.